MAKING COCHLEAR-IMPLANT ELECTRODE ARRAY INSERTION LESS INVASIVE, SAFER, AND MORE EFFECTIVE THROUGH DESIGN, MAGNETIC STEERING, AND IMPEDANCE SENSING

By

Katherine E. Riojas

Dissertation

Submitted to the Faculty of the

Graduate School of Vanderbilt University

in partial fulfillment of the requirements

for the degree of

DOCTOR OF PHILOSOPHY

in

Mechanical Engineering

August 31st, 2021

Nashville, Tennessee

Approved:

Robert J. Webster III, Ph.D.

Robert F. Labadie, M.D., Ph.D.

Nabil Simaan, Ph.D.

Jack Noble, Ph.D.

Jason Mitchell, Ph.D.

Acknowledgments

The following dissertation work would not have been possible without the guidance, support, and collaboration of a long list of people. First and foremost, thank you to my advisor Dr. Bob Webster for always believing in me and helping me to enter the world of medical devices and surgical robotics. Without your recruitment and support, I would not have been lucky enough to end up at Vanderbilt in the MED Lab and in VISE. Thank you for giving me the freedom to pursue the things that excited me throughout graduate school, for helping me see what mattered most in each project, and for being understanding when things inevitably pivot (and for your guidance through those pivots). Next, thank you to all of the members of my dissertation committee, including first Dr. Rob Labadie who I am lucky to have as a second advisor and to whose lab (the CAOS lab) I was fortunate enough to work in alongside the MED Lab. Thanks for enabling me to watch numerous cochlear implant surgeries, for inspiring me to continue pursuing cochlear implant technologies throughout graduate school, and for helping me complete the cadaver experiments in Chapter 2 and Chapter 3. And a particular thank you for believing in the tool in Chapter 2 throughout the hurdles of development all the way to clinical translation. Thank you to Dr. Nabil Simaan for teaching me an invaluable course on Robot Manipulators where I learned skills and techniques that I have used throughout this dissertation work and will use beyond. Additionally, thank you for providing guidance that was crucial in the development of the kinematic model of Chapter 4. Next, thank you to Dr. Jack Noble for also teaching me a key course of my graduate school tenure which drastically improved my coding abilities, for answering my numerous questions about the Cochlear Implant Processing software, and for helping prepare for the clinical trial in Chapter 2. Finally, thank you to Dr. Jason Mitchell for helping brainstorm designs for the insertion tool in Chapter 2, for being the invaluable continuous thread in the minimally invasive clinical trials, and for teaching me to use the Microtable equipment. In sum, thank you to all of the committee members for their discussions and feedback through the years that have greatly improved this work.

I have had the pleasure to work with many talented engineers, computer scientists, and clinicians during my time at Vanderbilt. I will try to name everyone in this acknowledgement, but nonetheless, a sweeping generalization - thank you to everyone in VISE. This institute is such a unique group of amazing and kind people who love learning and doing exciting research, and the atmosphere itself makes each and every member better for it. In particular, I would like to thank Dr. Trevor Bruns, a graduate of the MED Lab and CAOS Lab. Trevor has an eye for detail, love for learning, and talent for engineering that made working with him not only fun, but makes those working with him better engineers. Thank you to Josephine Granna for discussing my research in Chapter 4 with me on a regular basis, I greatly appreciate our meetings and your advice. Additionally, I feel very fortunate to have had the opportunity to work with Richard Hendrick, Neal Dillon, Patrick Anderson, Patrick Wellborn, and Loris Fichera during the beginning of graduate school and/or throughout graduate school. They helped teach me what graduate school in the MED Lab and CAOS lab is all about and provided crucial advice and support as I was getting started. Thank you to the residents Dr. Mike Freeman and Dr. Miriam Smetak for providing the dissected cochlea models used in the cadaveric experiments of Chapter 3 and Chapter 4. Finally, thank you to Max Emerson, Tayfun Efe Ertop, Margaret Rox, and James Ferguson for fearlessly going through classes with me and for always being ready to 'hit the whiteboard' and discuss problems. And another sweeping thank you to all of the past and present CAOS and MED Lab

members. I feel very lucky to have joined a group of not only great engineers, but great people. A thank you also to Myrtle Daniels, Bill Rodriguez, and Michelle Bukowski for their tireless daily efforts to keep the Mechanical Engineering department and VISE moving in the right direction. Our interactions were always a bright spot in my day. A big thanks goes to the National Institutes of Health (Award Numbers R01DC008408 and R01DC013168) and the National Science Foundation (Graduate Research Fellowship DGE-1445197/1937963) for providing the funding that made the projects in this dissertation possible.

Most importantly, thank you to my incredible family and friends. Knowing that they all were just a walk/drive/flight/phone call away made all of the difference and I could not have persevered through the ups and downs of graduate school without them.

TABLE OF CONTENTS

LIST OF TABLES

LIST OF FIGURES

Chapter 1

Introduction

1.1 Motivation

1.1.1 Hearing and Hearing Loss

Traditional hearing individuals begin their sensation of sound when a sound wave travels down their ear canal to their eardrum and causes it to vibrate. An image including the outer, middle, and inner ear is shown in Fig. 1.1(a) for reference. Eardrum vibrations subsequently cause the three small bones of the inner ear—the ossicles—to also vibrate, which amplifies the vibrations and sends them to the cochlea (Fig. 1.1(b)). The spiral-shaped cochlea has two main channels—the scala tympani (ST) and the scala vestibuli (SV), which are each filled with a conductive fluid called perilymph [1]. The channels are separated by an elastic structure called the basilar membrane as well as a third channel called the scala media (SM) (Fig. 1.1(c)) [1], [2]. The transferred vibration causes a fluid wave to propagate through the SV and out the ST (connected via an opening at the apex called the helicotrema) and a traveling wave moves along the basilar membrane which is lined with sensory hair cells [1]. The traveling wave on the membrane causes these hair cells to move and causes pores in the stereocilia on top of the hair cells to open. Chemicals move into these pores, which causes the original mechanical motion of the sound wave to be converted to an electric signal. The auditory nerve then carries that information to the brain for interpretation [2], [3].

For individuals with hearing loss, one or multiple components of this hearing pathway is not or are not functioning properly. Hearing loss is the fourth leading cause of disability globally and can lead to a variety of challenges, one of the largest being difficulty communicating with others [4]. This difficulty can lead to feelings of isolation and challenges navigating certain environments. Hearing loss has also been linked with changes in cognitive ability, even correlated with increased likelihood of dementia and Alzheimer's disease [5], [6]. Hearing aids and cochlear implants (CIs)

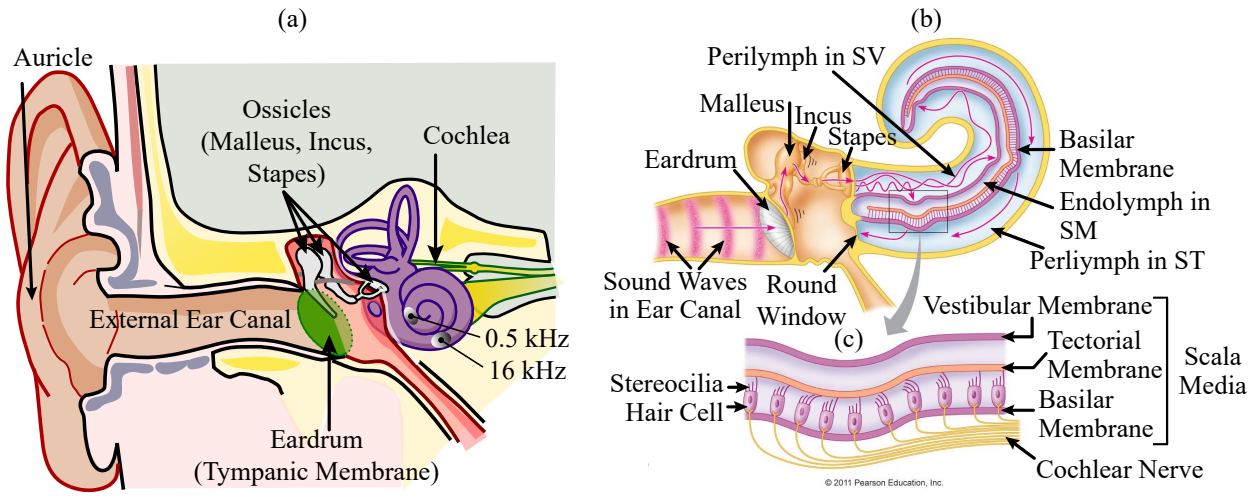

Figure 1.1: (a) *Anatomy of Human Ear with Cochlear Frequency Mapping* by InductiveLoad/ CC-BY-SA-3.0: Full hearing pathway including outer, middle, and inner ear and (b) Sound transduction by hair cells ©2011 Pearson Education Inc., obtained from [9]: Detailed view of hearing pathway showing a sound wave vibrating the eardrum, which then vibrates the ossicles, which then sends a pressure wave down the SV and back through the ST. (c) This wave vibrates the hair cells that line the basilar membrane. The vibration of the hair cells enables the conversion of the sound wave to an electric signal and the auditory nerve sends this information to the brain.

are two of the main devices used to help augment or restore hearing to those with some or profound hearing loss [4]. Hearing aids simply amplify sound, but an individual is still relying on the surviving hair cells of their cochlea to interpret these signals [7]. For individuals with profound sensorineural hearing loss caused by inner ear malfunction, CIs are typically recommended because they bypass the traditional hair cell pathway and use surgically implanted electrode arrays (EAs) to directly stimulate the auditory nerve [8] (see Fig. 1.2). The work in this dissertation focuses on improving CI surgery.

1.1.2 Hearing Restoration - Cochlear Implants

A CI is one of the most successful neuroprosthetic devices to date [10]. This device sends digitized sound stimulus information from a microphone/battery pack/speech processor system to an external transmitting coil held in place by magnets [11]. For a particular CI, a processing strategy is selected (such as continuous-interleaved sampling) and the audiologist will define a user's unique "MAP", or set of processor instructions [12]. The implanted receiver/stimulator

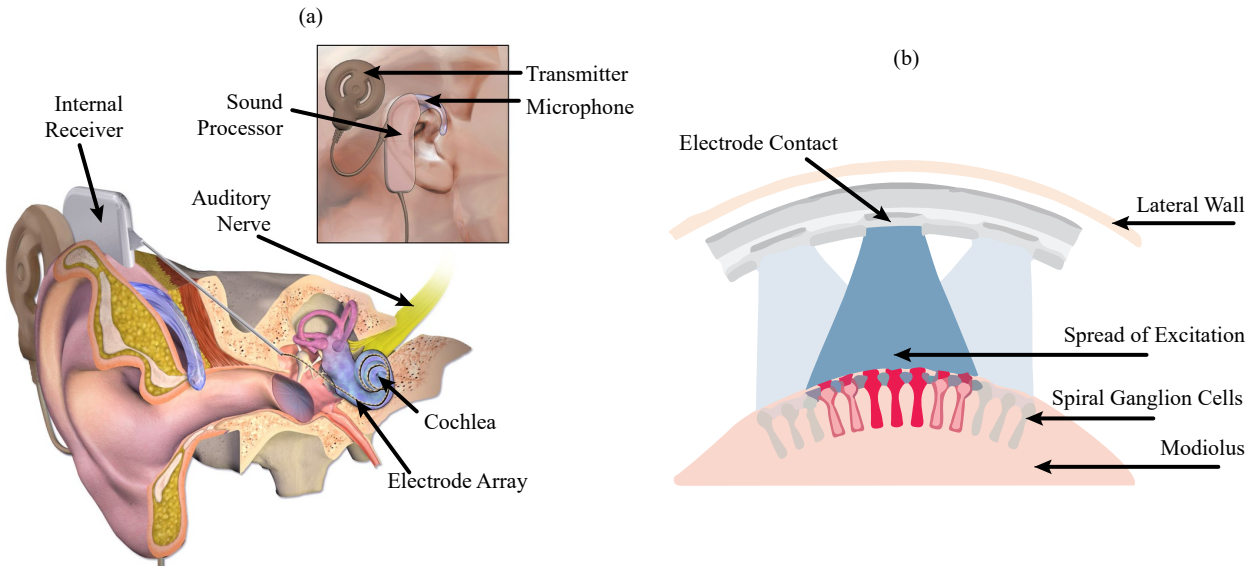

Figure 1.2: (a) Overview of CI components. The microphone detects mechanical sound waves and the processor encodes these sounds and sends them to the internal (subcutaneous) receiver that is electromagnetically coupled to the transmitter. The internal receiver then sends the digital information to the cochlea for auditory nerve stimulation. Source: Blausen.com staff (2014). "Medical gallery of Blausen Medical 2014". WikiJournal of Medicine 1 (2). DOI:10.15347/wjm/2014.010. ISSN 2002-4436. (b) Within the cochlea, the digitized sound information is emitted from the electrode contacts to stimulate the spiral ganglion cells that lie along the modiolar wall. Modified image from: https://pronews.cochlearamericas.com/perimodiolar-advantage-cochlear-ci532-slim-modiolar-electrode/

receives electromagnetically transmitted information from the processor and sends these inputs to the EA implanted in the cochlea (see Fig. 1.2(a)) [10]. Current flows to or between electrode contacts (depending on stimulation strategy) on the implanted EA to activate neural endings near the electrode-neuron interface (near the modiolus, the central core of the cochlea that houses spiral ganglion neurons) (Fig. 1.2(b)) [13]. The neural pathway frequency map for natural hearing is well-known and consists of decreasing characteristic frequency along the length of the cochlea [14] (see Fig.1.1(a)). Because of this neural ending frequency-dependent layout, EA efficacy is very sensitive to EA placement [10], [15]. The preferred placement of the EA is in the ST of the cochlea because it is larger and will hold the EA closer to the neural endings [16].

1.1.3 Cochlear-Implant Electrode Array Types

It is important to note that there are two main EA types - termed "straight" and "precurved" for the remainder of this dissertation [17]. Originally, the first EA was a single wire electrode [18]. As EAs have become more advanced, more stimulation sites and more advanced carriers (i.e., silicone) have been added, but the same principle of a flexible carrier with electrode(s) contacts has been utilized. The mechanism of curvature of these straight EAs is by contact with the lateral wall (wall opposite the modiolus) and the final scalar position of these EAs is along the lateral wall (see Fig. 1.3(a)). As more research has been done to improve CI efficacy, it was discovered that the optimal configuration of an EA is to have the electrode contacts close to the neural endings they stimulate, i.e., hugging the modiolus [19]. This intimate placement goal led to the development of precurved, styleted (also called peri-modiolar) EAs, see Fig. 1.3(b). When the stiff (relative to the EA body) stylet is in place, the precurved EA body is held in a straight configuration and it will return to its precurved shape upon stylet removal. These EAs can be inserted with the stylet in place, and the stylet is removed upon completion of the insertion such that the silicone carrier ideally conforms to the modiolar wall. However, this approach can lead to intracochlear trauma due to the stylet stiffness. To overcome this issue, an "Advanced-Off-Stylet" (AOS) technique was developed, in which the stylet is held in place after the carrier reaches the basal turn, and then the surgeon continues to advance the silicone carrier while holding the stylet in place such that the curvature gradually increases throughout the insertion and ideally no EA component contacts the lateral wall. Unfortunately, this ideal AOS insertion is challenging for a surgeon to implement in practice.

Both of these EA types are used frequently in CI surgery and both have inherent advantages and disadvantages which will be detailed in Sec. 1.4 after explaining intracochlear trauma and its relationship to hearing outcomes. However, regardless of EA type, quality insertion remains a challenge in CI surgery.

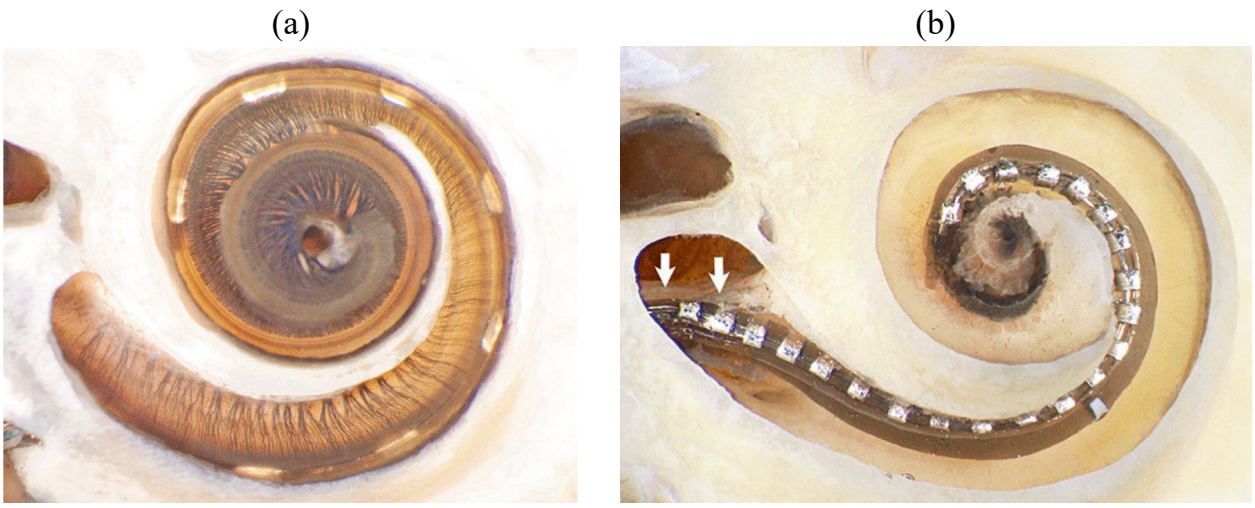

Figure 1.3: CI EA types [20]: (a) straight, lateral-wall EAs are flexible, silicone electrode carriers that bend upon contact with the lateral wall of the ST. The final goal position of these arrays is along the lateral wall and (b) precurved, styleted, perimodiolar EA. These EAs are initially straight when the stylet is in place. The precurvature of the EAs causes the EA to bend upon stylet removal into a cochlea-like curvature. The final goal position of these arrays is along the modiolus.

1.1.4 Limitations of Cochlear Implant Surgery

Since FDA approval of CIs in 1984, CI recipients have experienced significant speech perception improvements [21]. Improvements can be attributed to multiple channels and sites of stimulation, more sophisticated sound coding strategies, and individuals with residual hearing receiving implants [22]. Despite this success, there is a large disparity in the number of CI candidates and the number of people who elect to get a CI, with only about 6% of candidates electing to get a CI as of 2010 [23]. This disparity results from a myriad of different factors, but two factors that can contribute to fewer individuals electing to get this procedure are the invasiveness of the surgery and variable and/or suboptimal hearing outcomes.

Regarding invasiveness, the current state-of-the-art CI surgical procedure requires a mastoidectomy to insert the EA, an invasive procedure that requires the removal of a pocket of bone behind the external ear [24]. If access to the cochlea for EA implantation could be made less invasive, more candidates may elect to get the procedure and may enjoy the benefits that a CI can bring.

Regarding variable and suboptimal hearing outcomes, clinical outcomes to cochlear implantation still vary greatly, and many implanted individuals struggle with speech perception in unfavor-

able (e.g., noisy) listening conditions [25]–[28]. Two sources of variable outcomes and deteriorating performance in noisy conditions are intracochlear trauma during EA insertion and poor final intracochlear placement [29], [30].

Next, the current attempts to reduce the invasiveness of the EA insertion procedure will be detailed, as well as non-robotic insertion tools associated with the traditional and with the minimally invasive approaches. Then, definitions and quantification of intracochlear trauma (and its effect on hearing outcomes) will be discussed. This discussion will lead to detailing developed robotic insertion tools and steering mechanisms to decrease insertion trauma. Finally, current attempts to improve feedback with the aim of improving intracochlear placement and reducing trauma during EA insertion will be discussed.

1.2 Minimally Invasive Cochlear Implant Surgery

Traditional CI surgery requires performing a mastoidectomy. Recent research has investigated whether the mastoidectomy could be avoided and access to the cochlea could be obtained in a less invasive fashion. There are a variety of different surgical techniques to avoid mastoidectomy including the pericanal technique, the suprameatal approach, the transcanal (veria) approach, and a single drilled tunnel to the cochlea [31]–[33]. The single drilled tunnel approach achieves the best angle of approach for EA insertion into the cochlea [34]. This single drilled tunnel approach will be termed minimally invasive cochlear implant surgery (MICIS) for the remainder of this work.

MICIS leverages image guidance technology and preoperative segmentation of patient anatomy to plan a safe drill path to the cochlea. A variety of approaches have been employed to guide the drill along the specified trajectory both in a research and clinical setting. Research implementations include a parallel robot [35], [36], an industrial robot arm guided by optical tracking of the robot and the patient [37], [38], and a hand-drilled conical path using image guidance [39]. Clinical implementations include using a custom serial robot arm in conjunction with optical tracking [40] and using patient-specific microstereotactic frames [32]. MICIS has been shown to be a safe and effective method of achieving less invasive cochlea access, with increased reliability, increased

standardization, and decreased scarring compared to the standard approach [39]. Decreasing the invasiveness could also lead to shorter time to activation, potentially expediting hearing rehabilitation [41]. Despite the success of the minimally invasive approach, the final step of the procedure—insertion of the EA, remains a significant challenge due to the visualization and dexterity limitation imposed by the decreased invasiveness and the narrow tunnel surrounded by spiculated bone that can deflect the EA from its path [42]. Insertion down the tunnel is particularly challenging for the more flexible, large-diameter straight EAs. It would be desirable to have a tool to use in upcoming clinical procedures to help perform this final step. It would be particularly useful if this insertion tool was not only compatible with the image-guided MICIS workspace, but also non-robotic and easily sterilizable to enable expedited clinical translation. Current non-robotic tools will be detailed below.

1.3 Non-Robotic Cochlear Implant Insertion Tools

There are a variety of commercial and developmental insertion tools for CI EA insertion. The focus of this section is on non-robotic tool options. Primarily, this category is comprised of what will be termed "traditional" tools from CI manufacturers. Examples of these tools can be seen in Fig. 1.4 including forceps (angled, straight, cupped), claws, graspers, and custom tools for specific EAs. These tools are meant to be operated within the relatively wide field of a mastoidectomy (with few maneuverability constraints) and thus are often not compatible with MICIS. Even if a tool is compatible with MICIS (e.g., forceps), they are difficult to use within the resulting MICIS workspace, they still rely on a surgeon's hand-eye coordination to thread the EA successfully into the cochlea, and they do not protect the EA on its journey through the bony drilled tunnel. A few custom tools have been developed such as the split-tube design used after robotic MICIS [40], and Kratchman *et al.* developed a manual tool for AOS insertion that is compatible with the MICIS workspace of [32]; however, this tool is not compatible with larger diameter EAs. Chapter 2 will focus on conception, development, and clinical translation of a new manual insertion tool for MICIS EA insertion of larger diameter EAs.

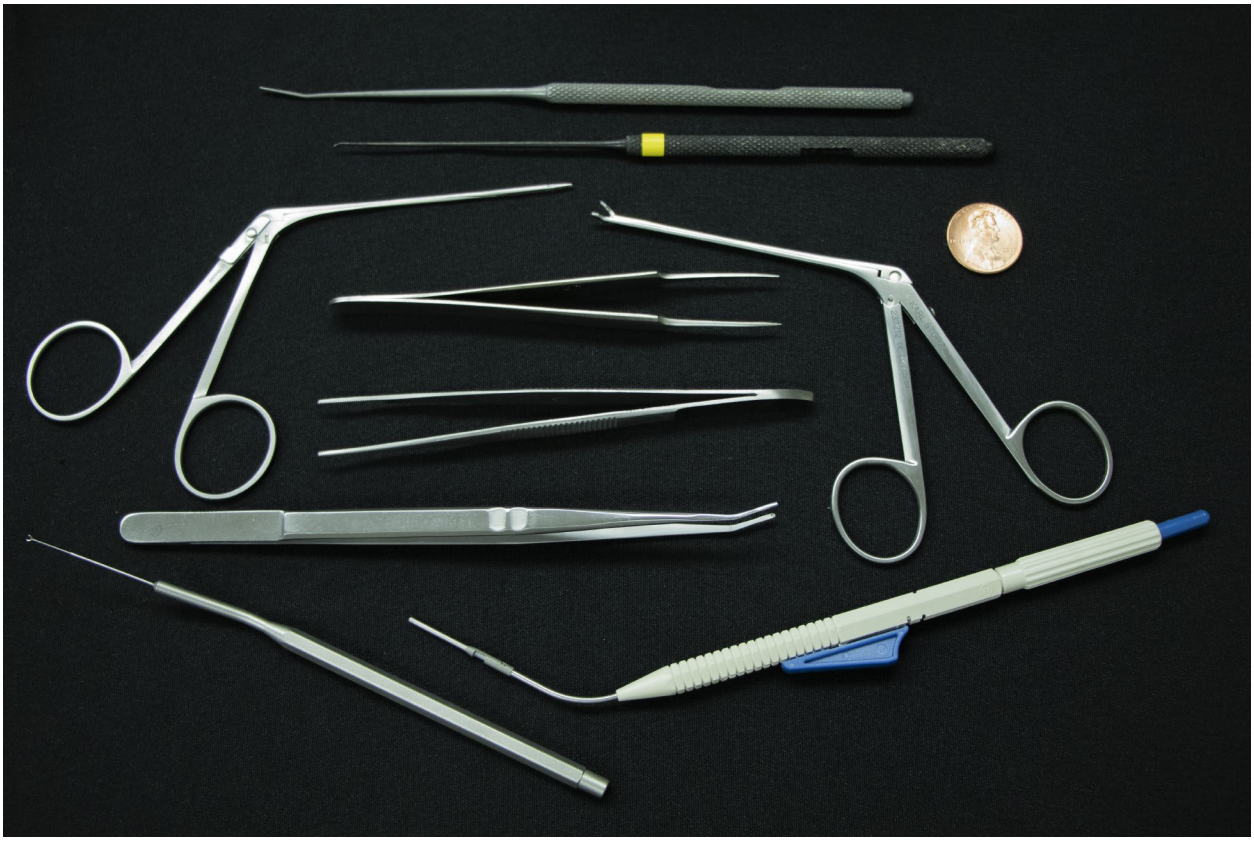

Figure 1.4: Examples of commercial CI EA insertion tools such as forceps, graspers, claws, and a custom tool (bottom-right)

Besides development of new tools that can be compatible with the MICIS workspace, a primary area of insertion tool development is in reducing trauma during insertion to improve hearing outcomes. This is the main motivation for robotic tools for CI EA insertion. Intracochlear trauma and reasoning for trauma reduction will be explained next. Then, robotic insertion tool developments will be discussed.

1.4 Trauma and Trauma Quantification

As previously mentioned, CI surgeons strive to optimize the interface between an EA and the neural endings it is attempting to stimulate whenever possible. One way they do this is by using a "soft-surgery" [43] technique to achieve an atraumatic insertion. This minimization of trauma essentially means preserving the patient's natural inner ear structures as much as possible so as to maintain the natural hearing pathway. This minimization can lead to improved hearing outcomes and improved residual hearing preservation [44]. This preservation is especially important as electro-acoustic stimulation (i.e., combining a CI with a hearing aid) becomes more popular and has been shown to generate better hearing outcomes than electric stimulation alone [29], [45]. Researchers typically use a scale of 0-4 to grade trauma on histologic cochlea specimens. Grading details can be viewed in Table 1.1.

Because histologic results cannot be obtained in real-time, forces have been used as a surrogate for trauma and have shown to be linked to trauma [46]–[48]. Force data has been used in laboratory settings for evaluating tools and techniques for force reduction (and thus implied trauma reduction) [46], [49]–[57]. The force required to cause trauma is near or below the limits of human perception [58]–[61]. Thus, as will be discussed in Sec. 1.5, robotic tools have been in development for many years, with the first clinical use of a robotic tool for CI EA insertion in 2020 [62]. Often, in evaluating new tools and techniques, the overall force norm is used for evaluation; however, recent advancements have shown that force direction with respect to the coordinate frame of the cochlea [63] plays an important role [64]. Typical reported metrics are the average force, the peak force, and more recently proposed metrics are the jerk of the insertion force profile ($d\boldsymbol{F}/dt$), the number

Table 1.1: Intracochlear trauma grading scale [47], [65]

Grade	Description
0	No observable macroscopic trauma
1	Elevation of the basilar membrane
2	Rupture of the basilar membrane
3	Dislocation of EA into SV (i.e., translocation)
4	Fracture of osseous spiral lamina or modiolus, or tear in tissues of stria vascularis/spiral ligament complex

of sudden rises in force, the change in force momentum, and the amount of time the force was above a certain threshold [56].

There are typically four main insertion complications to avoid when inserting an EA: translocation (grade 3 trauma), tip fold-over, tip scraping, and buckling. Examples of these complications can be viewed in Fig. 1.5. A translocation (also termed scalar deviation) is when the EA ruptures the basilar membrane and moves from the ST to the SV (Fig. 1.5(a)). This transposition disrupts the traditional hearing pathway and thus results in a total loss of residual hearing [16]. Tip fold-over occurs when the most apical section of the EA bends back on itself such that there is a fold in a section of the apical end of the EA [66] (Fig. 1.5(b)). When fold-over occurs, it causes at least one, if not both, of the electrode contacts involved in the fold to not be effective at stimulating neural endings (because they would cause interference, or are facing the wrong direction) [67]. Tip scraping (Fig. 1.5(c)) is when the tip of the EA damages the lateral wall upon insertion and may lead to damage of structures needed for residual hearing [68], [69]. Finally, buckling occurs when the flexible EA body gives way under insertion forces and axial insertion forces no longer translate to tip movement. A discontinuity in curvature occurs as a result, such as in Fig. 1.5(d). This buckling can occur both inside the cochlea (potentially damaging important inner ear structures like the spiral lamina [20]) or outside the cochlea in the natural middle ear space, prohibiting further advancement of the EA and resulting in a shallow angular insertion depth (AID) [42].

1.4.1 Advantages and Disadvantages of Electrode Array Types

Now that the relationship between trauma and hearing outcomes has been discussed, the relationship between insertion of a certain type of EA and the resulting hearing outcomes can be

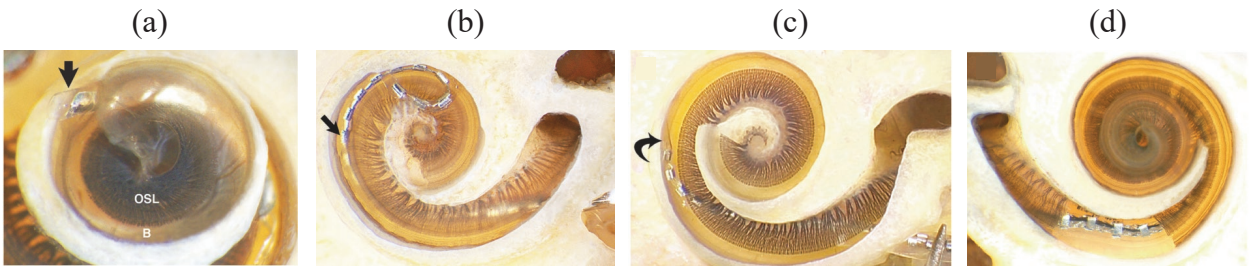

Figure 1.5: Examples of cochlear trauma [20] (a) Translocation of the EA from the ST to the SV (b) Tip fold-over of the EA where the most apical EA section has folded back on itself, and (c) Tip scraping, where the tip of the EA scrapes along the lateral wall, causing damage, and (d) Buckling of the EA inside of the cochlea that prohibits further advancement and affects final intracochlear position. In this case, the buckling event caused fracture of the osseous spiral lamina.

considered. The two main types of EAs—straight and precurved, have very different mechanical characteristics, which dictate both 1) final EA placement and 2) typical insertion trauma. First, straight EAs are able to stimulate lower frequency neurons because they can achieve insertions deeper than 360° [17]. Deeper AIDs have been shown to lead to better hearing outcomes [70]. These EAs also typically have lower incidence of intracochlear insertion trauma, but are more susceptible to buckle and not achieve a full insertion [44]. Another disadvantage of these EAs is an increase in the distance between the electrode contacts and the neural endings they are attempting to stimulate. This distance can result in a higher required current threshold for stimulation, increased contact interaction (cross-talk), and less focal stimulation of spiral ganglion cells [71]. Electrode contact cross-talk can occur as neural fibers are activated by multiple contacts [72]. This interference can manifest as poorer speech understanding for the user in challenging listening conditions [73], [74]. This disadvantage is where the precurved EAs possess their main advantage. Precurved EAs have the potential to achieve "modiolar-hugging" as their final position, with the electrode contacts ideally curved along and touching the modiolus. A disadvantage of these EAs is that insertion is more challenging because insertion requires correctly timing and coordinating two motions (silicone EA carrier advancement and stylet removal) as well as correctly aligning the planar curvature of the precurved EA with the plane of curvature of the ST. These types of EAs are inherently much stiffer than the very flexible straight EAs, and tip fold-over, tip scraping, and

translocation are more common when using precurved EAs compared to straight EAs [16], [66]. If the stylet is removed too late and/or if the curvatures are misaligned, the stiffened tip can scrape along the lateral wall and even translocate into the SV [12], [16], [66]. If the stylet is removed too early, the tip is likely to fold-over [16], [53].

1.5 Robotic Cochlear Implant Insertion Tools

There have been a variety of robotic tools developed for CI EA insertion. The main purpose of these tools is to reduce insertion trauma as defined and detailed in Sec. 1.4. If a CI trajectory is specified, EA insertion can be largely reduced to linear advancement of the EA along that trajectory, especially for straight EAs. Such placement occurs at the limits of human perception with intracochlear trauma during insertion—including tip fold-over and translocation—occurring relatively frequently [16]. For precurved EAs, a second motion is necessary to control stylet motion during insertion. These insertion motions can be automated by highly precise actuators such as those described in [75] which consists of a linear advancement coupled with a stylet stop. Comparison of a modified version of this tool to manual, human insertion showed that while a human at their best may outperform the robot, the robotic insertion tool consistently and repeatably achieved low insertion forces [50] likely to be associated with less intracochlear trauma and improved audiological outcomes [29] as compared to the human operator. Another automated solution, building on the work of Zhang *et al.* [76], was created by Pile *et al.* who developed a 4-Degree-of-Freedom (DOF) solution using a wire-actuated parallel robot design that can be teleoperated or autonomous [77]. This robot was the first robot to incorporate control feedback in CI insertion [78]. The latest automated insertion tool from the RobOtol (a teleoperated otologic surgery robot developed at Pierre and Marie Curie University in Paris, France) developers can be coupled to the RobOtol and has demonstrated smoother insertion force profiles compared to manual insertions [56]. The RobOtol platform has been used as an instrument holder to perform the first clinical robotic CI EA insertion [62], [79]. Recently, a simple automated insertion tool was developed using a syringe as the EA holder and hydraulically actuating the holder via an infusion pump [80]. Finally, clinical

implementation of another robotic insertion tool was reported by the iotaMotion team (Iowa City, IA, USA), who have developed a small, head-mounted insertion robot that is compatible with a variety of different straight EAs and whose angle of approach is set manually by the surgeon [81], [82].

Attempting to steer EAs throughout the insertion has also been a subject of research for some time because it would be advantageous to be able to control EA intracochlear placement [83] and avoid wall contact. This work led to the development of the AOS technique for precurved EA insertion, the development of tendon-actuated EAs [84], the use of shape-memory wires embedded in the EA to achieve modiolar hugging after insertion [85], and using an external permanent magnet to steer a magnet-tipped commercial EA within the ST [68].

Chapter 3 builds on the work of the previously developed automated insertion tools and [68] by developing a robotic system for less traumatic insertion using magnetic steering combined with image guidance and a nonmagnetic automated insertion tool [86]. This chapter details the first-in-cadaver implementation of CI EA magnetic steering.

Trauma is not the only important factor that affects hearing outcomes, EA placement is also crucial to achieving optimal results. Next, recent and current efforts toward improving intraoperative surgeon feedback to determine this placement will be discussed.

1.6 Feedback During Electrode Array Insertion

CI outcomes are very sensitive to EA placement [87]; however, very few feedback mechanisms currently exist for a surgeon when inserting an EA [88]. A surgeon can watch the EA enter the cochlea (and count the number of electrode contacts still outside the cochlea to deduce insertion depth), and can use limited tactile feedback when inserting by hand to know when to halt or alter the insertion. Unfortunately, as mentioned, the forces to cause trauma are near or below the limits of human perception [59], [60], so this is not a sufficient feedback mechanism. Tracking EA travel is difficult since traditional endoscopes and image guidance tools for EA localization are not compatible with this procedure due to size constraints and lack of line of sight. Additionally,

traditional magnetic tracking is not applicable because the sensors are too large to be incorporated into an EA and they lack the resolution necessary for sufficient localization.

A few technologies and techniques exist for intraoperatively evaluating commercial EA integrity and placement within the operating room, and these are typically used *after* insertion. These technologies and techniques can be separated into imaging techniques and audiologic strategies. The first imaging technique that has been shown to be beneficial is using postoperative computerized tomography (CT) to determine final EA placement. This approach has been shown to be extremely useful in determining CI positioning [89], but is limited by CT scanner availability, cost, patient radiation exposure, and lack of real-time recording during insertion. Sequential fluoroscopy has also been used during an insertion, but also increases a patient's radiation exposure and does not truly provide feedback in real-time [90].

Clinical tools used by audiologists include: electrically-evoked compound action potentials, electrically-evoked stapedial reflex threshold, electrocochleography, and impedance telemetry [91]. Here, each approach will be detailed as it is currently used clinically and its potential utility for providing real-time insertion information will be suggested. First, ECAP is the measure of the peripheral response of the auditory nerve to electric stimuli. Electrically-evoked compound action potentials have been shown to be a useful predictor of preservation of residual hearing preservation [92]; however, results relating these measures to EA positioning have been variable [93]–[95]. A second audiologic measure, stapedial reflex threshold, is obtained by visualizing the contraction of the stapedius muscle upon electric stimulation [91]. This binary measure is not useful for informing fine EA placement, but can indicate that the peripheral/brainstem portion of the auditory pathway is functioning correctly. The third listed technique—electrocochleography—measures the electrical potential responses of the hair cells and spiral ganglion cells of the cochlea to an external sound stimulus while the surgeon is inserting the EA. Electrocochleography has been shown to be useful during EA insertion in real-time in helping to prevent residual hearing damage [96]–[100]. However, this technology has only been shown to detect large differences in intracochlear scalar position (i.e., translocations) and relation to scalar location is complex [101]. Lastly, impedance

telemetry is traditionally used clinically after the EA has been inserted. This measure involves sending a known current pulse to an electrode contact and either measuring its voltage response to a ground (contact impedance), or measuring the voltage response of the other electrode contact(s) to the stimulated electrode contact [102]. Abnormally low values indicate a short circuit and abnormally high values indicate an open circuit [91]. Impedance values are readily available in traditional CI manufacturer hardware and require very little workflow change. More importantly, these values have been shown to have a promising correlation with E-M distances [83], [103], [104], with recent work showing the benefit of modeling the equivalent circuit components of the voltage response [88], [105], [106]. It is recommended that more work be done to clarify the reliability of this technique [104].

Impedance sensing is a promising audiologic technique that could provide clear feedback of EA insertion progress. Chapter 4 focuses on leveraging bipolar impedance sensing and the equivalent circuit model to correlate bipolar impedance components to E-M proximity and then use sensed impedance values as a feedback mechanism in insertion.

1.7 Dissertation Overview and Contributions

The focus of this dissertation is on the advancement of the tools, techniques, and systems that surgeons use for CI EA insertion to enable them to achieve improved insertions that will lead to superior patient hearing outcomes. Improvement goals include design and development of a MICIS-compatible tool for more successful insertion in a minimally invasive CI case, decreasing insertion trauma through robotic assistance and steering, and improving final EA placement through intraoperative real-time monitoring. Below, the contributions of each chapter of this work are summarized.

1.7.1 Clinical Translation of a Manual Insertion Tool for Minimally Invasive Cochlear Implant Surgery

MICIS has been shown to be capable of achieving safe and accurate minimally invasive access to the cochlea without a mastoidectomy [32], [33]. Despite this success, the final step in

MICIS of EA insertion remains a challenge due to changes to the surgical workspace that yield a long porous drill path with limited visualization and dexterity. Commercially available tools are not designed to fit within the narrow confines of the MICIS workspace. As such, a new insertion tool is needed that assists the surgeon in easily threading the EA down the drill path and into the cochlea. This tool should be able to be quickly translated (and thus although many promising automated tools have been developed, it should not be automated for this application) to enable use in ongoing clinical trials and should assist with insertion of straight (more flexible) EAs that are more susceptible to buckling. Kratchman *et al.* developed a manual insertion tool compatible with the MICIS workspace [107]; however, this tool was designed for precurved EAs and could not easily be adapted for larger diameter straight EAs. The main contribution of Chapter 2 is the development of a rapidly translatable MICIS insertion tool that enables straightforward, successful insertion of these large diameter straight EAs. This chapter describes the conception, fabrication, evaluation, and the first clinical translation of this new manual insertion tool. The resulting MICIS workspace for a population (N = 97) was evaluated to advise tool and testing phantom model design. The repeatability of the MICIS drill path generation using the probabilistic algorithm in [108] was evaluated for the first time. A clinically realistic testing phantom model was designed that can be used as a surgical trainer to evaluate insertion force profiles for varying MICIS EA insertion techniques. Tested insertion force profiles with this platform indicated very little difference between the insertion force profile with the new tool and with the traditional tool (surgical forceps). Cadaver insertions demonstrated that increased AIDs can be achieved with the new tool compared to traditional tools and the tool increased the ease of the insertion. Clinical translation was achieved for the first time with this tool and enabled a complete insertion (full ST) in a MICIS case.

1.7.2 System Development for Magnetically Steered Robotic Cochlear-Implant Electrode Array Insertion

Reducing trauma during CI EA insertion is essential for improving hearing outcomes [29]. Many promising robotic tools have been developed to enable smooth, controlled insertions [50], [55], [56], [62], [75]–[77], [80], [81], [109], [110] and potentially steer the EA [68], [76], [85]. In Chapter 3, this work is built on by developing a system that combines a robotic insertion tool, image guidance, and magnetic steering using an external, programmable electromagnet to enable an atraumatic insertion. This is the first system that demonstrates magnetic steering of commercial CI EAs with an electromagnet, and this system enables the first magnetically steered EA insertions into a cadaveric cochlea. To create this system, a method for preoperative, patient-specific trajectory planning was developed that generates the tool position and orientation and the prescribed magnetic field vectors for each point along the patient's insertion path. A robotic insertion tool was designed that is nonmagnetic, easily adaptable to clinical EAs of different diameters, and features a new gripping/detachment mechanism. It was demonstrated that the use of image guidance in conjunction with electromagnetic steering enables a less traumatic insertion compared to either a robotic insertion with image guidance alone or a manual insertion in phantom models. For the first time, it was shown that this result holds for magnetic steering in a cadaveric model, an important result signifying that the in-vitro model results are clinically relevant.

1.7.3 Using Real-Time Electrode Array Insertion Impedance Feedback to Inform Array Positioning and Modulate Insertions

Surgeons have little feedback when inserting an EA in the operating room. They can watch the cochlea entrance and attempt to detect minuscule force changes to predict EA insertion progress and approximate EA placement. Recent work has focused on using an existing non-invasive and non-radioactive audiologic tool—impedance sensing—to gain valuable position information [83], [88], [103], [104], [111]. In Chapter 4, building particularly on the results from [88], [104], the insertion impedance profile vs. E-M proximity was evaluated in phantom models of varying geom-

etry for a straight EA type whose relationship had not yet been evaluated. This straight EA features dual-sided EA contacts, and the characterization of the proximity relationship of impedance to E-M was quantified for the first time for this contact geometry. It was shown that real-time impedance values can detect entry behavior of individual electrode contacts accurately and repeatably. A kinematic model for a straight EA was developed, and based on the phantom experiment evaluation, impedance knowledge was incorporated to improve the shape estimation and this model was validated using to-scale ST insertion experiments. It was also shown for the first time explicitly that the real-time relationship between access resistance and E-M proximity translates to cadaveric cochlea. Finally, building on the work of [78], impedance feedback was used to advise EA insertion and the 'pull-back' technique (i.e., when the surgeon purposely pulls a precurved EA back after insertion is complete to decrease E-M distance) with the aim of improving EA placement using a precurved EA. This pull-back technique is already routinely used clinically, but the surgeons do not have any feedback as to when to stop pulling the EA body back to achieve optimal positioning. In this study, real-time impedance values successfully advised the actuators when to stop the pull-back technique in real-time and achieve close modiolar positioning without reducing AID.

Chapter 2

Clinical Translation of an Insertion Tool for Minimally Invasive Cochlear Implant Surgery

In a traditional CI surgical procedure, a surgeon grips the EA body near the opening of the cochlea and has full visualization of the EA entering the cochlea during the insertion. In MICIS, the surgery is made less invasive by drilling a single tunnel to the cochlea, but visualization restrictions and dexterity limitations are introduced, increasing the challenge of achieving a successful insertion. Traditional insertion tools are typically not compatible with the MICIS workspace, do not provide adequate assistance for threading the EA semi-blindly into the cochlea, and/or do not protect the EA on its journey through the spiculated bone and middle ear air gap. There is a need for a MICIS insertion tool that solves the challenges associated with using traditional tools in MICIS, and that could be quickly translated to enable successful insertion of large diameter straight EAs.

This chapter describes the conception and development of a manual insertion tool for EA insertion during MICIS. This tool addresses an important need in MICIS by enabling the surgeon to consistently and effectively advance the EA down the long narrow tunnel of spiculated bone. Tool development began with brainstorming and initial feasibility testing of a wide variety of designs. Next, once the first version was deemed feasible, this tool was tested in a phantom model to analyze clinical viability. Based on these experiments, modifications to the device were made and testing in cadavers was performed using the second version of the tool. Based on these results and further analyses, a third version of the tool was designed and fabricated and eventually clinically translated.

Contributions of this chapter include 1) population analysis of patient-specific parameters in the resulting MICIS workspace, 2) development of a simple and safe insertion tool for use in MICIS, 3) creation of a clinically realistic phantom model for MICIS testing and training, 4) experimental evaluation of the developed tool in phantoms and in cadavers, and 5) clinical translation of the tool.

The content in this chapter led to two conference publications [42], [112], a case report in

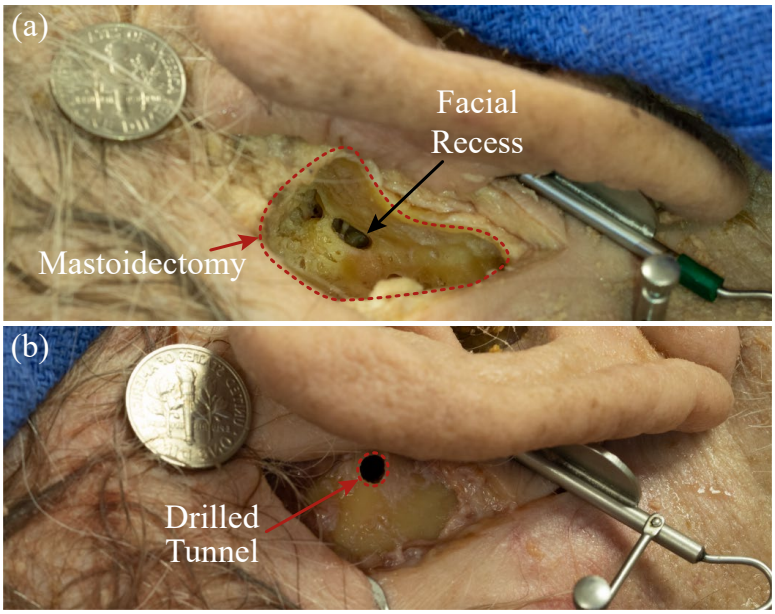

Figure 2.1: Surgical Comparison (a) traditional mastoidectomy in which the skull behind the ear is carefully removed using a high-speed surgical drill. The middle ear is entered from the facial recess. (b) MICIS uses CT guidance to drill a tunnel directly from the surface of the skull to the middle ear

Otology and Neurotology [113], and a first author journal publication in the American Society of Mechanical Engineers (ASME) Journal of Medical Devices [114]. Contributions in this chapter also enabled the experiments in [115].

2.1 Introduction

CIs have helped restore the perception of sound to hundreds of thousands of individuals worldwide [116]. Traditional CI surgery requires a mastoidectomy to access the inner ear structures. Mastoidectomy involves removing a pocket of bone from behind the external ear (see Fig. 2.1(a)), a procedure during which the surgeon must rely on experience, hand-eye coordination, tactile feedback, and visual cues to avoid vital structures [117]. These vital structures include the facial nerve, which controls motion of the face, and the chorda tympani, which controls some components of taste. There have been a variety of efforts to minimize the invasiveness of this procedure and obviate the need for mastoidectomy. Some of these approaches include the pericanal technique, the transcanal technique, and the suprameatal approach [31], [118]–[122]. These methods have suc-

cessfully avoided mastoidectomy; however, the angle of approach for insertion of the EA into the cochlea is suboptimal [34].

Recent research has investigated whether image-guided approaches that leverage patient-specific anatomical knowledge could be used to avoid mastoidectomy in favor of a single drilled linear trajectory to the cochlea, termed minimally invasive cochlear implant surgery (MICIS) (see Fig. 2.1(b)). Specifically, this method calls for the creation of a drilled path to the channel within the cochlea closest to the auditory nerve endings, the ST. A variety of approaches have been employed to guide the drill along the specified trajectory including a parallel robot [35], [36], an industrial robot arm guided by optical tracking of the robot and the patient [37], [38], a hand-drilled conical path using image guidance [39], a custom serial robot arm in conjunction with optical tracking [40], and use of microstereotactic frames [32].

All of these approaches share a common theme in that they help realize a minimally invasive single drill path to the cochlea which avoids critical anatomy. However, the surgically-created tunnel creates geometric constraints for the surgeon to insert the active end of the CI—the EA—into the cochlea. The surgeon is tasked with threading the EA down a narrow tunnel of spiculated bone, punctuated with irregularly shaped air cells, through the middle ear air gap, and into the ST of the cochlea with highly restricted visual feedback. During insertion, the EA can sometimes blindly detour into a partially opened mastoid air cell and/or buckle in the middle ear space. This deflection is a particular issue for the more flexible straight EAs (as opposed to the EAs that have a stylet in them resulting in a stiffer overall structure).

As a result, despite promising results and potential advantages of a single tunnel approach—i.e., it is less invasive, safer for vital anatomy, and facilitates an optimal insertion vector—the final step of EA insertion through the tunnel and into the cochlea remains a challenge. Fig. 2.2 displays the approximate shape of the surgical space resulting from MICIS [32]. In this chapter, a solution to this challenge using a novel manual insertion tool for MICIS is described.

A variety of automated inssertion tools for CI EAs have been developed in the past featuring innovative designs [54], [56], [76], [77], [80], [81], [86], [123], [124]. These tools are capable

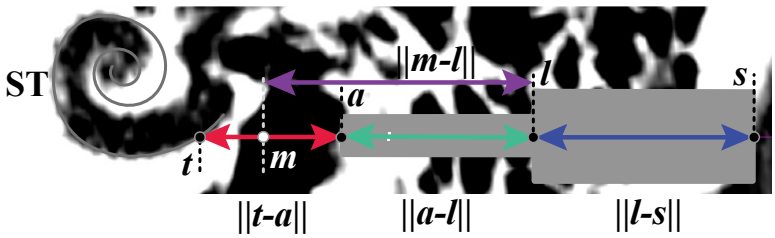

Figure 2.2: MICIS Workspace Definitions: The minimally invasive approach consists of two stage drilling – a lateral 3.8 mm tunnel of length $\|\boldsymbol{l} - \boldsymbol{s}\|$ and a 1.6 mm medial tunnel of relative length $\|\boldsymbol{m} - \boldsymbol{l}\|$. After drilling the tunnel, the middle ear air space (where $\boldsymbol{m}$ resides) must be traversed to place the CI EA within the ST component of the cochlea beginning at the target, $\boldsymbol{t}$

of achieving super-human accuracy and speed. While these automated solutions could prove very useful in the future, the goal of this work was to develop a simple manual tool that could be quickly translated to the operating room. Manual insertion tools include traditional surgical instruments (e.g., forceps, claws, and guidance tools such as [125]). Typically, these tools are not compatible with the MICIS workspace, and if they are, they do not solve the inherent challenges associated with this approach. Specific manual MICIS tools include a tool by Caversaccio *et al.* who used a metal split-tube design [40], but this tool is not compatible with the workspace of [32] to solve the aforementioned challenges. Kratchman *et al.* have developed a tool compatible with the workspace of [32]; however, this tool is not compatible with larger diameter, straight EAs that are very susceptible to buckling [107]. Next, the specific design constraints for the tool are described.

2.2 Design Constraints

Design constraints are defined as shown in Fig. 2.2. The two-stage drilling process consists of a 3.8 mm lateral drill path that extends a distance $\|\boldsymbol{l} - \boldsymbol{s}\|$ from the skull surface, followed by a narrower 1.6 mm medial drill path that is $\|\boldsymbol{m} - \boldsymbol{l}\|$ long and ends in the air-filled middle ear—-an area where the EA is susceptible to buckling. The surgeon does not have direct visualization inside the drilled channel, but can obtain vision of the middle ear through the ear canal by lifting the eardrum. The exact dimensions of Fig. 2.2 are determined for each patient using their preoperative CT scan and corresponding surgical plan. To accommodate this variation, one of the design constraints of the insertion tool was that it be easily customizable or generalizable to most patients. The design

needed to accommodate the MED-EL Standard EA, because it has one of the largest diameters of any commercial EA, which provides adaptability, since the tool can also insert EAs with smaller diameters. The largest diameter of the MED-EL Standard measures approximately 1.4 mm, which only allows for about 0.2 mm of clearance in the 1.6 mm diameter medial channel (0.1 mm wall thickness for a tube). The tool also needed to be quickly translatable to the operating room, so it needed to not be automated and needed to be easily sterilizable. All of these constraints were considered during every stage of the design process.

In summary, user requirements for this tool are that it be a manual (i.e., not automated) tool that enables a clinician to perform the device's intended use which is to thread a straight EA down the porous tunnel of bone and insert it safely and effectively into the cochlea. These requirements lead to the following design requirements that the tool be (i) manually actuated, (ii) able to accommodate the MED-EL Standard and FLEX series EAs, (iii) must be able to accommodate any viable MICIS candidate, (iv) sterilizable and able to be fully disassembled from the EA, (v) must not damage the EA, (vi) must demonstrate an improvement over traditionally used tools, and (vii) it must not limit the final EA insertion depth.

2.3 Initial Tool Development

2.3.1 Design Iteration

Based on the design criteria detailed in Sec. 2.2, numerous designs were prototyped for feasibility before more rigorously testing the first version of the tool. Here, some of the brainstormed and attempted designs are summarized. Design ideas can be separated into two groups based on actuation location: designs that attempted to grip the EA at the cochlea opening, within the middle ear space (termed "proximal grip point") or designs that attempted to grip the EA from outside of the skull (termed "distal grip point"). Some of the explored designs can be viewed in Fig. 2.3. Briefly, proximal grip point attempts included trying to fabricate a tube whose radius could be decreased to grip the EA and subsequently increased to release the EA, thereby allowing the EA to be inched along the desired insertion vector (Fig. 2.3(a)-(c)). The main issue with this mechanism

of actuation was the difficulty of manufacturing within the 0.1 mm of allowable wall thickness. Additional proximal variants included using a 'C'-shaped tube set that would grip the tube when twisted closed and release when twisted such that the slit portions were aligned (Fig. 2.3(d)). While initially promising, the space constraints made it very difficult to source a tube that had sufficient torsional rigidity while still maintaining the ability to machine an effective 'C' profile. Finally, there was an attempt to create two short tubular compression grippers that would be connected via rods from the middle ear space, through the drilled path, and to the skull opening (Fig. 2.3(e)). Fabrication of the attachment rods that were sufficiently rigid, but small enough to fit within the space constraints proved difficult, and removal of the grippers was not straightforward.

Regarding distal grip point variants, a simple push tube set was initially tested (with or without spring-loading) or compression tube set (Fig. 2.3(f-h)) similar to what has been done with other insertion tools in the literature. Unfortunately, the space constraints were still a limiting factor with commercially available metal tubing and the goal was to limit the number of parts that needed to be translated for simple manual actuation. Friction of the EA inside the metal tubing was another limiting factor for sliding the EA through a tube with tight clearance. Another distal variant idea was to use peelable heat shrink that would grip the EA tightly until peeled, such that if the heat shrink is peeled apart and advanced forward the EA would also be advanced and eventually released from the tool (Fig. 2.3(i)). This design could potentially be a proximal or distal grip point variant depending on where the peeling of the heat shrink begins. In this design, it was very difficult to apply the force vector in the correct direction to enable appropriate advancement and also peel the tubing.

Finally, it was discovered that polyimide tubing, an extremely thin yet stiff tubing, could be used to bridge the middle ear space, and a compression variant that is similar to Fig. 2.3(g) but that uses roller wheels to slightly compress the silicone surrounding the transmitting wire was selected that could translate the EA forward with minimal movement of tool components (i.e., no translating components to free the surgeon to focus on the EA entering the cochlea). Next, the initial design will be described in more detail.

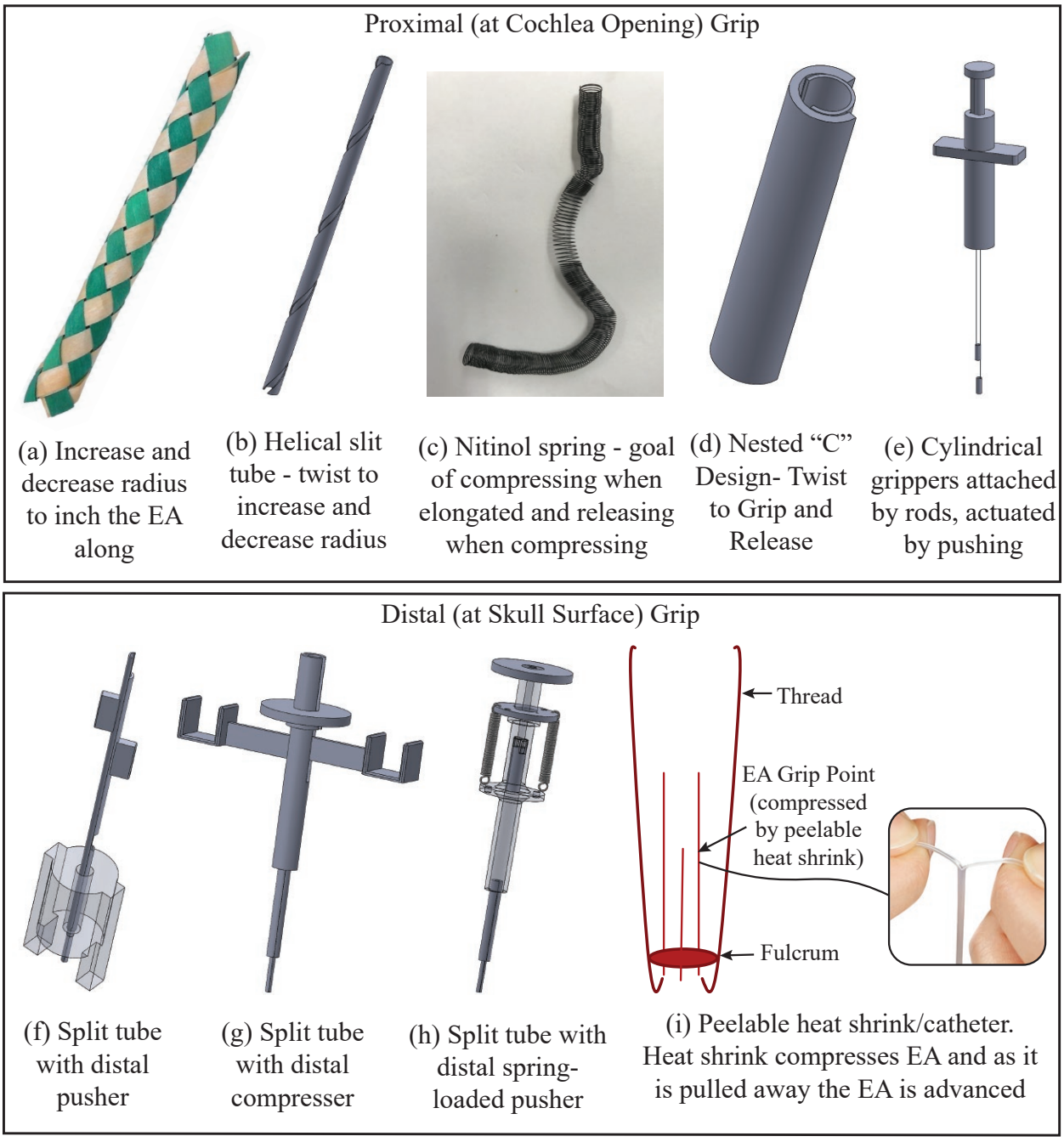

Figure 2.3: Attempted designs and concepts for initial tool design

2.3.2 Initial Tool Design

The initial design concept is shown in Fig. 2.4. The tool actuates the EA via a roller mechanism that creates a mid-channel bottleneck. The surgeon is able to apply a steady axial force by rotating the roller wheels. This rotational motion is converted to axial motion of the EA via contact between the roller wheels and the silicone outer sheath of the EA. The proximal end of the tool—the end closest to the cochlea—consists of a polyimide tube with inner diameter 1.45 mm, and an outer diameter 1.51 mm, satisfying the aforementioned tolerance of 0.1 mm maximum wall thickness allowable in the medial drill channel. This design features a static contact point and no vertical translation of components which helps to keep the insertion simple and smooth, and frees the surgeon to focus on monitoring insertion progress. The tool geometrically mimics the drilled channel; it contains a rigid distal end piece with an inner diameter of 1.7 mm that houses the roller mechanism. The roller wheels rotate on pins that are press fit into the rigid end piece. A support entry tube extends into the 3.8 mm drilled channel to constrain the EA, and minimize frictional effects by reducing the length of the EA within the polyimide tube. The polyimide tube extends into the medial channel and bridges the middle ear air gap, providing the necessary support to prevent buckling. The entire tool is 3D printed on a Formlabs™ 3D printer (Model Form 2: Formlabs Inc.; Somerville, MA), and is made out of autoclavable and biocompatible dental resin.

Initial testing proceeded using the phantom model shown in Fig. 2.5(a-c) to evaluate the performance of the newly developed insertion tool compared to the traditional approach (i.e., surgical forceps). The visualization capabilities of an actual MICIS procedure were replicated by attaching a plate to the top of the phantom model that had a 10 mm diameter hole in it to mimic an ear canal opening Fig. 2.5(a). The phantom model was oriented in a clinically representative orientation and held using a clamp, as shown in Fig. 2.5 for (b) the traditional surgical forceps and (c) new roller tool. An experienced CI surgeon performed six insertions with the new roller tool and six insertions with surgical forceps using MED-EL Standard EAs. Before each trial, the ST was refilled with soapy water to minimize friction and maintain consistency between tests. For each insertion, the insertion duration, whether buckling occurred, and final insertion depth (measured by count-

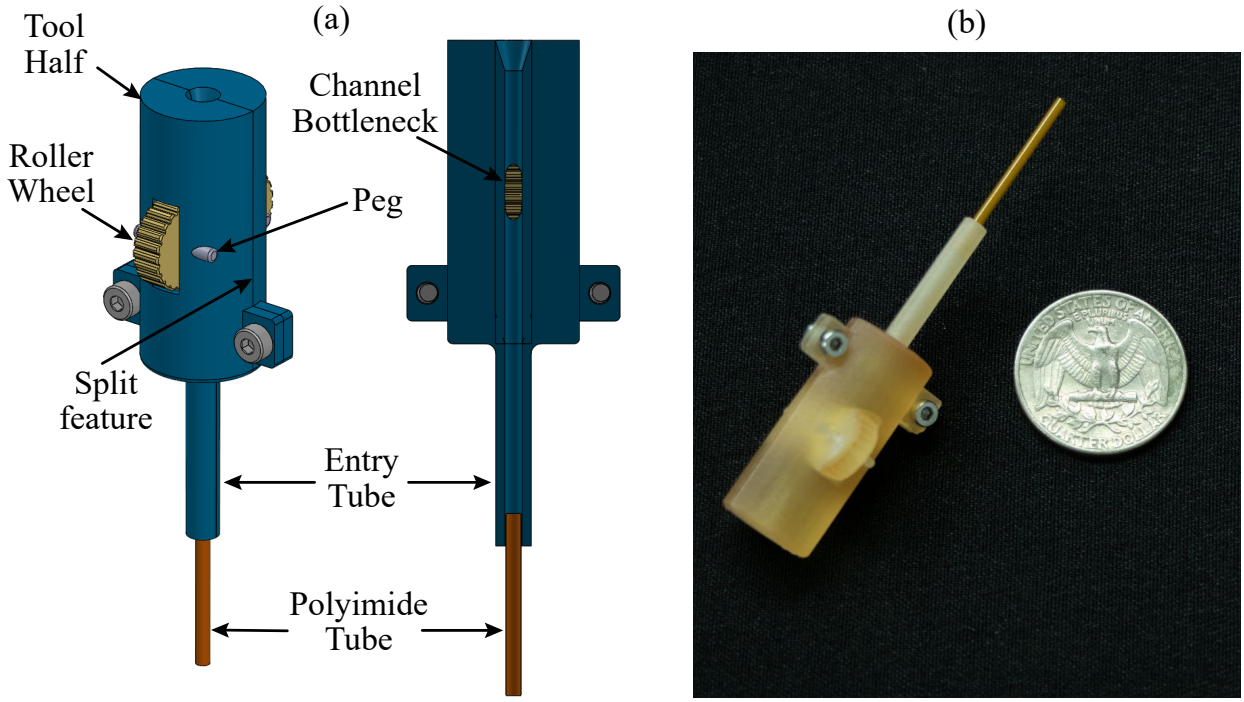

Figure 2.4: (a) Initial tool design and (b) Assembled device with autoclavable 3D printed pieces and United States quarter dollar for scale (diameter of 24.3 mm)

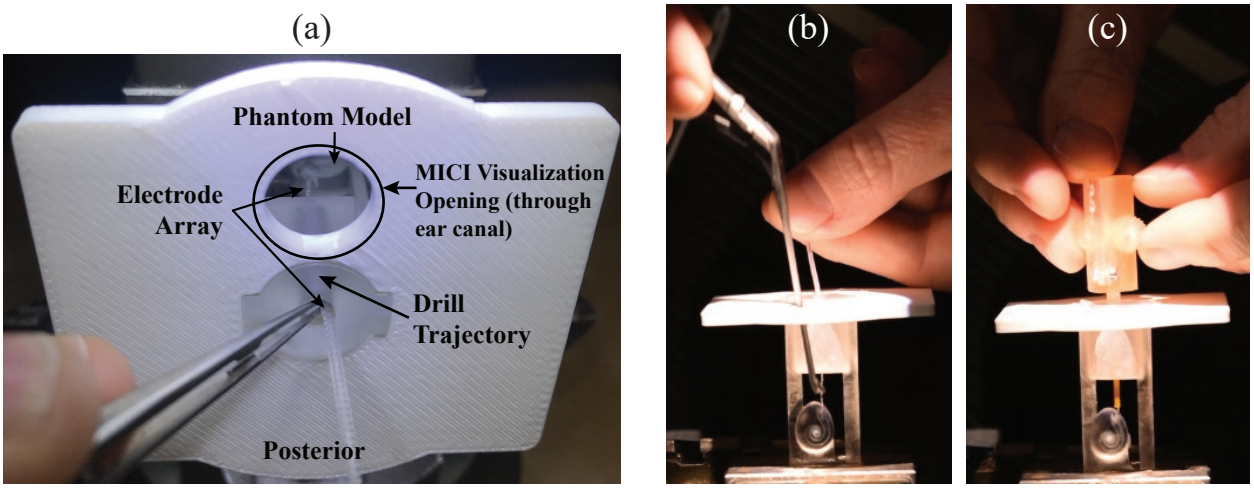

Figure 2.5: (a) Top view of testing phantom showing the mimicked MICIS visualization, (b) experimental setup using traditional insertion tools, and (c) experimental setup using the roller tool.

Table 2.1: Insertion Buckling Comparison

	Trial	Buckling	Insertion Depth
Traditional Tool	1	Y	11/12
	2	N	12/12
	3	Y	11/12
	4	Y	11/12
	5	Y	11/12
	6	Y	11/12
New Tool	1	N	12/12
	2	N	12/12
	3	N	12/12
	4	N	12/12
	5	N	12/12
	6	N	12/12

Table 2.2: Insertion Duration Comparison

	Duration of Insertion (s)						
	T1	T2	T3	T4	T5	T6	Avg.
Traditional Tool	185	81	157	101	142	85	125
New Tool	80	97	124	71	142	80	99

ing the number of electrode contacts along the length of the EA that were fully inserted into the cochlea with 12/12 indicating complete insertion) were recorded.

Data collected from experiments can be viewed in Table 2.1 and Table 2.2. As can be seen in Table 2.1, no bucking occurred with the roller tool (0/6) compared to almost universal buckling with surgical forceps (5/6). Insertion depth was somewhat deeper with the roller tool (complete insertion in all cases) versus surgical forceps (average 11.2 electrode contacts out of 12 inserted into the cochlea). Table 2.2 shows average insertion durations, with the traditional tool requiring on average 26 more seconds for an insertion and higher insertion duration variability. Note that the roller wheel EA insertion time does not include post-implant disassembly so the comparison is made solely on insertion time.

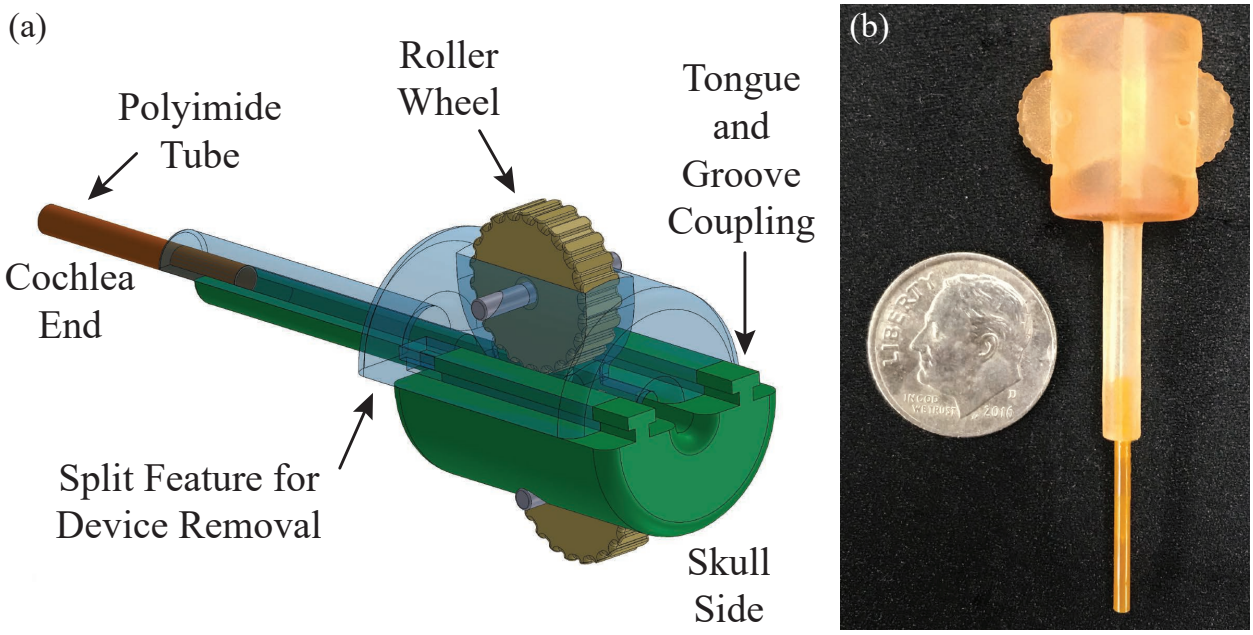

Figure 2.6: (a) Second generation tool design and (b) Assembled device with autoclavable 3D printed pieces and US dime for scale (diameter of 17.91 mm)

2.3.3 Tool Updates after Phantom Testing

Tool updates after phantom testing included shrinking the overall assembly and making disassembly easier using a tongue-and-groove connection between the tool halves. Additionally, the bottleneck diameter was increased to decrease frictional issues and backlash. All edges were made as smooth as possible to increase safety for the patient and for the EA. Tolerances were adjusted such that the printed model required little to no finishing work. This updated design was then tested in cadaver models using the established MICIS workflow. The workflow of this procedure can be viewed in Fig. 2.7. Preoperative planning was first performed by segmenting critical structures in the CT scan of the patient using automated segmentation methods described previously [126]–[128]. A drilling trajectory was created based on these preoperative scans targeting the medial axis of the ST [108] (see Fig. 2.7(a) for results from these steps). Next, a patient-specific microstereotactic frame, a Microtable®, was milled using a computer numeric control (CNC) milling machine [129]. The microtable was then affixed to the cadaver head and the minimally invasive tunnel was drilled in two steps—a 3.8 mm tunnel lateral to the facial nerve and a 1.6 mm tunnel in close prox-

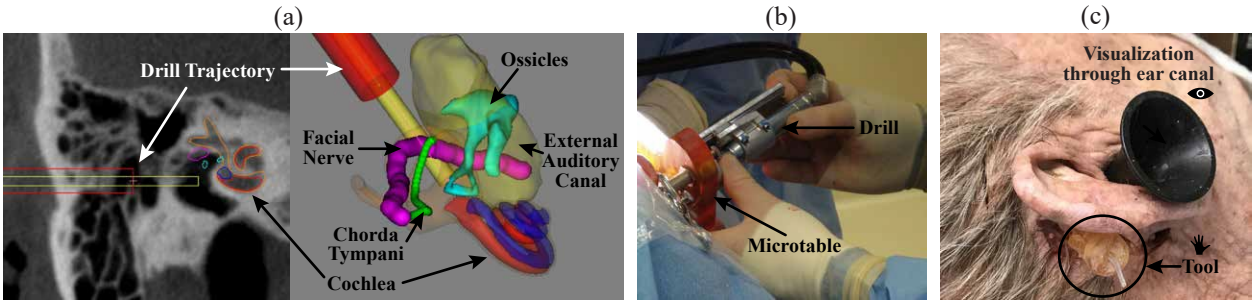

Figure 2.7: Workflow during initial cadaver studies

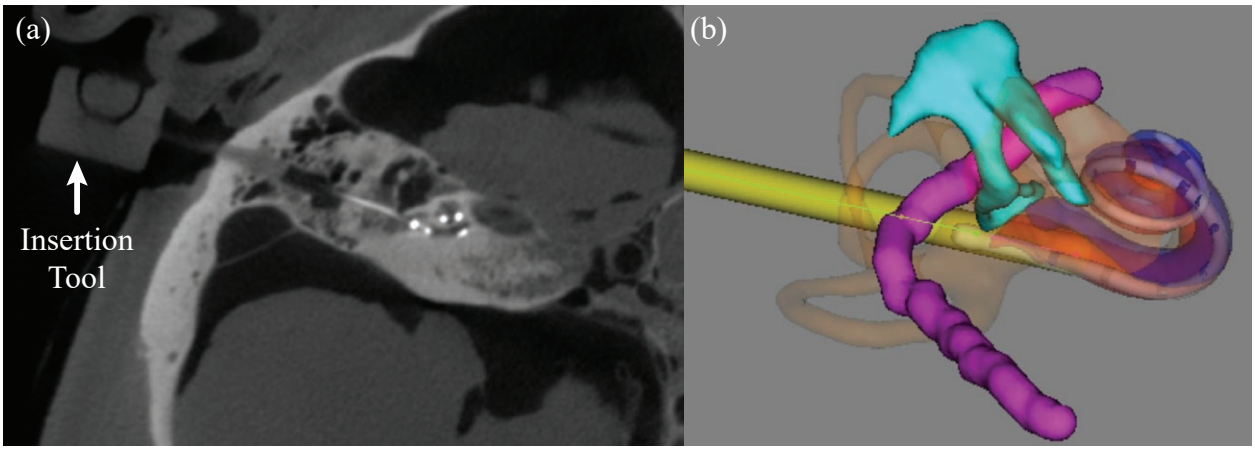

Figure 2.8: (a) CT Scan and (b) reconstructed EA position from first cadaver studies with the tool

imity to the facial nerve (see Fig. 2.7(b)). After this step, the tympanic membrane was raised from an external auditory canal (EAC) approach enabling visualization and preparation of the cochlea. Such preparation included removal of the bone comprising the round window overhang and reflection of the round window membrane posteriorly creating an opening into the ST. Next, the insertion tool was positioned on the cadaver head and secured by mating of the ~3.8 mm portion of the device tube (3.5 mm for clearance) with the 3.8 mm tunnel. For this initial positioning, a metal stylet was placed through the lumen of the insertion tool such that the stylet could be seen as it approached but did not enter the cochlea. With proper alignment visually confirmed, the stylet was removed and the EA was threaded into the insertion tool until the tip could be seen just outside the cochlea. Finally, with the surgeon viewing the cochlea via the EAC (see Fig. 2.7(c)), the roller wheels of the insertion tool were manually actuated enabling slow, smooth insertion of the EA.

Initial tests with this device were carried out using two cadaver heads (four ears). Insertions

Table 2.3: Angular insertion depth comparison of the traditional tool and new tool for the four tested ears

	Angular Insertion Depth (AID) (°)			
Insertion Technique	**Cadaver 1, Left Ear**	**Cadaver 1, Right Ear**	**Cadaver 2, Left Ear**	**Cadaver 2, Right Ear**
Traditional Tool	702	601	699	710
New Tool	664	544	708	555

were done using a traditional tool (surgical forceps) and the new insertion tool. Initial testing was done using a mixture of water and a small amount of Healon (sodium hyaluronate) for lubrication; however, both the traditional approach and new tool yielded similar partial insertions near only about 250°. These partial insertions were most likely due to a post-mortem change in the frictional properties of the ST. As a result, to overcome this increased friction, soapy water was used as the lubricant for testing comparison. Post-insertion CT scans were collected and compared for all four ears. Resulting AIDs from the cadaveric trials are tabulated in Table 2.3, and a resulting CT scan and a 3D reconstruction from an insertion with the new tool can be seen in Fig. 2.8. With both insertion techniques, similar insertion success was achieved; all trials resulted in complete insertions (12 of 12 electrode contacts intracochlear). For both techniques, similar AIDs were observed (average AIDs near 680° for the traditional tool and near 620° for the new tool). Although both techniques resulted in similar insertion success, using the roller tool enabled the surgeon to blindly advance the EA along the optimal trajectory while focusing visual and fine motor attention on the entrance of the cochlea as accessed via the EAC (see Fig. 2.7(c)). Using the new tool made it significantly easier to insert the EA without buckling. Of note, this version of the tool did not feature a method of removing the tool completely, although cutting the polyimide tubing after insertion was complete and tearing a pre-perforated polyimide tube were investigated.

2.4 Steps to Clinical Translation

The previously detailed work focused on initial concept design and feasibility in phantoms and cadavers. The remainder of this chapter focuses on refinement of this design and performance

of the steps needed to achieve United States Food and Drug Administration (FDA) approval for clinical use. The contributions of this work are as follows: 1) population analysis (N = 97) of patient-specific parameters for both roller tool design and phantom model generation and verification that patient-specific designs can be suitably built for all viable candidates, 2) developing a method for and testing roller tool disassembly around an EA, 3) improving tool concentricity, 4) miniaturizing the roller tool for compatibility with the geometric requirements of the rest of the CI system (i.e., subcutaneous receiver permanently attached to the EA by a transmitting wire), 5) creating a clinically realistic MICIS testing setup that could be used as a general surgical trainer for MICIS in the future, 6) evaluating the insertion force profile of the roller tool versus surgical forceps, and 7) evaluating cadaver performance with full mock implantation including disassembly and removal of the roller tool, with all work leading to 8) clinical translation in a first live human case.

2.5 Methods

2.5.1 MICIS Parameter Analysis

In this section, methodology toward contribution 1 to determine the MICIS population parameters (i.e., distances along the drill path of the air gap, medial drilling, and lateral drilling in Fig. 2.2) for the implementation in [32] is described. These distances were quantified for three main reasons. First, such analysis would help determine if the insertion tool could be a one-size-fits-all design or if the 3D printed housing and/or distal polyimide sheath length would have to be adjusted on an individual basis. Second, population analysis would enable the design of a minimally invasive phantom model representative of the surgical population. Finally, this analysis could provide further insight into anatomic nuances that may rule out some candidate patients from MICIS.

Ninety-seven temporal bone scans were analyzed under IRB-approved protocols. All scans were acquired on clinical CT scanners, and median voxel size for this dataset was 0.25 x 0.25 mm in the plane of scan and 0.34 mm between slices. For each patient CT scan, MICIS was planned, and the resulting drill path was analyzed. To perform this planning, the temporal bone anatomy was

first segmented using an atlas-based approach [126]–[128]. A 3rd-year otolaryngology resident surgeon verified that all segmentations were anatomically valid. Any questionable segmentations were further validated by a very experienced CI surgeon (> 500 implants over 20 years).

Based on the segmented anatomy, a drill trajectory was generated automatically [108]. Critical points along the trajectory ($\boldsymbol{t}$, $\boldsymbol{m}$, $\boldsymbol{a}$, $\boldsymbol{l}$, and $\boldsymbol{s}$) were identified as shown in Fig. 2.2. All points lie along the trajectory axis. Point $\boldsymbol{t}$ (target point) is the most lateral (toward skull surface) point of the ST along the axis. Point $\boldsymbol{m}$ is the end of the medial drilling, selected to lie within the middle ear space and at least 1 mm past any mastoid bone given that the medial drill tip is conical with a height of approximately 0.8 mm. Thus, this selection ensures that the medial drill bit enters the middle ear to its full diameter. Next, the first point along the trajectory moving laterally from the cochlea where the drill path was surrounded by 50% of bone was identified and labeled $\boldsymbol{a}$, specifying the boundary of the middle ear air gap. The level/window for determining this point was set to 500/1000 HU for all scans for standardization; inter-scanner intensity variability was neglected.

Point $\boldsymbol{l}$ was chosen 10 mm behind point $\boldsymbol{m}$ based on established drilling protocols with the medial drill bit length being either 10 mm or 13 mm longer than the lateral drill bit length. The shorter differential is preferred given better access and more stable drilling. If this $\boldsymbol{l}$ (10 mm from $\boldsymbol{m}$) placed the lateral drill bit within 4 mm of the facial nerve or within 0.4 mm of the EAC, $\boldsymbol{l}$ was placed 13 mm lateral to $\boldsymbol{m}$. If this trajectory still resulted in the lateral drill path being closer than 4 mm to the facial nerve or 0.4 mm to the EAC, the candidate was omitted from subsequent analysis and was not considered a MICIS candidate. Finally, intersection of the skull surface with the midline trajectory was labeled as point $\boldsymbol{s}$.

The minimum distance between the drill path and facial nerve and between the drill path and EAC was automatically determined for each plan by first creating an object file of the lateral drill path to compare to the object files of the segmented anatomy. Then, using the definitions shown in Fig. 2.9, the minimum distance was calculated by solving

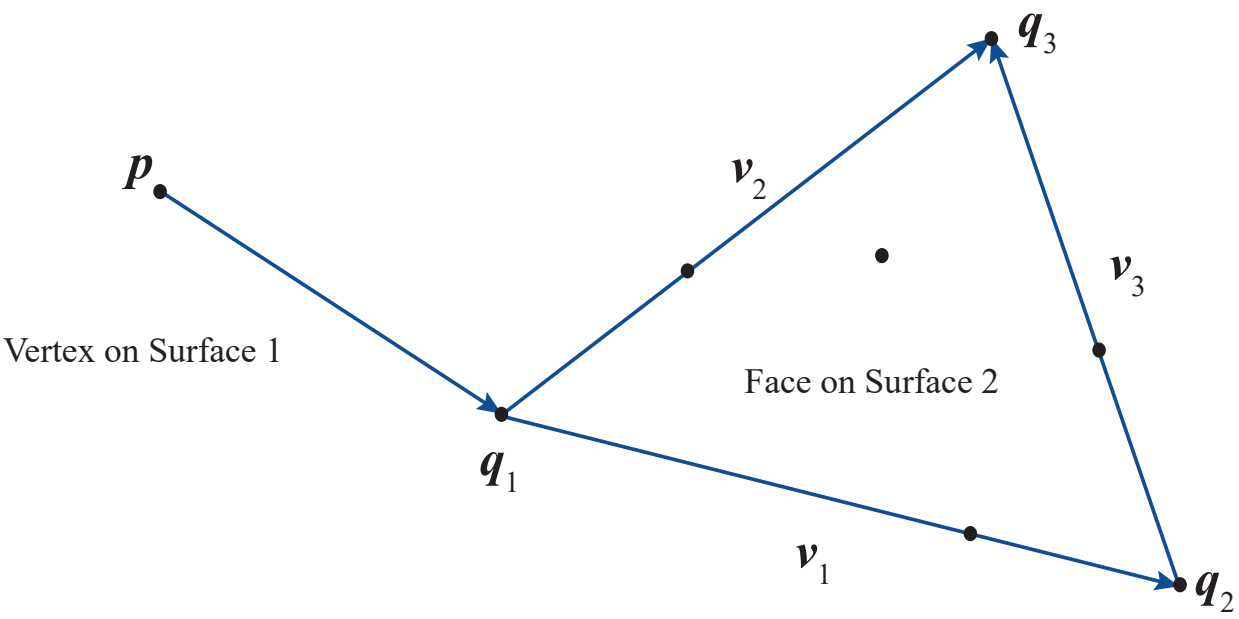

Figure 2.9: Parameter definitions for minimum distance calculation

$$min_{a,b} \|\boldsymbol{q}_1 - \boldsymbol{p} + a\boldsymbol{v}_1 + b\boldsymbol{v}_2\|^2 \tag{2.1}$$

for a and b using a least-squares solution. Then, the closest point $\boldsymbol{p}_{c1}$ is

$$\boldsymbol{p}_{c1} = \boldsymbol{q}_1 + \begin{bmatrix} \boldsymbol{v}_1 & \boldsymbol{v}_2 \end{bmatrix} \begin{bmatrix} a \\ b \end{bmatrix} \quad a, b > 0 \; and \; a + b < 1. \tag{2.2}$$

The closest point may also lie on an edge or a vertex, and coefficients d, e, and $f \in [0, 1]$ were computed using the following equations:

$$\begin{aligned} min_d \|\boldsymbol{p} - (\boldsymbol{q}_1 + d\boldsymbol{v}_1)\|^2, \\ min_e \|\boldsymbol{p} - (\boldsymbol{q}_1 + e\boldsymbol{v}_2)\|^2, \\ min_f \|\boldsymbol{p} - (\boldsymbol{q}_2 + f\boldsymbol{v}_3)\|^2. \end{aligned} \tag{2.3}$$

Then, the closest points in each of these cases are

$$\begin{aligned} \boldsymbol{p}_{c2} &= \boldsymbol{q}_1 + d\boldsymbol{v}_1, \\ \boldsymbol{p}_{c3} &= \boldsymbol{q}_1 + e\boldsymbol{v}_2, \\ \boldsymbol{p}_{c4} &= \boldsymbol{q}_2 + f\boldsymbol{v}_3. \end{aligned} \tag{2.4}$$

The minimum of the four computed distances was computed in both directions (i.e., from the vertices of surface 1 to the faces of surface 2 and vice versa), and the overall minimum was the determined closest distance between the two surfaces.

2.5.2 New Tool Design

This section briefly describes the basic tool design concept originally presented in [112] and [42]. The new tool that is the subject of this work was created by integrating lessons learned during the clinical translation process, as stated in contributions 2-4. These contributions are the development of a tool disassembly method, improving device concentricity, and overall tool miniaturization. First, full removal of the EA from the tool is now realized using slit polyimide. Disassembly proceeds by holding the EA stationary with tweezers and first removing the tool half without the polyimide attached. Then, while still holding the EA in place, the polyimide-attached tool half is pulled out via the slit. Of note, the polyimide has a helical slit with a high pitch (see Fig. 2.10(a)) which enables it to be removed around the transmitting wire while minimizing the chance that the EA will shift out of the slit during insertion. A second tool design change is the addition of the second tongue-and-groove feature on the guide cylinder of the tool (see Fig. 2.10(a)) to ensure the two tool halves remain concentric with one another. Finally, miniaturization of the tool was necessary for clinical use because the EA is permanently attached to an internal receiver buried below the soft tissue of the skull behind the ear (see Fig. 2.11). The results from Sec. 2.5.1 were used to advise the miniaturization (i.e., dimensions r, h, and g in Fig. 2.10(a)) as described in Sec. 2.6.2.

In general, this insertion tool design is composed of two 3D printed halves that slide together with a tongue-and-groove joint. Each tool half has a roller wheel to aid in EA advancement. A

polyimide sheath is glued to the end of one tool half with a drop of medical grade superglue. This tool was designed to accommodate the MED-EL Standard and FLEX series EAs (MED-EL, Innsbruck, Austria) but could easily be modified to accommodate other EAs. The MED-EL Standard EA has a silicone diameter of approximately 1.3 mm around the transmitting wires (as do the FLEX series EAs), but the Standard has a 1.4 mm silicone stopper ring indicating full insertion. For the remainder of this chapter, the electrode transmitting wires housed in silicone will be referred to as "the transmitting wire" for simplicity. To use this tool, the EA is threaded into the lumen of the tool and once the last electrode contact is past the wheels, the wheels slightly compress the transmitting wire and can be used to advance the EA slowly and consistently out of the tool and into the cochlea.

Device assembly was standardized using the assembly jig shown in Fig. 2.10(b). Most of the tool (mandrel, wheels, axles, and tool halves) is made of Dental SG Resin on a Form 2 (Formlabs, Somerville, MA) 3D printer. This material adheres to EN-ISO 10993-1:2009/AC:2010, EN-ISO 20795-1:2013, and EN-ISO 7405:2009/A1:201 standards. A drop of Loctite 4981 superglue that adheres to ISO-10993 standards (Henkel AG & Company, Düsseldorf, Germany) holds the distal polyimide sheath (Microlumen®, Oldsmar, FL) to one of the paired entry chambers. The polyimide sheath is chemically inert and adheres to requirements for United States Pharmacopeia Class VI compliance. The tool was 3D printed to enable design flexibility, and to increase the speed and ease of fabrication. The Form 2 3D printer has a maximum resolution of 0.025 mm and a spot size of 0.14 mm, so this manufacturing method is suitable for standard machining tolerances. All 3D printed components were printed according to the protocols for medical grade devices available on the Formlabs website. (This material is used regularly for creation of dental drill guides for dental implants). According to a Formlabs study involving 84 printed Dental SG surgical guides, 93% of the intaglio surface area was accurate within ± 0.1 mm, demonstrating high accuracy and repeatability [130]. Sterilization validation of the fully assembled tool (Fig. 2.10(c)) was performed at SMP GmbH (Tübingen, Germany) and the device was validated to be wrapped and sterilized at 132°C for 4 minutes.

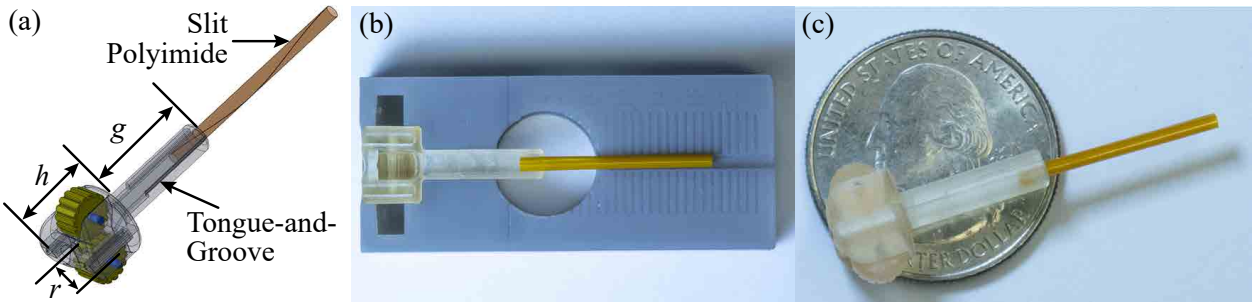

Figure 2.10: Manual roller insertion tool (a) transparent CAD design showing paired entry chambers which slide together via a tongue-and-groove mechanism, (b) half of tool in assembly jig facilitating length sizing and adhesion of the slit polyimide sheath, and (c) assembled tool in comparison to a United States quarter dollar (diameter of 24.3 mm)

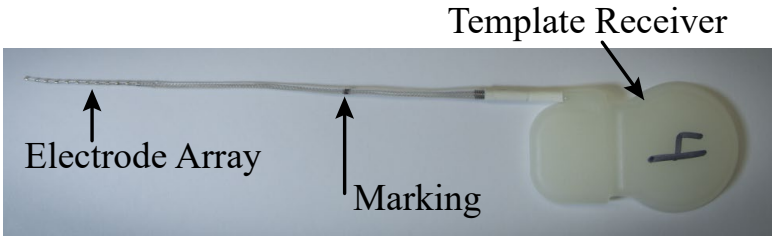

Figure 2.11: Assembled EA with template receiver with distance from the stopper of the EA to the center of the template receiver of approximately 121 mm

2.5.3 Phantom User Study

In this section, contributions 5 and 6 are described: development of a MICIS phantom and evaluation of the insertion force profile noting that higher forces have been correlated with increased cochlear trauma and poorer patient hearing outcomes [29], [47], [48]. The experimental setup (Fig. 2.12) was designed to mimic that of an actual MICIS using the scan analysis described in Sec. 2.5.1 and the determined mean values. This model differs from a previously developed MICIS phantom model [131] in that it is designed for clinically realistic insertion force profile evaluation instead of for drilling accuracy evaluation. This model could be used as a general surgical trainer for MICIS, as practice for a specific MICIS candidate, or to compare insertion methods for a particular candidate.

To create a clinically realistic model, the patient scan with the closest parameter values to the mean values determined in the analysis ($\|\boldsymbol{t}-\boldsymbol{a}\| = 5.3$, $\|\boldsymbol{a}-\boldsymbol{l}\| = 8.0$, $\|\boldsymbol{l}-\boldsymbol{s}\| = 14.4$) mm (see Sec. 2.6.1) was selected. The values of the selected patient were (5.5, 7.5, 14.1) mm. The seg-

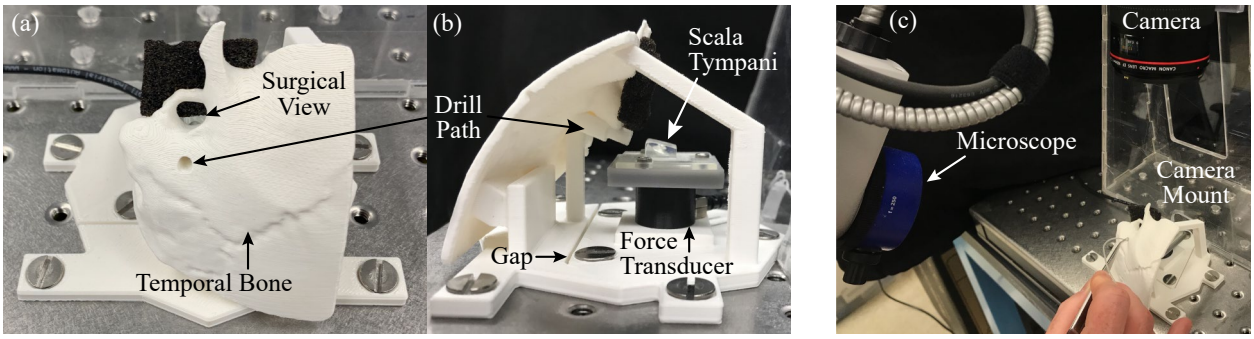

Figure 2.12: Minimally Invasive Phantom Test Setup: (a) Surgical view, (b) Side view showing ST model mounted on force transducer, and (c) Experimental setup with surgeon inserting using traditional forceps

mented ST object file was exported and the skull was isosurfaced. Meshmixer (Autodesk, San Rafael, California) was used to trim the skull object to a reasonable size that still included all vital bone for the procedure visualization and insertion. Meshmixer was also used to modify the bone to be 3D printable—i.e., to fill holes and extrude the skull surface to generate a 3D printable mesh. After generating the printable object file in Meshmixer, Solidworks (Solidworks, Waltham, MA) was used to assemble all exported anatomy with their origins coincident and coordinate systems aligned such that they were in the correct anatomical orientation relative to each other. The remainder of the assembly was designed to accommodate and mount the temporal bone and a force transducer (Nano17, ATI Industrial Automation, Apex, NC; SI-12-0.12 calibration). With this calibration, the transducer has a sensing range of 12 N in the X-Y axes, 17 N in the Z axis, and a resolution of 1/320 N in all axes. Data were acquired using the ATI Network Force/Torque sensor system. Note the decoupling gap in Fig. 2.12 that was incorporated to decouple forces on the temporal bone from forces on the ST. The ST model and ST holder were both printed using stereolithography. The remainder of the components were printed using fused deposition modeling.

Insertion force profile data were collected to demonstrate phantom model functionality and to ensure that the tool was not introducing any undesirable force spikes or artifacts as compared to standard forceps insertion. IRB approval was acquired for this user study, and an expert surgeon inserted an unused MED-EL Standard EA into the soapy-water-filled ST model 4 times using the roller tool and 4 times using traditional tools (i.e., surgical forceps), with the order chosen

randomly for each of the 4 comparisons. Force data (1 kHz) and video (60 fps) of the ST were recorded for each trial (experimental setup shown in Fig. 2.12(c)) with the surgeon blind to these recordings. Individual and average insertion force profiles vs. AID are reported in Sec. 2.6.3.

2.5.4 Cadaver Experiments

In this section, the performed cadaver study for simulated-use human factors validation testing to evaluate clinical viability of this device is described (contribution 7). Cadaver insertions were performed primarily to verify that 1) the tool dimensions accommodate receiver placement, 2) the removal method is effective, and 3) the EA is unharmed during insertion. An unused MED-EL Standard EA was used for each of the eight ears studied. A MED-EL Synchrony template receiver was attached to each EA at the same distance as a clinical CI (see Fig. 2.11). Pictures were taken of the EA before and after insertion to document any potential damage. Saline was used as a lubricant for all eight ears. For the final head, soapy water was also used for each ear (after saline insertions had been performed).

MICIS was performed as previously described [32] and is summarized in Fig. 2.13. First, a preoperative scan was taken using the Xoran XCAT™ CT scanner (Xoran Technologies LLC, Ann Arbor, MI). Critical anatomy was segmented and a safe drill path was automatically planned as described in Sec. 2.5.1 (Fig. 2.13(a)). An expert surgeon validated the segmentations for clinical viability. After segmentation validation, the tool was adjusted to be patient-specific—the polyimide sheath was cut to length based on the patient-specific drill path. The transmitting wire was marked at the point at which insertion would be complete relative to the most lateral point of the insertion tool (see Fig. 2.11) (i.e., when this mark was about to enter the insertion tool, the EA was fully inserted within the cochlea). The tool was then steam sterilized. While the tool was in the autoclave, fiducial anchors were placed (Fig. 2.13(b)) and an intraoperative scan was taken. This intraoperative scan was registered to the preoperative plan, and the microtable was designed using automatic custom MATLAB® (Mathworks, Natick, MA) code. The patient-specific microtable was fabricated, assembled (Fig. 2.13(c)), and verified with post-fabrication measurements. During

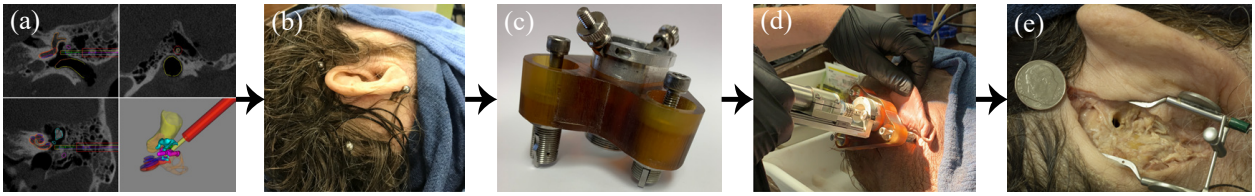

Figure 2.13: MICIS workflow: (a) Patient-specific plan is generated on preoperative CT scan. (b) Fiducial anchors are placed and an intraoperative CT scan is taken. The intraoperative CT scan is registered to the preoperative plan, and based on the registered plan, (c) a microstereotactic frame is milled and assembled (<10 minutes). (d) The frame is mounted to the head using the fiducial markers and the tunnel is drilled in two stages (lateral and medial tunnels) to (e) gain access to the cochlea

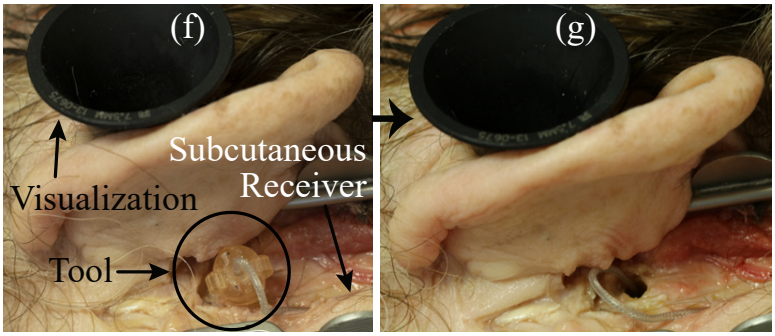

Figure 2.14: New Steps of MICIS (labeled (f) and (g) as a continuation of Fig. 7): (f) After subcutaneous placement of the template receiver, the EA is inserted using the new insertion tool and (g) the tool is removed after EA insertion

microtable assembly, the surgeon lifted the tympanomeatal flap for access to the middle ear, created a small periosteal incision for the drill path, and created a subperiosteal pocket for the receiver, as in standard CI surgery. The microtable was mounted and lateral drilling (3.8 mm diameter) was performed (Fig. 2.13(d)) and a verification CT scan was taken. After visual verification of the path, medial drilling (1.6 mm diameter) was performed and the microtable was removed (Fig. 2.13(e)). The round window overhang was taken down with a 1 mm diamond drill bit and the round window membrane reflected to gain ST access. For each ear, an insertion using an unused MED-EL Standard EA was done with traditional tools (i.e., forceps) and with the roller tool (Fig. 2.14(f)). The ST was refilled with saline between each insertion, and the tool and EA were dipped in distilled water between each insertion. For the final head, soapy water was also used to test full insertion capabilities of the tool. The tool was removed when insertion was complete (Fig. 2.14(g)), and a

final CT scan was acquired.

2.5.5 Clinical Implementation

After the rigorous testing reported above, the updated roller tool and the steps described in Fig. 2.14 were incorporated into the preexisting workflow (Fig. 2.13) for clinical trials of MICIS at Vanderbilt (contribution 8). Approval of an amendment to a previously submitted investigational device exemption from the FDA was obtained prior to clinical use allowing use of the roller tool as part of this feasibility trial.

In the implementation of MICIS described in this chapter, the fiducial spheres are localized using an automatic algorithm, but the fiducial bone anchors could instead be used for localization and registration. Recently, it was discovered that if the bone anchors are localized using the available automated algorithm instead of localizing the sphere centers, there is an unacceptable level of error for this procedure. Quantification and correction of this error are investigated and specified in Appendix A. This analysis could be used if it is necessary for the bone anchors to be localized instead of the spheres for this surgery.

Prior to clinical implementation, a criterion was defined that the manufactured microtable needed to meet if the surgery would move forward based on the predicted target registration error (TRE). Calibrated calipers with spheres of the same dimension as the fiducial spheres was used to evaluate the dimensions of the manufactured microtable. A target probe was substituted for the drill, with the target at the same distance as the specified target and six dimensions of the microtable were measured using these calipers—all three distances between legs and all three distances from each leg to the target. A coordinate frame was established for these distances as shown in Fig. 2.15. The fiducial closest to the mastoid is established as the origin of this frame, $\boldsymbol{f}_{1a}$ with the $\hat{x}$-axis lying from this fiducial $\boldsymbol{f}_{1a}$ to the posterior fiducial $\boldsymbol{f}_{2a}$, and all three fiducial positions defining the $\hat{x}$-$\hat{y}$ plane. The actual target point location $\boldsymbol{f}_{4a}$ is then computed using the definitions

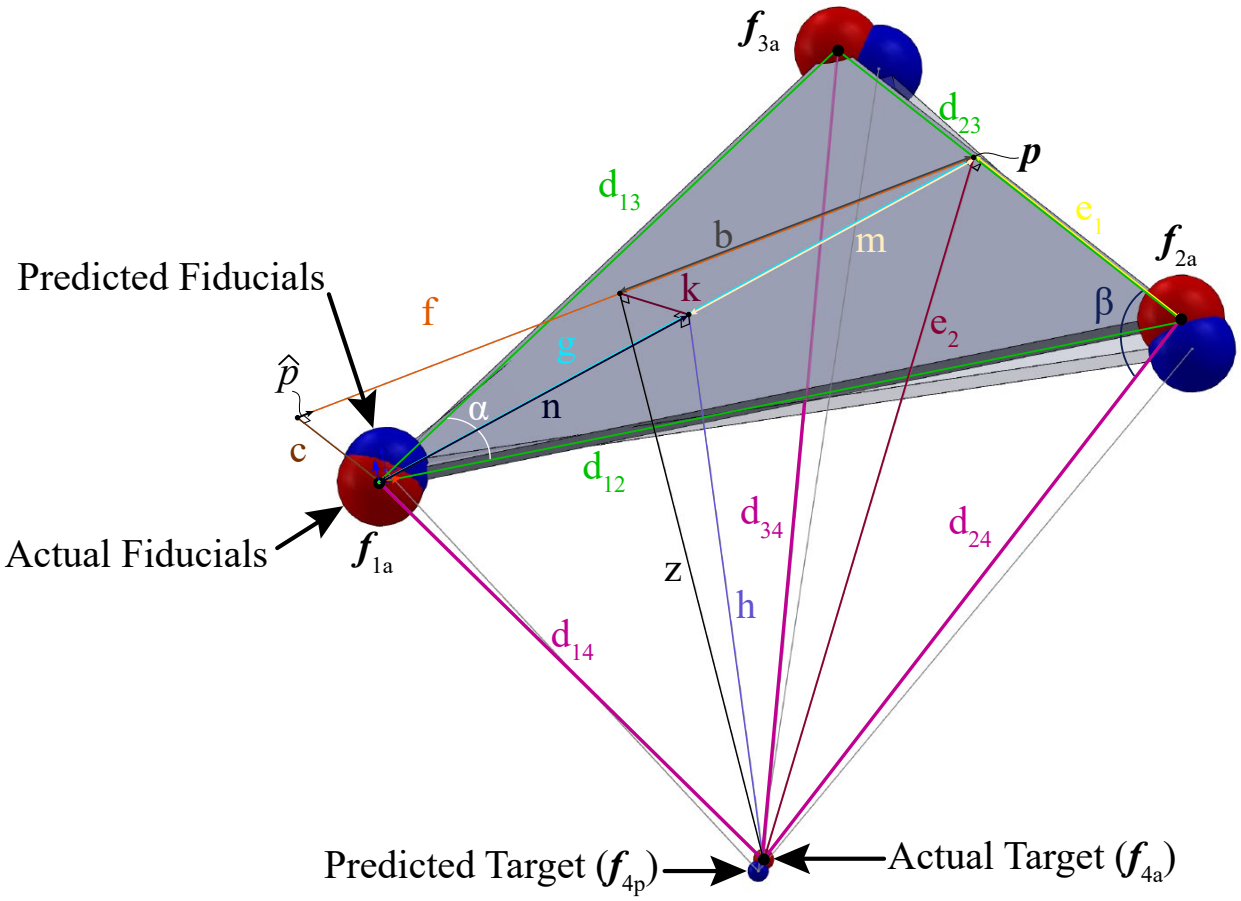

Figure 2.15: Coordinate frame definitions for TRE calculation. The measured fiducial positions are shown in red and the predicted fiducial positions shown in blue.

in Fig. 2.15 as

$$\boldsymbol{f}_{4a} = \boldsymbol{p} - b\hat{\boldsymbol{p}} - \begin{bmatrix} 0 \\ 0 \\ z \end{bmatrix}. \tag{2.5}$$

After establishing a coordinate frame for the actual microtable fiducial positions and predicted target, the transformation between the actual fiducials to the predicted fiducials was computed by finding the transformation that minimizes the fiducial registration error (FRE)

$$FRE = \sqrt{\frac{1}{3}\sum_{i=1}^{3} FRE_i^2}. \tag{2.6}$$

Using the rigid transformation that minimizes (2.6), this transform was applied to the predicted target point to transform the predicted position to the desired position and compute the TRE as

$$TRE = \left\| \boldsymbol{f}'_{4a} - \boldsymbol{f}_{4p} \right\|, \tag{2.7}$$

where $\boldsymbol{f}'_{4a}$ is the actual target point transformed into the predicted frame.

The smallest distance between the medial drill path and the facial nerve for the patient λ was calculated and it was specified that the following condition must be satisfied to proceed with the surgery

$$(\lambda - TRE) < 0.35\, mm. \tag{2.8}$$

2.6 Results

2.6.1 MICIS Parameter Analysis

In the analysis, 19 of the 97 patients (20%) would not tolerate a MICIS plan given proximity limitations most typically with the lateral aspect of the EAC. This result is fairly consistent with that reported in [132] for a drill bit diameter of 1.6 mm where exclusion was determined based on facial recess size and system accuracy instead of absolute proximity to adjacent structures. Interestingly, most of these omissions needed to be determined visually on the CT scan and not automatically using only the segmentations. Automated proximity analysis between structures only identified 4 out of the 19 of the candidates for omission because it was the lateral-most portion of the EAC that was the violating area most often—a region of the EAC not typically segmented. Of the remaining 78 patients who could accommodate a MICIS trajectory, 18 required the 13 mm differential between the medial and lateral drill bits (i.e., the larger diameter, lateral drill bit did not go as far into the skull). As with those patients excluded from MICIS, the primary reason for the larger differential was proximity of the lateral drill to the EAC. In the automated proximity analysis, 29% of plans collided with the segmented chorda tympani, a percentage slightly higher,

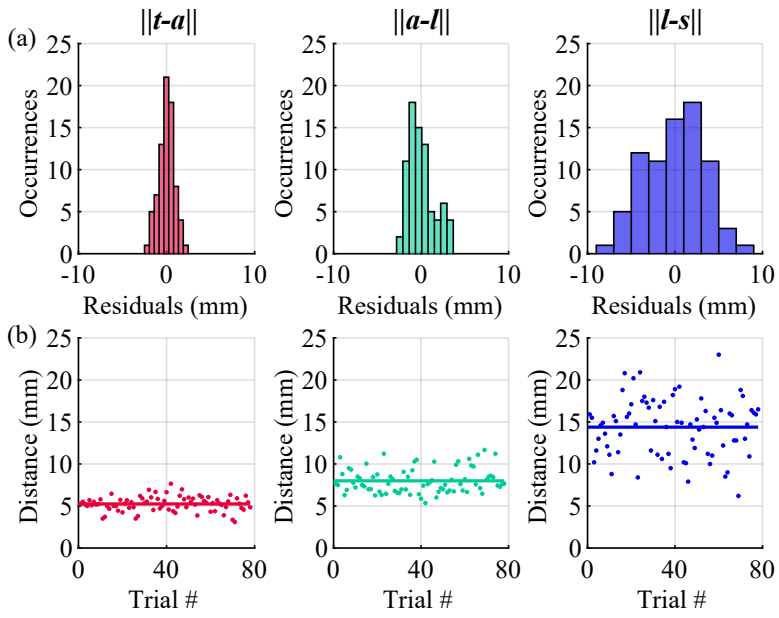

Figure 2.16: MICIS parameter analysis results (a) Histogram of results and (b) Mean values which are 5.3 mm for middle ear space ($||\boldsymbol{t} - \boldsymbol{a}||$), 8.0 mm for the medial drilling ($||\boldsymbol{a} - \boldsymbol{l}||$), and 14.4 mm for the lateral drilling ($||\boldsymbol{l} - \boldsymbol{s}||$)

but fairly consistent with past reporting [108], [133]. It is also important to note that 30 ears out of the 97 ear dataset came from 15 heads. In other words, the left and right ear were both included from those 15 heads. Ears from the same head were not excluded because there was no evidence that the whole MICIS surgical workspace will behave symmetrically. In 3 cases, one ear of a head met the omission criteria, and the other did not. After this analysis, histograms were generated for the parameters: $||\boldsymbol{t} - \boldsymbol{a}||$, $||\boldsymbol{a} - \boldsymbol{l}||$, and $||\boldsymbol{l} - \boldsymbol{s}||$ with N = 78 after omissions (Fig. 2.16(a)). The hypothesis of normality for each parameter could not be rejected by a Kolomogorov-Smirnov test with 5% significance (p = 0.96, 0.08, 0.50) respectively. The mean for each parameter is plotted as a horizontal line in Fig. 2.16(b). The mean values were (5.3, 8.0, and 14.4) mm respectively. The overall drill path lengths (addition of the three distances in Fig. 2.16(b)) were between 21 mm and 36 mm with a mean of 28 mm, consistent with past reported approximations of 30 mm [38], [134] and maximum of 35 mm [35].

Before proceeding, it is important to note how repeatable these study results are since the automatic drill trajectory generated is not an analytic result but rather an iterative result with many

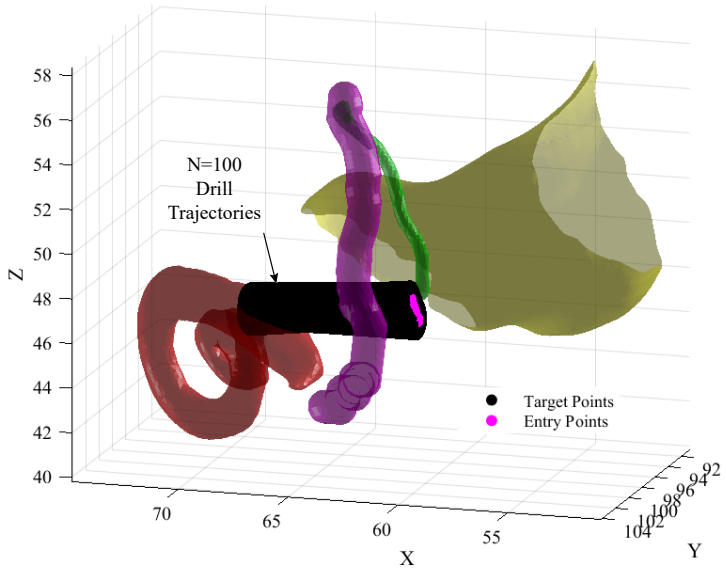

Figure 2.17: Typical result from generating 100 independent trajectories for a patient scan

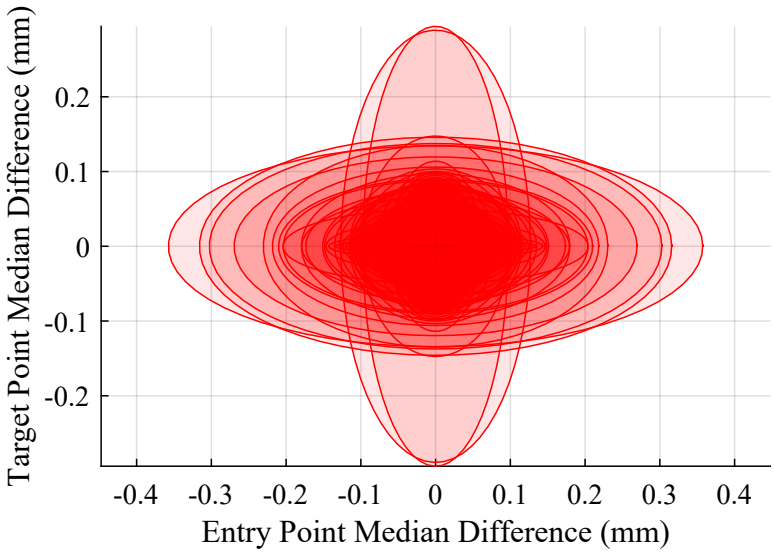

Figure 2.18: Median entry point difference (horizontal axis of ellipse) and median target point difference (vertical axis of ellipse), with an ellipse drawn for each of the 94 scans with 100 trajectories. Note that higher opacity indicates more scans within a region, and lower opacity indicates outliers.

possible solutions that is generated by finding a path that does not violate anatomical restrictions. To investigate repeatability of such trajectories, N = 100 independent drill trajectories were generated automatically by wrapping the methods detailed in [108] in a loop and applying the automated algorithm 100 times for each patient scan (see Fig. 2.17). For 94/97 scans, this method was successful at generating 100 trajectories. For the remaining 3 scans, only a subset of 100 acceptable trajectories could be found. For a given MICIS candidate, this enabled analysis of how much the drill path entry point and target point would vary if the path were regenerated using the automated algorithm. Furthermore, by looking at the median maximum variation for the population, insight is gained into study repeatability.

For these independent drill paths for each scan, the maximum deviation of the target point, entry point, and path length was analyzed. The median maximum deviation for the target point was 0.51 mm, the median maximum deviation for the entry point was 0.92 mm, and the median maximum path length deviation was 0.07 mm. Fig. 2.18 shows a plot of the median deviation of the entry point on the horizontal axis and median deviation of the target point on the vertical axis of an ellipse drawn for each of the 94 scans with N = 100 trajectories, where outliers can be viewed by those ellipses with low opacity. Note, the path length in this simulation is only accounting for the distance between the automatically generated target point to the automatically generated entry point in the facial recess. The median maximum values show that a given patient's optimal insertion vector parameter lengths tend to have small variation, supporting the idea that results from the parameter analysis would be repeatable. Parameter analysis results were used to update the tool design and inform phantom model creation as will be described next.

2.6.2 New Tool Design

The parameter analysis indicated that the same 3D printed tool could be used for all patients (parameters h, r, and g in Fig. 2.10(a)), but the distal tube would need to be customized to account for interpatient variation. Fortunately, the distal tube is a flexible and easily trimmable sheath made of polyimide. In regard to the 3D printed tool dimensions, initial cadaver studies with disassembly

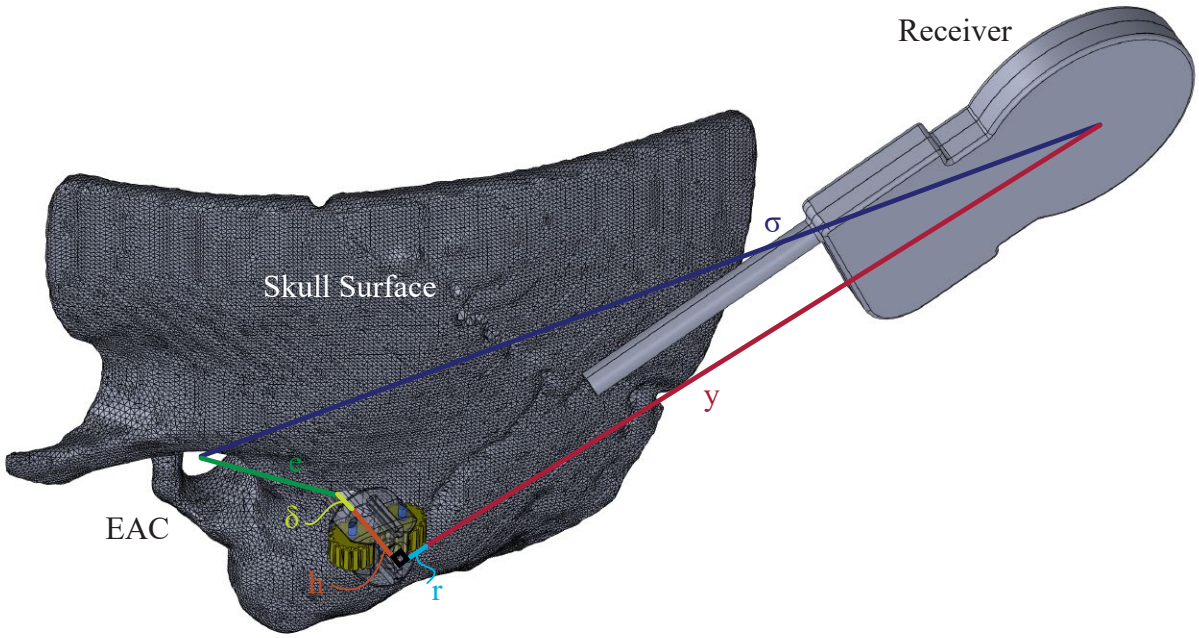

Figure 2.19: Tool sizing parameter definitions

revealed that the slack in the EA transmitting wire once the receiver is placed was a limiting factor in tool geometry above the skull surface, specifically h and r. This constraint is highly dependent upon the distance between the drilled tunnel and internal receiver placement which is variable due to patient and surgeon preference. Considering an EA fully inserted in the cochlea, the distance from the cochlea opening to the internal receiver center measures approximately 121 mm [135]. Subtracting off the maximum drill path length (from Sec. 2.6.1 = 36 mm) leaves 85 mm outside of the skull. Fig. 2.19 is then used to estimate tool sizing. The distance from the drill tunnel opening on the surface of the skull to the center of the subcutaneously-placed internal receiver will be approximately σ = 69 mm (79 mm average from [136] minus an assumed 10 mm distance e between the EAC and the drill tunnel opening). All of these distances are assumed to be in a plane that intersects with the tool centerline and is coincident with the vector connecting the receiver center to the tool opening center (i.e., y) and it is assumed that the EA does not have curvature limitations. Given these restrictions, the sum of the tool height (h) and tool radius (r) needs to be less than 16 mm. The dimensions h and r were specified to meet this constraint and be the

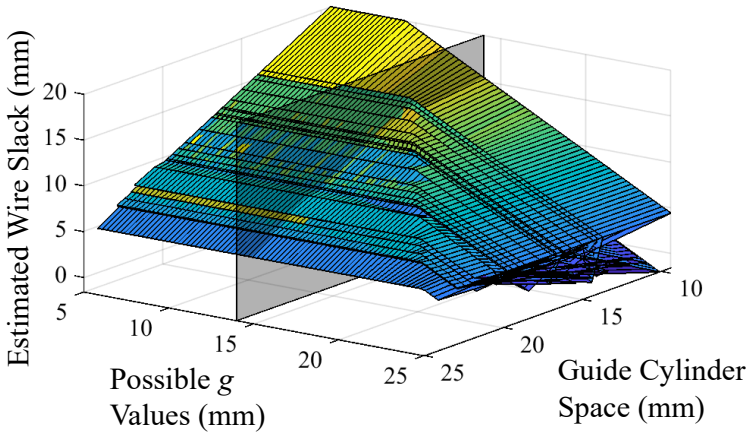

Figure 2.20: Surface graph of estimated wire slack for varying values of g and guide cylinder space magnitudes ($||\boldsymbol{t} - \boldsymbol{s}|| + \delta$) with plane drawn at 14 mm which intersects with the approximate "knee" of the surface, the largest g that maximizes the available transmitting slack for a large number of candidates

minimum possible that still enables wheel actuation, which was found to be $h = 7$ mm and $r = 4.5$ mm. The sum of this choice of h and r is well below the constraint to give the surgeon the most flexibility in placement of the internal receiver and also take into consideration the curvature of the surface of the skull, which adds between $\delta = 0.6$ mm and 4.5 mm to the overall path length, with a mean of 2.8 mm.

Based on the analysis, the 3D printed guide cylinder of the tool was made 14 mm long which is the lower bound of the 95% confidence interval of $||\boldsymbol{l} - \boldsymbol{s}||$ (rounded to the nearest whole number for ease of verifying distances in the operating room) to work for the largest number of patients possible. If the mean or upper bound is chosen, the surgeon may risk having too much of the tool outside of the skull, without enough slack to insert the EA through the tool. To verify this choice, Fig. 2.20 plots the estimated wire slack for a range of choices of guide cylinder lengths (g) to all viable candidate guide cylinder spaces ($||\boldsymbol{l} - \boldsymbol{s}|| + \delta$ for each scan). The choice of g should be based on maximizing wire slack while minimizing the amount of the EA in the polyimide tube when possible to reduce friction. Guide cylinder space is plotted on the x-axis (range [9.4, 24.1] mm), possible choices of g are plotted on the y-axis (range [5, 25] mm), and the resulting estimated

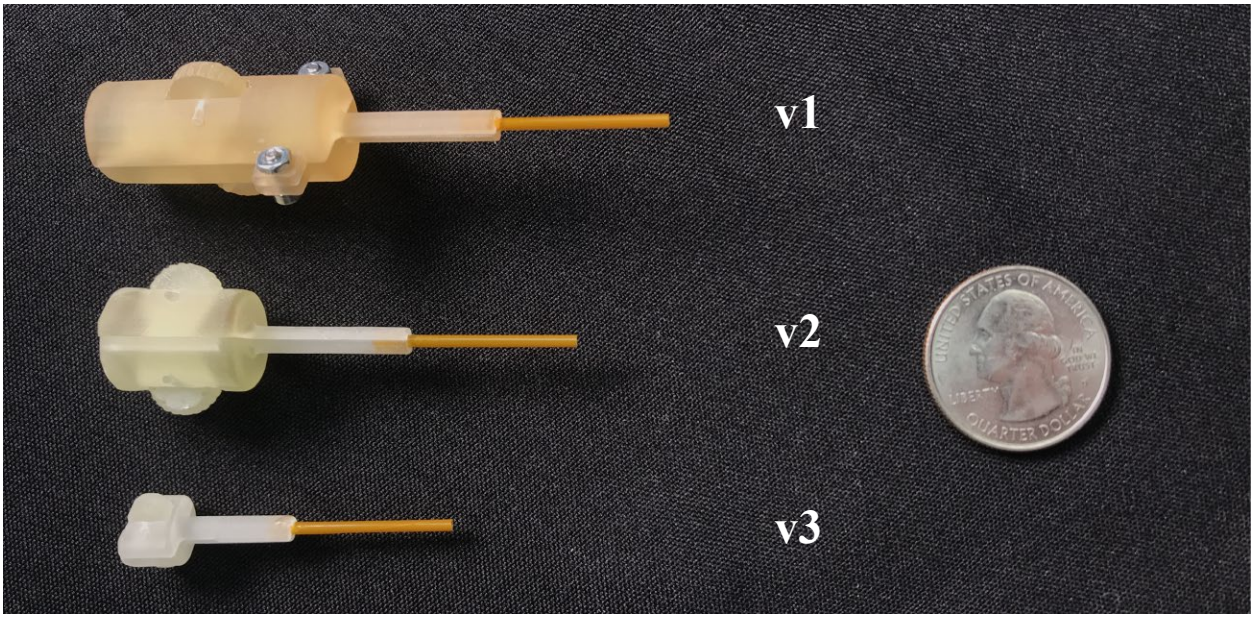

Figure 2.21: Tool comparison showing the three versions of the roller tool

wire slack for all 78 viable candidates is plotted on the z-axis (range [-1.6, 20] mm). This plot demonstrates that the 14 mm choice occurs at approximately the knee of the graph (plane drawn at y = 14 mm), and was determined to be a good tradeoff between maximizing slack for a large number of patients and minimizing friction. A comparison figure of the three tool versions can be viewed in Fig. 2.21.

2.6.3 Phantom User Study

Results from the phantom user study are shown in Fig. 2.22. Force data was binned into 5° increments. For standardization, an insertion was deemed complete after the force exceeded 34 mN, the minimum highest force for any of the eight trials. Additionally, forces that corresponded to $0\,^{\circ}/s$ of movement were omitted from analysis because the stop and start of movement throughout each insertion was not consistent between trials. Since data is binned to generate an average insertion profile, this stationary force data would skew the data (e.g., lead to inappropriate weighting of low forces if the EA was left in place while readjusting the microscope in one trial and not another). Thick lines indicate the binned average of the roller tool insertions (dashed blue line) and forceps insertions (solid red line), smoothed using a moving average over 5 points (i.e., over 25°). Fig. 2.22

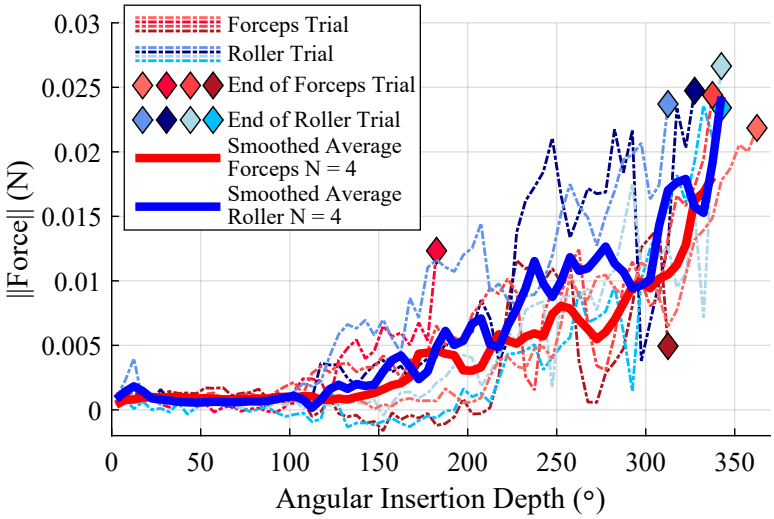

Figure 2.22: Force vs. angular insertion depth in phantom user study. Individual trials are shown as thin, dashed lines for the forceps (shades of red) and roller tool (shades of blue) trials. The smoothed average curves are shown as solid lines for the forceps (red) and roller tool (blue). These results demonstrate that the force profile of the insertion tool is similar to that of the traditional forceps approach, but with more consistently deep insertions

shows similar insertion force magnitudes for both insertion techniques. Roller tool insertions exhibited slightly higher forces but more consistently deep angular depths (note the forceps trial that only reached about 180°). More importantly, the roller tool did not introduce any unexpected large force spikes (all roller insertions reached at least 310° before exceeding the 34 mN threshold).

2.6.4 Cadaver Experiments

Results from the cadaver study (N = 8 ears) demonstrated that the roller tool qualitatively increased the ease of insertion as reported by the surgeon. Post-experiment EA pictures indicated that the transmitting wires and individual electrode contact positions were qualitatively unchanged by insertions through the roller tool. Tool sterilization, sizing, and removal were successful in all cases. Quantitatively, insertions with the roller tool resulted in AIDs that were on average 15% deeper than insertions using the traditional tool. Using a one-sided paired t-test analysis, this percent increase was statistically significant for a significance of 10% (p-value = 0.07).

The average percent difference in angular insertion depth between when the tool was still in place and when it was disassembled and removed around the EA was 5%. Using a two-sided

paired t-test, this percent difference was not statistically significant for a significance of 10% (p-value = 0.65), indicating that tool removal did not have a statistically-significant effect on final EA position. In interpreting these results, it is noted that the sample size is relatively small, and additional experiments would be useful to improve the robustness of these statistics in the future.

For both ears of head four, after testing with saline as an intracochlear fluid on each side, soapy water was used as a lubricant to decrease friction further and ensure that the tool would not restrict the EA from reaching full insertion for any reason. In the left ear, the resulting AIDs were (551°, 696°, and 682°) for the forceps, roller tool after insertion, and roller tool after tool removal, respectively. In the right ear, the corresponding AIDs were (424°, 536°, and 545°). These results validated that the chosen tool dimensions did not obstruct the EA from achieving a full insertion in a cadaveric cochlea with the subcutaneous receiver in place.

2.6.5 Clinical Implementation

After rigorous pre-clinical testing, this tool was used in an FDA investigational human feasibility trial of MICIS for EA insertion. After manufacturing of the microtable, it was verified that the resulting error satisfied (2.8). The tool was sterilized per the sterilization protocol described earlier and delivered to the operating room. After drilling was complete, steps (f) and (g) of Fig. 2.14 were performed and the roller tool enabled threading of a MED-EL FLEX28 EA down the drilled tunnel, through the middle ear space, and into the cochlea after the internal receiver was placed. The tool enabled a full insertion of the EA, with all 12 electrode contacts intracochlear in the ST and a final AID—after disassembly and removal of the tool—of 557°.

2.7 Discussion

Through design verification and validation, user and design requirements for the tool have been demonstrated to be met. Requirements (i) and (ii) were verified with initial design and testing presented in prior work. In [112], it was shown that the new manual tool design would enable insertion of MED-EL Standard and FLEX series EAs, and in [42], this result was further validated with cadaveric workflow, but without full tool disassembly or receiver placement. In this work, a

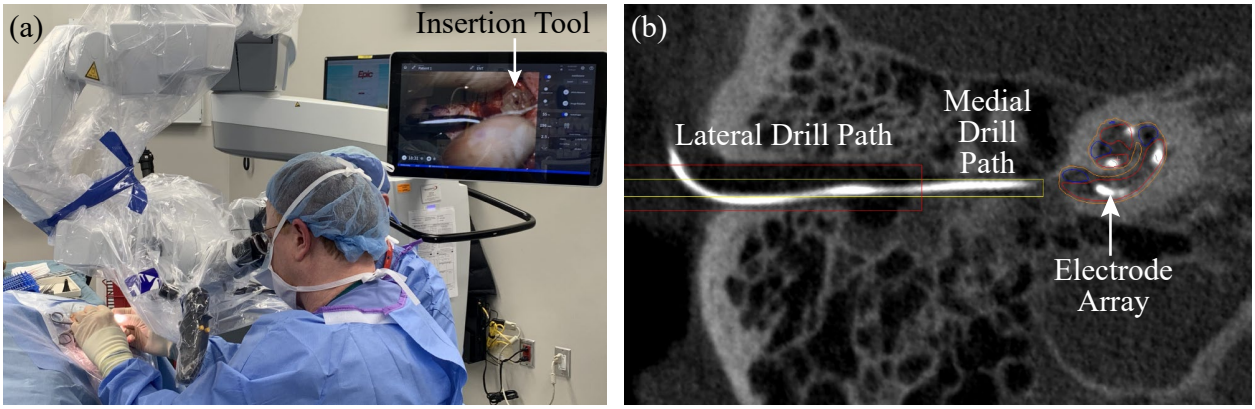

Figure 2.23: (a) Clinical use of tool and (b) Resulting clinical case postoperative scan with preoperative plan overlaid

population parameter analysis was performed to determine whether a single manual 3D printed tool could accommodate all viable candidates, and this analysis was used to specify tool dimensions to accomplish requirement (iii). This population analysis indicated that one 3D printed tool could be used with polyimide adjustments to make the tool patient-specific. In this analysis, approximately 1 in 5 CI candidates have anatomy that was not favorable for MICIS. The determined results of the distances $||\boldsymbol{t} - \boldsymbol{a}||$ and $||\boldsymbol{t} - \boldsymbol{s}||$ are generalizable to any MICIS with a similar choice of insertion vector (i.e., tangential to the basal turn). While other parameters may be more specific to the Vanderbilt implementation of MICIS, this analysis shows that the middle ear ($||\boldsymbol{t} - \boldsymbol{a}||$) and facial recess ($||\boldsymbol{a} - \boldsymbol{l}||$) depths have less variability than the lateral mastoid depth ($||\boldsymbol{l} - \boldsymbol{s}||$). Additionally, the analysis highlighted that EAC proximity to the lateral drill path should be visually checked on the surgical plan to ensure patient safety (15/19 omitted candidates were excluded based on this visual check in this study). Automatic drill path variability investigation showed that, for a given patient, path variation tended to be small. This is an important result given that drill path determination is a probabilistic and not an analytic result. Small variation implies that results from this study should be relatively replicable.

Next, for design requirement (iv), an external company validated a sterilization protocol for the tool since the standard sterilization routines for the Dental SG resin from Formlabs could not be guaranteed to be valid with the addition of the polyimide and superglue. A complete disassembly

method was developed that featured helically slit polyimide and resulted in very little change to the final angular insertion depth (approximately 5%). Avoidance of EA damage (requirement (v)) was qualitatively determined using high resolution pictures of the EA before insertion, after insertion through the tool, and after insertion into a cadaveric cochlea. These pictures indicated that tool use likely will not damage the transmitting wire or active end of the EA. Note that the interaction between the helically cut polyimide and the silicone body of the EA is still quantitatively unknown and depends on a variety of factors. This interaction should be investigated further in the future to quantitatively ensure that regardless of situation, the cut edge of the tube does not cause any functional change to the EA.

For each experimental evaluation, the roller tool was compared to surgical forceps for fulfillment of design requirement (vi). Before introducing a new tool into the operating room, it is important that both the device developers and the clinicians/surgeons are confident that the new tool introduces a significant advantage over traditional tools to warrant its introduction. Experimental evaluation included a comparison of the insertion force profiles where it was demonstrated that the roller tool did not introduce any undesirable force spikes and demonstrated similar force magnitudes to the surgical forceps. The described phantom model was successfully used for force profile evaluation on a clinically representative MICIS model. Furthermore, this test setup could be used as a general surgical trainer in the future for surgeons learning MICIS EA insertion, for surgeons practicing for a particular MICIS candidate, or to compare different insertion approaches on the same model as was done in this work. A similar model could be created using the details described in Section 2.5.3 for a different MICIS candidate.

In cadaveric insertions, the roller tool yielded 15% higher insertion depths when compared with forceps. Additionally, it was qualitatively demonstrated in both phantom and cadaver insertions that the roller tool made it significantly easier to thread the EA into the cochlea opening (a non-trivial task when using the forceps due to visualization and dexterity limitations, as well as the prevalence of buckling of the EA in the middle ear space). All of these results indicated that the roller tool introduced a sufficient enough advantage to move it to the operating room. Finally, it

was verified that the chosen tool dimensions based on the population analysis did not obstruct the EA from achieving a full insertion in a cadaveric cochlea with the subcutaneous receiver in place (requirement (vii)). This finding is important because insertion depth has been correlated with postoperative audiologic performance [70] and thus, should not be restricted whenever possible.

With the user and design requirements met, this tool was translated to the operating room for the first time, and enabled a full ST insertion in a clinical case. No backup tools were needed, although three were available. There are many important areas of future work for this tool. The tool should be evaluated with different straight EA types (simply by modifying the inner diameter and bottleneck diameter of the tool) to verify functionality across types. Additionally, future work could investigate the addition of a stylet arrestor to enable insertion of precurved EAs with this tool, although the buckling issue is much less prevalent with these stiffer EAs in MICIS. A third area of future work should be expanding the number of clinical cases to include more patients and achieve a statistically significant measure of clinical success. Another interesting study would be evaluating whether this tool could be useful for traditional, mastoidectomy-based CI surgeries as opposed to only the minimally invasive situation. A final area of future work would be determining how beneficial this tool is to novice users (in MICIS and in traditional CI surgery) compared to its usefulness to expert users in a similar setting.

2.8 Conclusion

The developed insertion tool outperforms traditional tools (i.e., surgical forceps) used for insertion of EAs in MICIS qualitatively by ease of use and quantitatively by AID. In its current design, this tool can only be used with straight, non-styleted EAs. Successful introduction into the operating theater was performed for the first time.

2.9 Acknowledgments

The developers thank Anandhan Dhanasingh of MED-EL for the EAs used in experiments. R.F.L. is a consultant for Advanced Bionics and Spiral Therapeutics. This project was supported by Award Number R01DC008408 from the National Institute on Deafness and Other Communication

Disorders of the National Institutes of Health and by the National Science Foundation Graduate Research Fellowship DGE-1445197/1937963.

Chapter 3

Magnetically Steered Robotic Insertion of Cochlear-Implant Electrode Arrays: System Integration and First-In-Cadaver Results

CI EAs must be inserted accurately and precisely to avoid damaging the delicate anatomical structures of the inner ear. Reducing trauma during CI EA insertion can lead to better hearing outcomes. A variety of robotic tools have been developed to decrease the likelihood that intracochlear trauma will occur compared to manually inserting EAs. Additionally, researchers have investigated steering the EA to further reduce trauma using a variety of methods including tendon actuation, embedded shape-memory wires, or magnetic steering. Magnetic steering has the benefit of enabling the steering of commercial straight EAs with just the addition of a small magnet on the tip of the EA that is embedded in the same silicone as the EA body. Benchtop studies have demonstrated reduced insertion forces (which are correlated with insertion trauma), but this force reduction has not yet been shown to translate to a cadaveric model.

This chapter focuses on the development and testing of a system to magnetically steer and robotically insert CI EAs. The work in this chapter presents several advancements toward the goal of deploying magnetic steering of CI EAs in the operating room. Main contributions of this chapter include integration of image guidance with developed patient-specific insertion plans, design and incorporation of a new nonmagnetic insertion tool, and use of an electromagnetic source, which provides programmable control over the generated field and whose magnetic field can be made inert when not in use. System feasibility is demonstrated by magnetically steering EAs into a cadaver cochlea for the first time. These experiments show that magnetic steering decreases average insertion forces in comparison to image-guided robotic insertions alone in both phantoms and cadavers.

The work detailed in this chapter led to a first author conference publication in the International Conference of Robotics and Automation and a journal publication in Robotics and Automation Letters [86]. Much of this chapter consists of content from [86] (© 2020 IEEE) reprinted with

permission. This work also led to a paper in Otology and Neurotology on the development of a force sensing basilar membrane phantom model [137].

3.1 Introduction

CIs are among the most successful neuroprosthetic devices, restoring hearing to hundreds of thousands of deaf or partially deaf people worldwide [116]. Traditionally, the CI EAs are inserted manually into the ST chamber of the cochlea [138], with insertion technique varying between surgeons (e.g., forces, speeds, angle of approach) [139]. Intracochlear trauma occurs frequently, which can impair residual hearing, increase the stimulation currents required, and result in more crosstalk between electrode contacts and nerve fibers, reducing implant performance [71], [140].

Reducing trauma has been shown to help preserve residual low-frequency hearing capability and can lead to improved speech perception [45]. Preserving residual hearing is also increasingly important for electroacoustic stimulation strategies, which combine a CI with an acoustic hearing aid [141], [142]. Trauma reduction can also simplify cochlear revision procedures by reducing the amount of intracochlear ossification and fibrosis [143], [144].

Robotic approaches to EA insertion have been an area of focus for some time, since robots offer greater precision in insertion technique, which may lead to less traumatic insertions [50]. Zhang *et al.* developed a direct kinematics calibration method using mechanics-based models [145], and showed that variability can be decreased using robot-assisted insertion and optimized path planning, and that robots enable insertion speed and other desired parameter values to be more easily reproduced [146]. Pile *et al.* developed a parallel robot with four DOF to insert precurved EAs using the AOS technique [77] They showed that the robot could maintain insertion forces below 80 mN in a cochlea phantom throughout the insertion and confirmed many of the aforementioned benefits of a robotic insertion approach. Pile *et al.* also provided workspace and parameter requirements for robotic insertion. Image guidance approaches have been shown to decrease the invasiveness of the surgical procedure and provide an optimal insertion vector for EA placement [32], [40]. In particular, Caversaccio *et al.* clinically demonstrated a safe and effective robotic ap-

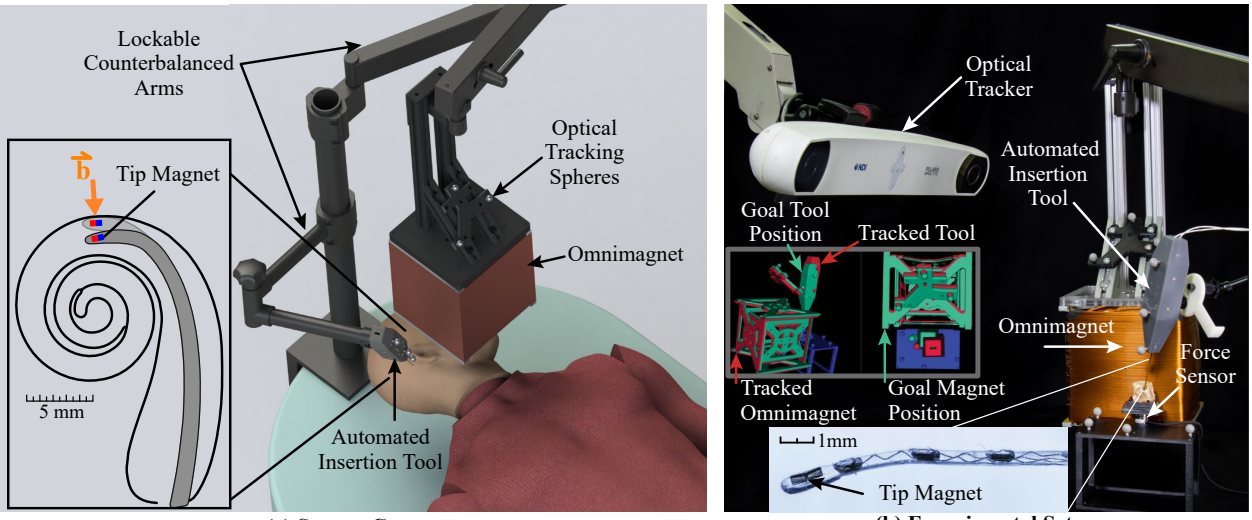

(a) System Concept **(b) Experimental Setup**

Figure 3.1: System for magnetically steered robotic insertion of cochlear-implant EAs. The automated insertion tool and Omnimagnet are both optically tracked and secured on counterbalanced positioning arms. The surgeon loads the EA into the tool and uses image guidance to align the tool and Omnimagnet with the preoperatively planned poses, at which point the arms are locked in place and the planned magnetically steered insertion trajectory is accomplished © 2020 IEEE.

proach for drilling a direct access tunnel to the cochlea [40]. These works demonstrate the benefits of automation in CI surgery and motivate developing an automated tool that enables the surgeon to automatically insert the EA along the optimally planned trajectory in a clinical setting.

Prior EA insertion tools have used a variety of innovative mechanisms of gripping and carrying EAs along the desired path. These methods include: utilizing a blunt pin and linear motion through a slotted tube [54], [107], using two titanium tube halves and manually inserting the EA [33], using a gripper with two arms rotating around a pivot point to grasp the EA [123], [124], [147], and utilizing a collet-style gripper and a parallel robot to guide EA insertion [77].

Going beyond robotic insertion, steering (i.e., bending of the EA body) has the potential to further reduce intracochlear trauma by reducing forces between the EA and the ST walls and avoiding tip impingement. Steering may also enable deeper insertions, which may enable the patient to perceive lower-frequency sounds than would otherwise not be possible [70]. One EA steering method utilizes a magnetic field source adjacent to the patient's head to steer a magnet-tipped EA inside of the ST and reduce insertion forces. This concept was first introduced in

[68], where a benchtop system used a permanent magnet—which could be rotated with one DOF to change the applied-field direction, and translated with one DOF to change the applied-field strength—to steer a 3:1 scaled EA-like device in a 3:1 scaled ST phantom. A similar system was later evaluated using commercially available EAs with a magnet embedded in the tip [148], inserted into improved 1:1 scale ST phantoms [149], where a significant decrease in insertion forces was reported compared to robotic insertion without magnetic steering.

In this chapter, a complete system (see Fig. 3.1) is presented that represents the culmination of prior work on subsystems and algorithms [68], [108], [126], [148]–[152] for magnetically steered robotic insertion of EAs. The goal of the current system is to bridge the gap between the benchtop and practical animal and cadaver experiments. Specific new contributions in this work include: 1) introducing the first fully nonmagnetic automated insertion tool, with a novel slotted-tube approach to controllably release tapered flexible EAs after insertion, 2) incorporating silhouette-based image guidance for practical, accurate insertion-tool and magnet alignment to a preoperative plan in the operating room, 3) replacing the moving permanent-magnet field source with a safer, stationary Omnimagnet [153] electromagnetic source, 4) introducing a stronger, cubic-core Omnimagnet, and 5) the first demonstration of magnetically steering an EA in a cadaveric specimen, verifying that force reductions shown previously in phantom models translate to the cadaver setting.

3.2 Methods

3.2.1 Image Guidance and Patient-Specific Paths

In this section, the preoperative steps for generating a magnetically steered insertion plan are described. The state-of-the-art insertion trajectory algorithm is incorporated to generate the planned patient-specific insertion vector, and then develop methodology to automatically generate a full magnetic steering plan given only the patient-specific anatomy and insertion vector. Outputs of the automated plan are the aligned Omnimagnet and insertion tool position and orientation (patient-specific), as well as the magnetic field vectors along the ST (using an average cochlea model registered to the patient's ST).

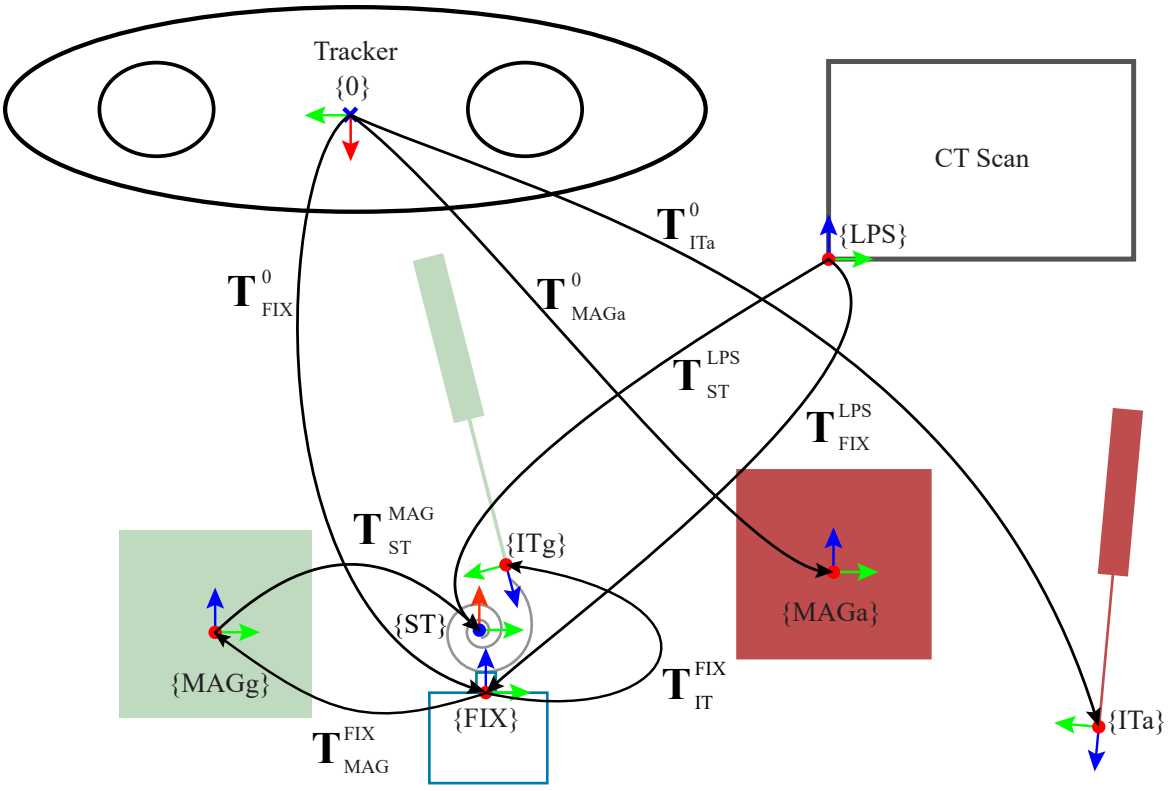

Figure 3.2: Transform definitions used in preoperative planning for the magnetic steering system

3.2.2 Patient-Specific Insertion Planning

The image-guided workflow requires tracking or computing the transformation matrices shown in Fig. 3.2. To begin this process, a preoperative CT scan was acquired of the cochlea model affixed to the cochlea fixture with the fiducial markers attached (which are localized in the preoperative plan). The inner-ear anatomy was segmented using the atlas-based approach of [126] and the optimal insertion vector was computed as described in [108] (see Fig. 3.3). This vector defines the alignment of the automated insertion tool. The atlas-based segmentation has been used to segment in-vivo clinical CT scans with a mean surface error of 0.21 mm [127].

The steering method works by creating a magnetic field vector that is orthogonal to the insertion path at the location of the magnetic tip of the EA, as depicted in the inset of Fig. 3.1(a). This is done in order to create a torque on the embedded magnet, to cause bending in the continuum body of the EA, and thus reduce the normal force on the ST wall. The path was generated using the equations

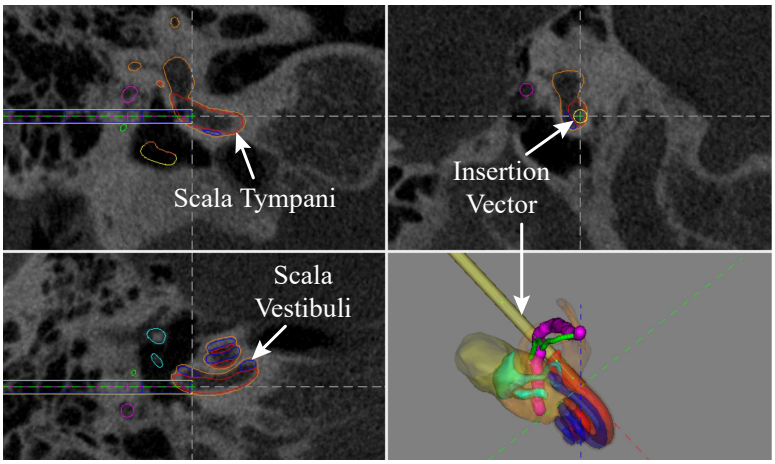

Figure 3.3: Patient-specific segmentation of cochlear anatomy and automatically generated insertion vector (yellow) [108], [126], [127] © 2020 IEEE.

in [149] that describe an average ST model based on anatomical data. The magnetic field path was registered to the medial axis segmented from the patient's ST. In order to compute the prescribed magnetic field vectors, the initial CT scan was first used to compute $\boldsymbol{T}_{FIX}^{ST}$, the rigid transform between the fixture and attached ST model. This transform is unchanged during experiments. To find this transform, the segmented medial axis points and the fiducial markers were converted from Left-Posterior-Superior (LPS) CT coordinates to the corresponding coordinate system of their associated model. For the fixture, standard point registration [154] was used to find the transform between the fiducial markers in the CT frame to the prescribed markers in the tool definition file that will be optically tracked. This generates $\boldsymbol{T}_{LPS}^{FIX}$. For the medial axis, a standard cochlea frame was fit as defined in [63] to the segmented axis to find $\boldsymbol{T}_{LPS}^{ST}$. Then, the transform between the fixture and cochlea frames was computed as

$$\boldsymbol{T}_{ST}^{FIX} = \boldsymbol{T}_{LPS}^{FIX} \boldsymbol{T}_{LPS}^{ST\ -1}. \tag{3.1}$$

Next, the medial axis was interpolated and smoothed to ensure that the points were equally spaced and numerical integration was performed along the path to determine the insertion depths at each point. For these points, the normal vectors (pointing toward the helicotrema) were computed for

magnetic field vector prescription. This computation assumes the tip-magnet of the EA has the north-pole pointing forward (pointing along the ST toward the helicotrema). If the tip magnet of the EA is magnetized with the south pole pointing forward, these normal vectors were flipped.

After normal vector computation, these normal vectors were transformed from the cochlea frame to the Omnimagnet frame. Both the fixture and Omnimagnet were constrained to be planar to the table. That is, they can only rotate about their $\hat{z}$ axes (Fig. 3.1(b)). The translation of the ST origin in the Omnimagnet frame was explicitly specified, $\boldsymbol{p}$. The Omnimagnet frame and the fixture frame $\hat{x} and \hat{y}$ axes were also constrained to be aligned. These constraints enabled computation of $\boldsymbol{T}_{FIX}^{MAGg}$ and subsequent computation

$$\boldsymbol{T}_{ST}^{MAGg} = \boldsymbol{T}_{FIX}^{MAGg} \boldsymbol{T}_{ST}^{FIX}. \tag{3.2}$$

This transformation matrix was then used to transform the normal vectors in the ST frame to the Omnimagnet frame. Using the shape of the experimentally determined field magnitudes in [148], the magnetic field magnitudes were prescribed to increase in a ramp-like manner (see Fig. 3.4). The field is zero during the initial linear portion of insertion, when there is no need for bending. Upon reaching the basal turn of the cochlea, the magnetic field turns on. As the EA is inserted deeper, and the ST curvature increases, the field ramps up to apply a larger moment to the tip of the EA. The field eventually saturates at the maximum power output of the electrical system.

Finally, the insertion tool orientation to be aligned with the prescribed insertion vector $\boldsymbol{v}$ was computed. To do this, the insertion vector in CT space was first transformed to the ST frame as

$$\boldsymbol{v}^{ST} = \boldsymbol{T}_{LPS}^{ST} \boldsymbol{v}^{LPS}. \tag{3.3}$$

This vector becomes the $\hat{z}$-axis of the insertion tool coordinate system. The $\hat{y}$-axis of the coordinate system was computed such that it lies along the curl axis of the EA. Finally, a cross product was used to determine the $\hat{x}$-axis. The translational component was found by assuming the insertion frame origin is the first trajectory/medial axis point. This computation yields $\boldsymbol{T}_{ITg}^{ST}$.

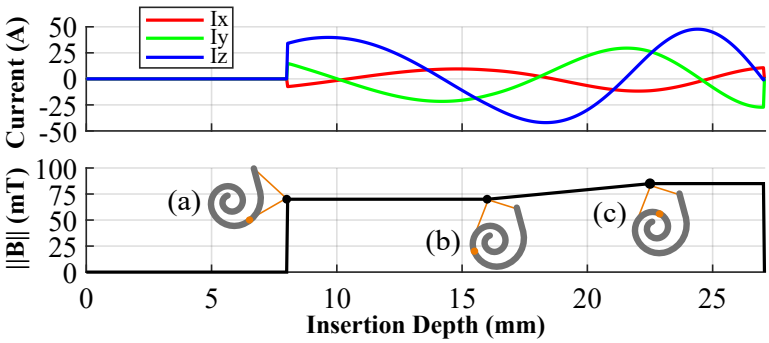

Figure 3.4: Preoperative plans for magnetic steering specify (top) the Omnimagnet coil currents required to generate (bottom) the prescribed magnetic field magnitudes based on (a) turning on the field after the initial straight insertion, then (b) ramping up the magnetic field magnitude as the ST curvature increases, until (c) saturating at the maximum power © 2020 IEEE.

For image guidance purposes, the pose of the insertion tool and pose of the Omnimagnet relative to the fixture were needed. The transform $\boldsymbol{T}_{ITg}^{FIX}$ was computed as

$$\boldsymbol{T}_{ITg}^{FIX} = \boldsymbol{T}_{ST}^{FIX}\boldsymbol{T}_{ITg}^{ST}, \tag{3.4}$$

and

$$\boldsymbol{T}_{MAGg}^{FIX} = \boldsymbol{T}_{ST}^{FIX}\boldsymbol{T}_{ST}^{MAGg^{-1}}. \tag{3.5}$$

This preoperative planning specifies the goal transforms of the Omnimagnet and insertion tool relative to the fixture and enables display of the goal poses in image guidance software for user alignment.

3.2.3 Image Guidance

Using 3D Slicer, OpenIGTLink, and the Plus Server App [155], [156], a custom GUI extension (see screenshot in Fig. 3.1(b)) was developed that connects to the NDI Polaris Spectra optical tracker (Northern Digital Instruments, Ontario, Canada), which tracks and displays the movement of the insertion tool, Omnimagnet, and cochlea fixture in real time. The program guides the user to the correctly aligned tool pose determined in Sec. 3.2.2 by displaying the real-time position of the object (shown in red in the screenshot on Fig. 3.1(b)) to the desired pose (shown in a green in the

screenshot of Fig. 3.1(b)). The user then manually manipulates each device until the tracked pose and desired pose are aligned, at which point the user locks the device in place. The angular error between the aligned and goal positions can be computed by finding the following transformations and computing the $\hat{z}$-axis angular error

$$\begin{aligned} \boldsymbol{T}_{ITg}^{ITa} &= (\boldsymbol{T}_{ITa}^{0})^{-1}\boldsymbol{T}_{FIX}^{0}(\boldsymbol{T}_{FIX}^{ITg})^{-1}, \\ \boldsymbol{T}_{MAGg}^{MAGa} &= (\boldsymbol{T}_{MAGa}^{0})^{-1}\boldsymbol{T}_{FIX}^{0}(\boldsymbol{T}_{FIX}^{MAGg})^{-1}. \end{aligned} \tag{3.6}$$

3.2.4 System Hardware and Workflow

An overview of the robotic system is shown in Fig. 3.1. A basic overview of the workflow with the proposed system is as follows. A patient-specific plan was first generated using the patient's preoperative CT scan. This preoperative plan includes 1) generating an optimal insertion vector and corresponding insertion-tool pose (position and orientation), 2) calculating the Omnimagnet pose that corresponds to the plan, and 3) registering the planned magnetic field vectors to the individual's ST (and the corresponding Omnimagnet coil currents to produce these vectors). Using this preoperatively generated plan, the surgeon will manually align the counterbalanced automated insertion tool and the counterbalanced Omnimagnet, and lock them in place. Both devices are optically tracked, enabling users to precisely align them using a custom image-guidance extension in 3D Slicer [155], [156]. The surgeon will then simply hold a button to run the prescribed trajectory that synchronously coordinates insertion depth and magnetic field to produce a smooth, atraumatic insertion. When insertion is complete, the Omnimagnet is powered off and the insertion tool is removed. The Omnimagnet, insertion tool, and force sensor interface with one another using custom Robot Operating System (ROS) nodes [157]. In the following sections, the system components are described including the Omnimagnet and the new automated insertion tool for EA advancement and deployment.

3.2.5 Omnimagnet

Magnetically steering the EA through the spiral-shaped cochlea requires strong, controllable magnetic fields. Prior work has exclusively considered a permanent magnet as the field source [68], [148]. However, as noted in [151], it may be desirable to use an electromagnetic source for three reasons: First, an electromagnet has a controllable magnetic dipole, meaning that it does not need to be physically moved during EA insertion to vary the field strength at the cochlea, eliminating any potential risk of collision with the patient or other objects. Second, an electromagnet can be turned off and is inert when not in use, making handling, storage, and use of ferrous surgical equipment safer. Third, the relatively short duration of a surgical EA insertion (less than 30 seconds) would allow high levels of current to be sourced through the coils without reaching unsafe temperatures.

In the system presented in this work, the permanent-magnet source has been replaced with an Omnimagnet electromagnetic source [153]. An Omnimagnet comprises three nested orthogonal coils and a ferromagnetic core. Three control inputs (the current in each coil) provide control of the magnetic dipole of this magnetic field source, which can be used to generate a desired magnetic field vector $\boldsymbol{B}$ at an arbitrary location in space. In the original conception of the Omnimagnet [158], and all prior embodiments, the ferromagnetic core was spherical. In this chapter, the Omnimagnet was reoptimized for a cubic core, which has the effect of increasing the achievable dipole strength by approximately 35% for a given overall package size and current density. The prototype cubic-core Omnimagnet has overall cubic dimension of approximately 200 mm, with a ferromagnetic cubic core of dimension 102 mm, with the dimensions of the individual coils (and their electrical resistances) provided in Table 3.1. The Omnimagnet uses 16 AWG square-cross-section copper magnet wire (MWS Precision Wire Industries, Westlake Village, CA). The final prototype is 22 kg, which is passively supported by a lockable counterbalanced arm (Dectron, Wilsonville, OR).

As described in [153], the control equation for an Omnimagnet, assuming a basic dipole model, is

$$\boldsymbol{I} = \frac{2\pi}{\mu_0} \|\boldsymbol{p}\|^3 \, \boldsymbol{M}^{-1}(3\hat{\boldsymbol{p}}\hat{\boldsymbol{p}}^T - 2\mathbb{I})\boldsymbol{B}. \tag{3.7}$$

where $\boldsymbol{I}$ (units A) is the 3×1 array of coil currents, $\boldsymbol{p}$ (units m) is the vector from the center of the

Omnimagnet to the desired point in space at which a desired magnetic field vector $\boldsymbol{B}$ (units T) is to be generated, $\boldsymbol{M}$ is a linear transformation that maps the current array $\boldsymbol{I}$ to the Omnimagnet's dipole moment $\boldsymbol{m}$ (units A·m^2), $\hat{\boldsymbol{p}} \equiv \boldsymbol{p}/\|\boldsymbol{p}\|$, $\mu_0 = 4\pi \times 10^{-7}$ T $\cdot$ m $\cdot$ A^{-1} is the permeability of free space, and $\mathbb{I}$ is the 3×3 identity matrix.

To utilize the Omnimagnet, a high-voltage DC supply powers three servo drive amplifiers (ADVANCED Motion Controls, Camarillo, CA), which regulate the current through each coil. The amount of current is set via analog inputs (± 10 V). Custom control boards receive commands over Ethernet from custom ROS nodes and generate the required analog voltage signals for each servo drive. To determine the current scaling for each coil, a certified calibrated 3-axis magnetic field sensor (3MTS, Senis, Zug, Switzerland) was used to experimentally measure the magnetic field and compare to (3.7).

As an additional layer of safety, a dedicated microcontroller was implemented to monitor thermocouples embedded throughout the Omnimagnet, which shuts off the amplifiers if predefined temperature thresholds are exceeded. This microcontroller also monitors the temperature between insertion trials, which enabled verification that the Omnimagnet had sufficiently cooled down before running another experiment.

It is important to address the safety of placing the Omnimagnet (or any strong magnetic source) near the patient's head. Strong magnetic fields are commonly used in medical diagnosis and treatment, such as Magnetic Resonance Imaging (MRI) and Transcranial Magnetic Stimulation (TMS), and a wide variety of magnetically driven medical devices have been developed [159], [160]. Safety limits for magnetic fields are based on the nature of the magnetic field, which is typically classified as: static fields, time-varying gradient fields (100 to 1000 Hz), and radiofrequency (RF) fields (10 to 100 MHz) [161]–[163]. According to the FDA's Criteria for Significant Risk Investigations of Magnetic Resonance Diagnostic Devices (2014), a static field producing less than 8 T is considered a nonsignificant risk in adults and children over the age of one month. Other sources specify that static field exposure to the head should be limited to 2 T to ensure patient comfort [161], [162]. Current research in magnetic steering of EAs utilizes quasistatic fields of

Table 3.1: Properties of the Omnimagnet coils, including axial length (L), inner width (W), thickness (T), and resistance (R)

	L (mm)	W (mm)	T (mm)	R (Ω)
Inner Coil	117	105	11.2	3.5
Middle Coil	140	128	8.4	3.8
Outer Coil	154	152	6.9	4.0

less than 100 mT, which is well below the safety limits imposed by the FDA, or recommended by other researchers. Therefore, it does not seem that the magnitude or rate of change of the magnetic fields used in magnetic steering of EAs poses any significant risk to a patient.

3.2.6 A New Insertion Tool Compatible with Magnetic Steering

Deploying an EA in the presence of strong magnetic fields presents unique constraints not encountered by previous designs of clinically-viable automated insertion tools: the insertion tool must not contain ferromagnetic components, and to be used clinically the insertion tool has to hold, push, and release the implant gently and controllably. To achieve both of these specifications, a new insertion tool and a new grasping mechanism was designed to interface with the EA (Fig. 3.5). The tool is constructed from a 3D printed plastic housing (Formlabs, Somerville, MA), two piezoelectric linear actuators (SLC-1770-L-E-NM, SmarAct, Oldenburg, Germany), Nitinol tubes/rods, and brass fasteners. Three spherical, retroreflective markers are attached to the body of the tool to create a rigid body for optical tracking.

Details of the insertion tool assembly can be viewed in Fig. 3.5(a). Tube parameters were chosen to accommodate the dimensions of the FLEX28 EA (MED-EL, Innsbruck, Austria), but could be easily adapted for use with other EAs. The distal end of the tool consists of three nested Nitinol tubes and rods, and an outer polyimide sheath. The innermost Nitinol rod assists with EA detachment and is attached to a linear actuator. The middle Nitinol tube has an approximately 10-mm-long slot for grasping the EA, and is attached to another linear actuator. The outer Nitinol tube has a slot spanning the length of the tube and serves as a guide for the EA during deployment.

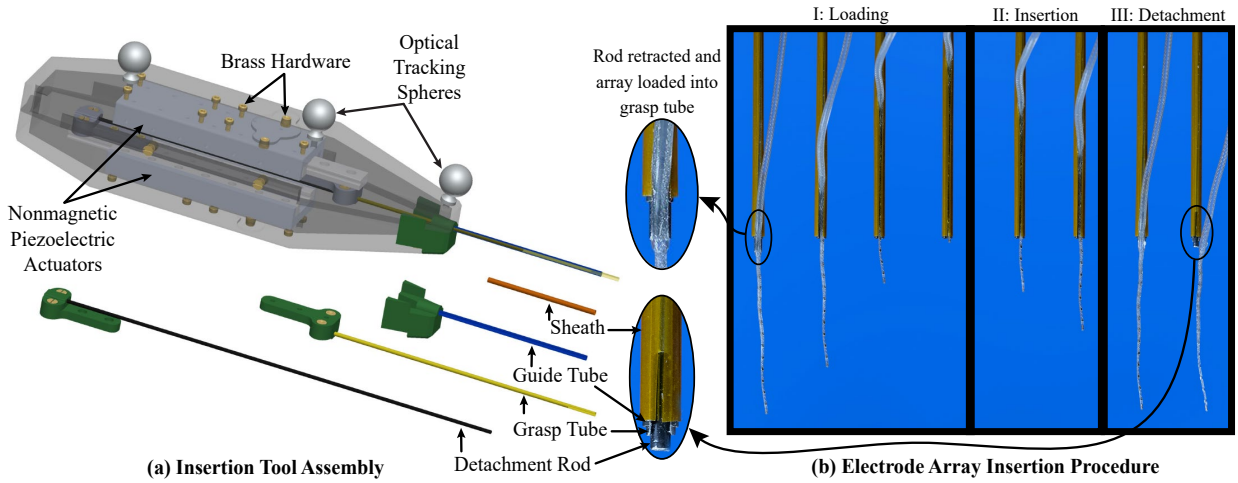

Figure 3.5: (a) Insertion tool assembly. The inner detachment rod and middle grasp tube are each attached to an actuator. The outer guide tube is connected to a detachable tip piece so that if an EA of a different diameter is to be used, it can simply be replaced with a tube of a different diameter. (b) Diagram showing tube operation for EA deployment. Step I: Loading- Load EA into the grasp tube slot and retract until the tip of the EA reaches the guide tube opening. Step II: Insertion- Insert EA by advancing the grasp tube and detachment rod simultaneously. The polyimide sheath constrains the tapered end of the EA during deployment. Step III: Detachment- Retract the grasp tube over the stationary detachment rod, which gently releases the EA from the grasp tube © 2020 IEEE.

Finally, a polyimide sheath with a lengthwise slit surrounds the outermost Nitinol tube to constrain the thinner, tapered region of the FLEX28 (which tapers to a tip diameter that is less than half that of the proximal end) and to keep the much thinner tip of the flexible EA concentric with the proximal end. The absolute insertion depth limit of the tool is 43 mm, enabling insertion of the longest EAs currently available (the FLEXSOFT and Standard EAs by MED-EL are 31.5 mm long [17]). EA insertion proceeds as described in Fig. 3.5(b).

3.3 Experimental Methods

3.3.1 Phantom Experiments

Proof-of-concept experiments were conducted in the phantom model developed in [149], which is useful because it is transparent and enables one to view the motion of the EA during insertion. Four insertions were performed using the robotic system and proposed workflow. To ensure that magnetic steering provided unique benefits in terms of reaction forces beyond those derived from

Table 3.2: Experimental Conditions for Testing Insertions with Magnetic Steering © 2020 IEEE

Method	Robotic Insertion	Image-Guided Alignment	Magnetic Steering
Manual	No	No	No
Robotic	Yes	Yes	No
Robotic & Magnetic Steering	Yes	Yes	Yes

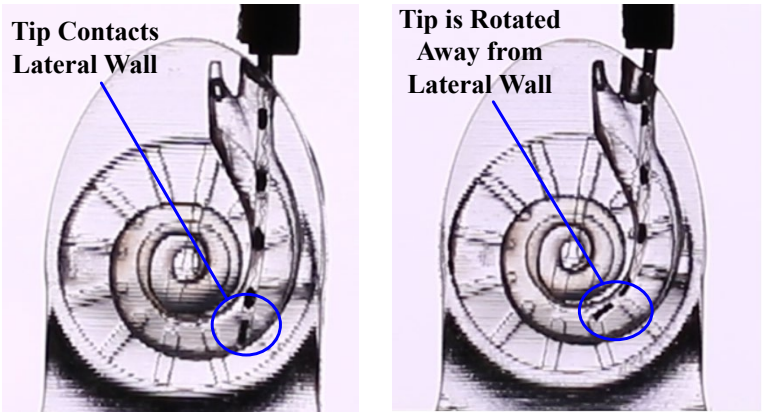

(a) Without Magnetic Steering **(b) With Magnetic Steering**

Figure 3.6: Robotic insertion into a phantom (a) without and (b) with magnetic steering. The tip of the EA is torqued away from the lateral wall in the magnetically steered case, lowering the contact force of the EA with the wall © 2020 IEEE.

robotic insertion alone, experiments were performed as follows: 1) unaided manual insertions by an experienced surgeon, 2) robotic insertions using the new insertion tool described in this chapter, with image-guided pre-insertion alignment but no magnetic steering, and 3) robotic insertions with image guidance and magnetic steering. Table 3.2 shows a summary of these cases.

A 3D-printed ST phantom with a 1.2 mm cochleostomy opening (Fig. 3.6, see [149] for details) was secured into a fixture with cyanoacrylate. This fixture was then mounted to a Nano17 Titanium force/torque transducer (ATI Industrial Automation, Apex, NC) attached to a frame with optical fiducial markers. A CT scan of this assembly was then acquired. As described in Sec. 3.2.1, the preoperative scan was used to generate the insertion plan.

The phantom model was filled with 0.9% saline solution before each insertion as in [148]. For manual insertions, a surgeon performed four unaided insertions with a new, unmodified FLEX28 EA, using the standard forceps that are used clinically for inserting EAs (see Fig. 3.7). In cases

of robotic insertion, both with and without magnetic steering, a magnet-tipped FLEX28 EA was used. All magnet-tipped EAs were fabricated by MED-EL and included two cylindrical axially magnetized magnets (each 0.25 mm in diameter by 0.41 mm in length) embedded in silicone at the tip of the EA (see inset of Fig. 3.1(b)). The EA was loaded into the insertion tool, and the Omnimagnet and insertion tool were aligned using image guidance according to the prescribed preoperative plan, with a maximum angular alignment error of less than 1°. The support arms were locked in place and the final poses of the tool and magnet were recorded. The insertion tool then deployed the EA at a constant velocity of 1.25 mm/s (this velocity was selected in view of a 0.025–7.5 mm/s range in the literature [145], [164]).

The final insertion method followed the same procedure as robotic insertion described above, but also used magnetic steering during insertion. The magnetic field of the Omnimagnet was updated at a rate of 80 Hz. Four insertions with a robotic approach and four insertions with a robotic approach and magnetic steering were completed using the same magnet-tipped EA, alternating between using magnetic steering and robotic insertion alone. For all insertions, force measurements were acquired at a rate of 50 Hz. Since the EA tip could be visualized through the transparent phantom in these experiments, forces could be mapped to angular insertion depths using video collected during insertion at 60 fps.

3.3.2 Cadaver Experiments

The same three experimental methods used in the phantom experiments (see Table 3.2) were also conducted with a formalin-fixed cadaver cochlea. The cochlea was secured in a fixture using paraffin wax and hot-melt adhesive. A patient-specific insertion plan was generated in the same manner previously described. Unaided manual insertions were performed by an experienced surgeon with a new, unmodified FLEX28 EA (see Fig. 3.7). For image-guided robotic insertions, the automated insertion tool was aligned with a maximum angular alignment error of less than 2°. A second magnet-tipped FLEX28 EA was used to perform robotic insertion experiments, alternating between robotic insertion alone and robotic insertion combined with magnetic steering (a first-

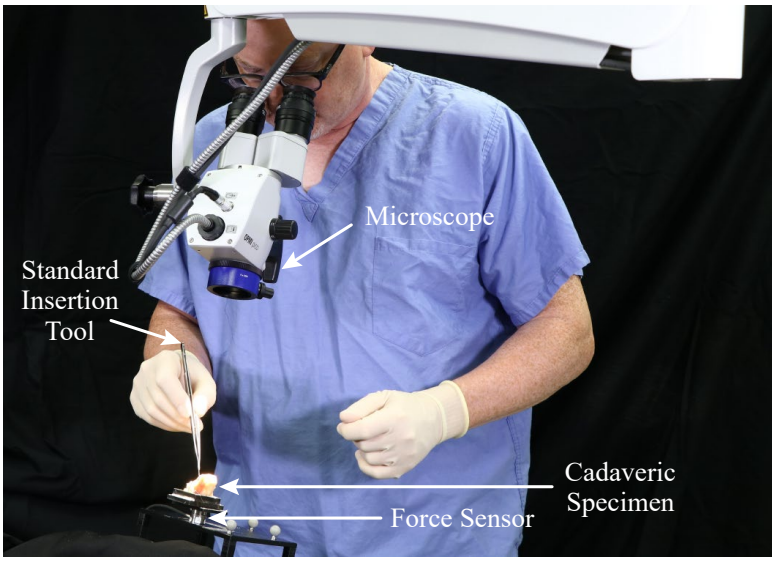

Figure 3.7: A surgeon performing a traditional EA insertion, shown here with the cadaveric cochlea © 2020 IEEE.

of-its-kind experiment). Workflow proceeded identically to the phantom experiments, with three insertions performed using each method. A force threshold of 125 mN was enforced during robotic insertions. After insertion, the EA was released from the insertion tool as described in Sec. 3.2.6 and a postoperative CT scan was acquired.

3.4 Results

A comparison of the first contact point with the lateral wall of the ST with and without magnetic steering is shown in Fig. 3.6; this result is qualitatively consistent with the results of [148]. Mean insertion force magnitudes, $\|\boldsymbol{F}\| = \sqrt{F_x^2 + F_y^2 + F_z^2}$, and the difference, $\Delta\|\boldsymbol{F}\|$, in insertion forces for both phantom and cadaver experiments are shown in Fig. 3.8, where the shaded region around each curve indicates one standard deviation from the mean. In each case, force samples were grouped into bins and then averaged. A bin of 3° was used for phantom experiments and a bin of 0.125 mm was used for cadaver experiments (since there was no direct visualization of angular depths during insertion). Diamonds mark the final depths of each individual insertion. For robotic methods this was defined as when the force increased 35 mN or more over 1 mm of actuator travel (indicative of EA buckling); for manual insertions it was at the surgeon's discretion. A one-tailed

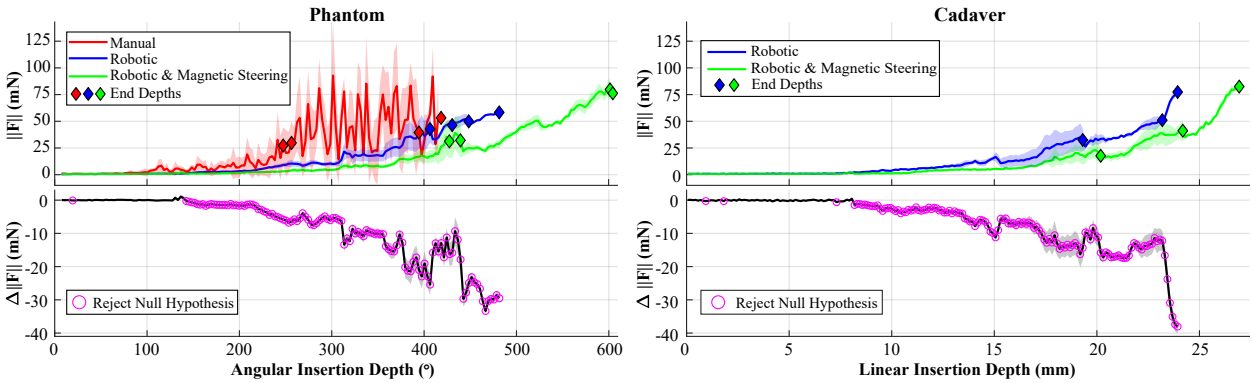

Figure 3.8: (Top) Mean insertion forces with respect to angular insertion depth for phantom experiments and linear insertion depth for cadaver experiments, illustrating that magnetic steering achieves forces that are typically lower than for robotic insertion alone. Shaded regions indicates ±1 standard deviation from the mean. Diamonds mark the final depth of each individual insertion. (Bottom) Difference in force, ΔF, between robotic insertion and magnetically steered robotic insertion. Magenta rings indicate a statistically significant decrease in force between the two methods © 2020 IEEE.

t-test analysis (as detailed in [148]) was performed, and the depths where the null hypothesis can be rejected with 95% confidence (i.e., statistically significant force reduction) are indicated with rings. All force reductions observed after the magnetic field was turned on (approximately 140° for phantom insertions, 8.0 mm for cadaver insertions) were statistically significant. Compared to robotic insertion alone, magnetic steering reduced forces by an average of 53.8% during phantom insertions and 48.8% during cadaver insertions.

The forces recorded during manual insertions in the cadaver are shown in Fig. 3.9. Note that the force data for the manual cadaver insertions is plotted vs. time since the surgeon is inserting into opaque bone, and there are no actuators to give position information in real-time.

Fig. 3.10 shows the average final AIDs for each type of phantom and cadaver insertion. For phantom experiments, the inclusion of magnetic steering resulted in deeper insertions on average compared to robotic-only or manual insertions. The average angular insertion depth for the manual insertions in cadavers was slightly higher than that of the other methods. Note that a force threshold cutoff was not enforced in these manual insertions.

The maximum temperature rise observed for the inner, middle, and outer Omnimagnet coils

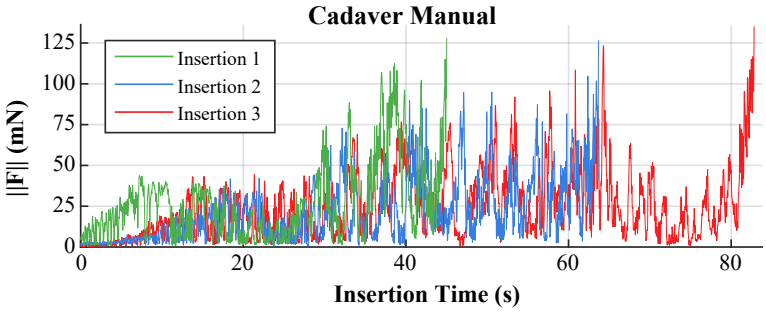

Figure 3.9: Forces observed during manual cadaver insertions exhibited more variability and larger, more frequent spikes compared to robotic methods © 2020 IEEE.

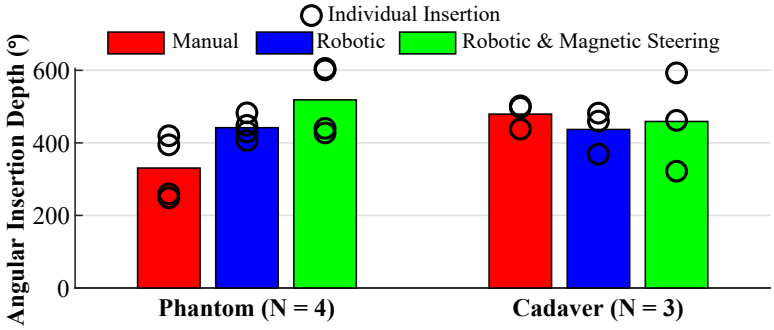

Figure 3.10: Comparison of the average final angular insertion depths for each insertion method. Depths of individual insertions are shown as black rings © 2020 IEEE.

was 1.6 °C, 10 °C, and 34 °C, respectively. These values are all within the Omnimagnet's operating range. It is also important to note that the Omnimagnet is never in direct contact with the patient, and is moved away after EA insertion is complete.

In summary, in both phantom and cadaver experiments, robotic insertions were smoother (with fewer force spikes) than the manual insertions, and magnetic steering significantly reduced forces with respect to robotic insertion alone.

3.5 Toward Clinical Deployment

The system described in the chapter was designed to be used in experiments with live guinea pigs, and will have to be scaled up (approximately 30%) to be used as a clinical system with living humans. This is due to the increased distance between the cochlea and the applied dipole. In [151], the optimal placement and size of a spherical NdFeB permanent magnet was found (i.e., an

ideal dipole-field source), based upon the magnetic field values suggested in [148] for the same embedded EA tip magnets used here. This result can be used to design an equivalent-strength (measured at the location of the cochlea) Omnimagnet. Alternatively or in addition, since the Omnimagnet can be rotated such that only two coils are required, simply removing the outermost coil and enlarging the other two would enable an increase in strength that is independent of any increase in overall size.

Additionally, note that the volume of the embedded magnet in the tip of the EA scales cubically with its length. Since this volume is proportional to the strength of the permanent magnet, substantial increases in torque can be achieved with even modest increases in the size of the embedded magnet. This increase is possible since the magnets used in this work took up less than 40% of the cross-sectional area of the EA's tip. Such an increase may preclude the need for any size increase of the Omnimagnet.

A conservative sensitivity analysis was performed of registration errors of the dipole-field source (i.e., the Omnimagnet) with respect to the cochlea. A worst-case 3.2% error in field magnitude is expected and 1.7° error in field direction due to a 1 mm error in Omnimagnet position. A worst-case 1.3% error in field magnitude and 2.0° error in field direction due to a 1° error in the Omnimagnet dipole $\boldsymbol{m}$ is expected. These values should be insensitive to changes in the size of the field source.

However, it was also found that the dipole model used in (3.7) has non-negligible error in the region of interest. In the future, a calibrated model that includes the first three terms of the magnetic-field expansion (the dipole term being the first) could be used to reduce the modeling error to less than 1% [165]. Measuring the EA position in real-time is challenging because many of the traditional sensing methods used in robotics (e.g., electromagnetic/optical tracking) either require line of sight, lack the necessary accuracy, or are too large to integrate. Future work could incorporate novel sensing methods to enable closed-loop control.

If closed-loop control methods are implemented in the future that include force feedback, the full force vector should be utilized in control to provide directionality knowledge, as opposed to

the force norm which was used as a comparison tool in this work.

3.6 Conclusion

A new robotic system to improve CI EA insertion has been presented. The primary goal of this system was to build upon prior benchtop proof-of-concept magnetic steering systems and transition toward a more clinically-focused design. A workflow for utilizing preoperative imaging to compute patient-specific insertion vectors and a magnetic guidance plan was developed. Patient safety was improved by replacing an actuated permanent magnet with a static electromagnet. The first nonmagnetic automated insertion tool was also introduced, which is capable of deploying and releasing clinical EAs with a new set of tubes that accommodates tapered EAs and gently releases the EA after deployment. Accurate pre-insertion alignment of the insertion tool was achieved by incorporating image-guidance software paired with an optical tracking system. The system was experimentally validated by performing magnetically steered robotic insertions in a ST phantom and a first-of-its-kind magnetically steered robotic insertion into a cadaveric cochlea, demonstrating in both cases that magnetic steering lowers forces by approximately 50% compared to robotic insertion alone.

3.7 Acknowledgements

This work was supported in part by the National Institutes of Health under Award Number R01DC013168 and the National Science Foundation Graduate Research Fellowship under DGE-1445197/1937963. The developers thank Anandhan Dhanasingh of MED-EL for providing the EAs used in these experiments.

Chapter 4

Real-Time Impedance Sensing During Cochlear-Implant Electrode Array Insertion to Inform Insertion Progress and Final Positioning

Traditional insertion of CI EAs is done manually in a semi-blind manner. The surgeon relies on limited tactile feedback and the view of the EA entering the cochlea to control the insertion process. EA impedance sensing is a standard clinical tool used *after* insertion is complete in the operating room to assess EA integrity and ensure there are no short or open circuits.

Recently, researchers have investigated the merit of using impedance sensing *during* the insertion. The CI electrode-electrolyte interaction has been modeled as an equivalent circuit which enables the calculation of physically relevant impedance components such as electrode contact properties (polarization resistance and polarization capacitance) and electrolyte properties (access resistance). The total impedance values and these impedance components have both been shown to correlate with the space between the EA contacts and the modiolus (E-M proximity). This work has shown promise toward providing a tool that could determine EA placement without exposing a patient to radiation, and that could provide a surgeon or automated tool with valuable information to modulate the insertion and improve final EA placement.

Past work on evaluating the relationship between impedance and E-M proximity has been limited to only a few EA types and should be expanded to include more EA types and expanded to further evaluate the reliability of using this technique to inform EA positioning. Additionally, the relationship of the equivalent circuit *bipolar* impedance components to E-M proximity has not yet been correlated and should be assessed. The possibility of using impedance values to determine a straight EA's shape should also be explored to assess whether these values can be used to inform a surgeon or robotic tool of the EA shape in real-time such that insertion adjustment could be made if necessary to improve final placement and/or reduce intracochlear trauma. This exploration should include characterization of the behavior of dual-sided electrode contacts in relation

to modiolar proximity because these types of contacts are fairly common, but the relationship has not been evaluated. In cadavers, the real-time relationship between impedance and E-M proximity has never been quantified due to difficulties in gaining real-time E-M proximity information in the opaque cochlea. This quantification is an important step to verify that the phantom models used in experiments are providing clinically meaningful information that directly translates to human models. Finally, incorporation of impedance into the control of a robotic insertion tool could be beneficial to improve final EA placement. Excellent past work has demonstrated closed-loop control of stylet actuation guided by impedance feedback. Building on this work, impedance feedback could be used to inform the 'pull-back' technique (a technique where a surgeon purposely pulls back a precurved EA after insertion to enable closer modiolar-hugging). This pull-back technique is already blindly used clinically with limited tactile feedback. It would be valuable to give the surgeon a tool to guide the pull-back process such that they know when to stop the insertion before reducing AID.

In this work, the aforementioned next steps were performed. First, a kinematic model was developed for straight EA shape estimation, and then open-loop testing was performed to test reliability of the sensing method with two different straight EAs of the same type and to enable model validation. The relationship between E-M proximity and dual-sided EA contact impedance measures was explored and quantified for the first time. The first demonstration of the real-time relationship between impedance and E-M proximity in a cadaveric model was also performed. Finally, building on past work [78], impedance feedback was used to guide the pull-back technique in real-time. This feedback enabled the robotic insertion tool to know when to stop (once the EA had achieved close modiolar-positioning) and thus could translate to better final EA positioning with a precurved EA and thus lead to better audiologic outcomes.

The contributions in this chapter have led to one journal paper in press and two journal papers currently under development. The first paper demonstrated initial development of the research sensing system that is agnostic to the EA manufacturer, initial phantom experiments demonstrating functionality of this system, and the equivalent circuit impedance relationship with the E-M areas.

This paper has been accepted as a journal article in Transactions on Biomedical Engineering. The second journal paper will focus on the straight EA kinematics, straight EA phantom experiments, and experimental validation of the kinematic model. Finally, the last journal paper will focus on implementation of impedance sensing to guide precurved EA insertion for improved modiolar hugging.

4.1 Introduction

CIs successfully restore hearing to hundreds of thousands of people worldwide [116]; however, the ultimate success of these implants—hearing quality—is highly correlated with insertion quality. Deeper angular insertion depths, smaller distance between electrode contacts and the neural endings they are attempting to stimulate, and minimal trauma have been shown to lead to better audiologic outcomes [29], [30]. Unfortunately, in a typical insertion, surgeons insert the EA with little visual feedback (i.e., watching the EA enter the entrance of the cochlea) and limited tactile feedback [166]. Many efforts have been made to try to give surgeons improved intraoperative feedback during this challenging step of the procedure.

Traditional feedback mechanisms commonly used in medical devices and surgical robotics are unfortunately not applicable to CI EA insertion due to lack of line of sight (omitting optical tracking) and space constraints/accuracy requirements (omitting magnetic tracking and endoscopy). Imaging feedback tools for analysis of CI placement include preoperative CT scans with customized insertion plans [167], postoperative CT [89], preoperative Magnetic Resonance Imaging to determine candidacy [168], and real-time fluoroscopy during surgery [90], but these techniques are burdened by cost, patient radiation exposure, and/or lack of true real-time visualization [102]. Custom EAs have also been designed that incorporate strain gauges [169] or scanning electrochemical microscopy [170] for position sensing, but integrating sensors into commercial EAs is not currently feasible.

All of these limitations have led to the search for another source of intraoperative position feedback, ideally one that does not impede workflow, add radiation, add cost, or involve design of a

new EA. In this paragraph examples of possible tools that could be adapted to detect spatial EA information are presented that are already used by audiologists in the operating room post-insertion. These tools include electrically-evoked compound action potentials, electrocochleography, and impedance sensing. First, electrically-evoked compound action potentials involve stimulating an EA contact and recording the auditory nerve response. In some studies, this measure has been shown to correlate with EA position [94] and speech outcomes [92]; however, results are variable and other studies have not found such correlation [93], [95], [171]. Electrocochleography involves the use of an external sound stimulus to generate and measure hair cell responses to ensure residual hearing is maintained. This technique has been shown to potentially help preserve residual hearing [96], [98], [99], and some studies have even shown correlation to large changes in scalar location [101]; however, interpretation is complex due to dependency on neural responses [101] and detection of small scalar shift has not been demonstrated. Perhaps most importantly, the response time is not ideal as hair cell damage can occur before perception is possible [103], although there are current efforts underway to improve interpretation of this feedback [172].

Electrical impedance (hereafter referred to simply as impedance) sensing involves sending a biphasic, charge-balanced current pulse to an electrode contact and measuring either its response (contact impedance), the response of all of the non-stimulated contacts (electric field imaging), the response of one or more (but not necessarily all) non-stimulated contact(s) to a ground (monopolar stimulation), or the response between two or more contacts (bipolar/multipolar). It has been shown that the impedance values resulting from the electrode-electrolyte interaction can be modeled as an equivalent circuit to gain more specific information from the single measurement [88], [105], [106], [111], [166], [173]–[176]. CI impedance values have been shown to change over time and correlate with EA and/or intracochlear changes in post-implanted clinical cases [105], [174], [177]. These values have also been shown to be able to predict extracochlear electrode contacts in cadaveric models after EA insertion [102].

Using a custom EA, Watanabe was one of the first to show the correlation between electrochemical measures and ST wall proximity [103]. After this work, total impedance both experimentally

([83], [104]) and simulated ([178]) as well as the resulting equivalent circuit components [88] were shown to correlate with the space between the EA body and the modiolar wall (E-M proximity) [83], [88], [104]. In particular, Pile *et al.* demonstrated the correlation between the manufacturer-provided real-time bipolar (1.5 s for 21 pairs) impedance values and the E-M area in phantom and cadaver models using a 4 DOF robotic platform for insertion [104]. They showed that impedance values for the precurved EA could be used to distinguish between insertion techniques. Giardina *et al.* analyzed the relationship between the equivalent circuit model components from [105] and the E-M distance using monopolar stimulation in pseudo-real-time in a plastic phantom model with a straight EA [88]. They fit a linear regression model to these measures and found a strong correlation between the access resistance and the E-M distance. Aebischer *et al.* demonstrated that impedance values could be used after insertion to predict the overall insertion depth of a straight EA without CT scanning [111]. Dong *et al.* showed that retrospective analysis of the access resistance component of the postoperative impedance could be used to detect translocation without imaging [179]. Additionally, recent work by Klabbers *et al.* demonstrated that viewing a heatmap of the transimpedance matrix can be more reliable than fluoroscopy imaging to accurately detect tip fold-over after insertion [180]. Finally, Lee *et al.* have shown that impedance differences can detect when the pull-back technique (i.e., pulling a precurved EA back after the insertion has been deemed complete to decrease E-M distance) has been used as opposed to a typical insertion [181].

This work builds on the work of the aforementioned groups, most notably, the recent results from [104] and [88]. The reliability of using impedance sensing for E-M proximity detection should be further investigated, and the use of this modality for different EA types should be explored. Additionally, the current state-of-the-art has not demonstrated the relationship between the equivalent circuit components and E-M proximity for bipolar impedance sensing as they did in [88] for monopolar stimulation. This use of the equivalent circuit components could decrease standard deviation and increase model correlation. Shortening the current path (i.e., such that it is not traveling through heterogeneous tissue and is just traveling between EA contacts in the perilymph) will likely be more reliable than monopolar stimulation [104]. Furthermore, no study has used

impedance feedback to help predict the EA shape during an insertion. It is common for straight EAs to feature fully-banded or dual-banded contacts. To perform this shape estimation, the relationship between impedance and E-M proximity needs to be explored for dual-sided contacts for the first time. The real-time relationship between impedance and E-M proximity has not yet been quantified in a cadaveric model due to difficulties in imaging the insertion progress through the opaque cochlea. This is an important next step to verify that the phantom model results are providing clinically meaningful information that directly translates to human models. Finally, a feedback mechanism could prove useful for manual or robotic tool control in CI EA insertion. The only robotic CI insertion tool that has been operated in closed-loop was developed by Pile *et al.* and used force feedback to detect and react to EA tip fold-over [182]. They then modified the control scheme to use sensed impedance values to adjust precurved EA stylet actuation [78]. This was an exciting step toward using impedance feedback for improved EA placement.

In this work, the aforementioned challenges were addressed with the following contributions: 1) development of a kinematic model for EA tip and shape estimation using impedance sensing and open-loop evaluation of the impedance profiles (including characterization of dual-sided EA contact behavior) in phantom models of varying complexity. Next, 2) real-time impedance feedback was used to guide the pull-back technique and improve insertion of a precurved EA. Finally, 3) quantification of real-time impedance to E-M space metrics in a cadaveric model was performed. The results of these contributions will move the state-of-the-art closer toward using impedance sensing in the operating room for improving EA placement.

4.2 Review of Bipolar Impedance Model

The following section details estimation of E-M proximity given bipolar impedance measurements. One electrode contact serves as the source (stimulating EA contact) and one serves as the sink (recording EA contact) in bipolar stimulation. First, an equivalent circuit model of the electrode-electrolyte interface is presented and this model is used to predict the electrical response to clinical electrical current pulses. Relation of this response to modiolar proximity is then de-

scribed.

4.2.1 Equivalent Circuit

Here, it is assumed that the contribution of each electrode contact to electrolyte interface i can be modeled as a resistor and capacitor in parallel (R_{pi} and C_{pi}) in series with a resistor (R_{ai}). The parallel resistor R_{pi} represents the electrode contact reaction resistance (also termed the charge transfer resistance or polarization resistance) and describes the electrical resistance experienced as electrons on the polarized electrode surface are transferred into charged ions in the electrolytic solution (in this case, the perilymph). The parallel capacitor C_{pi} represents the ordinary double layer capacitance of the electrode contact surface, also termed the polarization capacitance, created by the thin insulating space between the charged electrode surface and the nearby ions. Finally, the series resistance R_{ai} represents the electrolyte access resistance of the conductive perilymph, which has been shown to have high correlation with E-M proximity [88].

First, the total impedance for one contact that includes R_{ai}, R_{pi}, and C_{pi} is defined as Z_i. Next, the electrode contact properties R_{pi} and C_{pi} are assumed to be equivalent for each contact in a pair (i.e., in Fig. 4.1(a), $R_{p1} = R_{p2}$ and $C_{p1} = C_{p2}$). The access resistances R_{a1} and R_{a2} are also assumed to be equivalent. These assumptions of equivalence are reasonable provided that the exposed surface area, size, manufacturing method, and material of the two contacts are the same. Differences in surface area should be accounted for if this relationship does not hold true [177]. Given all of these assumptions, Fig. 4.1(a) then becomes two equivalent impedances Z_1 and Z_2 in series, and so the simple equivalent circuit model between two electrode contacts is assumed as shown in Fig. 4.1(b), where $R_a = 2R_{a1}$, $C_p = 2C_{p1}$, and $R_p = 2R_{p1}$ [106], [173], [174].

4.2.2 Impedance Measurement

Electrical impedance Z is the ratio of voltage to current in a circuit, $Z = V/I$. Therefore, to compute Z, a known current or known voltage must be applied to the electrode contact of interest and then the response of the opposing electrode contact in the pair needs to be measured. In the case of commercial CIs, a controlled current pulse is emitted and the voltage response is recorded

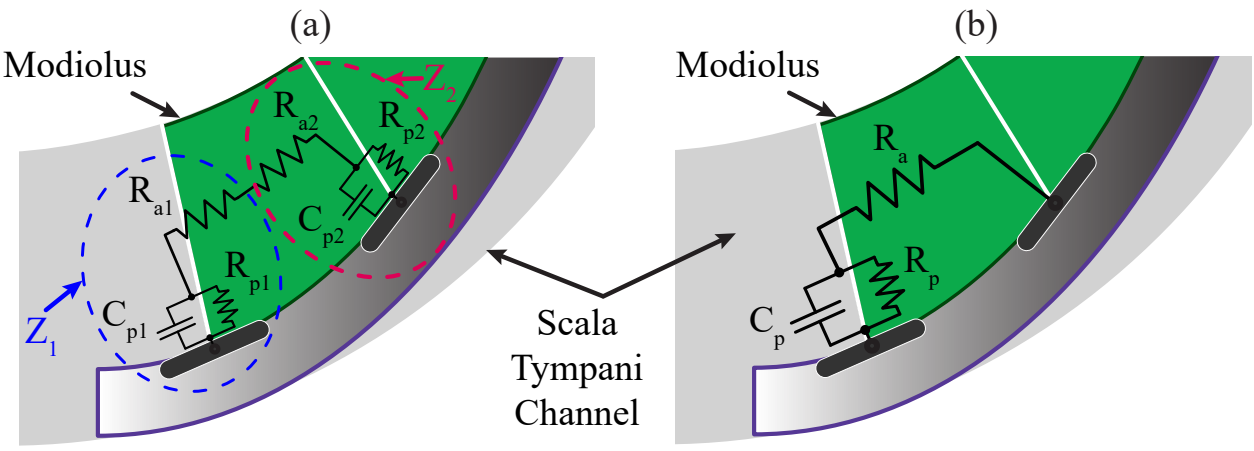

Figure 4.1: (a) Equivalent circuit for electrode/electrolyte interaction shown for bipolar impedance sensing where current is sent from electrode contact 1 and the response is recorded at contact 2. (b) Equivalent circuit model with the assumption that $Z_1 = Z_2$, and thus $Z_{total} = 2Z_1$.

to determine the corresponding impedance. Thus, a charge-balanced biphasic pulse is applied such as that illustrated in 4.2(a). The measured voltage response (see Fig. 4.2(b)) begins with a sharp rise due to the double-layer capacitances initially behaving as short circuits. This means that the only impedance component seen at that first instance is the access resistance of the perilymph. Thus, the access resistance R_a can be computed using the measured initial voltage V_a as $R_a = V_a/I$, where I is the maximum current value of the initial positive current input. The access resistance and current are constant over the positive current pulse time (in Fig. 4.2 t = 100 us), and so V_a is constant as well and simply biases any additional voltage created by other circuit elements.

As the current continues through the end of the positive phase, the charge across the capacitive element increases, causing the voltage to increase as well. This can be seen in Fig. 4.2(b-c). The parallel resistance and capacitance cause the measured voltage at time t, $V_t(t)$, to follow a standard first-order response (blue curve on Fig. 4.2(b-c)) of

$$V_t(t) = V_a + V_p\left[1 - \exp\left(\frac{-t}{R_p C_p}\right)\right], \tag{4.1}$$

where V_p is the peak voltage. Since R_p and C_p are related to the electrode contact geometry (i.e., exposed surface area) and contact material properties, they can be assumed to remain constant for a

given pair of electrode contacts. The total impedance at time t is $V_t(t)/I(t)$ and assuming a constant current I during the positive pulse, the measured Z_t is

$$Z_t(t) = \frac{V_a + V_p\left[1 - \exp\left(\frac{-t}{R_pC_p}\right)\right]}{I}. \tag{4.2}$$

The derivative of (4.2) is taken and a first-order response is fit by computing the least-squares solution (with form: $y = mx + b$) of the linearized model (see Fig. 4.2(d)) to generate

$$\dot{Z}_t(t) = \frac{1}{C_p}\exp\left(\frac{-t}{R_pC_p}\right). \tag{4.3}$$

Taking the natural logarithm of each side and assuming R_p, C_p and t are positive yields

$$\ln \dot{Z}_t(t) = \frac{-1}{R_pC_p}t + -\ln C_p. \tag{4.4}$$

The slope, m_Z, and intercept, b_Z, of the best-fit line to (4.4) yield the desired parameter estimates:

$$b_Z = -\ln C_p \implies C_p = \mathrm{e}^{-b_Z} \tag{4.5}$$

$$m_Z = \frac{-1}{R_pC_p} \implies R_p = \frac{-1}{m_ZC_p}. \tag{4.6}$$

Substituting these values into (4.2) enables computation of R_a.

4.2.3 Modiolar Proximity

Pile *et al.* [104] experimentally demonstrated an inverse relationship between the volume of fluid (approximated as a planar trapezoid between EA contact pairs) and bipolar impedance values. They also showed that this relationship could be approximated by a calibrated power-law equation. Bipolar impedance measurements have an important advantage over monopolar measures in that they are less dependent on biological influences since the signal does not need to travel through tissue to reach an external ground. Here, the goal is to approximate the E-M proximity relationship

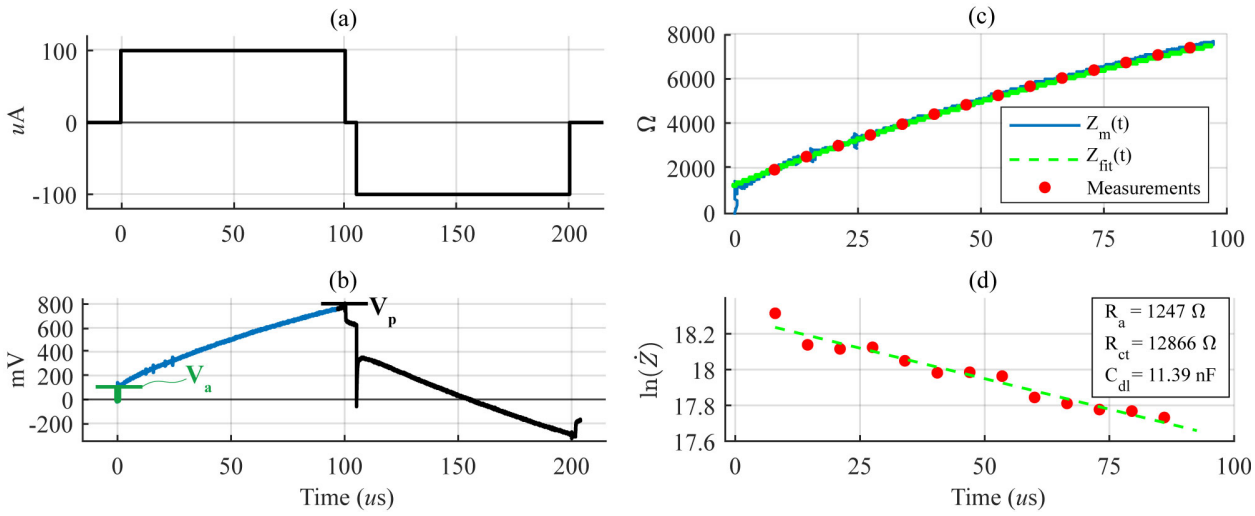

Figure 4.2: (a) Typical charge-balanced biphasic current pulse that is sent to the stimulating contact. (b) Measured voltage response from the positive current pulse. The region of the response curve where the capacitor initially behaves as an open circuit is shown in green, and the voltage response V_a can be used to compute the access resistance R_a. The blue region of the curve shows the voltage response when the capacitive elements start to charge and the response can be approximated as a first order system response. The peak voltage V_p is the highest voltage reached at the end of the positive current pulse. (c) Impedance values with the total Z_t shown in blue, the first order fit shown in green, and the measured values shown in red. (d) The linearized impedance fit shown in green based on measurements shown in red.

for the access resistance R_a as opposed to the entire impedance Z_t. Beginning with a power law function of the form

$$R_a(\alpha) = c_1\alpha^{c_2} + c_3, \tag{4.7}$$

where R_a is the access resistance (i.e., resistance of the trapped volume of perilymph), α is the area between the pair of contacts of interest and their corresponding closest points on the modiolus, and the coefficients for model fitting are c_1, c_2, and c_3.

First, these coefficients are solved for so that the area can be calculated for a given access resistance. Since there is an inverse relationship between R_a and α, the exponent c_2 must be negative. This means c_3 represents the horizontal asymptote of the function, which corresponds to the access resistance in an open channel, i.e.,

$$c_3 = \lim_{\alpha\to\infty} R_a(\alpha). \tag{4.8}$$

Subtracting c_3 from each side of (4.7) and taking the natural logarithm of each side yields a linear equation

$$\ln\left(R_a(\alpha) - c_3\right) = c_2 \ln\alpha + \ln c_1, \tag{4.9}$$

where it is again arranged in slope-intercept form of $y = mx + b$ and

$$y = \ln\left(R_a(\alpha) - c_3\right), \tag{4.10}$$

$$x = \ln\alpha, \tag{4.11}$$

$$b_A = \ln c_1, \tag{4.12}$$

$$m_A = c_2. \tag{4.13}$$

After having found the coefficients for the power function, it can be rearranged (4.7) to obtain

$$\alpha(R_a) = \left(\frac{R_a - c_3}{c_1}\right)^{-c_2}, \tag{4.14}$$

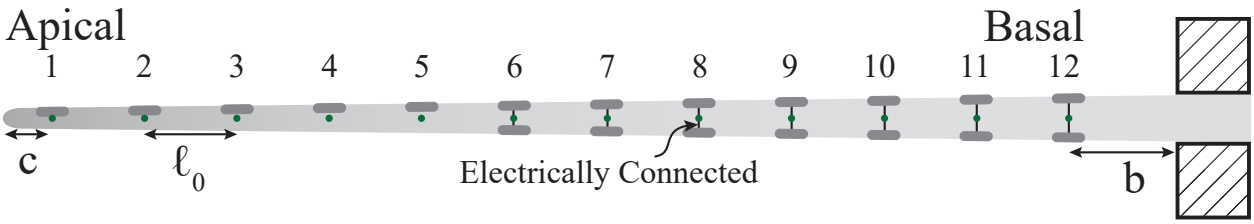

Figure 4.3: Parameter definitions of c, ℓ_0, b, and contact numbering scheme: side view of EA with the apical end on the left, beginning with contact 1 to contact 12 on the basal end on the right.

the final model for estimating the area as a function of the access resistance between a pair of electrode contacts. The methodology toward the contributions of this chapter will be described next.

4.3 Methods

In this section, development of a kinematic model for straight EA shape estimation and tip localization will first be detailed. Next, the phantom model experimental testing protocol will be described for reliability testing, dual-sided contact behavior exploration, and model validation. Precurved EA testing methodology will then be detailed, including robotic insertions with impedance advised pull-back. Finally, the experimental setup and protocol for cadaver model testing will be described. For every experiment in this work, the measured impedance was the access resistance component of the equivalent circuit model.

4.3.1 Kinematic Model

In this section, a two-dimensional model for EA tip position and overall EA shape estimation is derived using patient cochlea morphology, linear insertion depth, and sensed access resistance data. For n electrode contacts, the electrode contact positions are estimated by modeling the intracochlear portion of the straight EA as a series of rigid links connected by revolute joints. It is assumed that these contacts are connected by continuous splines to form the EA shape. The following section assumes there are n electrode contacts and thus $n - 1$ pairs of contacts. For each pair of contacts i and $i + 1$, the associated access resistance is termed R_i.

First, EA parameters are defined as shown in Fig. 4.3. Given these definitions, the total considered length of the EA a is

$$a = (n-1)\ell_0 + c. \tag{4.15}$$

Preoperatively, a matrix is created containing the series of lateral-wall points (radially offset by a small distance to account for the EA body) to obtain the free-fitting matrix of points $\boldsymbol{D}$ and compute the gradient to obtain the tangent vectors $\boldsymbol{T}$ at each point on $\boldsymbol{D}$. The points in $\boldsymbol{D}$ define the predicted final position of the EA body, that is, where it would naturally lie after a completed "normal" insertion. Given $\boldsymbol{D}$, numerical integration is performed along the path length to generate $\boldsymbol{d}$, a vector of the cumulative summed distances at each point. Then, for a given insertion depth q_1, this vector $\boldsymbol{d}$ is used to determine the corresponding closest point in $\boldsymbol{D}$. This closest point gives the initial tip localization $\boldsymbol{e}_0$ as the closest point in $\boldsymbol{D}$ that corresponds to q_1. This initial guess only requires knowledge of q_1 and an assumption of conformation to the lateral wall.

Fig. 4.4 shows the parameter definitions that will be used to estimate the EA shape. Given the initial tip estimation, the tip tangent $\boldsymbol{t}_0$ is found from $\boldsymbol{T}$ by finding the closest point on $\boldsymbol{D}$. The first (most apical) electrode contact location $\boldsymbol{e}_1$ can then be computed as

$$\boldsymbol{e}_1 = \boldsymbol{e}_0 - c\boldsymbol{t}_0. \tag{4.16}$$

A check is performed to ensure that $\boldsymbol{e}_1$ lies within the boundaries of the ST. If it does not, $\boldsymbol{e}_1$ is recomputed by returning to $\boldsymbol{e}_0$ and integrating along $\boldsymbol{D}$ for a distance c and then adjusting the position of $\boldsymbol{e}_1$ to lie at this point. Next, since straight EAs are actuated by contact with the lateral wall, the subsequent ST tangent angles can be used to estimate the remaining contact locations. The rotation matrix associated with contact i, $\boldsymbol{R}_i$, is computed as

$$\boldsymbol{R}_i = \begin{bmatrix} | & | & 0 \\ \boldsymbol{t}_i & \boldsymbol{n}_i & 0 \\ | & | & 1 \end{bmatrix} \tag{4.17}$$

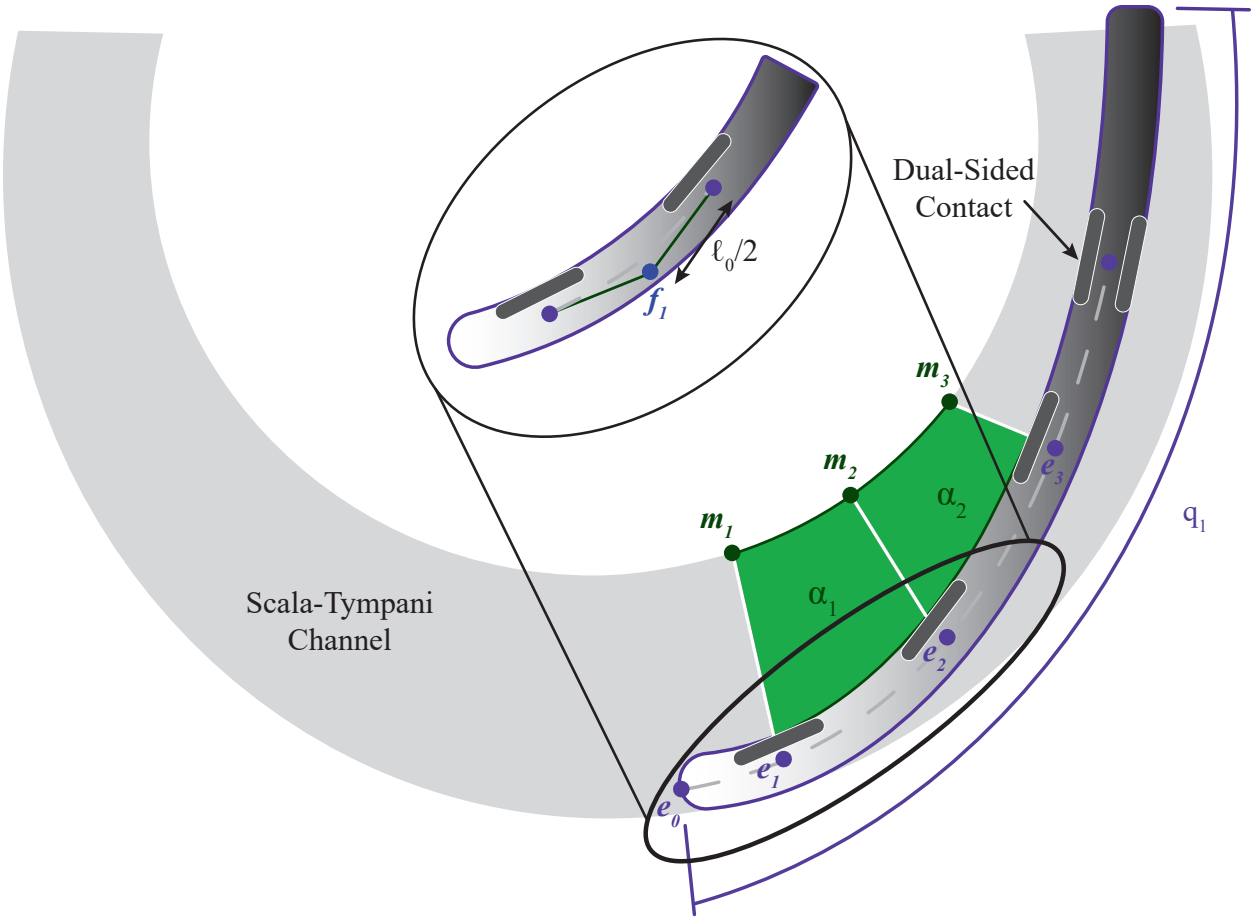

Figure 4.4: Kinematic model parameter definitions for straight EA insertion

where $\boldsymbol{t_i}$ is the tangent vector of the closest point on $\boldsymbol{D}$ and $\boldsymbol{n}_i$ is the normal vector at the same location, and planar rotation is assumed. The midpoint $\boldsymbol{f}_i$ between contacts is computed as

$$\boldsymbol{f}_i = \boldsymbol{e}_i - \boldsymbol{R}_i \begin{bmatrix} \ell_0/2 \\ 0 \\ 0 \end{bmatrix} = \boldsymbol{e}_i - \frac{\ell_0}{2}\boldsymbol{t}_i \tag{4.18}$$

A check for boundary containment of $\boldsymbol{f}_i$ is again performed and its location is adjusted if necessary, using $\ell_0/2$ instead of c for integration. Subtraction from the midpoint is repeated by finding the

Table 4.1: Specification of Kinematic Domains

Domain	EA Behavior	Resistance Indication to Move to Next Domain
1	Moving straight based on angle of approach	Switch 1: Sharp drop in resistance of pair 1
2	Contacting lateral wall and bending	Switch 2: Smooth drop in resistance pairs 1 and 2
3	EA starts to fully relax into the wall	Switch 3: Most apical dual-sided contact resistance rise
4	Conformation to lateral wall	N/A

closest ST tangent $\boldsymbol{t}_i$ at $\boldsymbol{f}_i$ and subtracting it from the midpoint location

$$\boldsymbol{e}_{i+1} = \boldsymbol{f}_i - \frac{\ell_0}{2}\boldsymbol{t}_i. \tag{4.19}$$

Again, a check is performed to ensure containment within the boundary and the point is recomputed if necessary. This process is continued until all n electrode contact locations are estimated.

The EA shape is assumed to be comprised of continuous splines. Using theory described in [183], the mathematical spline is a piecewise polynomial with degree K and continuity at common joints of derivatives of order $K-1$. In this work, cubic splines $\boldsymbol{s}(p)$ are used as described by the equation

$$\boldsymbol{s}(p) = \boldsymbol{B}_1 + \boldsymbol{B}_2 p + \boldsymbol{B}_3 p^2 + \boldsymbol{B}_4 p^3 \qquad 0 \le p \le p_2, \tag{4.20}$$

where the constant coefficients $\boldsymbol{B}_1$, $\boldsymbol{B}_2$, $\boldsymbol{B}_3$, and $\boldsymbol{B}_4$ are specified by the boundary conditions:

$$\boldsymbol{s}(0) = \boldsymbol{s}_1 \qquad \boldsymbol{s}'(0) = \boldsymbol{s}'_1 \tag{4.21}$$

$$\boldsymbol{s}(p_2) = \boldsymbol{s}_2 \qquad \boldsymbol{s}'(p_2) = \boldsymbol{s}'_2. \tag{4.22}$$

The two points of interest $\boldsymbol{s}_1$ and $\boldsymbol{s}_2$ are specified, as well as the start and end tangency, $\boldsymbol{s}'_1$ and $\boldsymbol{s}'_2$, respectively. Applying the boundary conditions to (4.20), the equation of a single spline segment is:

$$\boldsymbol{s}(p) = \boldsymbol{s}_1 + \boldsymbol{s}'_1 p + \left(\frac{3\,(\boldsymbol{s}_2 - \boldsymbol{s}_1)}{p_2^2} - \frac{2\boldsymbol{s}'_1}{p_2} - \frac{\boldsymbol{s}'_2}{p_2}\right)p^2 + \left(\frac{2\,(\boldsymbol{s}_1 - \boldsymbol{s}_2)}{p_2^3} - \frac{\boldsymbol{s}'_1}{p_2^2} - \frac{\boldsymbol{s}'_2}{p_2^2}\right)p^3. \tag{4.23}$$

All of these calculations are independent of any knowledge of sensed impedance values and they

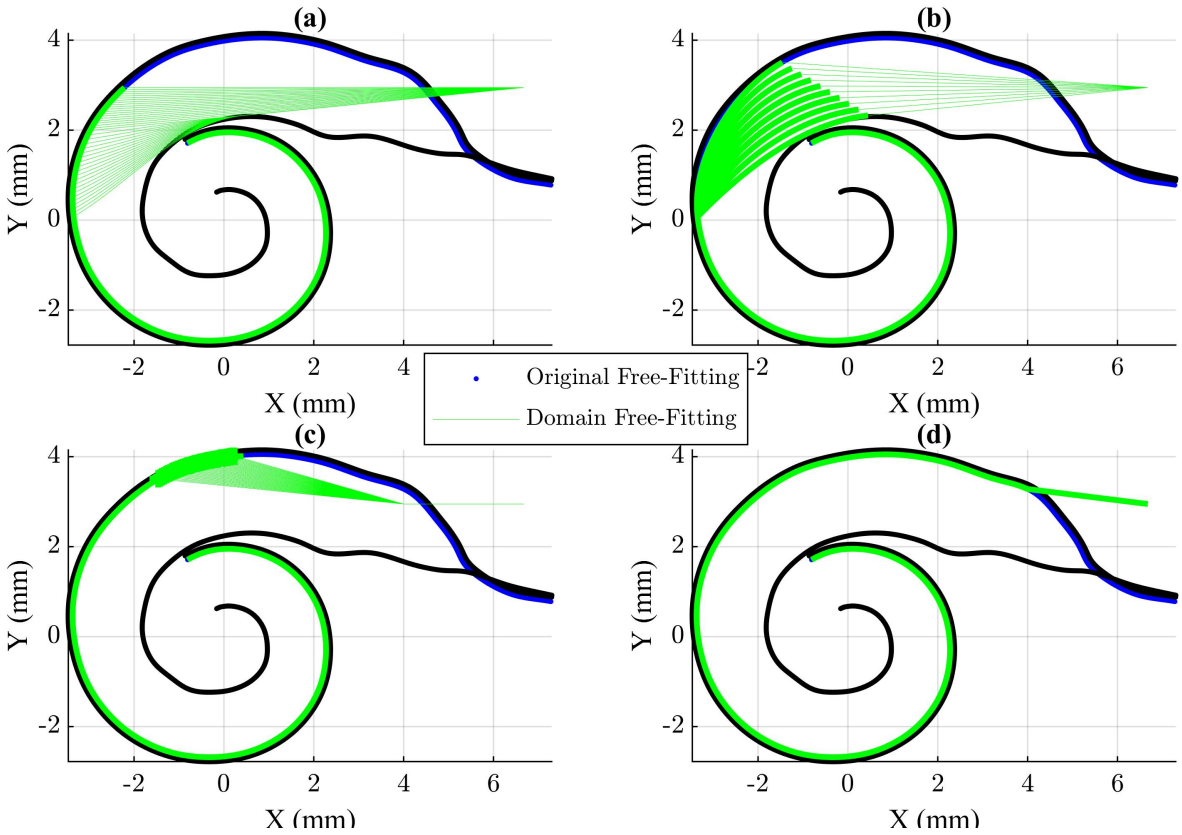

Figure 4.5: Four determined kinematic domains in a “normal” insertion.

are under the assumption that the EA will conform perfectly to the predicted free-fitting shape $\boldsymbol{D}$. In other words, at any point of the insertion, the EA is restricted to lie along the lateral wall. This is not always the case, particularly at the beginning of an insertion when the EA is moving straight prior to contacting the lateral wall for the first time. Next, access resistance information will be used to improve the accuracy of the model will be described.

4.3.1.1 Incorporation of Access Resistance into Kinematics

As previously stated, the actuation method for bending this type of EA is contact with the walls of the cochlea. Because the cochlea is such a small, enclosed structure and because of the limited actuation potential of this EA, an additional set of preoperatively determined shape domains can be incorporated into the originally determined free-fitting shape $\boldsymbol{D}$ to predict the overall EA shape and improve model accuracy. Access resistance knowledge is used to determine the switching

locations between shape domains.

To incorporate resistance values, first, four different domains were determined based on preliminary observation of "normal" insertions in a plastic ST model with a cochleostomy. Then, the switch points between domains were determined using the resistance values. These points and their associated domains are detailed in Table 4.1 and a picture of each of the domains for one trial is shown in Fig. 4.5. In the first domain, the EA simply moves straight along its insertion vector, in the second, the EA contacts the lateral wall and the tip begins to relax, in the third the EA is gradually conforming more and more of itself to the wall, and in the fourth, full conformation to the wall is assumed. One of the most important insights from preliminary testing was that the real-time resistance values (and their derivatives) can particularly indicate when the shape of the EA changes and give valuable information as to insertion progress such as the point at which the EA tip contacts the lateral wall. The access resistance values were analyzed for each insertion trial (4 trials were performed) to determine domain switching points and predict the EA positioning at each step. See Fig. 4.6 for visualization of these points for one of the trials (other trials removed for clarity) both on (a) the derivative plot and on (b) the resistance graph. This plot shows the three determined switch points (marked as a black star, diamond, and triangle), and the corresponding insertion depth at which this switch happens. Threshold values used to find the switch points are shown in Fig. 4.6 as black horizontal lines of different line styles. Resistance derivative threshold values are denoted with δ_i where i is the switch point number (between 1 and 3) that the threshold value is used to determine. On the resistance plot, an entrance threshold $K = 4000\,\Omega$ was used to determine if a contact had entered the model. Next, more detail on switch point determination will be provided.

Switch point 1 was defined by first finding the point that $R_2 < K$ (meaning the second pair is inside the ST) to shorten the search interval. Then, the first sharp drop in R_1 was found in this interval, when $dR_1 < \delta_1$. This is when the tip of the EA reaches the basal turn. Then, the point of contact with the lateral wall was determined as when the resistance of pair 1 is no longer changing significantly, i.e., $dR_1 < \delta_2$ for 1% of the number of sample points. This indicates the point at

which the resistance of pair 1 has dropped sharply when passing the basal turn, but is no longer changing significantly as the EA tip has reached the lateral wall. Next, switch point 2 was defined as when the EA tip resistances (pairs 1 and 2) are no longer changing significantly and the tip relaxes into the wall fully. This point was computed by finding when

$$dR(t)_{tip} + dR(t-1)_{tip} + ... + dR(t-n)_{tip} < \delta_3. \tag{4.24}$$

In (4.24), t is the current sample, n is the nearest integer to 1% of the number of sample points, and $dR(t)_{tip} = \sqrt{dR(t)_1^2 + dR(t)_2^2}$. Finally, the point at which full conformation to the lateral wall was assumed was defined as when both pairs that feature the most apical dual-sided contact (contact 6) resistances rise significantly. This behavior indicates that contact 6 has relaxed into the wall and essentially the remainder of the insertion just follows the lateral wall. Pair 5 features one single-sided contact and one dual-sided contact, while pair 6 features both dual-sided contacts. As such, this point was computed by finding the maximum location of $dR(t)_5 + dR(t)_6$. This switch point will most likely change depending on EA contact spacing and overall length, but could be calibrated for a particular EA as was done here for the FLEX28. The resulting comparison of the predicted shape with impedance incorporation to the experimental insertions is detailed in Sec. 4.5 after discussing the experimental methods.

4.4 Experiments

To investigate real-time bipolar access resistance insertion profiles, four different experiments were performed with a straight EA and two experiments were performed with a precurved EA. In the phantom model experiments, each experiment included a modular testing platform, a robotic insertion tool [86], a digital camera for proximity determination, a custom printed circuit board (PCB) for impedance sensing, and either a straight (FLEX28, MED-EL, Innsbruck, AT) or pre-curved (CI532, Cochlear Limited, Sydney, AU) EA. The general phantom setup can be seen in Fig. 4.7. One cadveric experiment was also performed with a straight EA (FLEX28) to assess clinical viability of this sensing method. Each experiment provides a unique contribution toward

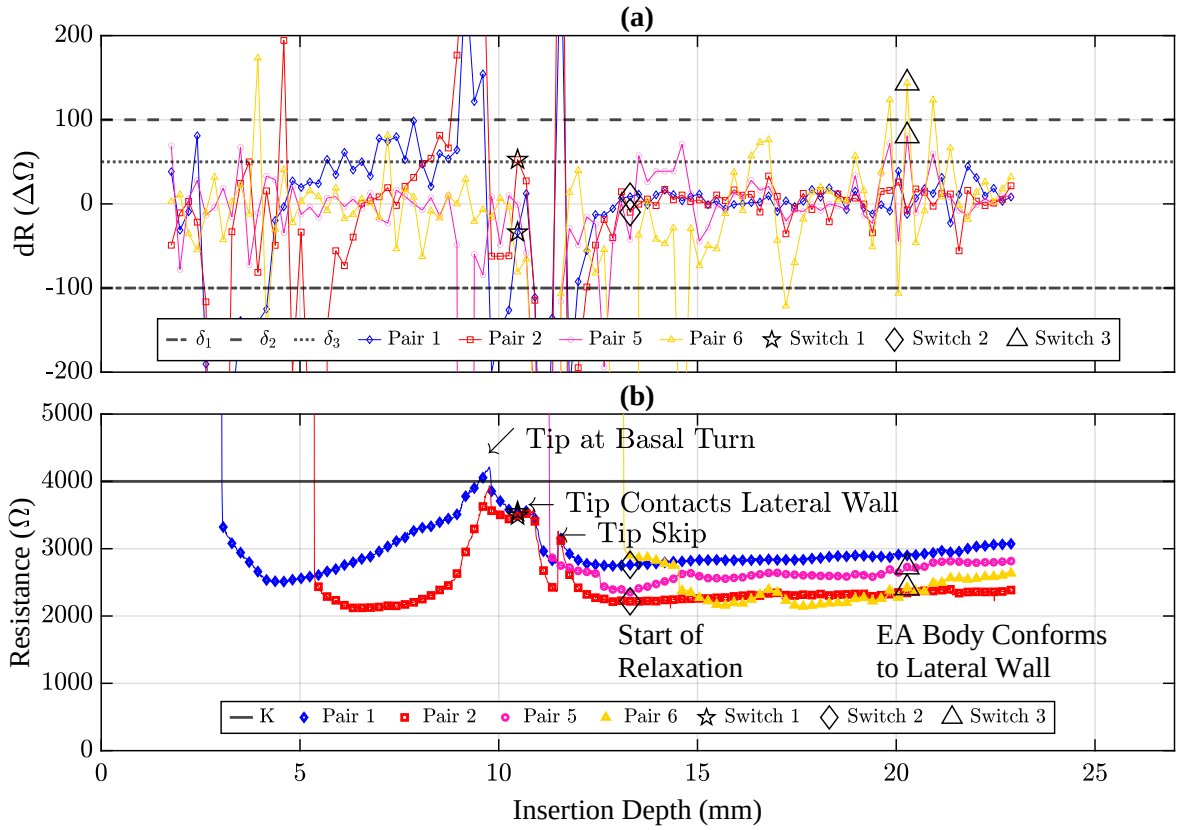

Figure 4.6: (a) Graph of the numerical derivative of the resistance in trial 1 of pairs 1, 2, 5, and 6. These values were used to determine the points at which the domains should switch, along with knowledge gained from Experiments 1-3. (b) Corresponding graph showing the resistance in trial 1 with annotations of switch points and other important points of the insertion. On both plots, a black horizontal line indicates a threshold value that was used in switch point determination.

Table 4.2: Experimental Conditions for Impedance Experiments

Exp.	EA	Model	# Recorded Impedance Pairs	Speed (mm/s)	Contribution
1	Straight (FLEX28)	Phantom 1	11	0.5	Real-time detection of intracochlear electrode contacts
2	Straight (FLEX28)	Phantom 2	4	0.5	Characterization of dual-contact behavior
3	Straight (FLEX28)	Phantom 3	11	0.2	Real-time insertion impedance profile evaluation and kinematic model validation
4	Precurved (CI532)	Phantom 3	11	0.4	Real-time insertion impedance profile evaluation of CI532
5	Precurved (CI532)	Phantom 3	4	0.4	Demonstration of use of impedance feedback to adjust the pull-back technique
6	Straight (FLEX28)	Cadaver	4	0.2	Evaluation of translatability

understanding the utility of access resistance sensing in EA localization. A summary of each experiment can be viewed in Table 4.2, and each of the experiments will be described in detail next.

4.4.1 Experiments 1-3: Straight EA Phantom Model Testing

This section will describe the methodology for the first three experiments. Namely, the investigation of the access resistance profiles of a straight, FLEX28 EA in plastic phantom models of varying complexity (phantom models 1, 2, and 3 in Fig. 4.7 (a-c)). All models were printed in WaterShed XC material at Protolabs (Maple Plain, MN, USA). For a given trial of any of these three experiments, the straight EA was first inspected to ensure it was straight and undamaged. If needed, the EA was straightened or replaced. The phantom model was filled with artificial perilymph (saline) before each trial. Next, with the hinged phantom model swung out of the way, the EA was loaded into the tool as in [86]. The hinged phantom model was then locked in place with the pin after the EA was loaded. Access resistance, video, and actuator data were simultaneously recorded. Robotic EA insertion proceeded at the speed detailed in Table 4.2 for each experiment until insertion was complete or until further insertion would cause EA damage. For impedance measurements, a pulse width of 55 μs at a pulse magnitude of 100 μA was used, and the microcon-

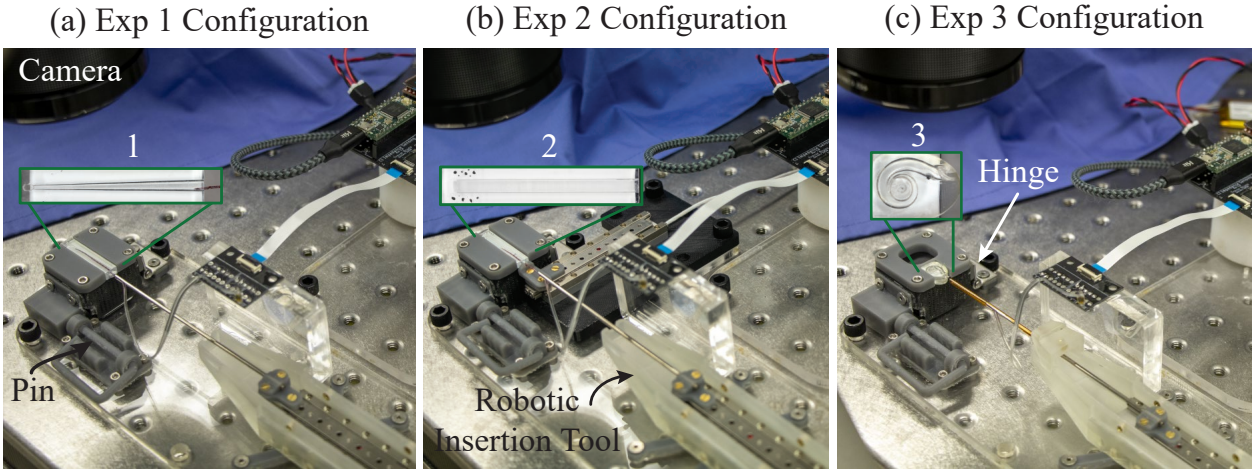

Figure 4.7: Experimental setup for phantom model insertions: (a) tapered phantom model 1 experiments, (b) rectangular constant cross-section phantom model 2 experiments, and (c) to-scale ST model phantom model 3 experiments.

troller obtained a voltage measurement every 8.5 µs during the positive half of the biphasic pulse. To improve effective resolution, if measuring the impedance of 4 pairs of contacts, voltage samples during 20 consecutive pulses were recorded and individually averaged together for an effective frequency of 60 Hz. When measuring 11 pairs of contacts, only 14 consecutive pulses were averaged together for an effective frequency of 30 Hz.

After Effects (Adobe Inc., San Jose, CA, USA) was used to segment the spatial information of the EA components from video. Video and access resistance values were synchronized in MATLAB (Natick, MA, USA) if needed. Data was collected for four trials in each phantom with two different EAs (for a total of eight trials per experiment). The two different EAs will be termed EA1 and EA2 for the remainder of this chapter. To decrease data processing time, a small dot of paint was added at each contact location on the silicone (i.e., the exposed surface area of the contact was unchanged), and hair dye was used to dye the EA body.

4.4.1.1 Experiment 1

The first experiment utilized phantom model 1 - a tapered model (Fig. 4.7(a) inset) that was designed to resemble an 'unrolled' ST, with a slot opening equal to the maximum length and width of a cross section reported in [149], and opposite end with the minimum reported length and width.

A lofted cut connects these two cross sections, such that the cross-sectional area of the model monotonically decreases with increasing insertion depth. For this model, the EA was inserted from 0 mm (all electrode contacts outside the model) to 25 mm and retracted back to zero to investigate the reliability of the access resistance sensing measurement in contact entry detection, as well as a repeatability comparison of the access resistance profile for insertion compared with retraction. All 11 bipolar access resistance measurements were recorded at 30 Hz, and video was recorded at 30 fps.

4.4.1.2 Experiment 2

The second experiment used phantom model 2 (Fig. 4.7(b) inset) which is a constant cross section, rectangular model with a width corresponding to the maximum width in [149], and a height chosen to be slightly larger than the basal end of the EA. For this model, a linear actuator was fixed with its travel perpendicular to the phantom model channel (see Fig. 4.7(b)). The EA was swept from side-to-side (±1.8 mm). The purpose of this experiment was to characterize the dual-sided EA contact access resistance to E-M proximity relationship. As such, 4 pairs of electrode contacts were recorded for this experiment, one single-sided contact pair (contacts 4-5), a single and dual-sided contact pair (contacts 5-6), and two dual-sided contact pairs (contacts 6-7 and contacts 7-8). See Fig. 4.3 for visualization of these contact locations. The 4 access resistance pairs were recorded at 60 Hz and video was recorded at 60 fps.

4.4.1.3 Experiment 3

Finally, the third experiment used phantom model 3 (Fig. 4.7(c) inset), a plastic to-scale ST model [149]. For this model, the EA was inserted from 0 mm (corresponding to the tip of the EA just inside the model) all the way until the basal end of the EA buckled. All 11 access resistance pairs were recorded for this experiment at 30 Hz and video was recorded at 30 fps. Data from these experiments were used to inform and validate the kinematic model. Additionally, the buckling portion of the insertion was used to evaluate whether the characterization determined in Experiment 2 for dual-sided contacts could be used to reliably predict a buckling occurrence.

Table 4.3: Experimental Conditions for Experiment 5

Trial Type	Insertion Depth	Percent Cutoff
(i)	12 mm	40%
(ii)	12 mm	60%
(iii)	13 mm	40%
(iv)	13 mm	60%

4.4.2 Experiments 4 & 5: Precurved EA Phantom Model Testing

Using the same phantom model 3 as was used in Experiment 3, Experiments 4 and 5 were performed using a precurved CI532 EA in conjunction with the experimental setup shown in Fig. 4.8(a). A gripper was designed (Fig. 4.8(b)) to be able to actuate the stylet and EA separately in these insertions. This EA has 22 electrode contacts, all single-sided.

4.4.2.1 Experiment 4

In Experiment 4, the open-loop behavior of all of the available pairs of electrode contacts along the 22-contact precurved EA was evaluated. This evaluation was done in two stages (since the custom impedance sensing PCB is limited to measuring a maximum of 11 pairs in its current configuration), and the purpose of the evaluation was to assess the general insertion access resistance profile of this EA. First, five insertion and retraction trials of the most apical 11 pairs were performed and access resistance and video were recorded (30 Hz and 30 fps). Next, five insertion and retraction trials were performed for the most basal 11 pairs. In each trial, the EA was inserted from 0 mm to 11 mm, held for 10 seconds, and then retracted back to 0 mm. In this experiment, the 0 mm datum was defined as when the EA and external stylet were inserted to the point where the external stylet stopper was at the cochleostomy entrance.

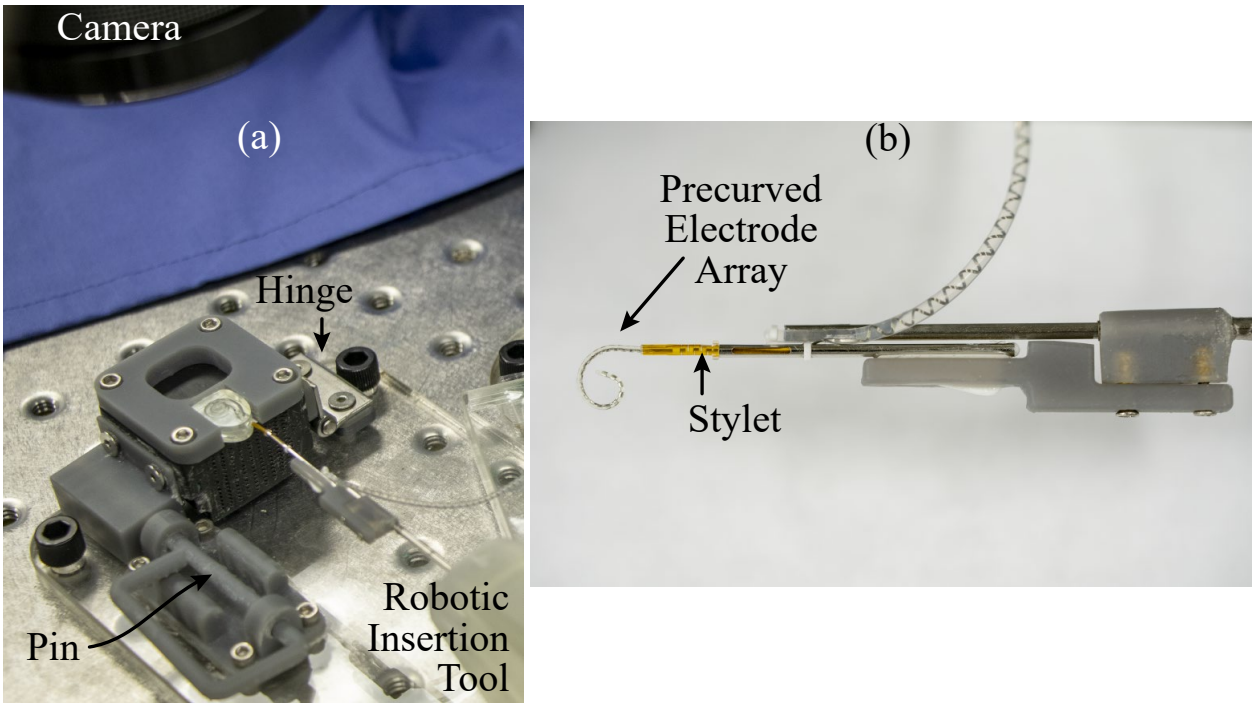

Figure 4.8: (a) Experimental setup for phantom model insertions with the CI532 precurved EA (b) Closeup of gripping mechanism

4.4.2.2 Experiment 5

After Experiment 4 was complete, preliminary experiments with the pull-back technique were used to select the electrode contacts with the most dramatic response to the pull-back for use in Experiment 5. The goal of this experiment was to use the access resistance values to advise when to stop retracting the EA (i.e., to inform when modiolar hugging had been achieved, and when any further pulling would result in reduced AID). A ROS architecture was used to stream access resistance data to the linear actuators inside the automated insertion tool. The same experimental protocol as Experiment 5 was repeated, except that during the resting portion of the insertion, the resistance of each of the 4 recorded pairs was recorded and logged. Then, after the ten second hold, retraction began and the actuators were stopped once all four pairs rose at least a certain percentage of their resting state value. This experiment was repeated for two different over-insertion lengths, 12 mm and 13 mm, as well as two different percent cutoff values, 40% and 60%. Three trials were completed for each configuration, leading to a total of 12 trials. A summary of these settings is

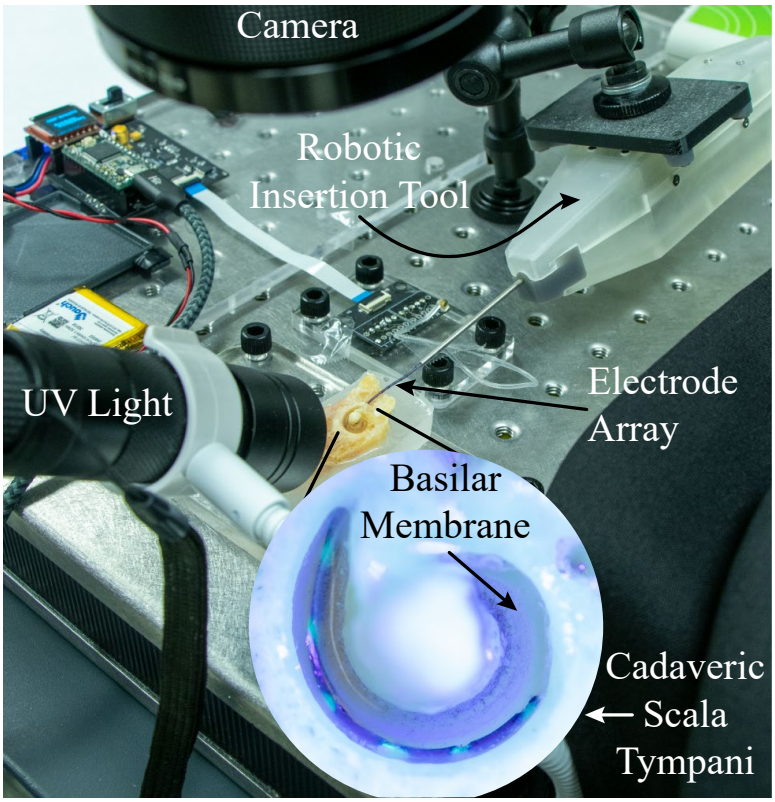

Figure 4.9: Cadaver Experimental Setup: View of insertion tool mounted at an angle that enables insertion through the round window into the dissected cochlea, (Inset) Dissected ST close-up view with EA inside. Note, the EA cannot be seen well through the basilar membrane without dying the EA. Fluroescent green paint is also used to mark the individual contact locations and a UV light is utilized to be able to see them through the membrane.

shown in Table. 4.3.

4.4.3 Experiment 6: Cadaver Testing

Experiment 6 involved using a "deroofed" cadaveric cochlea (see Fig. 4.9), to perform the first ever correlation between real-time access resistance and E-M proximity in a cadaveric model. This result is extremely important to help remark on the translation potential of impedance sensing as a positioning feedback mechanism. Workflow proceeded as detailed in Sec. 4.4.1, but the automated insertion tool was mounted on a separate arm for alignment with the cadaver ST. Additionally, the EA was jogged back and forth to sweep a sufficient range of scalar positions. Because of the only semi-translucent nature of the membrane (and in particular the osseous spiral lamina), electric

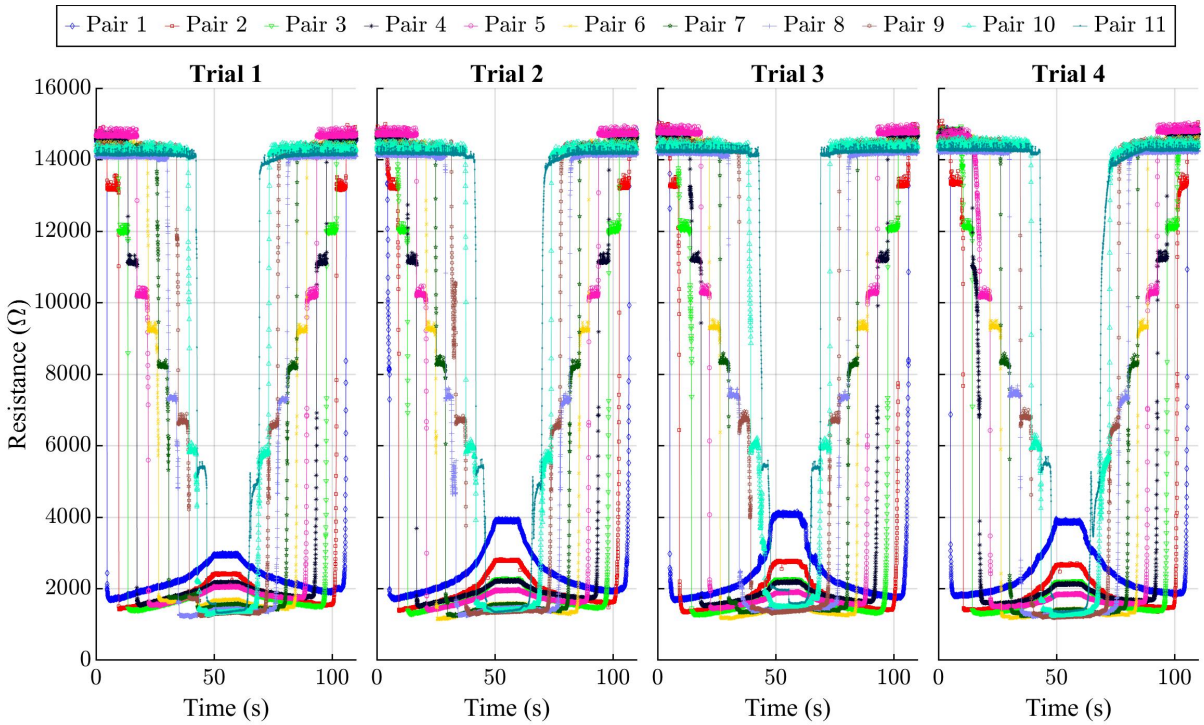

Figure 4.10: Raw access resistance vs. time for the four trials of experiment 1 with EA1

green silicone paint (Pyscho Paint™, Smooth-On Inc. Macungie, Pennsylvania, USA) was painted on the silicone, 90° from the exposed contact surface area to be able to track the contact locations. A UV light was shone on the surface of the model as (see Fig. 4.9 inset). The bipolar access resistance of the most apical 4 pairs of electrode contacts were recorded for these insertions at 60 Hz and video was simultaneously recorded at 60 fps. Four insertions into one cadaveric cochlea were performed and video and resistance data were processed and synchronized as in Sec. 4.4.1.

4.5 Results

In this section, experimental results from each of the six experiments are detailed. First, the straight EA phantom model experimental results are discussed (phantom models 1-3 with two different FLEX28 EAs). Then, the precurved EA (CI532) experiments in phantom model 3 are discussed, and finally, results from the cadaveric insertions with a FLEX28 are presented.

4.5.1 Experiments 1-3: Straight EA Phantom Experiments

4.5.1.1 Experiment 1

For the phantom model 1 experiment, the resulting access resistance vs. time plot is shown in Fig. 4.10 for EA1 and Fig. 4.11 for EA2. These plots show a few important properties of impedance sensing for localization with CI EAs. First, it can be seen that the resistances of the pairs as they travel through the model increased steadily with time, which is what would be expected with a monotonically decreasing cross section and the assumption that smaller conductive volume between two contacts leads to higher resistance. Of note, both the single-sided pairs and dual-sided pairs resistances increased with increasing insertion depth. Second, this plot shows that the individual measurements are related since they are all within the same conductive medium and all are along the same EA body (with wires running next to one another). This can be seen by the stair-step behavior that occurs for pairs 2-11. When one electrode contact of a pair first enters the conductive fluid, the resistance of that pair reduces to a lower plateau value, but is still quite noisy. Then, once both electrode contacts have entered the fluid, the signal drops sharply and is much cleaner. These experiments showed that this behavior occurs with both insertion and retraction. Interestingly, the magnitude of the initial drop in resistance was very consistent with each additional electrode contact that enters the model. Since the EA by design has evenly spaced contacts, it seems there may be a relationship between length of the EA inside the saline and resistance drop. Further investigation of this phenomenon is presented in Sec. 4.6.

It should be noted that EA2 had a slightly kinked tip upon opening its package (see Fig. 4.12) and this kink might have contributed to the noisier signal of the most apical pair. Regardless, all of the raw resistance data from trials with this EA are included in this section for completeness. For EA1, trial 1, the first pair's resistance does not reach quite as high of resistance magnitude as the other trials for the same insertion depth. This difference is due to the sensitivity of the measure to small fluctuations in proximity in that region (when the cross section is extremely narrow), and differences in the positioning of the EA in the channel due to its flexibility.

Another way of viewing these results is by looking at the resistance vs. linear insertion distance

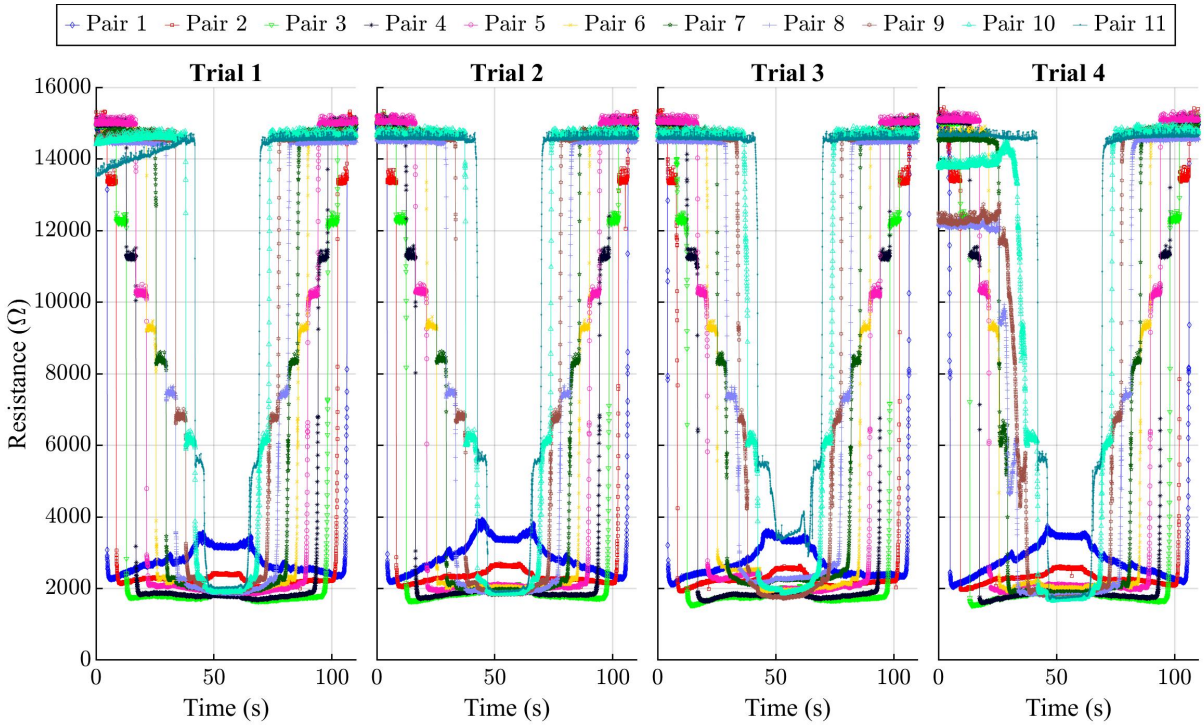

Figure 4.11: Raw access resistance vs. time for the four trials of experiment 1 with EA2

Figure 4.12: Photo of EA2 showing the tip portion of the EA for reference.

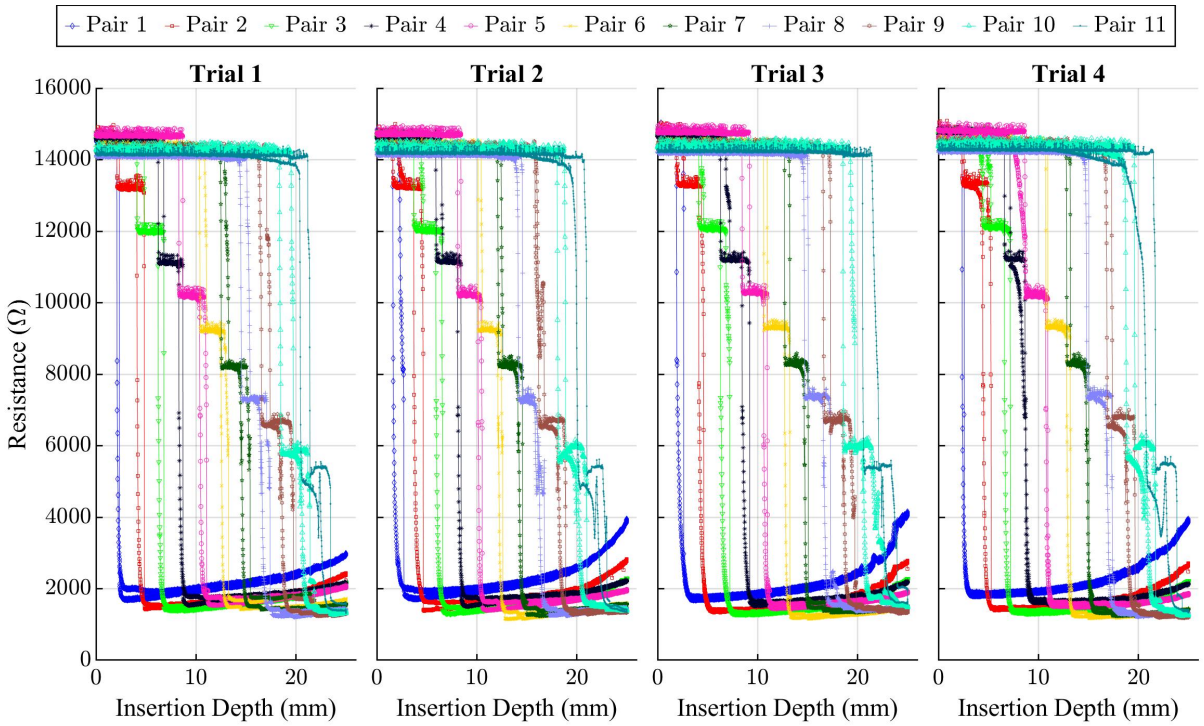

Figure 4.13: Raw access resistance vs. linear insertion distance for the four trials of experiment 1 with EA1

in Fig. 4.13 for EA1 and Fig. 4.14 for EA2. Because each experiment involved insertion from 0 mm to 25 mm and retraction back to zero, the horizontal distance between the vertical lines on these plots shows the difference in the insertion and retraction resistance-detected entering and exiting of each pair. Note that saline build-up tended to occur as the EA was being inserted, and so some of the difference in the detected enter and exit can be attributed to more or less saline being at the phantom model opening. In sum, Figs. 4.10, 4.11, 4.13, 4.14 support that this sensing method is extremely repeatable in this model and that it has good potential for real-time detection of intracochlear electrodes as was done in [102] after insertion was complete.

4.5.1.2 Experiment 2

Next, the goal of Experiment 2 was to assess whether the access resistance of the dual-sided contacts follow a predictable profile with proximity change to a wall. Recall that in this experiment, the access resistance between contacts 4 and 5 (single-sided), 5 and 6 (single and dual-sided), 6

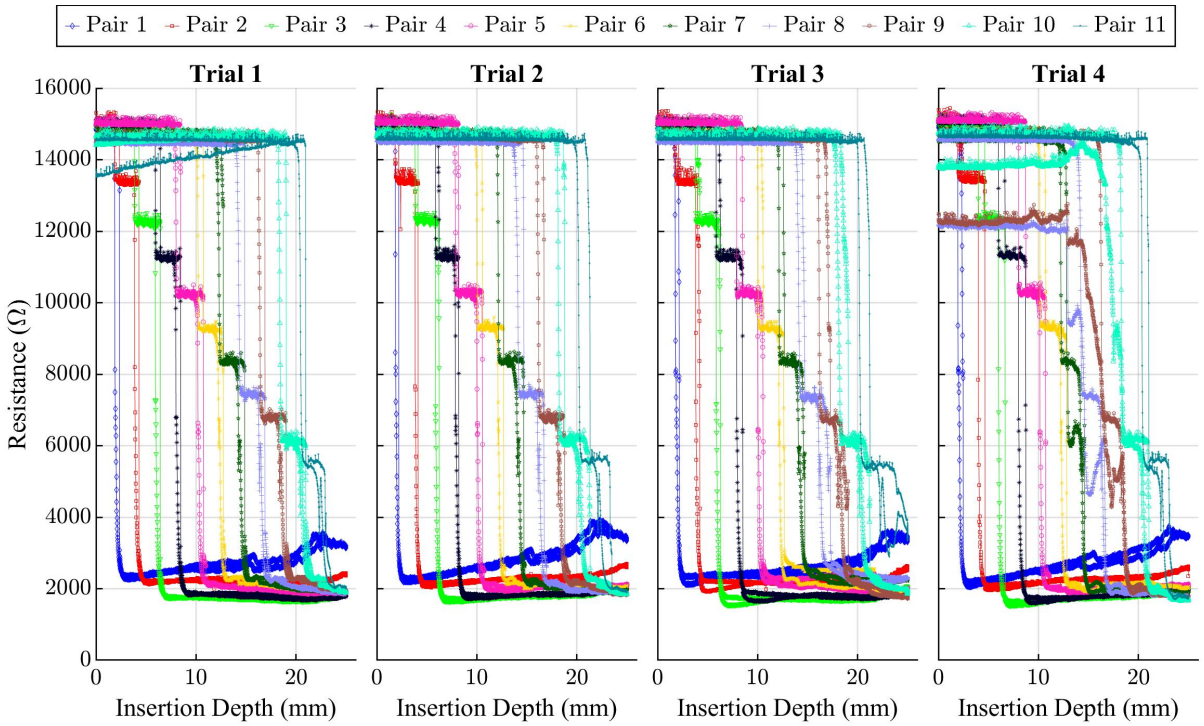

Figure 4.14: Raw access resistance vs. linear insertion distance for the four trials of experiment 1 with EA2

and 7 (dual-sided), and 7 and 8 (dual-sided) were sensed. Note that the 'home' position of the EA before each trial is slightly different since the actuator with the gripper attached was re-zeroed each time with slight adjustments to investigate the sensitivity of the measure to the starting position. Additionally, the EA is of course not rigid, and so the actual sweep reaction of the EA body is not consistent between trials. For each of the eight trials (4 trials with EA1 and 4 trials with EA2), the five electrode contacts of interest and their corresponding closest point on each wall were computed. Using this information, the area between a pair of contacts and their closest modiolar points was computed and smoothed with a moving average over 10 points. Access resistance data and the computed areas were synchronized for each trial, and a frame from the synchronized video and resistances from trial 1 with EA1 is shown in Fig. 4.15. The bottom wall in Fig. 4.7(2) will be referred to as 'Wall 1' and the top wall as 'Wall 2' as shown.

The grouped access resistance vs. the areas to Wall 1 can be viewed in Fig. 4.16 and vs. areas to Wall 2 in Fig. 4.17. Trial 2 of EA1 was omitted from this grouping because of a large air

bubble that significantly altered the resistance measures. These plots show the consistency of the relationship across multiple trials and multiple EAs as well as the model fit for each pair. For each pair, the relationship between access resistance and area to Wall 2 is essentially a reflection about the y-axis of the resistance relationship with the area to Wall 1. The single-sided pair exhibits a power-law relationship with Wall 1 (the wall the contacts are facing) as expected and a non-linear least squares fit was used to determine the coefficients in $c_1 x^{c_2} + c_3$ that best fit the data. For Wall 2, the resistance values exhibit the opposite power-law relationship with area, that is, as the proximity to Wall 2 decreases, the resistance also decreases. Both resulting model fits are plotted in Figs. 4.16(a) and 4.17(a).

For the dual-sided pairs, the relationship between resistance and areas seems to essentially follow two opposite power-law relationships that are symmetric about the center of the channel. The lowest resistance is in the center of the channel, when the area relative to both walls is close to equal. A non-linear least squares fit was used to find the coefficients in $c_1 x^{c_2} + c_3 x^{c_4} + c_5$ that would best fit these data. These model fits are plotted in Figs. 4.16(c-d) and 4.17(c-d). Overall, these pairs do indeed exhibit a significant access resistance change when E-M proximity changes, and the change follows a consistent relationship. The sensitivity of this measure in the middle area regions is quite low however, and these values will most likely primarily be useful for contact detection as opposed to detecting more granular scalar position changes. Finally, Pair 5-6 has both a single-sided and dual-sided electrode contact. This relationship is a bit unclear, but seems to be able to be modeled as a combination of two power-law relationships that are not symmetric about the center of the channel, and as such, the same equation as the dual-sided pair $c_1 x^{c_2} + c_3 x^{c_4} + c_5$ was fit and is plot in Figs. 4.16(b) and 4.17(b).

4.5.1.3 Experiment 3

The access resistance vs. linear insertion distance from Experiment 3 can be viewed in Figs. 4.18 for EA1 and 4.19 for EA2. The entry behavior of each electrode pair follows a similar stair-step pattern as was seen in Experiment 2. Of note, near about 10 mm, the EA skips across the plastic

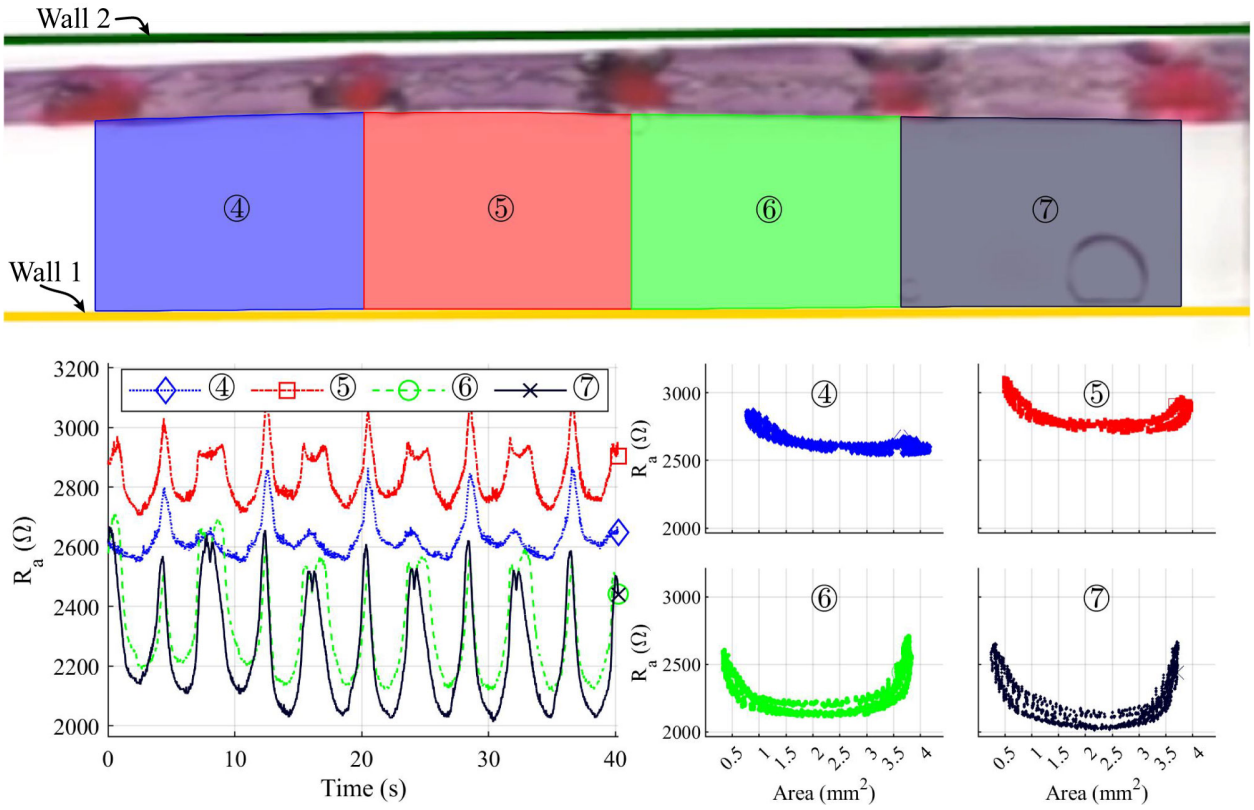

Figure 4.15: Synchronized trial 1 EA1 Experiment 2: (Top) Trial video with segmented polygons overlaid for pair ④, ⑤, ⑥, and ⑦, (Left) Resistance vs. Time for pair ④ (dotted blue line with diamond marker), pair ⑤ (dash-dot red line with square marker), pair ⑥ (dashed green line with circle marker), and pair ⑦ (solid black line with 'x' marker) (Right) Resistance vs. segmented area for each of the pairs ④-⑦, with the single-sided pair ④ results shown in the top left plot, single and dual-sided pair shown in the top-right plot ⑤, and the bottom plots displaying the dual-sided contact pair behavior ⑥ and ⑦.

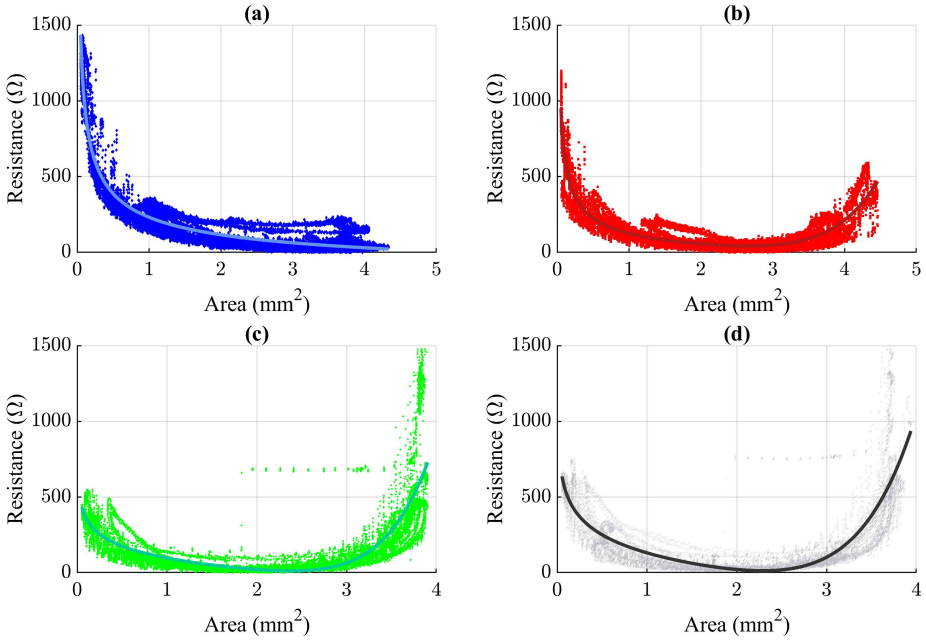

Figure 4.16: Grouped results for 7 trials (3 with EA1 and 4 with EA2) of (a) the single-sided pair, (b) the single and dual-sided pair, and (c-d) dual-sided pairs over 4 trials for EA1 with area on the horizontal axis indicating area between each contact and its corresponding closest point on wall 1.

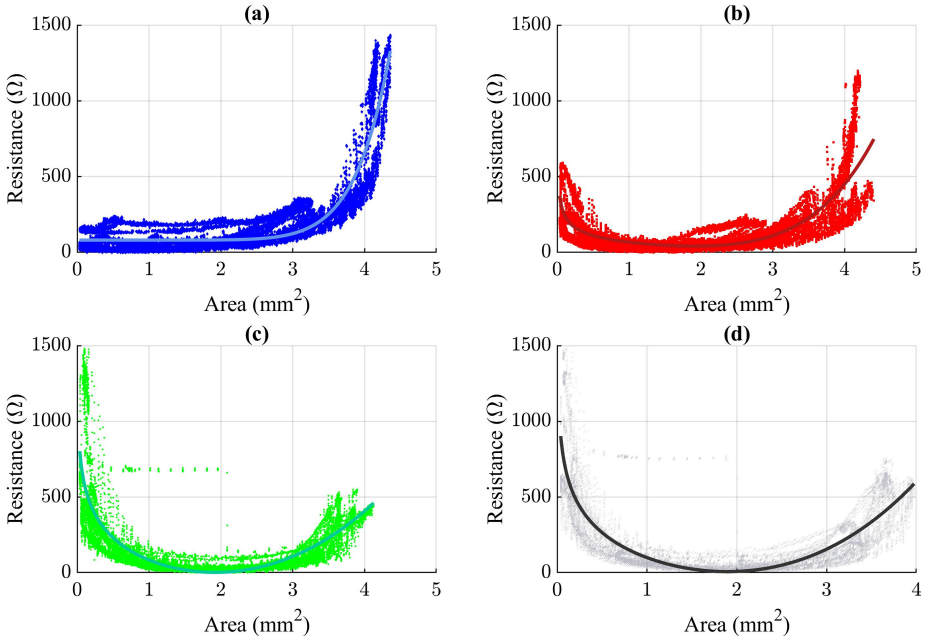

Figure 4.17: Grouped results for 7 trials (3 with EA1 and 4 with EA2) of (a) the single-sided pair, (b) the single and dual-sided pair, and (c-d) dual-sided pairs with area on the horizontal axis indicating area between each contact and its corresponding closest point on wall 2. Note each plot is just a reflection of its analog in Fig. 4.16

(a side effect of the prototyping method for the phantom model). This skipping can be seen in the access resistance profile at this insertion distance by the rapid jump of pair 1-2 and pair 2-3. This skipping occurred repeatedly at this point in each trial and the access resistance insertion profiles followed a similar profile in each trial. Although this skipping is an artifact of the plastic model, it demonstrates the real-time detection capability of an anomaly using this technique. As mentioned in Sec. 4.4.1, the EA was purposely inserted until buckling at the basal end of the EA. The goal of this purposeful buckling was to see if buckling of the EA in the dual-sided EA contacts could be detected by the access resistance change and using knowledge gained about the resistance/proximity relationship from Experiment 2. In these plots, the change is very small, since the buckling that was induced was not severe enough to drastically change the area (to maintain EA integrity between trials), so the resistance values were likely traveling along the flat portion of the curve shown in Fig. 4.16. It is likely that if the EA got much closer to the wall, there would be a sharper rise.

The primary purposes of this experiment were to generally assess the real-time insertion access resistance profile of this EA, but also to inform and validate the kinematic model. As mentioned, EA2 had a slightly bent tip, and as such, the curvature of the EA during insertion into the ST model and available final depth were limited. Additionally, as can be seen in Fig. 4.19, because of the bend, the pair 1 resistance values have an unreasonable amount of noise and variation in every trial. As a result, only the trials from EA1 are used for model validation. The resistance profile was used to assess how the access resistance data could be incorporated into the kinematic model to improve accuracy. Validation of the model with and without resistance knowledge will be described next.

4.5.1.4 Model Validation

An image of the final simulated shape using the kinematic model can be viewed in Fig. 4.20. The kinematic model simulation was validated in two ways. First, the AID vs. linear insertion depth profiles were compared for each trial. The AID was defined as the angle between the zero vector (vector from round window to center) and the most apical electrode contact. Next, the

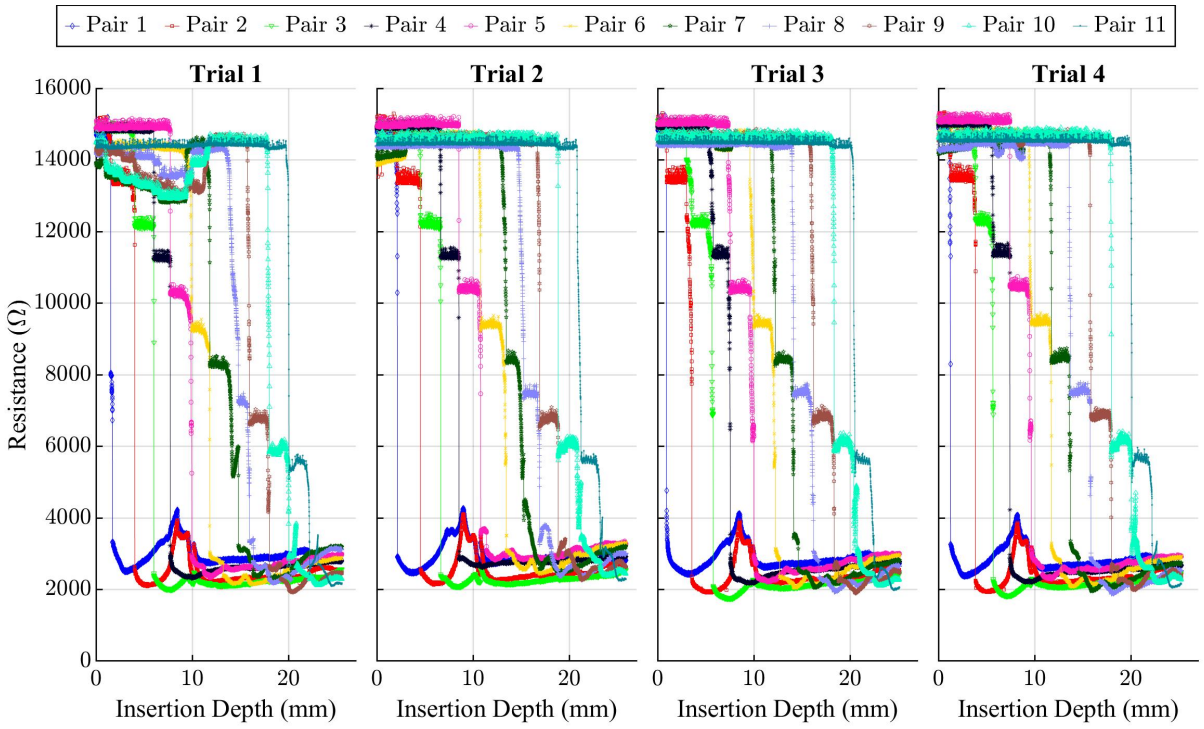

Figure 4.18: Raw access resistance vs. linear insertion distance for the four trials of experiment 3 with EA1

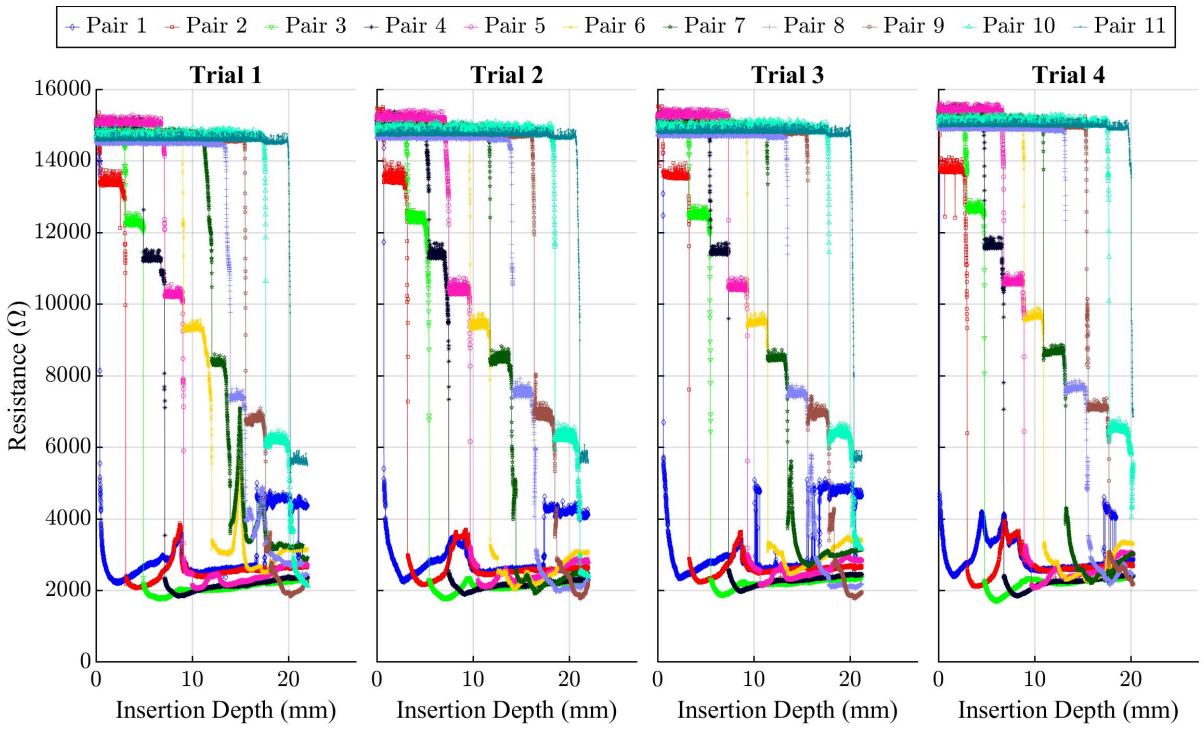

Figure 4.19: Raw access resistance vs. linear insertion distance for the four trials of experiment 3 with EA2

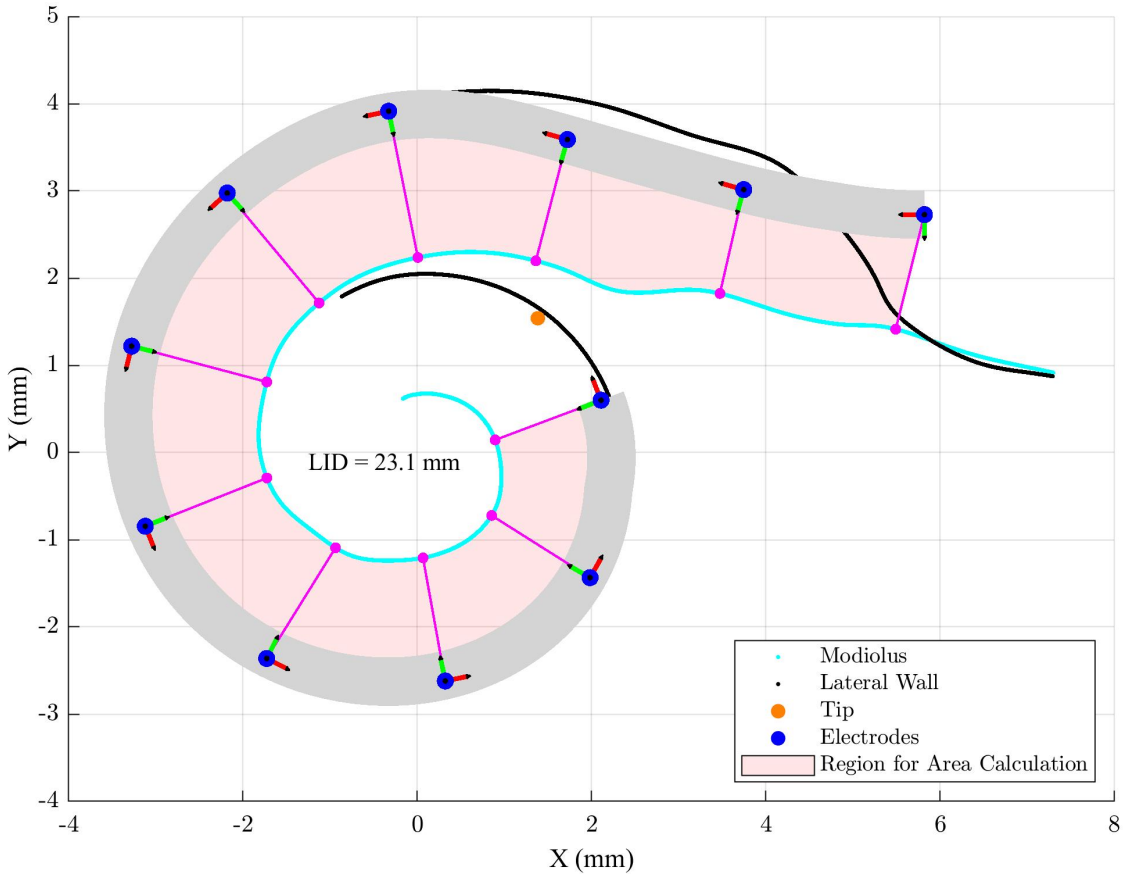

Figure 4.20: Final shape result from simulation using the developed kinematic model

centerline shape of the EA body in simulation was compared to the segmented EA medial axis from experimental trials.

The predicted AID vs. linear insertion of the kinematic model (dashed lines) with and without domains and the actual AID from experimental trials (solid lines) are shown in Fig. 4.21. This plot shows that by using resistance values to determine at which domain the EA is in at a given linear insertion depth, the kinematic model predicts some of the more dynamic behavior of the actual EA movement, particularly for insertion depths less than 15 mm. Notice that the magenta dashed line that simply assumes lateral wall conformation essentially predicts a straight line for AID vs. linear insertion depth. The experimental access resistance vs. insertion depth profiles displayed consistent behavior for each of the four trials, and thus the determined switch points locations were similar between trials. Despite this consistency, the model still captures some of the

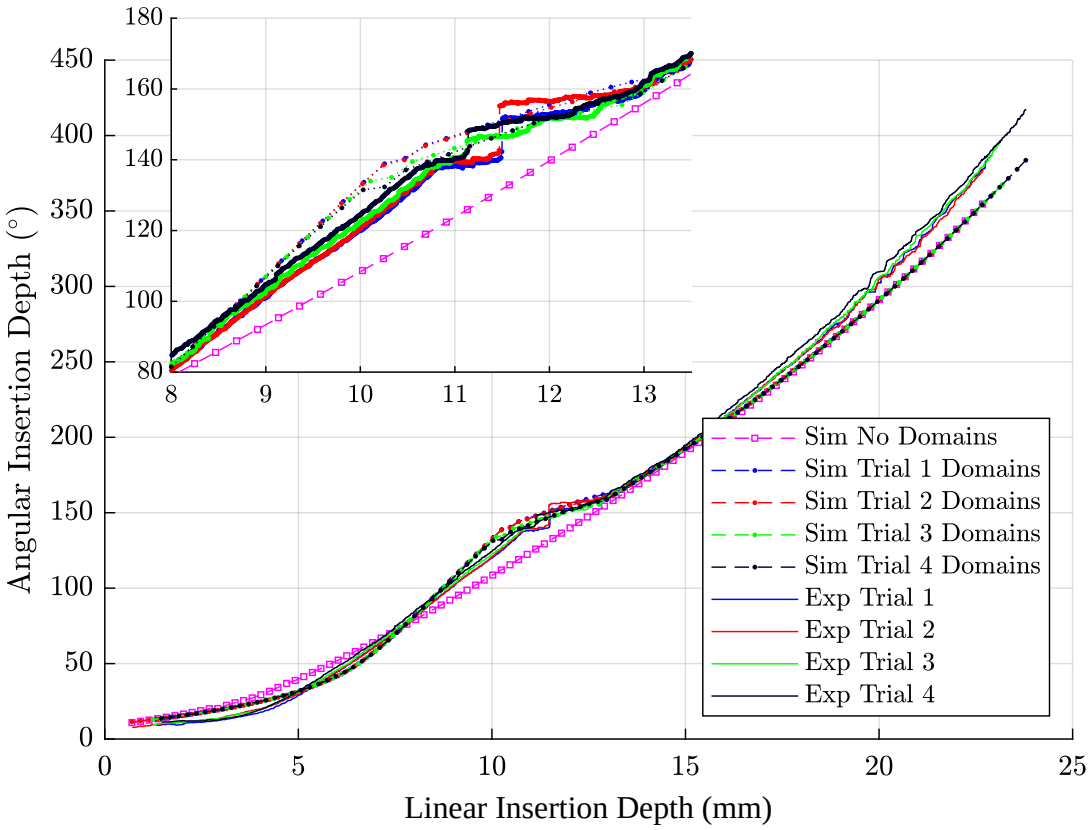

Figure 4.21: Angular insertion depth comparison for the simulation and experimental results of Experiment 3 demonstrating the utility of the domain incorporation in prediction of the non-linear angular insertion depth change at low insertion depths.

differences between trials (see Fig. 4.21 inset), such as different lateral-wall contact linear insertion depths.

The maximum-minimum distance between splines was computed for each simulation step and is shown in Fig. 4.22. Note that because the basal end of the EA was not simulated, only those components of the two shapes that were at least 4 mm inside the ST were compared. There is a clear increase in shape agreement between simulation and experiment when using the domains for each trial. Additionally, the maximum variation in the spline shapes increases with increasing insertion depth. This is a result of the higher sensitivity of the model to the ST shape at higher curvatures. Small errors in predicted ST shape in this region map to higher errors in AID. In this case, the 3D-printed ST model was printed vertically, and so the helix is slightly compressed near 300° (X $\sim$ 2 mm in Fig. 4.20), so the actual free-fitting shape naturally does not agree with the

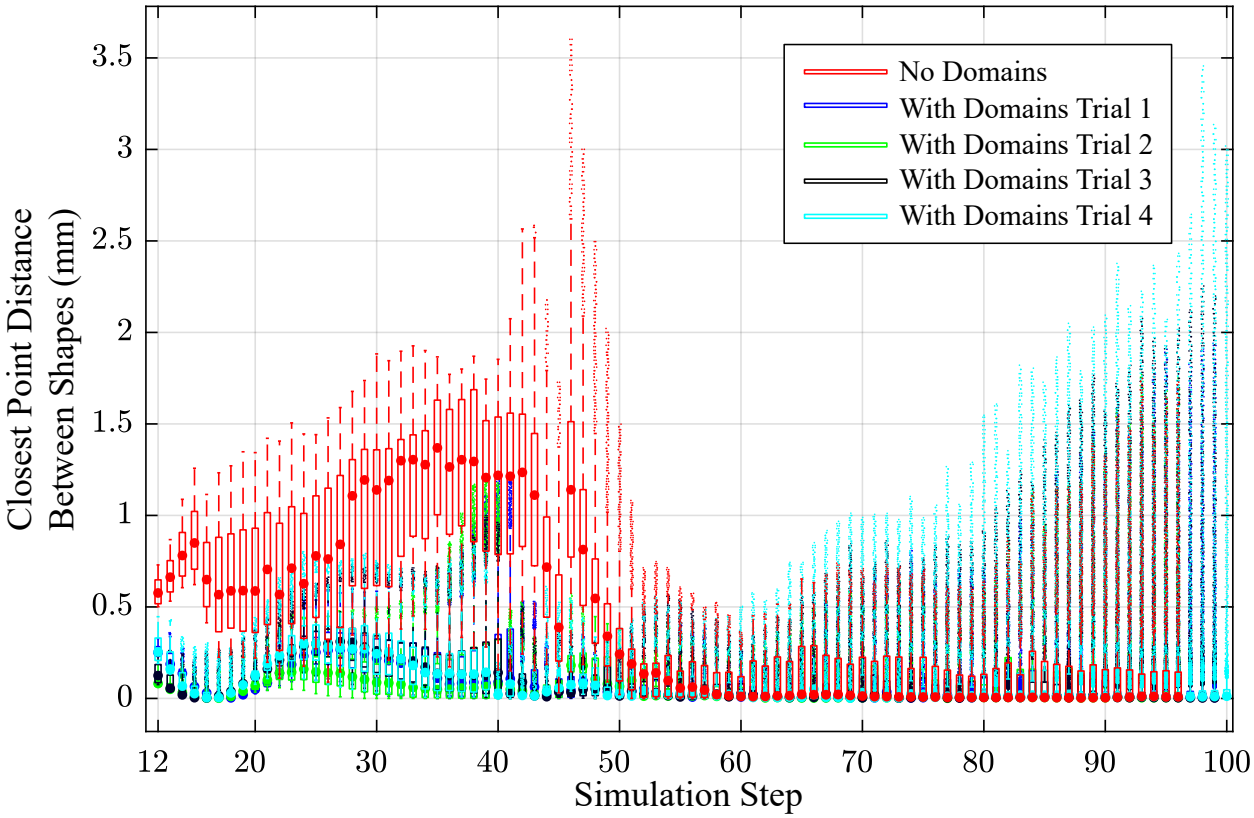

Figure 4.22: Boxplot showing range of closest point distances between splines at each simulation step for each trial with and without the incorporation of domains. Note the error reduction in the first half of the insertion when using domain switching.

theoretical shape well in this region and this is reflected in the model error.

4.5.2 Experiment 4 & 5: Precurved EA Phantom Experiments

4.5.2.1 Experiment 4

For Experiment 4, the access resistance vs. time plots for the most apical 11 pairs can be viewed in Fig. 4.23 and for the most basal 11 pairs in Fig. 4.24. It is important to note that this EA features an external stylet. This has unique implications when using impedance sensing, because it essentially negates the use of the sensing method when the EA contacts in a sensed pair are inside the stylet since the EA body and its contacts are enclosed. Additional complication is introduced in this region due to the slotted openings in the polyimide which introduce large fluctuations. As a result, as previously described in Sec. 4.4.2.1, the zero point of these experiments was defined as

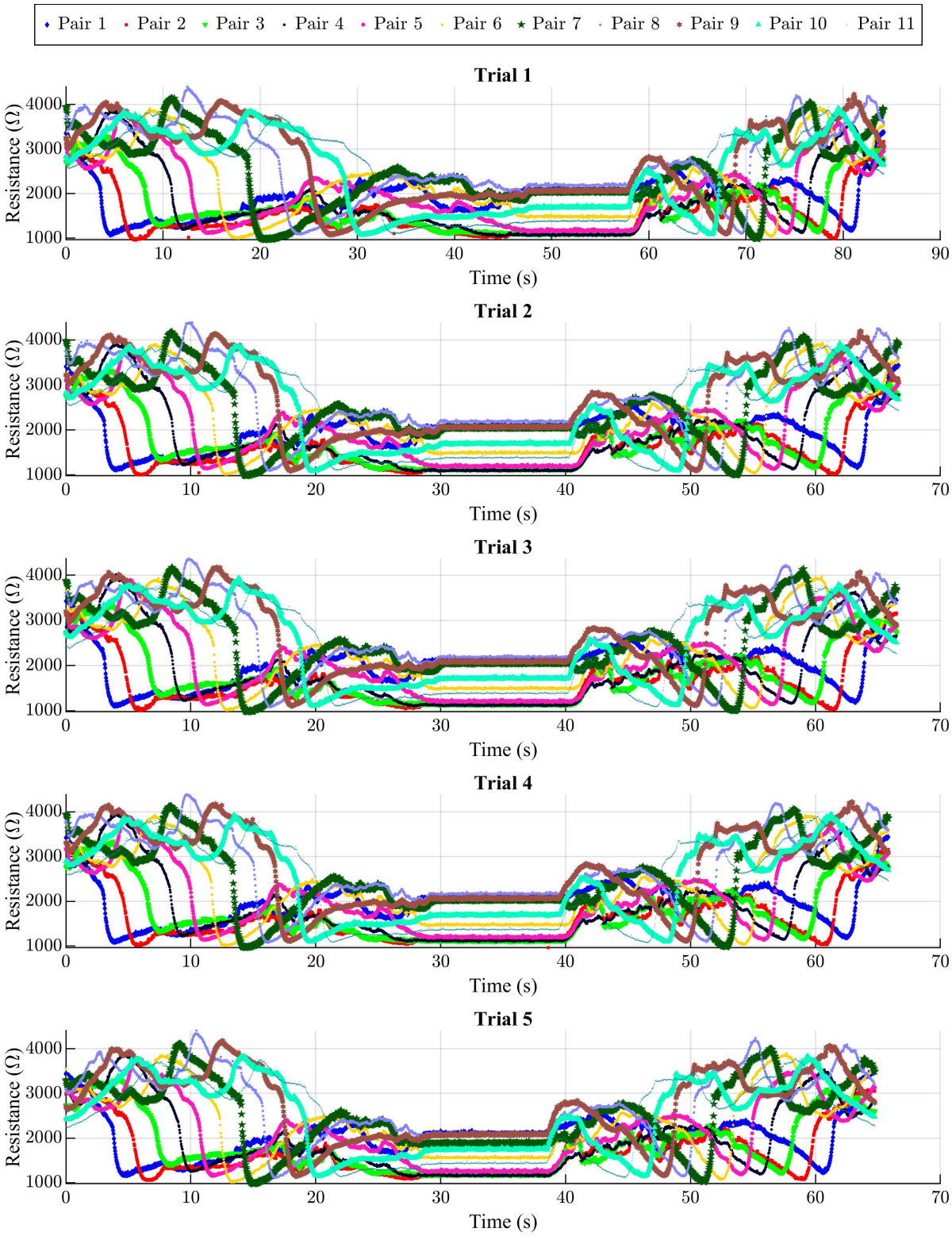

Figure 4.23: Open-loop experiments evaluating the insertion access resistance profile during a normal insertion of the most apical 11 pairs of contacts. Exit behavior from the polyimide is clear for each of the 11 pairs with each subsequent sharp drop in impedance starting from pair 1 (blue) to pair 11 (teal).

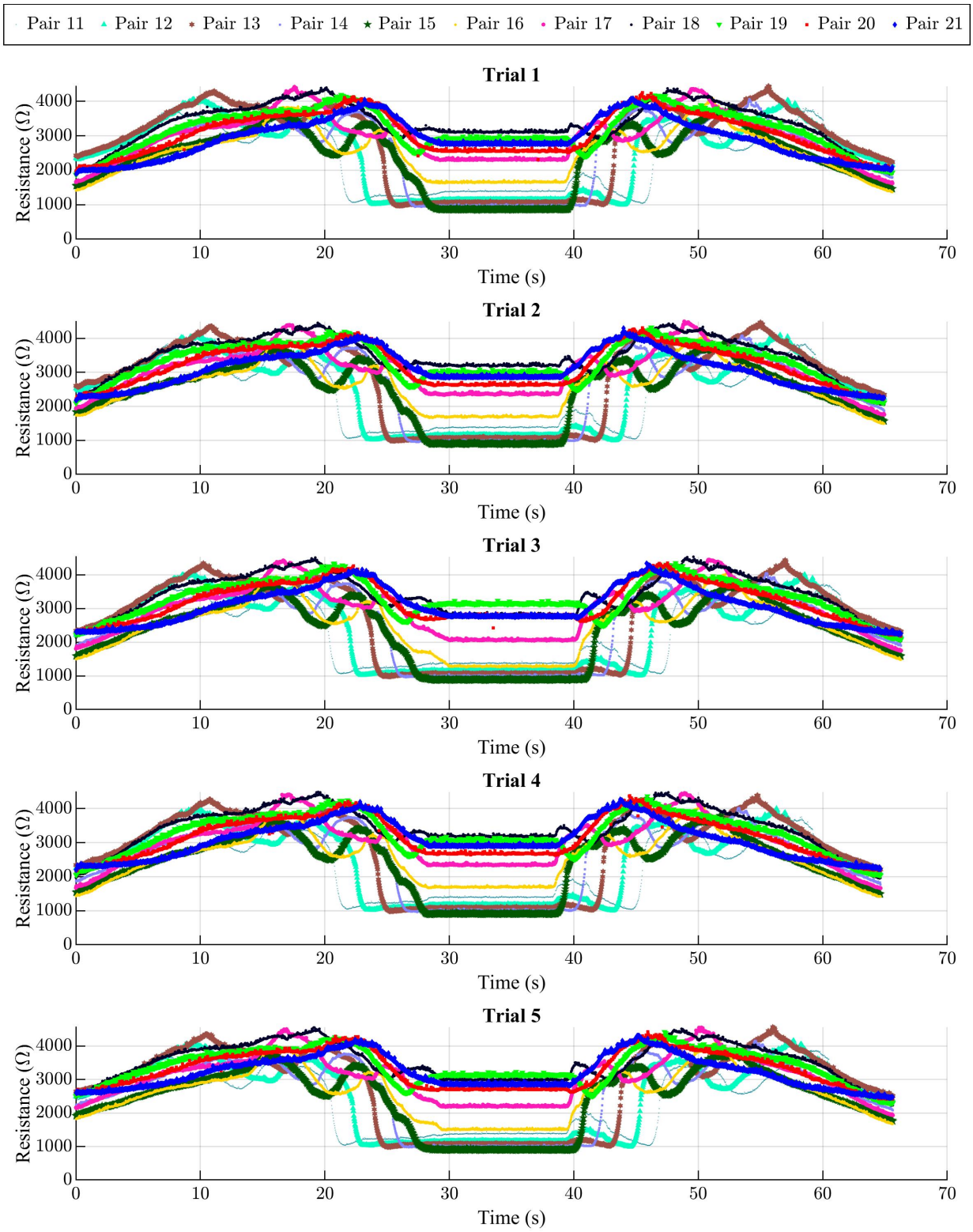

Figure 4.24: Open-loop experiments evaluating the insertion access resistance profile during a normal insertion of the most basal 11 pairs of contacts. Exit behavior from the polyimide stylet is again clear, although all of the pairs do not exit the polyimide and thus do not exhibit the sharp drop in resistance.

when the stylet was completely inserted into the model (about 5 mm), and the EA tip was at the opening of the stylet. These plots show that the access resistance insertion profile for this setup was very repeatable. The exit of the EA contacts from the stylet could be very reliably detected based on the sharp drop in resistance upon exit.

4.5.2.2 Experiment 5

Using results from preliminary testing with the same setup as in Experiment 4, but inserting to 12 or 13 mm instead of 11 mm, 4 contact pairs with sharp responses to the pull-back were selected for use in Experiment 5. Assuming the same numbering scheme as in the straight EA case (see Fig. 4.3) where the most apical electrode contact is referred to as '1', pairs 10-11, 11-12, 12-13, and 13-14 were selected to advise the actuators when to stop the insertion in Experiment 5. A total of 12 trials were performed, and a summary of these trial types is shown in Table. 4.3. The access resistance vs. time data for all trials is shown in Fig. 4.25. Using an image taken during the 'at-rest' portion of the insertion (once the specified insertion depth had been achieved) and the final retracted position, the average of the distances between the control contacts to their closest points on the modiolus (termed $\overline{m}$ for the remainder of this chapter), and the overall AID were determined. These values were then recomputed with the 'post-pull-back' image. These computations enabled a comparison showing the difference in EA positioning before and after the pull-back portion of a trial. An overview of these results is shown in Fig. 4.26 where the reduction in AID is shown on the horizontal axis and the reduction in modiolar distance on the vertical axis. These results demonstrate that for most types of insertion with the specified feedback, the pull-back portion successfully increased modiolar hugging and did not substantially affect AID. The 60% rise would clearly not work for a 12 mm insertion since the $\overline{m}$ before the pull-back is already quite small, and so the tracked electrodes have to essentially be inside the stylet for the access resistance to rise high enough to meet the cutoff criterion.

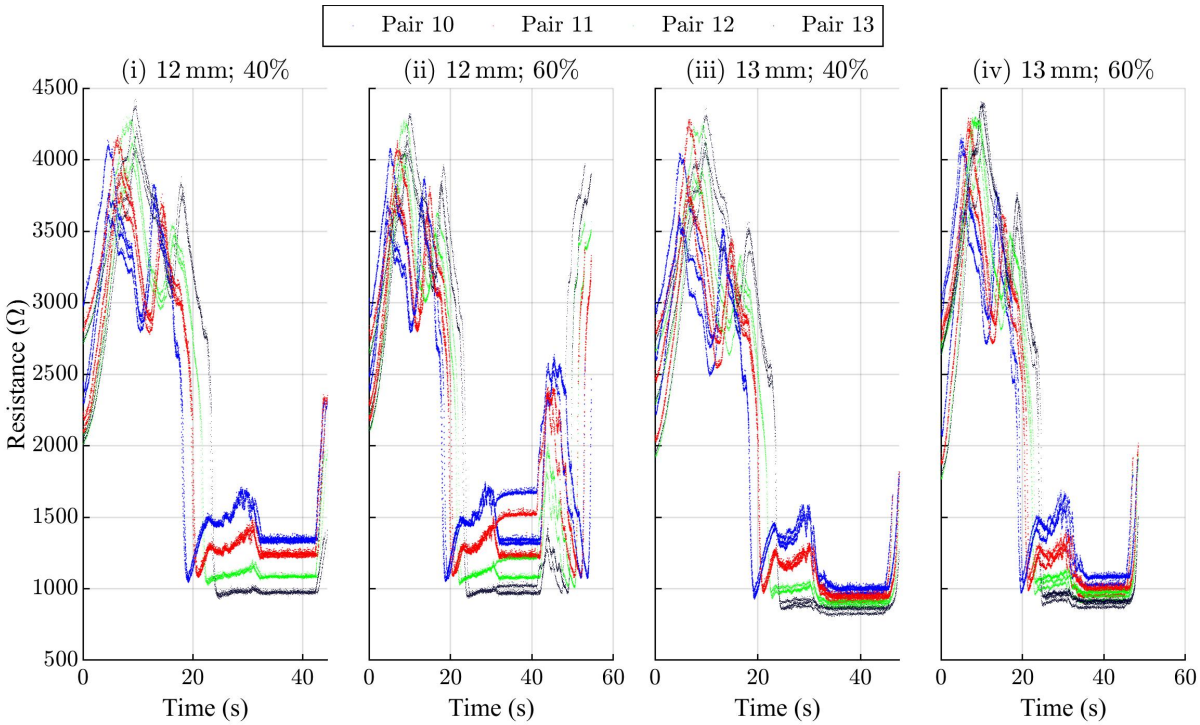

Figure 4.25: Raw access resistance vs. time with the 4 trials overlaid for Experiment 5 trials of types (i - iv) showing the resistance profile before the linear actuator stop.

4.5.3 Experiment 6: Straight EA Cadaver Experiments

Finally, the results for Experiment 6 will now be detailed. The goal of this experiment was to assess if the previously determined power-law relationship between the resistance of single-sided pairs and E-M proximity holds in a human cochlea. Accurate segmentation of the medial axis of the opaque cochlea near the round window in the images introduced unnecessary error since there are 4 tracked pairs available for assessment. Near the basal turn, the modiolus extents are much more clearly defined in the video. As such, the most distal three electrode contacts were segmented and the areas between their closest point on the modiolus and the EA body were computed for each video frame and then smoothed with a moving average over 10 points. These areas were then synchronized with the measured access resistance values and plotted. A plot of the synchronized video, access resistance vs. time, and access resistances vs. areas can be viewed in Fig. 4.27. The overall grouped access resistance vs. areas for the four trials can be viewed in Fig. 4.28. This figure demonstrates that the pairs follow a power-law relationship as in the

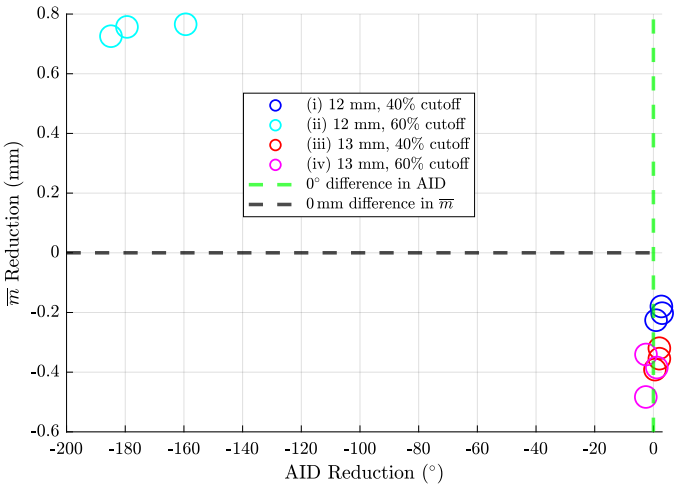

Figure 4.26: Overview of reduction in modiolar distance vs. AID reduction for all trials types (i) - (iv) of Experiment 5. On the y-axis, the reduction in average elecrode contact-to-modiolus distance ($\overline{m}$) after pull-back is shown. Note the desired outcome is for the $\overline{m}$ to be reduced after pull-back. Positive results on the y-axis indicate that upon pull-back, the electrode contacts got further from the modiolus. A grey dashed line is shown at this 0 mm for ease of viewing those trials that exhibited an increase in $\overline{m}$. On the x-axis, the reduction in angular insertion depth after pull-back is shown. Note that the desired outcome is for the AID to remain unchanged after pull-back (i.e., a reduction of 0°). A green dashed line is shown at this 0° location for ease of viewing those trials that had non-zero reductions. These results show that with access resistance feedback and this experimental protocol, most trial types exhibited very little change in AID, but a decrease in the distance to the modiolus as desired.

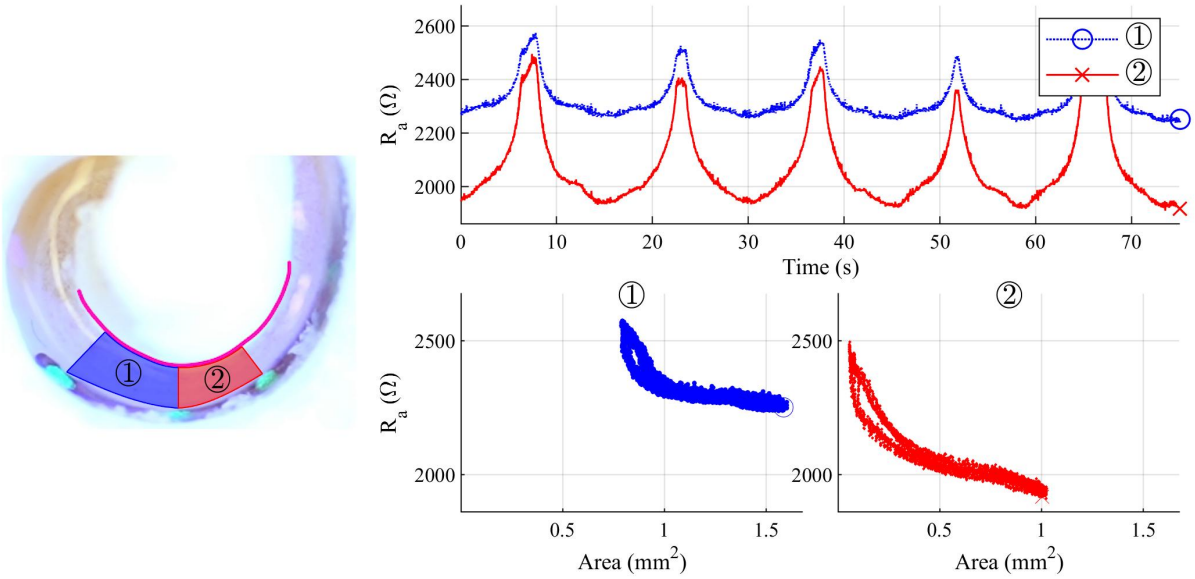

Figure 4.27: Synchronized trial 1 of Experiment 6: (Left) Trial video with segmented polygons overlaid on cadaveric ST for pair ① and pair ② (Top-Right) Resistance vs. Time for pair ① (dotted blue line with circle marker) and pair ② (solid red line with 'x' marker), and (Bottom-Right) Resistance vs. segmented area for each of the tracked pairs ① and ②.

plastic model—implying that benchtop results will likely translate in some capacity to a human model. Additionally, there is no additional smoothing or outlier removal of the resistance data in this grouped plot, so this plot demonstrates that the noise level is not significantly increased when inserting into a human cochlea. A limitation of this interpretation is that saline is still being used as a surrogate for human perilymph in this model. One other interesting result from this experiment was that when the actuators were not moving, there was a low amplitude, low frequency (~1 Hz) sinuosoidal variation in the access resistance data. Upon further investigation, it was discovered that this sinusoidal variation was due to mechanical movement of the EA due to the resonant frequency of the room where experiments were performed on the tenth story of a building.

4.6 Discussion & Conclusion

Results from this work imply that real-time access resistance sensing could prove useful as a feedback tool during clinical CI EA insertion. Main limitations from the results include pixel resolution limitations for computing areas and the 2D assumption in the correlation between access

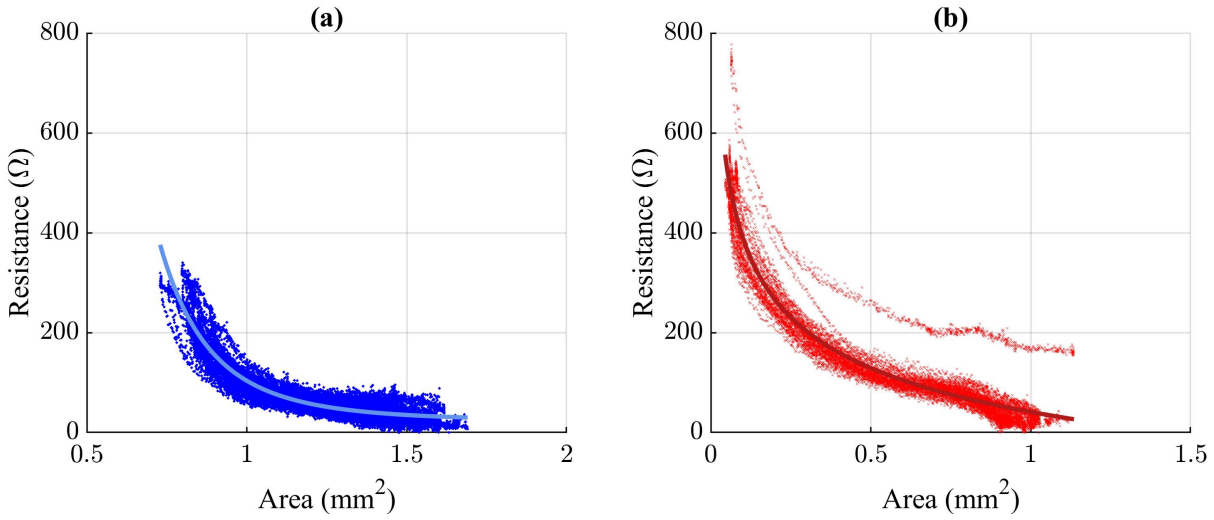

Figure 4.28: Grouped access resistance vs. area results for the four cadaver trials (a) pair 1-2 and (b) pair 2-3

resistance and proximity. Experiment 1 showed that the real-time access resistance measure can be used to reliably predict the entry and exit behavior of individual electrode contacts for two different EAs. It was also shown that the entry of each contact exhibited a stair-step response as described in Sec. 4.5.1.1. This overall stair-step effect is most likely a result of using the more apical contact in a pair as the source such that the charged contact enters the saline first. If that is the cause, the stair-step behavior could be a result of the parasitic capacitance of the other grounded EA contact/wires. To test this theory, Experiment 1 was repeated with EA1, but with the source and sink of each pair flipped. Results from this investigation are shown in Fig. 4.29 and demonstrate that the stair-step behavior was drastically reduced. However, despite this result, the setup in the initial trials actually provides a bit more information, because it can be clearly seen when one of the contacts in a pair enters the conductive medium, and so depending on the application, the original setup may be advantageous.

Experiment 2 demonstrated that the dual-sided contacts have potential to add useful information during insertion and exhibit predictable behavior. As expected, their access resistance response is less sensitive to proximity changes (compared to single-sided contacts) due to their dependence on the proximity to both walls. Additionally, simply knowing the resistance value of a pair is not

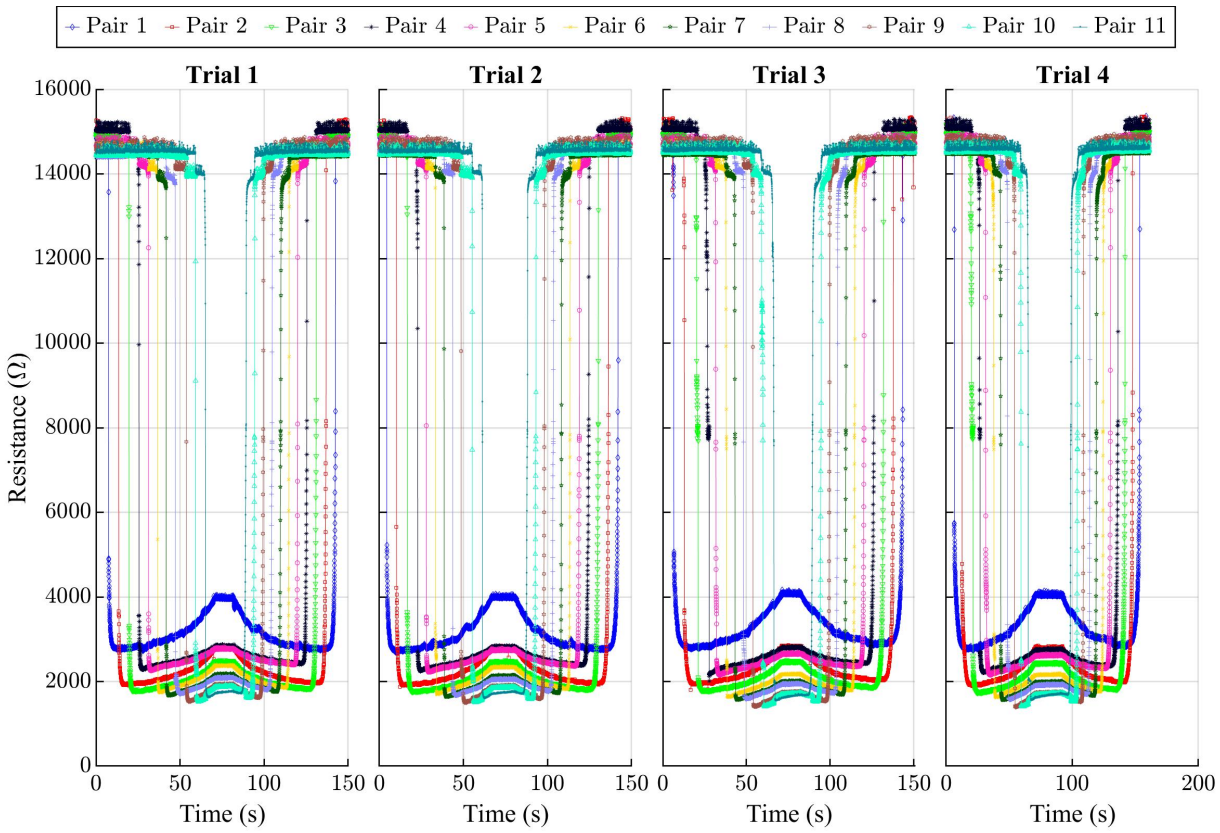

Figure 4.29: Raw access resistance vs. time for the four trials of the redo of Experiment 1 trial with EA1 with the canode and anode of each pair flipped

enough information to know which wall the contact is closer to, and future work could investigate different techniques to parse this information.

In Experiment 3, it was discovered that the real-time insertion profile of an insertion in a to-scale ST phantom model is very repeatable and that critical points of an insertion, such as initial lateral-wall contact, can be identified by the access resistance profile. It was demonstrated that the access resistance values and their derivatives can be used to improve prediction of overall EA shape. Future work could investigate the use of impedance to detect anomalies like tip fold-over and more severe buckling with this technique. The most useful method for presenting this shape information to surgeons during insertion should also be investigated.

Experiment 4 demonstrated that the same sensing setup could be used with a precurved EA, and the real-time access resistance insertion profile for this EA was evaluated for the first time. It was evident from this experiment that the external stylet complicates the use of sensing in regions where the electrode contacts of interest are inside the stylet.

The sensed resistance values of the precurved EA were successfully used in Experiment 5 to detect at what point optimal EA positioning had been achieved. This is important because traditionally, surgeons rely only on haptic feedback to know when modiolar hugging has been achieved. From Fig. 4.26, it is evident that for most insertion types (see Table 4.3 all but type (ii)), the AID was relatively unchanged (as desired) when using access resistance feedback to know when to stop, and the distance to the modiolus was reduced as desired. The type (ii) insertion was not hypothesized to work well, but was performed to show a case of what could happen if the pull-back technique were performed poorly due to limited feedback.

Experiment 6 demonstrated that the previously determined power-law relationship holds in a cadaveric model, implying it is likely that benchtop results may translate to clinical insertions. Future work should investigate the effect of different morphologies on the relative utility of impedance sensing and create a more statistically significant measure of the translatability of this relationship.

In summary, these data demonstrate that bipolar impedance sensing, specifically the access resistance component of the impedance, has high potential for informing EA positioning and im-

proving insertions in the future. This modality could provide reliable real-time EA position information without adding extra cost to a procedure or impeding hospital workflow. Results from benchtop cadaver experiments in this work proved promising; however, before clinical translation, an important next step will be to perform a sensitivity analysis to see how variations in different factors that were not present in these benchtop experiments could affect position feedback efficacy in humans (e.g., sensitivity to perilymph properties, decay law properties, etc).

4.7 Acknowledgements

This work was supported in part by the National Science Foundation Graduate Research Fellowship under DGE-1445197/1937963. The developers thank Anandhan Dhanasingh of MED-EL and Peter Gibson of Cochlear Ltd. for providing the EAs used in these experiments.

Chapter 5

Future Work and Conclusions

5.1 Future Work

5.1.1 Chapter 2: Clinical Translation of a Manual Insertion Tool for Minimally Invasive Cochlear Implant Surgery

Chapter 2 focused on the development of an insertion tool for MICIS. The developed manual insertion tool helped solve the critical last step of the procedure by enabling a surgeon to insert an EA easily down the narrow tunnel of spiculated bone and into the ST with minimal buckling.

There are many interesting areas of future work for this tool. The tool should be evaluated with different straight EA types (simply by modifying the inner diameter and bottleneck diameter of the tool) to verify functionality across types. Additionally, future work could investigate the addition of a stylet arrestor to enable insertion of precurved EAs with this tool, although the buckling issue is much less prevalent with these stiffer EAs in MICIS. A third area of future work will be expanding the number of clinical cases to include more patients and achieve a more statistically significant measure of clinical success. Another interesting study would be evaluating whether this tool could be useful for traditional, mastoidectomy-based CI surgeries as opposed to only the minimally invasive situation. A final area of future work would be determining how beneficial this tool is to novice users (in MICIS and in traditional CI surgery) compared to its usefulness to expert users in a similar setting.

5.1.2 Chapter 3: System Development for Magnetically Steered Robotic Cochlear-Implant Electrode Array Insertion

Chapter 3 focused on the development of a robotic system that includes image guidance, a nonmagnetic automated insertion tool, and magnetic steering using a novel electromagnet (the Omnimagnet) to enable atraumatic CI EA insertion. Image guidance and preoperative planning were shown to help align the robotic tool and electromagnet with a preoperatively determined

trajectory and magnetic steering demonstrated reduced insertion forces (and implied decreased trauma) in phantom models and for the first time, in cadaveric specimens.

Future work of this system will investigate its efficacy in a live guinea pig model to experimentally verify the implication that reduced insertion trauma yields improved hearing outcomes. Additional necessary future work will be developing a cooling system to prevent overheating and increase the available safe duration of use for the Omnimagnet. Another important area of future investigation will be determining a safe way to remove the tip magnet from the EA. If this cannot be done, either a patient will not be able to have MRI done, or it must be conclusively shown that the forces and torques induced on the small tip magnet when entering the MRI are not dangerous. Finally, the magnetic field source magnitude should be increased to provide more torque on the magnet-tipped EA by scaling up the external magnet, the magnet on the tip of the EA, or both. This increase in magnitude would allow the magnet to be in the optimal position as described by [151].

5.1.3 Chapter 4: Using Real-Time Electrode Array Insertion Impedance Feedback to Inform Array Positioning and Modulate Insertions

Chapter 4 focused on the utility of impedance sensing in CI EA insertions. In particular, the real-time relationship between impedance and E-M proximity was evaluated in a cadaveric cochlea for the first time, showing that the benchtop relationship translates to human models. In phantom models, the relationship between impedance and E-M proximity for dual-sided EA contacts was demonstrated for the first time. Insertions into a uniformly tapered model provided further evidence of the utility of impedance sensing for detecting in real-time when individual contacts have entered the cochlea. By performing both insertion and retraction, this experiment also helped demonstrate the repeatability of this detection. Insertions into a plastic ST model were also performed to inform and validate kinematic model development that incorporates impedance sensing knowledge. Finally, work in this chapter further demonstrated the utility of using impedance sensing as a feedback mechanism in control with precurved EAs by using impedance feedback in real-time to

inform when to stop the pull-back technique.

In the future, further investigation should be done to evaluate and characterize the effects of morphology on the relationship between impedance to E-M proximity. Additionally, morphology's influence on the relative utility of using impedance sensing could be evaluated. In other words, do certain morphologic characteristics mean a patient would benefit more from a surgeon using impedance sensing to augment the insertion? This morphology investigation could be done in cadaveric models so that a more statistically relevant relationship between access resistance and proximity in cadaveric models could be developed. Future work could investigate the utility of adding more domains to the developed kinematic model to capture a wider spread of possible insertion effects (such as anomalies like tip fold-over) and/or explore the benefits of using a more sophisticated model for shape prediction. It should be clarified in the future how this progress and shape information should be presented to surgeons who would use this type of feedback while manually inserting the EA. This feedback could take different forms including a displayed GUI or an overlay on the microscope, and the optimal display method should be evaluated for intuitive and effective use. There are many areas of interesting future work for optimizing the impedance sensing method since only access resistance was explored in this work with a single stimulation setting. In this future, a parameter sweep within the range of safe values for the pulse magnitude, pulse width, and timing could be explored and ideally would be correlated with the desired number of measured pairs. Different stimulation schemes (such as tripolar) could also be investigated. The relationship between the equivalent circuit impedance elements and force should be explored to see if impedance values could be used as a surrogate for trauma detection since force measurement in a real-time surgical setting is challenging.

5.2 Conclusion

Chapter 2 detailed the design, development, and clinical translation of a manual insertion tool for MICIS. Initial design feasibility was first demonstrated in phantom and cadaver models. Next, all of the steps needed to clinically translate the device were taken. Namely, a population analysis

of potential MICIS candidates was performed, and this analysis enabled the design and fabrication of a clinically realistic testing/training phantom model for tool evaluation. Analysis results also led to translatable device dimension specifications. The insertion force profile was evaluated in this clinically realistic model and cadaver testing was performed for tool evaluation for clinical viability. Both experiments demonstrated that the new tool enables more consistently deep insertions than traditional tools (e.g., surgical forceps). Finally, the tool was clinically translated and achieved a full insertion in its first clinical case where the EA was fully inserted entirely within the ST of the cochlea.

Chapter 3 described the development of a system for improved CI EA insertion using magnetic steering combined with image guidance and an automated insertion tool. System development involved creating a method for preoperatively planning the tool pose and magnet pose that correspond to the planned Omnimagnet magnetic field vectors (created with programmed currents) and automated insertion tool linear insertion depths. An automated insertion tool was developed that is nonmagnetic and features a new gripping mechanism for tapered clinical EA advancement and detachment. Using the new system, reduced forces (and thus reduced implied trauma) were demonstrated in phantom models when using magnetic steering compared to a solely robotic or a manual insertion. Additionally, the usefulness of magnetic steering when inserting an EA into a cadaveric cochlea was demonstrated for the first time by showing force reduction with magnetic steering compared to a solely robotic insertion.

Chapter 4 focused on the insertion impedance profile and its potential utility in CI EA insertion. The impedance insertion profile of a straight EA was evaluated in a series of phantom models of increasing complexity, including a to-scale ST phantom. These experiments demonstrated that the dual-sided contact impedances exhibit predictable and repeatable behavior relative to changes in E-M proximity. A kinematic model was developed for predicting EA shape and using results from the to-scale ST experiments, the model was validated. The viability of using this sensing method in cadaveric models was demonstrated for the first time by directly relating bipolar impedance values to E-M proximity. Finally, impedance feedback was used to inform the pull-back of an

over-inserted precurved EA by advising the actuators when to stop the insertion as soon as close modiolar positioning had been achieved so that the AID was not decreased as a result of this retraction.

Bibliography

[1] D. C. Peterson and R. N. Hamel, *Neuroanatomy, Auditory Pathway*. StatPearls Publishing, Aug. 2019. [Online]. Available: http://www.ncbi.nlm.nih.gov/pubmed/30335344.

[2] *How Do We Hear?* | *NIDCD*. [Online]. Available: https://www.nidcd.nih.gov/health/how-do-we-hear.

[3] E. G. Wever, "The Physiology of Hearing: The Nature of Response in the Cochlea", *Fundamentals of Sensory Physiology*, pp. 199–223, 1986.

[4] L. L. Cunningham and D. L. Tucci, "Hearing Loss in Adults", *New England Journal of Medicine*, vol. 377, no. 25, A. H. Ropper, Ed., pp. 2465–2473, Dec. 2017, ISSN: 0028-4793. DOI: 10.1056/NEJMra1616601. [Online]. Available: http://www.nejm.org/doi/10.1056/NEJMra1616601.

[5] A. Wingfield and J. E. Peelle, "How does hearing loss affect the brain?", *Aging Health*, 2016. DOI: 10.2217/AHE.12.5.

[6] D. Bakhos, A. Villeuneuve, S. Kim, K. Hammoudi, and C. Hommet, "Hearing loss and Alzheimer's disease", *Gériatrie et Psychologie Neuropsychiatrie du Viellissement*, vol. 13, no. 2, pp. 195–204, Jun. 2015, ISSN: 1760-1703. DOI: 10.1684/pnv.2015.0539. [Online]. Available: http://www.john-libbey-eurotext.fr/medline.md?doi=10.1684/pnv.2015.0539.

[7] *Hearing Aids — Styles/Types & How They Work* | *NIDCD*. [Online]. Available: https://www.nidcd.nih.gov/health/hearing-aids.

[8] *Cochlear Implants* | *NIDCD*. [Online]. Available: https://www.nidcd.nih.gov/health/cochlear-implants.

[9] "Chapter 10 - Sensory", Tech. Rep. [Online]. Available: http://droualb.faculty.mjc.edu/Course%20Materials/Physiology%20101/Chapter%20Notes/Fall%202007/chapter_10%20Fall%202007.htm.

[10] B. S. Wilson and M. F. Dorman, "Cochlear implants: Current designs and future possibilities", *Journal of Rehabilitation Research and Development*, vol. 45, no. 5, pp. 695–730, 2008. DOI: 10.1682/JRRD.2007.10.0173.

[11] C. T. M. Choi and Y.-H. Lee, "A Review of Stimulating Strategies for Cochlear Implants Electrical Impedance Tomography View project Cochlear Implants View project A Review of Stimulating Strategies for Cochlear Implants", *Cochlear Implant Research Updates*, vol. 16, 2012. DOI: 10.5772/47983. [Online]. Available: www.intechopen.com.

[12] J. H. Noble, R. F. Labadie, R. H. Gifford, and B. M. Dawant, "Image-Guidance enables new methods for customizing cochlear implant stimulation strategies", *IEEE Transactions on Neural Systems and Rehabilitation Engineering*, vol. 21, no. 5, pp. 820–829, 2013, ISSN: 15344320. DOI: 10.1109/TNSRE.2013.2253333.

[13] J. Wouters, H. J. McDermott, and T. Francart, "Sound coding in cochlear implants: From electric pulses to hearing", *IEEE Signal Processing Magazine*, vol. 32, no. 2, pp. 67–80, Mar. 2015, ISSN: 10535888. DOI: 10.1109/MSP.2014.2371671.

[14] O. Stakhovskaya, D. Sridhar, B. H. Bonham, and P. A. Leake, "Frequency map for the human cochlear spiral ganglion: Implications for cochlear implants", *JARO - Journal of the Association for Research in Otolaryngology*, vol. 8, no. 2, pp. 220–233, Jun. 2007, ISSN: 15253961. DOI: 10.1007/s10162-007-0076-9. [Online]. Available: /pmc/articles/PMC2394499/?report=abstract%20https://www.ncbi.nlm.nih.gov/pmc/articles/PMC2394499/.

[15] J. T. Rubinstein, "How cochlear implants encode speech", *Current Opinion in Otolaryngology & Head and Neck Surgery*, vol. 12, no. 5, pp. 444–448, Oct. 2004, ISSN: 1068-9508. DOI: 10.1097/01.moo.0000134452.24819.c0. [Online]. Available: http://journals.lww.com/00020840-200410000-00016.

[16] A. Dhanasingh, "Cochlear duct length along the outer wall vs organ of corti: Which one is relevant for the electrode array length selection and frequency mapping using Greenwood

function?", *World Journal of Otorhinolaryngology - Head and Neck Surgery*, vol. 5, no. 2, pp. 117–121, Jun. 2019, ISSN: 20958811. DOI: 10.1016/j.wjorl.2018.09.004.

[17] A. Dhanasingh and C. Jolly, "An overview of cochlear implant electrode array designs", *Hearing Research*, vol. 356, pp. 93–103, Dec. 2017, ISSN: 18785891. DOI: 10.1016/j.heares.2017.10.005.

[18] A. Mudry and M. Mills, "The early history of the cochlear implant: A retrospective", *JAMA Otolaryngology - Head and Neck Surgery*, vol. 139, no. 5, pp. 446–453, May 2013, ISSN: 21686181. DOI: 10.1001/jamaoto.2013.293. [Online]. Available: https://jamanetwork.com/journals/jamaotolaryngology/fullarticle/1688121.

[19] J. P. Roche and M. R. Hansen, "On the Horizon: Cochlear Implant Technology", *Otolaryngologic Clinics of North America*, vol. 48, no. 6, pp. 1097–1116, Dec. 2015, ISSN: 15578259. DOI: 10.1016/j.otc.2015.07.009. [Online]. Available: https://www.ncbi.nlm.nih.gov/pmc/articles/PMC4641792/.

[20] C. G. Wright and P. S. Roland, "Microdissection in Cochlear Implant Research", in *Cochlear Anatomy via Microdissection with Clinical Implications*, Springer International Publishing, 2018, pp. 45–72. DOI: 10.1007/978-3-319-71222-2{_}3. [Online]. Available: https://doi.org/10.1007/978-3-319-71222-2_3.

[21] R. H. Gifford, J. K. Shallop, and A. M. Peterson, "Speech Recognition Materials and Ceiling Effects: Considerations for Cochlear Implant Programs", *Audiology and Neurotology*, vol. 13, no. 3, pp. 193–205, Apr. 2008, ISSN: 1420-3030. DOI: 10.1159/000113510. [Online]. Available: https://www.karger.com/Article/FullText/113510.

[22] A. A. Eshraghi, R. Nazarian, F. F. Telischi, S. M. Rajguru, E. Truy, and C. Gupta, "The Cochlear Implant: Historical Aspects and Future Prospects", *The Anatomical Record: Advances in Integrative Anatomy and Evolutionary Biology*, vol. 295, no. 11, pp. 1967–1980, Nov. 2012, ISSN: 19328486. DOI: 10.1002/ar.22580. [Online]. Available: http://doi.wiley.com/10.1002/ar.22580.

[23] D. L. Sorkin, "Cochlear implantation in the world's largest medical device market: Utilization and awareness of cochlear implants in the United States", *Cochlear Implants International*, vol. 14, no. SUPPL. 1, S4, Mar. 2013, ISSN: 14670100. DOI: 10.1179/1467010013Z.00000000076. [Online]. Available: /pmc/articles/PMC3663290/?report=abstract%20https://www.ncbi.nlm.nih.gov/pmc/articles/PMC3663290/.

[24] N. P. Dillon, R. Balachandran, A. Motte dit Falisse, G. B. Wanna, R. F. Labadie, T. J. Withrow, J. M. Fitzpatrick, and R. J. Webster, "Preliminary testing of a compact bone-attached robot for otologic surgery", in *Medical Imaging 2014: Image-Guided Procedures, Robotic Interventions, and Modeling*, vol. 9036, SPIE, Mar. 2014, p. 903 614, ISBN: 9780819498298. DOI: 10.1117/12.2043875.

[25] Q. J. Fu and G. Nogaki, "Noise susceptibility of cochlear implant users: The role of spectral resolution and smearing", *JARO - Journal of the Association for Research in Otolaryngology*, vol. 6, no. 1, pp. 19–27, Mar. 2005, ISSN: 15253961. DOI: 10.1007/s10162-004-5024-3. [Online]. Available: https://link.springer.com/article/10.1007/s10162-004-5024-3.

[26] L. K. Holden, J. B. Firszt, R. M. Reeder, R. M. Uchanski, N. Y. Dwyer, and T. A. Holden, "Factors affecting outcomes in cochlear implant recipients implanted with a perimodiolar electrode array located in scala tympani", *Otology and Neurotology*, vol. 37, no. 10, pp. 1662–1668, Nov. 2016, ISSN: 15374505. DOI: 10.1097/MAO.0000000000001241. [Online]. Available: https://www.ncbi.nlm.nih.gov/pmc/articles/PMC5113723/.

[27] J. Saliba, H. Bortfeld, D. J. Levitin, and J. S. Oghalai, "Functional near-infrared spectroscopy for neuroimaging in cochlear implant recipients", *Hearing Research*, vol. 338, pp. 64–75, Aug. 2016, ISSN: 18785891. DOI: 10.1016/j.heares.2016.02.005.

[28] D. S. Lazard, H. Innes-Brown, and P. Barone, "Adaptation of the communicative brain to post-lingual deafness. Evidence from functional imaging", *Hearing Research*, vol. 307, pp. 136–143, Jan. 2014, ISSN: 03785955. DOI: 10.1016/j.heares.2013.08.006.

[29] M. L. Carlson, C. L. W. Driscoll, R. H. Gifford, G. J. Service, N. M. Tombers, B. J. Hughes-Borst, B. A. Neff, and C. W. Beatty, "Implications of Minimizing Trauma During Conventional Cochlear Implantation", *Otology and Neurotology*, vol. 32, no. 6, pp. 962–968, Aug. 2011. DOI: 10.1097/MAO.0b013e3182204526. [Online]. Available: http://content.wkhealth.com/linkback/openurl?sid=WKPTLP:landingpage&an=00129492-201108000-00014.

[30] S. Chakravorti, J. H. Noble, R. H. Gifford, B. M. Dawant, B. P. O'Connell, J. Wang, and R. F. Labadie, "Further Evidence of the Relationship Between Cochlear Implant Electrode Positioning and Hearing Outcomes", *Otology & neurotology : official publication of the American Otological Society, American Neurotology Society [and] European Academy of Otology and Neurotology*, vol. 40, no. 5, pp. 617–624, Jun. 2019, ISSN: 15374505. DOI: 10.1097/MAO.0000000000002204.

[31] M. W. El-Anwar, A. S. Elaassar, and Y. A. Foad, "Non-mastoidectomy cochlear implant approaches: A literature review", *International Archives of Otorhinolaryngology*, vol. 20, no. 2, pp. 180–184, Apr. 2016, ISSN: 18094864. DOI: 10.1055/s-0035-1558871. [Online]. Available: http://dx.doi.org/.

[32] R. F. Labadie, R. Balachandran, J. H. Noble, G. S. Blachon, J. E. Mitchell, F. A. Reda, B. M. Dawant, and J. M. Fitzpatrick, "Minimally invasive image-guided cochlear implantation surgery: First report of clinical implementation", *The Laryngoscope*, vol. 124, no. 8, pp. 1915–1922, Aug. 2014, ISSN: 0023852X. DOI: 10.1002/lary.24520. [Online]. Available: http://doi.wiley.com/10.1002/lary.24520.

[33] M. Caversaccio, K. Gavaghan, W. Wimmer, T. Williamson, J. Ansò, G. Mantokoudis, N. Gerber, C. Rathgeb, A. Feldmann, F. Wagner, O. Scheidegger, M. Kompis, C. Weisstanner, M. Zoka-Assadi, K. Roesler, L. Anschuetz, M. Huth, and S. Weber, "Robotic cochlear implantation: surgical procedure and first clinical experience", *Acta Oto-Laryngologica*, vol. 137, no. 4, pp. 447–454, Apr. 2017. DOI: 10.1080/00016489.2017.1278573. [Online].

Available: http://www.ncbi.nlm.nih.gov/pubmed/28145157%20https://www.tandfonline.com/doi/full/10.1080/00016489.2017.1278573.

[34] V. Topsakal, M. Matulic, M. Z. Assadi, G. Mertens, V. Van Rompaey, and P. Van de Heyning, "Comparison of the surgical techniques and robotic techniques for cochlear implantation in terms of the trajectories toward the inner ear", *Journal of International Advanced Otology*, vol. 16, no. 1, pp. 3–7, Apr. 2020, ISSN: 21483817. DOI: 10.5152/iao.2020.8113. [Online]. Available: https://www.ncbi.nlm.nih.gov/pmc/articles/PMC7224420/.

[35] J. P. Kobler, K. Nuelle, G. J. Lexow, T. S. Rau, O. Majdani, L. A. Kahrs, J. Kotlarski, and T. Ortmaier, "Configuration optimization and experimental accuracy evaluation of a bone-attached, parallel robot for skull surgery", *International Journal of Computer Assisted Radiology and Surgery*, vol. 11, no. 3, pp. 421–436, Mar. 2016, ISSN: 18616429. DOI: 10.1007/s11548-015-1300-4.

[36] L. B. Kratchman, G. S. Blachon, T. J. Withrow, R. Balachandran, R. F. Labadie, and R. J. Webster, "Design of a bone-attached parallel robot for percutaneous cochlear implantation", *IEEE Transactions on Biomedical Engineering*, vol. 58, no. 10 PART 1, pp. 2904–2910, Oct. 2011, ISSN: 00189294. DOI: 10.1109/TBME.2011.2162512.

[37] S. Baron, H. Eilers, B. Munske, J. L. Toennies, R. Balachandran, R. F. Labadie, T. Ortmaier, and R. J. Webster, "Percutaneous inner-ear access via an image-guided industrial robot system", *Proceedings of the Institution of Mechanical Engineers, Part H: Journal of Engineering in Medicine*, vol. 224, no. 5, pp. 633–649, May 2010, ISSN: 09544119. DOI: 10.1243/09544119JEIM781.

[38] O. Majdani, T. S. Rau, S. Baron, H. Eilers, C. Baier, B. Heimann, T. Ortmaier, S. Bartling, T. Lenarz, and M. Leinung, "A robot-guided minimally invasive approach for cochlear implant surgery: preliminary results of a temporal bone study", *International Journal of Computer Assisted Radiology and Surgery*, vol. 4, no. 5, pp. 475–486, Sep. 2009. DOI:

10.1007/s11548-009-0360-8. [Online]. Available: http://link.springer.com/10.1007/s11548-009-0360-8%20http://www.ncbi.nlm.nih.gov/pubmed/20033531.

[39] S. Duret, C. Guigou, M. Grelat, and A. Bozorg-Grayeli, "Minimally Invasive Cochlear Implantation Assisted by Intraoperative CT Scan Combined to Neuronavigation", *Otology & Neurotology*, vol. 41, no. 4, e441–e448, Apr. 2020, ISSN: 1531-7129. DOI: 10.1097/MAO.0000000000002577. [Online]. Available: http://journals.lww.com/10.1097/MAO.0000000000002577.

[40] M. Caversaccio, W. Wimmerid, J. Ansoid, G. Mantokoudis, N. Gerber, C. Rathgeb, D. Schneider, J. Hermann, F. Wagnerid, O. Scheideggerid, M. Huth, L. Anschuetz, M. Kompis, T. Williamson, B. Bell, K. Gavaghan, and S. Weber, "Robotic middle ear access for cochlear implantation: First in man", *PLOS ONE*, 2019. DOI: 10.1371/journal.pone.0220543. [Online]. Available: https://doi.org/10.1371/journal.pone.0220543.t001.

[41] S. Günther, U. Baumann, and T. Stöver, "Early Fitting in Cochlear Implantation", *Otology & Neurotology*, vol. 39, no. 4, e250–e256, Apr. 2018, ISSN: 1531-7129. DOI: 10.1097/MAO.0000000000001745. [Online]. Available: http://journals.lww.com/00129492-201804000-00010.

[42] K. E. Riojas, N. Narasimhan, W. G. Morrel, J. Mitchell, T. Bruns, R. J. Webster, and R. F. Labadie, "A new manual insertion tool for minimally invasive, image-guided cochlear implant surgery", in *Medical Imaging 2019: Image-Guided Procedures, Robotic Interventions, and Modeling*, B. Fei and C. A. Linte, Eds., SPIE, Mar. 2019, p. 18, ISBN: 9781510625495. DOI: 10.1117/12.2512471. [Online]. Available: https://www.spiedigitallibrary.org/conference-proceedings-of-spie/10951/2512471/A-new-manual-insertion-tool-for-minimally-invasive-image-guided/10.1117/12.2512471.full.

[43] E. Lehnhardt, "Intracochlear placement of cochlear implant electrodes in soft surgery technique", *HNO*, vol. 41, no. 7, pp. 356–359, Jul. 1993, ISSN: 00176192. [Online]. Available: https://europepmc.org/article/med/8376183.

[44] F. Risi, "Considerations and rationale for cochlear implant electrode design-past, present and future", *Journal of International Advanced Otology*, vol. 14, no. 3, pp. 382–391, Dec. 2018, ISSN: 21483817. DOI: 10.5152/iao.2018.6372.

[45] A. Dalbert, A. Huber, N. Baumann, D. Veraguth, C. Roosli, and F. Pfiffner, "Hearing Preservation After Cochlear Implantation May Improve Long-term Word Perception in the Electric-only Condition", *Otology & Neurotology*, vol. 37, no. 9, pp. 1314–1319, Oct. 2016, ISSN: 1531-7129. DOI: 10.1097/MAO.0000000000001193. [Online]. Available: https://journals.lww.com/00129492-201610000-00018.

[46] Y. Nguyen, M. Miroir, G. Kazmitcheff, J. Sutter, M. Bensidhoum, E. Ferrary, O. Sterkers, and A. Bozorg Grayeli, "Cochlear implant insertion forces in microdissected human cochlea to evaluate a prototype array", *Audiology and Neurotology*, vol. 17, no. 5, pp. 290–298, Aug. 2012, ISSN: 14203030. DOI: 10.1159/000338406.

[47] M. Mirsalehi, T. S. Rau, L. Harbach, S. Hügl, S. Mohebbi, T. Lenarz, and O. Majdani, "Insertion forces and intracochlear trauma in temporal bone specimens implanted with a straight atraumatic electrode array", *European Archives of Oto-Rhino-Laryngology*, vol. 274, no. 5, pp. 2131–2140, May 2017, ISSN: 0937-4477. DOI: 10.1007/s00405-017-4485-z. [Online]. Available: http://link.springer.com/10.1007/s00405-017-4485-z.

[48] D. De Seta, R. Torres, F. Y. Russo, E. Ferrary, G. Kazmitcheff, D. Heymann, J. Amiaud, O. Sterkers, D. Bernardeschi, and Y. Nguyen, "Damage to inner ear structure during cochlear implantation: Correlation between insertion force and radio-histological findings in temporal bone specimens", *Hearing Research*, vol. 344, pp. 90–97, Feb. 2017, ISSN: 18785891. DOI: 10.1016/j.heares.2016.11.002.

[49] J. T. Roland, "A Model for Cochlear Implant Electrode Insertion and Force Evaluation: Results with a New Electrode Design and Insertion Technique", vol. 115, no. 8, pp. 1325–1339, Aug. 2005. DOI: 10.1097/01.mlg.0000167993.05007.35. [Online]. Available: http://doi.wiley.com/10.1097/01.mlg.0000167993.05007.35.

[50] O. Majdani, D. Schurzig, A. Hussong, T. Rau, J. Wittkopf, T. Lenarz, and R. F. Labadie, "Force measurement of insertion of cochlear implant electrode arrays in vitro: comparison of surgeon to automated insertion tool", *Acta Oto-Laryngologica*, vol. 130, no. 1, pp. 31–36, Jan. 2010, ISSN: 0001-6489. DOI: 10.3109/00016480902998281. [Online]. Available: http://www.tandfonline.com/doi/full/10.3109/00016480902998281.

[51] D. Schurzig, R. J. Webster, M. S. Dietrich, R. F. Labadie, and R. F. Labadie, "Force of cochlear implant electrode insertion performed by a robotic insertion tool: comparison of traditional versus Advance Off-Stylet techniques.", *Otology & Neurotology*, vol. 31, no. 8, pp. 1207–10, Oct. 2010, ISSN: 1537-4505. DOI: 10.1097/MAO.0b013e3181f2ebc3. [Online]. Available: http://www.ncbi.nlm.nih.gov/pubmed/20814345%20http://www.pubmedcentral.nih.gov/articlerender.fcgi?artid=PMC4104130.

[52] S. Helbig, C. Settevendemie, M. Mack, U. Baumann, M. Helbig, and T. Stöver, "Evaluation of an Electrode Prototype for Atraumatic Cochlear Implantation in Hearing Preservation Candidates", *Otology & Neurotology*, vol. 32, no. 3, pp. 419–423, Apr. 2011, ISSN: 1531-7129. DOI: 10.1097/MAO.0b013e31820e75d9. [Online]. Available: http://journals.lww.com/00129492-201104000-00010.

[53] R. J. S. Briggs, M. Tykocinski, R. Lazsig, A. Aschendorff, T. Lenarz, T. Stöver, B. Fraysse, M. Marx, J. T. Roland, P. S. Roland, C. G. Wright, B. J. Gantz, J. F. Patrick, and F. Risi, "Development and evaluation of the modiolar research array – multi-centre collaborative study in human temporal bones", *Cochlear Implants International*, vol. 12, no. 3, pp. 129–139, Aug. 2011, ISSN: 1467-0100. DOI: 10.1179/1754762811Y0000000007. [Online]. Available: http://www.tandfonline.com/doi/full/10.1179/1754762811Y0000000007.

[54] M. Miroir, Y. Nguyen, G. Kazmitcheff, E. Ferrary, O. Sterkers, and A. B. Grayeli, "Friction force measurement during cochlear implant insertion: Application to a force-controlled insertion tool design", *Otology and Neurotology*, vol. 33, no. 6, pp. 1092–1100, Jul. 2012, ISSN: 15317129. DOI: 10.1097/MAO.0b013e31825f24de. [Online]. Available: http://

content.wkhealth.com/linkback/openurl?sid=WKPTLP:landingpage&an=00129492-900000000-98550.

[55] J. P. Kobler, D. Beckmann, T. S. Rau, O. Majdani, and T. Ortmaier, "An automated insertion tool for cochlear implants with integrated force sensing capability", *International Journal of Computer Assisted Radiology and Surgery*, vol. 9, no. 3, pp. 481–494, Aug. 2014, ISSN: 18616429. DOI: 10.1007/s11548-013-0936-1. [Online]. Available: https://link.springer.com/article/10.1007/s11548-013-0936-1.

[56] Y. Nguyen, G. Kazmitcheff, D. D. Seta, M. Miroir, E. Ferrary, and O. Sterkers, "Definition of Metrics to Evaluate Cochlear Array Insertion Forces Performed with Forceps, Insertion Tool, or Motorized Tool in Temporal Bone Specimens", *BioMed Research International*, vol. 2014, 2014. DOI: 10.1155/2014/532570.

[57] P. Rohani, J. Pile, L. A. Kahrs, R. Balachandran, G. S. Blachon, N. Simaan, and R. F. Labadie, "Forces and trauma associated with minimally invasive image-guided cochlear implantation", in *Otolaryngology - Head and Neck Surgery (United States)*, vol. 150, Mosby Inc., Apr. 2014, pp. 638–645. DOI: 10.1177/0194599813519747. [Online]. Available: http://journals.sagepub.com/doi/10.1177/0194599813519747.

[58] T. Ishii, M. Takayama, and Y. Takahashi, "Mechanical properties of human round window, basilar and reissner's membranes", *Acta Oto-Laryngologica*, vol. 115, no. S519, pp. 78–82, 1995, ISSN: 00016489. DOI: 10.3109/00016489509121875. [Online]. Available: https://www.tandfonline.com/doi/abs/10.3109/00016489509121875.

[59] D. Schuster, L. B. Kratchman, and R. F. Labadie, "Characterization of intracochlear rupture forces in fresh human cadaveric cochleae", *Otology and Neurotology*, vol. 36, no. 4, pp. 657–661, Apr. 2015, ISSN: 15374505. DOI: 10.1097/MAO.0000000000000573. [Online]. Available: http://www.ncbi.nlm.nih.gov/pubmed/25233332%20http://www.pubmedcentral.nih.gov/articlerender.fcgi?artid=PMC4359032.

[60] L. B. Kratchman, D. Schuster, M. S. Dietrich, and R. F. Labadie, "Force Perception Thresholds in Cochlear Implantation Surgery", *Audiology and Neurotology*, vol. 21, no. 4, pp. 244–249, Oct. 2016. DOI: 10.1159/000445736. [Online]. Available: https://www.karger.com/Article/FullText/445736.

[61] K. Kesler, N. P. Dillon, L. Fichera, and R. F. Labadie, "Human Kinematics of Cochlear Implant Surgery: An Investigation of Insertion Micro-Motions and Speed Limitations", vol. 157, no. 3, pp. 493–498, Sep. 2017. DOI: 10.1177/0194599817704391. [Online]. Available: http://journals.sagepub.com/doi/10.1177/0194599817704391.

[62] S. Vittoria, G. Lahlou, R. Torres, H. Daoudi, I. Mosnier, S. Mazalaigue, E. Ferrary, Y. Nguyen, and O. Sterkers, "Robot-based assistance in middle ear surgery and cochlear implantation: first clinical report", *European Archives of Oto-Rhino-Laryngology*, May 2020, ISSN: 0937-4477. DOI: 10.1007/s00405-020-06070-z. [Online]. Available: http://link.springer.com/10.1007/s00405-020-06070-z.

[63] B. M. Verbist, M. W. Skinner, L. T. Cohen, P. A. Leake, C. James, C. Boëx, T. A. Holden, C. C. Finley, P. S. Roland, J. T. Roland, M. Haller, J. F. Patrick, C. N. Jolly, M. A. Faltys, J. J. Briaire, and J. H. Frijns, "Consensus panel on a cochlear coordinate system applicable in histologic, physiologic, and radiologic studies of the human cochlea", *Otology and Neurotology*, vol. 31, no. 5, pp. 722–730, Jul. 2010, ISSN: 15317129. DOI: 10.1097/MAO.0b013e3181d279e0. [Online]. Available: /pmc/articles/PMC2945386/?report=abstract%20https://www.ncbi.nlm.nih.gov/pmc/articles/PMC2945386/.

[64] E. Avci, T. Nauwelaers, V. Hamacher, and A. Kral, "Three-Dimensional Force Profile During Cochlear Implantation Depends on Individual Geometry and Insertion Trauma.", *Ear and Hearing*, vol. 38, no. 3, e168–e179, May 2017, ISSN: 1538-4667. DOI: 10.1097/AUD.0000000000000394. [Online]. Available: http://www.ncbi.nlm.nih.gov/pubmed/28045786.

[65] A. A. Eshraghi, N. W. Yang, and T. J. Balkany, "Comparative Study of Cochlear Damage With Three Perimodiolar Electrode Designs", *The Laryngoscope*, vol. 113, no. 3, pp. 415–419, Mar. 2003, ISSN: 0023-852X. DOI: 10.1097/00005537-200303000-00005. [Online]. Available: http://doi.wiley.com/10.1097/00005537-200303000-00005.

[66] J. Gabrielpillai, I. Burck, U. Baumann, T. Stöver, and S. Helbig, "Incidence for Tip Foldover During Cochlear Implantation", *Otology & Neurotology*, vol. 39, no. 9, pp. 1115–1121, Oct. 2018, ISSN: 1531-7129. DOI: 10.1097/MAO.0000000000001915. [Online]. Available: http://journals.lww.com/00129492-201810000-00009.

[67] M. G. Zuniga, A. Rivas, A. Hedley-Williams, R. H. Gifford, R. Dwyer, B. M. Dawant, L. W. Sunderhaus, K. L. Hovis, G. B. Wanna, J. H. Noble, and R. F. Labadie, "Tip fold-over in cochlear implantation: Case series", *Otology and Neurotology*, vol. 38, no. 2, pp. 199–206, 2017, ISSN: 15374505. DOI: 10.1097/MAO.0000000000001283. [Online]. Available: /pmc/articles/PMC5584995/?report=abstract%20https://www.ncbi.nlm.nih.gov/pmc/articles/PMC5584995/.

[68] J. R. Clark, L. Leon, F. M. Warren, and J. J. Abbott, "Magnetic Guidance of Cochlear Implants: Proof-of-Concept and Initial Feasibility Study", *Journal of Medical Devices, Transactions of the ASME*, vol. 6, no. 3, Aug. 2012, ISSN: 19326181. DOI: 10.1115/1.4007099.

[69] W. Gstoettner, P. Franz, J. Hamzavi, H. Plenk, W. Baumgartner, and C. Czerny, "Intracochlear position of cochlear implant electrodes", *Acta Oto-Laryngologica*, vol. 119, no. 2, pp. 229–233, Mar. 1999, ISSN: 00016489. DOI: 10.1080/00016489950181729. [Online]. Available: https://www.tandfonline.com/doi/abs/10.1080/00016489950181729.

[70] B. P. O'Connell, J. B. Hunter, D. S. Haynes, J. T. Holder, M. M. Dedmon, J. H. Noble, B. M. Dawant, and G. B. Wanna, "Insertion depth impacts speech perception and hearing preservation for lateral wall electrodes", *The Laryngoscope*, vol. 127, no. 10, pp. 2352–

2357, Oct. 2017, ISSN: 0023852X. DOI: 10.1002/lary.26467. [Online]. Available: http://doi.wiley.com/10.1002/lary.26467.

[71] A. N. Badi, T. R. Kertesz, R. K. Gurgel, C. Shelton, and R. A. Normann, "Development of a Novel Eighth-Nerve Intraneural Auditory Neuroprosthesis", *The Laryngoscope*, vol. 113, no. 5, pp. 833–842, May 2003, ISSN: 0023-852X. DOI: 10.1097/00005537-200305000-00012. [Online]. Available: http://doi.wiley.com/10.1097/00005537-200305000-00012.

[72] D. M. Landsberger, M. Padilla, and A. G. Srinivasan, "Reducing current spread using current focusing in cochlear implant users", *Hearing Research*, vol. 284, no. 1-2, pp. 16–24, Feb. 2012, ISSN: 03785955. DOI: 10.1016/j.heares.2011.12.009. [Online]. Available: https://pubmed.ncbi.nlm.nih.gov/22230370/.

[73] J. A. Bierer and L. Litvak, "Reducing Channel Interaction Through Cochlear Implant Programming May Improve Speech Perception", in *Trends in Hearing*, vol. 20, SAGE Publications Inc., Jan. 2016, p. 233 121 651 665 338. DOI: 10.1177/2331216516653389. [Online]. Available: http://journals.sagepub.com/doi/10.1177/2331216516653389.

[74] M. Padilla and D. M. Landsberger, "Reduction in spread of excitation from current focusing at multiple cochlear locations in cochlear implant users", *Hearing Research*, vol. 333, pp. 98–107, Mar. 2016, ISSN: 18785891. DOI: 10.1016/j.heares.2016.01.002.

[75] A. Hussong, T. Rau, H. Eilers, S. Baron, B. Heimann, M. Leinung, T. Lenarz, and O. Majdani, "Conception and design of an automated insertion tool for cochlear implants", in *IEEE Engineering in Medicine and Biology Society*, vol. 2008, IEEE, Aug. 2008, pp. 5593–5596. [Online]. Available: http://www.ncbi.nlm.nih.gov/pubmed/19163985%20http://ieeexplore.ieee.org/document/4650482/.

[76] J. Zhang, W. Wei, J. Ding, J. Thomas Roland, S. Manolidis, N. Simaan, J. T. Roland, S. Manolidis, and N. Simaan, "Inroads Toward Robot-Assisted Cochlear Implant Surgery Using Steerable Electrode Arrays", *Otology & Neurotology*, vol. 31, no. 8, pp. 1199–1206,

Oct. 2010, ISSN: 1531-7129. DOI: 10.1097/MAO.0b013e3181e7117e. [Online]. Available: https://insights.ovid.com/crossref?an=00129492-201010000-00006.

[77] J. Pile and N. Simaan, "Modeling, Design, and Evaluation of a Parallel Robot for Cochlear Implant Surgery", *IEEE/ASME Transactions on Mechatronics*, vol. 19, no. 6, pp. 1746–1755, Dec. 2014. DOI: 10.1109/TMECH.2014.2308479. [Online]. Available: http://ieeexplore.ieee.org/document/6775343/.

[78] J. Pile, "Wire-Actuated Parallel Robots for Cochlear Implantation With In-Vivo Sensory Feedback", PhD thesis, Vanderbilt University, 2015.

[79] S. Barriat, N. Peigneux, U. Duran, S. Camby, and P. P. Lefebvre, "The Use of a Robot to Insert an Electrode Array of Cochlear Implants in the Cochlea: A Feasibility Study and Preliminary Results", *Audiology and Neurotology*, pp. 1–7, 2021, ISSN: 14219700. DOI: 10.1159/000513509.

[80] T. S. Rau, M. G. Zuniga, R. Salcher, and T. Lenarz, "A simple tool to automate the insertion process in cochlear implant surgery", *International Journal of Computer Assisted Radiology and Surgery*, vol. 15, no. 11, pp. 1931–1939, Aug. 2020, ISSN: 18616429. DOI: 10.1007/s11548-020-02243-7. [Online]. Available: https://doi.org/10.1007/s11548-020-02243-7.

[81] C. R. Kaufmann, A. M. Henslee, A. Claussen, and M. R. Hansen, "Evaluation of Insertion Forces and Cochlea Trauma Following Robotics-Assisted Cochlear Implant Electrode Array Insertion", *Otology & Neurotology*, vol. 41, no. 5, pp. 631–638, Feb. 2020, ISSN: 1531-7129. DOI: 10.1097/mao.0000000000002608.

[82] B. Gantz, "First Clinical Experience with Robotics-assisted Insertion of Cochlear Implant Electrode Arrays", in *American Cochlear Implant Alliance*, 2021.

[83] C.-T. Tan, M. Svirsky, A. Anwar, S. Kumar, B. Caessens, P. Carter, C. Treaba, and J. T. Roland, "Real-time measurement of electrode impedance during intracochlear electrode

insertion", *Laryngoscope*, vol. 123, no. 4, pp. 1028–1032, Apr. 2013, ISSN: 0023852X. DOI: 10.1002/lary.23714.

[84] J. Zhang, K. Xu, N. Simaan, and S. Manolidis, "A Pilot Study of Robot-Assisted Cochlear Implant Surgery Using Steerable Electrode Arrays", in *INTERNATIONAL CONFERENCE ON MEDICAL IMAGE COMPUTING & COMPUTER ASSISTED INTERVENTION*, 2006, pp. 33–40. DOI: 10.1007/11866565{_}5. [Online]. Available: http://link.springer.com/10.1007/11866565_5.

[85] M. G. Zuniga, N. Suzaly, T. Lenarz, and T. S. Rau, "On the stiffness properties of custom-made silicone dummies for the development of cochlear implant electrode arrays with a shape memory wire", in *Laryngo-Rhino-Otologie*, vol. 99, © Georg Thieme Verlag KG, May 2020. DOI: 10.1055/s-0040-1711173. [Online]. Available: http://www.thieme-connect.de/DOI/DOI?10.1055/s-0040-1711173.

[86] T. L. Bruns*, K. E. Riojas*, D. S. Ropella, M. S. Cavilla, A. J. Petruska, M. H. Freeman, R. F. Labadie, J. J. Abbott, and R. J. Webster, "Magnetically Steered Robotic Insertion of Cochlear-Implant Electrode Arrays: System Integration and First-In-Cadaver Results", *IEEE Robotics and Automation Letters*, vol. 5, no. 2, pp. 2240–2247, Apr. 2020, ISSN: 23773766. DOI: 10.1109/LRA.2020.2970978.

[87] B. P. O'Connell, J. B. Hunter, and G. B. Wanna, "The importance of electrode location in cochlear implantation", *Laryngoscope Investigative Otolaryngology*, vol. 1, no. 6, pp. 169–174, Dec. 2016, ISSN: 23788038. DOI: 10.1002/lio2.42. [Online]. Available: http://doi.wiley.com/10.1002/lio2.42.

[88] C. K. Giardina, E. S. Krause, K. Koka, and D. C. Fitzpatrick, "Impedance Measures During in vitro Cochlear Implantation Predict Array Positioning", *IEEE Transactions on Biomedical Engineering*, vol. 65, no. 2, pp. 327–335, Feb. 2018, ISSN: 0018-9294. DOI: 10.1109/TBME.2017.2764881. [Online]. Available: http://ieeexplore.ieee.org/document/8078256/.

[89] R. F. Labadie, A. D. Schefano, J. T. Holder, R. T. Dwyer, A. Rivas, M. R. O'malley, J. H. Noble, and B. M. Dawant, "Use of intraoperative CT scanning for quality control assessment of cochlear implant electrode array placement", *Acta Oto-Laryngologica*, vol. 140, no. 3, pp. 206–211, 2020, ISSN: 0001-6489. DOI: 10.1080/00016489.2019.1698768. [Online]. Available: https://www.tandfonline.com/action/journalInformation?journalCode=ioto20.

[90] C. Perazzini, M. Puechmaille, N. Saroul, O. Plainfossé, L. Montrieul, J. Bécaud, L. Gilain, P. Chabrot, L. Boyer, and T. Mom, "Fluoroscopy guided electrode-array insertion for cochlear implantation with straight electrode-arrays: a valuable tool in most cases", *European Archives of Oto-Rhino-Laryngology*, vol. 1, p. 3, Jun. 2020, ISSN: 14344726. DOI: 10.1007/s00405-020-06151-z. [Online]. Available: https://doi.org/10.1007/s00405-020-06151-z.

[91] "Clinical Practice Guidelines: Cochlear Implants", Tech. Rep., 2019.

[92] A. M. Nassiri, R. J. Yawn, R. H. Gifford, D. S. Haynes, J. B. Roberts, M. S. Gilbane, J. Murfee, and M. L. Bennett, "Intraoperative electrically evoked compound action potential (ECAP) measurements in traditional and hearing preservation cochlear implantation", *Journal of the American Academy of Audiology*, vol. 30, no. 10, pp. 918–926, 2019, ISSN: 21573107. DOI: 10.3766/jaaa.18052.

[93] C. A. Miller, C. J. Brown, P. J. Abbas, and S. L. Chi, "The clinical application of potentials evoked from the peripheral auditory system", *Hearing Research*, vol. 242, no. 1-2, pp. 184–197, Aug. 2008, ISSN: 03785955. DOI: 10.1016/j.heares.2008.04.005. [Online]. Available: https://pubmed.ncbi.nlm.nih.gov/18515023/.

[94] P. Mittmann, A. Ernst, and I. Todt, "Intraoperative Electrophysiologic Variations Caused by the Scalar Position of Cochlear Implant Electrodes", *Otology and Neurotology*, vol. 36, no. 6, pp. 1010–1014, Jul. 2015, ISSN: 15374505. DOI: 10.1097/MAO.0000000000000736.

[95] T. J. Davis, D. Zhang, R. H. Gifford, B. M. Dawant, R. F. Labadie, and J. H. Noble, "Relationship between electrode-To-modiolus distance and current levels for adults with cochlear implants", *Otology and Neurotology*, vol. 37, no. 1, pp. 31–37, 2016, ISSN: 15374505. DOI: 10.1097/MAO.0000000000000896. [Online]. Available: /pmc/articles/PMC4675044/?report=abstract%20https://www.ncbi.nlm.nih.gov/pmc/articles/PMC4675044/.

[96] M. S. Harris, W. J. Riggs, K. Koka, L. M. Litvak, P. Malhotra, A. C. Moberly, B. P. O'Connell, J. Holder, F. A. Di Lella, C. M. Boccio, G. B. Wanna, R. F. Labadie, and O. F. Adunka, "Real-Time Intracochlear Electrocochleography Obtained Directly Through a Cochlear Implant", *Otology and Neurotology*, vol. 38, no. 6, e107–e113, Jul. 2017, ISSN: 15374505. DOI: 10.1097/MAO.0000000000001425.

[97] J. Lo, C. Bester, A. Collins, C. Newbold, A. Hampson, S. Chambers, H. Eastwood, and S. O'Leary, "Intraoperative force and electrocochleography measurements in an animal model of cochlear implantation", *Hearing Research*, vol. 358, pp. 50–58, Feb. 2018, ISSN: 18785891. DOI: 10.1016/j.heares.2017.11.001.

[98] W. P. Gibson, "The clinical uses of electrocochleography", *Frontiers in Neuroscience*, vol. 11, no. MAY, May 2017, ISSN: 1662453X. DOI: 10.3389/fnins.2017.00274.

[99] S. Haumann, M. Imsiecke, G. Bauernfeind, A. Büchner, V. Helmstaedter, T. Lenarz, and R. B. Salcher, "Monitoring of the Inner Ear Function During and After Cochlear Implant Insertion Using Electrocochleography", *Trends in Hearing*, vol. 23, Mar. 2019, ISSN: 23312165. DOI: 10.1177/2331216519833567.

[100] E. M. C. Trecca, W. J. Riggs, J. K. Mattingly, M. M. Hiss, M. Cassano, and O. F. Adunka, "Electrocochleography and Cochlear Implantation: A Systematic Review", *Otology & Neurotology*, vol. 41, no. 7, pp. 864–878, Aug. 2020, ISSN: 1531-7129. DOI: 10.1097/MAO.0000000000002694. [Online]. Available: https://journals.lww.com/10.1097/MAO.0000000000002694.

[101] K. Koka, W. J. Riggs, R. Dwyer, J. T. Holder, J. H. Noble, B. M. Dawant, A. Ortmann, C. V. Valenzuela, J. K. Mattingly, M. M. Harris, B. P. O'Connell, L. M. Litvak, O. F. Adunka, C. A. Buchman, and R. F. Labadie, "Intra-Cochlear Electrocochleography During Cochear Implant Electrode Insertion Is Predictive of Final Scalar Location", *Otology & Neurotology*, vol. 39, no. 8, e654–e659, Sep. 2018, ISSN: 15374505. DOI: 10.1097/MAO.0000000000001906. [Online]. Available: /pmc/articles/PMC6097527/?report=abstract%20https://www.ncbi.nlm.nih.gov/pmc/articles/PMC6097527/.

[102] S. R. de Rijk, Y. C. Tam, R. P. Carlyon, and M. L. Bance, "Detection of Extracochlear Electrodes in Cochlear Implants with Electric Field Imaging/Transimpedance Measurements", *Ear & Hearing*, vol. Publish Ah, no. Ci, pp. 1–12, 2020, ISSN: 0196-0202. DOI: 10.1097/aud.0000000000000837.

[103] H. Watanabe, "Unconventional Neural interface Intravascular Neural Interface and Electrochemical Endoscopy for Cochlear Implant", PhD thesis, New York University, 2012, ISBN: 9785984520973.

[104] J. Pile, A. D. Sweeney, S. Kumar, N. Simaan, and G. B. Wanna, "Detection of modiolar proximity through bipolar impedance measurements", *Laryngoscope*, vol. 127, no. 6, pp. 1413–1419, Jun. 2017, ISSN: 15314995. DOI: 10.1002/lary.26183.

[105] M. Tykocinski, L. T. Cohen, and R. S. Cowan, "Measurement and analysis of access resistance and polarization impedance in cochlear implant recipients", *Otology and Neurotology*, vol. 26, no. 5, pp. 948–956, Sep. 2005, ISSN: 15317129. DOI: 10.1097/01.mao.0000185056.99888.f3.

[106] L. Hou, "The Feasibility of a Novel Sensing System for Robotic Cochlear Electrode Array Feed for Hearing Preservation", PhD thesis, Brunel University London, 2019.

[107] L. B. Kratchman, D. Schurzig, T. R. McRackan, R. Balachandran, J. H. Noble, R. J. Webster, and R. F. Labadie, "A manually operated, advance off-stylet insertion tool for minimally invasive cochlear implantation surgery", *IEEE Transactions on Biomedical Engi-*

neering, vol. 59, no. 10, pp. 2792–2800, 2012, ISSN: 00189294. DOI: 10.1109/TBME.2012.2210220. [Online]. Available: http://ieeexplore.ieee.org..

[108] J. H. Noble, O. Majdani, R. F. Labadie, B. Dawant, and J. M. Fitzpatrick, "Automatic determination of optimal linear drilling trajectories for cochlear access accounting for drill-positioning error", *The International Journal of Medical Robotics and Computer Assisted Surgery*, vol. 6, no. 3, pp. 281–290, Sep. 2010, ISSN: 14785951. DOI: 10.1002/rcs.330. [Online]. Available: http://doi.wiley.com/10.1002/rcs.330.

[109] H. Ajieren, R. Reit, R. Lee, T. Pham, D. Shao, K. Lee, and W. Voit, "Robotic Insertion Aid for Self-Coiling Cochlear Implants", in *MRS Advances*, vol. 1, Materials Research Society, 2016, pp. 51–56. DOI: 10.1557/adv.2016.71.

[110] J. Granna, T. S. Rau, T.-D. Nguyen, T. Lenarz, O. Majdani, and J. Burgner-Kahrs, "Toward automated cochlear implant insertion using tubular manipulators", in *Medical Imaging 2016: Image-Guided Procedures, Robotic Interventions, and Modeling*, vol. 9786, SPIE, Mar. 2016, 97861F, ISBN: 9781510600218. DOI: 10.1117/12.2216854.

[111] P. Aebischer, S. Meyer, M. Caversaccio, and W. Wimmer, "Intraoperative Impedance-Based Estimation of Cochlear Implant Electrode Array Insertion Depth", *IEEE Transactions on Biomedical Engineering*, pp. 1–1, Jul. 2020, ISSN: 0018-9294. DOI: 10.1109/tbme.2020.3006934.

[112] N. Narasimhan, K. E. Riojas, T. L. Bruns, J. E. Mitchell, R. J. Webster, and R. F. Labadie, "A Simple Manual Roller Wheel Insertion Tool for Electrode Array Insertion in Minimally Invasive Cochlear Implant Surgery", in *Design of Medical Devices Conference Proceedings*, American Society of Mechanical Engineers Digital Collection, Apr. 2019, p. 3249. DOI: 10.1115/dmd2019-3249.

[113] R. F. Labadie, K. Riojas, K. Von Wahlde, J. Mitchell, T. Bruns, R. Webster 3rd, B. Dawant, J. M. Fitzpatrick, and J. Noble, "Clinical Implementation of Second-generation Minimally

Invasive Image-guided Cochlear Implantation Surgery", *Otology & Neurotology*, vol. 42, no. 5, pp. 702–705, 2021.

[114] K. E. Riojas, E. T. Tran, M. H. Freeman, J. H. Noble, R. J. Webster, and R. F. Labadie, "Clinical Translation of an Insertion Tool for Minimally Invasive Cochlear Implant Surgery", *Journal of Medical Devices, Transactions of the ASME*, vol. 15, no. 3, Sep. 2021, ISSN: 1932619X. DOI: 10.1115/1.4050203. [Online]. Available: https://pubmed.ncbi.nlm.nih.gov/33995757/.

[115] W. G. Morrel, K. E. Riojas, R. Webster III, J. H. Noble, and R. F. Labadie, "Custom mastoid-fitting templates to improve cochlear implant electrode insertion trajectory", *International Journal of Computer Assisted Radiology and Surgery*, 2020. DOI: 10.1007/s11548-020-02193-0. [Online]. Available: https://doi.org/10.1007/s11548-020-02193-0.

[116] *What Are Cochlear Implants for Hearing? | NIDCD*. [Online]. Available: https://www.nidcd.nih.gov/health/cochlear-implants.

[117] T. S. Rau, S. Witte, L. Uhlenbusch, G. J. Lexow, S. Hügl, L. A. Kahrs, O. Majdani, and T. Lenarz, "Minimally invasive mastoidectomy approach using a mouldable surgical targeting system. A proof of concept", *Current Directions in Biomedical Engineering*, vol. 4, no. 1, pp. 403–406, Sep. 2018, ISSN: 23645504. DOI: 10.1515/cdbme-2018-0096.

[118] L. Migirov, E. Dagan, and J. Kronenberg, "Suprameatal Approach for Cochlear Implantation in Children: Our Experience with 320 Cases", *Cochlear Implants International*, vol. 11, pp. 195–198, 2010, ISSN: 1467-0100. DOI: 10.1179/146701010X12671177818786. [Online]. Available: https://www.tandfonline.com/action/journalInformation?journalCode=ycii20.

[119] D. Marchioni, A. Grammatica, M. Alicandri-Ciufelli, E. Genovese, and L. Presutti, "Endoscopic cochlear implant procedure", *European Archives of Oto-Rhino-Laryngology*, vol. 271, no. 5, pp. 959–966, 2014, ISSN: 14344726. DOI: 10.1007/s00405-013-2490-4.

[120] R. Häusler, "Cochlear implantation without mastoidectomy: The pericanal electrode insertion technique", *Acta Oto-Laryngologica*, vol. 122, no. 7, pp. 715–719, 2002, ISSN: 00016489. DOI: 10.1080/00016480260349773.

[121] T. Kiratzidis, W. Arnold, and T. Iliades, "Veria Operation Updated I. The Trans-Canal Wall Cochlear Implantation", *Journal for Oto-Rhino-Laryngology, Head and Neck Surgery*, vol. 64, no. 6, pp. 406–412, 2002. DOI: 10.1159/000067578. [Online]. Available: www.karger.com/orl.

[122] P. Singhal, S. Nagaraj, N. Verma, A. Goyal, A. Keshri, K. K. Rajeev, S. Agarwal, and M. P. Sharma, "Modified Veria Technique for Cochlear Implantation by Postaural Approach", *Indian J Otolaryngol Head Neck Surg*, 2020. DOI: 10.1007/s12070-020-01895-w. [Online]. Available: https://doi.org/10.1007/s12070-020-01895-w.

[123] A. Hussong, T. S. Rau, T. Ortmaier, B. Heimann, T. Lenarz, and O. Majdani, "An automated insertion tool for cochlear implants: another step towards atraumatic cochlear implant surgery", *International Journal of Computer Assisted Radiology and Surgery*, vol. 5, no. 2, pp. 163–171, Mar. 2010. DOI: 10.1007/s11548-009-0368-0. [Online]. Available: http://link.springer.com/10.1007/s11548-009-0368-0.

[124] D. Schurzig, R. F. Labadie, A. Hussong, T. S. Rau, and R. J. Webster III, "Design of a Tool Integrating Force Sensing With Automated Insertion in Cochlear Implantation", *IEEE/ASME Transactions on Mechatronics*, vol. 17, no. 2, pp. 381–389, Apr. 2012, ISSN: 1083-4435. DOI: 10.1109/TMECH.2011.2106795. [Online]. Available: http://ieeexplore.ieee.org/document/5716675/.

[125] Fysh Dadd, Petr Gibson, Miroslaw Ackiewicz, etc, Peter Gibson, Miroslaw Mackiewicz, Katherine Meagher, Claudiu Treaba, Henry Hon Sang Tsu, and Desmond McCusker, *Cartridge for an Electrode Array Insertion Device*, Nov. 2016.

[126] J. H. Noble, B. M. Dawant, F. M. Warren, and R. F. Labadie, "Automatic identification and 3D rendering of temporal bone anatomy.", *Otology & Neurotology*, vol. 30, no. 4, pp. 436–

42, Jun. 2009, ISSN: 1537-4505. DOI: 10.1097/MAO.0b013e31819e61ed. [Online]. Available: http://www.ncbi.nlm.nih.gov/pubmed/19339909%20http://www.pubmedcentral.nih.gov/articlerender.fcgi?artid=PMC4437534.

[127] J. H. Noble, R. F. Labadie, O. Majdani, and B. M. Dawant, "Automatic segmentation of intracochlear anatomy in conventional CT", *IEEE Transactions on Biomedical Engineering*, vol. 58, no. 9, pp. 2625–2632, Sep. 2011, ISSN: 00189294. DOI: 10.1109/TBME.2011.2160262.

[128] J. H. Noble, R. H. Gifford, R. F. Labadie, and B. M. Dawant, "Statistical shape model segmentation and frequency mapping of cochlear implant stimulation targets in CT", in *International Conference on Medical Image Computing and Computer-Assisted Intervention*, vol. 15, Springer Verlag, 2012, pp. 421–428, ISBN: 9783642334177. DOI: 10.1007/978-3-642-33418-4{_}52.

[129] R. F. Labadie, J. Mitchell, R. Balachandran, and J. M. Fitzpatrick, "Customized, rapid-production microstereotactic table for surgical targeting: description of concept and in vitro validation", *International Journal of Computer Assisted Radiology and Surgery*, vol. 4, no. 3, pp. 273–280, May 2009, ISSN: 1861-6410. DOI: 10.1007/s11548-009-0292-3. [Online]. Available: http://www.ncbi.nlm.nih.gov/pubmed/20033593%20http://www.pubmedcentral.nih.gov/articlerender.fcgi?artid=PMC4425254%20http://link.springer.com/10.1007/s11548-009-0292-3.

[130] Formlabs, "Formlabs Application Guide: 3D Printing Surgical Guides with the Form 2", Tech. Rep. March, 2018.

[131] G. J. Lexow, M. Kluge, O. Majdani, T. Lenarz, and T. S. Rau, "Phantom-based evaluation method for surgical assistance devices in minimally invasive cochlear implantation", in *Medical Imaging 2017: Image-Guided Procedures, Robotic Interventions, and Modeling*, R. J. Webster and B. Fei, Eds., vol. 10135, International Society for Optics and Photonics,

Mar. 2017, 101352N. DOI: 10.1117/12.2254381. [Online]. Available: http://proceedings.spiedigitallibrary.org/proceeding.aspx?doi=10.1117/12.2254381.

[132] T. Williamson, K. Gavaghan, N. Gerber, S. Weder, L. Anschuetz, F. Wagner, C. Weisstanner, G. Mantokoudis, M. Caversaccio, and S. Weber, "Population Statistics Approach for Safety Assessment in Robotic Cochlear Implantation", *Otology and Neurotology*, vol. 38, no. 5, pp. 759–764, Jun. 2017, ISSN: 15374505. DOI: 10.1097/MAO.0000000000001357.

[133] K. Bhatia, K. P. Gibbin, T. P. Nikolopoulos, and G. M. O'Donoghue, "Surgical complications and their management in a series of 300 consecutive pediatric cochlear implantations", *Otology and Neurotology*, vol. 25, no. 5, pp. 730–739, 2004, ISSN: 15317129. DOI: 10.1097/00129492-200409000-00015.

[134] H. Eilers, S. Baron, T. Ortmaier, B. Heimann, C. Baier, T. S. Rau, M. Leinung, and O. Majdani, "Navigated, robot assisted drilling of a minimally invasive cochlear access", in *IEEE 2009 International Conference on Mechatronics*, 2009, ISBN: 9781424441952. DOI: 10.1109/ICMECH.2009.4957213.

[135] MEDEL, "Mi1200 SYNCHRONY Surgical Guideline", MED-EL, Tech. Rep., 2019.

[136] G. Grupe, G. Rademacher, S. Hofmann, A. Stratmann, P. Mittmann, S. Mutze, A. Ernst, and I. Todt, "Evaluation of Cochlear Implant Receiver Position and Its Temporal Changes", *Otology & Neurotology*, vol. 38, no. 10, e558–e562, Dec. 2017, ISSN: 1531-7129. DOI: 10.1097/MAO.0000000000001521. [Online]. Available: http://journals.lww.com/00129492-201712000-00061.

[137] C. M. Hendricks, M. S. Cavilla, D. E. Usevitch, T. L. Bruns, K. E. Riojas, L. Leon, R. J. Webster 3rd, F. M. Warren, and J. J. Abbott, "Magnetic Steering of Robotically Inserted Lateral-wall Cochlear-implant Electrode Arrays Reduces Forces on the Basilar Membrane In Vitro", *Otology & Neurotology*, 0.

[138] J. Pile and N. Simaan, "Characterization of friction and speed effects and methods for detection of cochlear implant electrode tip fold-over", in *Proceedings - IEEE International*

Conference on Robotics and Automation, 2013, pp. 4409–4414, ISBN: 9781467356411. DOI: 10.1109/ICRA.2013.6631202.

[139] R. Yasin, M. Dedmon, N. Dillon, and N. Simaan, "Investigating variability in cochlear implant electrode array alignment and the potential of visualization guidance", *The International Journal of Medical Robotics and Computer Assisted Surgery*, vol. 15, no. 6, Dec. 2019, ISSN: 1478-5951. DOI: 10.1002/rcs.2009. [Online]. Available: https://onlinelibrary.wiley.com/doi/abs/10.1002/rcs.2009.

[140] S. J. Rebscher, A. Hetherington, B. Bonham, P. Wardrop, D. Whinney, and P. A. Leake, "Considerations for design of future cochlear implant electrode arrays: electrode array stiffness, size, and depth of insertion.", *Journal of Rehabilitation Research and Development*, vol. 45, no. 5, pp. 731–47, 2008, ISSN: 1938-1352. [Online]. Available: http://www.ncbi.nlm.nih.gov/pubmed/18816423%20http://www.pubmedcentral.nih.gov/articlerender.fcgi?artid=PMC2562296.

[141] P. Mistrík, C. Jolly, D. Sieber, and I. Hochmair, "Challenging aspects of contemporary cochlear implant electrode array design", *World Journal of Otorhinolaryngology - Head and Neck Surgery*, vol. 3, no. 4, pp. 192–199, Dec. 2017, ISSN: 20958811. DOI: 10.1016/j.wjorl.2017.12.007.

[142] P. Wardrop, D. Whinney, S. J. Rebscher, J. T. Roland, W. Luxford, and P. A. Leake, "A temporal bone study of insertion trauma and intracochlear position of cochlear implant electrodes. I: Comparison of Nucleus banded and Nucleus Contour™ electrodes", *Hearing Research*, vol. 203, no. 1-2, pp. 54–67, May 2005, ISSN: 0378-5955. DOI: 10.1016/J.HEARES.2004.11.006. [Online]. Available: https://www.sciencedirect.com/science/article/pii/S0378595504003880.

[143] M. A. Somdas, P. M. Li, D. M. Whiten, D. K. Eddington, and J. B. Nadol Jr., "Quantitative Evaluation of New Bone and Fibrous Tissue in the Cochlea following Cochlear Implantation in the Human", *Audiology and Neurotology*, vol. 12, no. 5, pp. 277–284, Aug. 2007,

ISSN: 1420-3030. DOI: 10.1159/000103208. [Online]. Available: https://www.karger.com/Article/FullText/103208.

[144] K. A. Ryu, A.-R. Lyu, H. Park, J. W. Choi, G. M. Hur, and Y.-H. Park, "Intracochlear Bleeding Enhances Cochlear Fibrosis and Ossification: An Animal Study", *PLOS ONE*, vol. 10, no. 8, A. Y. W. Chang, Ed., e0136617, Aug. 2015, ISSN: 1932-6203. DOI: 10.1371/journal.pone.0136617. [Online]. Available: https://dx.plos.org/10.1371/journal.pone.0136617.

[145] J. Zhang, S. Bhattacharyya, and N. Simaan, "Model and Parameter Identification of Friction During Robotic Insertion of Cochlear-Implant Electrode Arrays", in *IEEE International Conference on Robotics and Automation*, 2009. [Online]. Available: http://research.vuse.vanderbilt.edu/arma/publications/JIan_icra09_published.pdf.

[146] J. Zhang, J. T. Roland, S. Manolidis, and N. Simaan, "Optimal Path Planning for Robotic Insertion of Steerable Electrode Arrays in Cochlear Implant Surgery", *Journal of Medical Devices*, vol. 3, no. 1, p. 011 001, Mar. 2009, ISSN: 19326181. DOI: 10.1115/1.3039513. [Online]. Available: http://medicaldevices.asmedigitalcollection.asme.org/article.aspx?articleid=1473872.

[147] P. Wilkening, W. Chien, B. Gonenc, J. Niparko, J. U. Kang, I. Iordachita, and R. H. Taylor, "Evaluation of virtual fixtures for robot-assisted cochlear implant insertion", in *Proceedings of the IEEE RAS and EMBS International Conference on Biomedical Robotics and Biomechatronics*, IEEE Computer Society, Aug. 2014, pp. 332–338, ISBN: 9781479931262. DOI: 10.1109/biorob.2014.6913798.

[148] L. Leon, F. M. Warren, and J. J. Abbott, "An In-Vitro Insertion-Force Study of Magnetically Guided Lateral-Wall Cochlear-Implant Electrode Arrays", *Otology and Neurotology*, vol. 39, no. 2, e63–e73, Feb. 2018, ISSN: 15374505. DOI: 10.1097/MAO.0000000000001647. [Online]. Available: https://pubmed.ncbi.nlm.nih.gov/29315180/.

[149] L. Leon, M. S. Cavilla, M. B. Doran, F. M. Warren, and J. J. Abbott, "Scala-tympani phantom with cochleostomy and round-window openings for cochlear-implant insertion experiments", *Journal of Medical Devices, Transactions of the ASME*, vol. 8, no. 4, Dec. 2014, ISSN: 1932619X. DOI: 10.1115/1.4027617.

[150] L. B. Kratchman, T. L. Bruns, J. J. Abbott, and R. J. Webster, "Guiding Elastic Rods with a Robot-Manipulated Magnet for Medical Applications", *IEEE Transactions on Robotics*, vol. 33, no. 1, pp. 227–233, Feb. 2017, ISSN: 15523098. DOI: 10.1109/TRO.2016.2623339.

[151] L. Leon, F. M. Warren, and J. J. Abbott, "Optimizing the Magnetic Dipole-Field Source for Magnetically Guided Cochlear-Implant Electrode-Array Insertions", *Journal of Medical Robotics Research*, vol. 03, no. 01, p. 1 850 004, Mar. 2018, ISSN: 2424-905X. DOI: 10.1142/s2424905x18500046. [Online]. Available: /pmc/articles/PMC6044464/?report=abstract%20https://www.ncbi.nlm.nih.gov/pmc/articles/PMC6044464/.

[152] T. L. Bruns and R. J. Webster, "An image guidance system for positioning robotic cochlear implant insertion tools", in *Medical Imaging 2017: Image-Guided Procedures, Robotic Interventions, and Modeling*, R. J. Webster and B. Fei, Eds., SPIE, Mar. 2017, pp. 10 135–101 350. [Online]. Available: http://proceedings.spiedigitallibrary.org/proceeding.aspx?doi=10.1117/12.2256043.

[153] A. J. Petruska and J. J. Abbott, "Omnimagnet: An omnidirectional electromagnet for controlled dipole-field generation", *IEEE Transactions on Magnetics*, vol. 50, no. 7, 2014, ISSN: 00189464. DOI: 10.1109/TMAG.2014.2303784.

[154] J. Michael Fitzpatrick, J. B. West, and C. R. Maurer, "Predicting error in rigid-body point-based registration", *IEEE Transactions on Medical Imaging*, vol. 17, no. 5, pp. 694–702, 1998, ISSN: 02780062. DOI: 10.1109/42.736021.

[155] A. Fedorov, R. Beichel, J. Kalpathy-Cramer, J. Finet, J. C. Fillion-Robin, S. Pujol, C. Bauer, D. Jennings, F. Fennessy, M. Sonka, J. Buatti, S. Aylward, J. V. Miller, S. Pieper, and R. Kikinis, "3D Slicer as an image computing platform for the Quantitative Imaging

Network", *Magnetic Resonance Imaging*, vol. 30, no. 9, pp. 1323–1341, Nov. 2012, ISSN: 0730725X. DOI: 10.1016/j.mri.2012.05.001.

[156] T. Ungi, A. Lasso, and G. Fichtinger, *Open-source platforms for navigated image-guided interventions*, Oct. 2016. DOI: 10.1016/j.media.2016.06.011.

[157] M. Quigley, B. Gerkey, K. Conley, J. Faust, T. Foote, J. Leibs, E. Berger, R. Wheeler, and A. Ng, "ROS: an open-source Robot Operating System", in *IEEE International Conference on Robotics and Automation Workshop*, 2009. [Online]. Available: http://stair.stanford.edu.

[158] A. J. Petruska and J. J. Abbott, "An omnidirectional electromagnet for remote manipulation", in *2013 IEEE International Conference on Robotics and Automation*, IEEE, May 2013, pp. 822–827, ISBN: 978-1-4673-5643-5. DOI: 10.1109/ICRA.2013.6630668. [Online]. Available: http://ieeexplore.ieee.org/document/6630668/.

[159] L. J. Sliker, G. C. Scuola, S. Sant'anna, and M. Rentschler, "Magnetically driven medical devices: A review", *Expert Review of Medical Devices*, 2015. DOI: 10.1586/17434440.2015.1080120. [Online]. Available: https://www.researchgate.net/publication/281146579.

[160] J. J. Abbott, E. Diller, and A. J. Petruska, "Magnetic Methods in Robotics", *Annual Review of Control, Robotics, and Autonomous Systems*, vol. 3, no. 1, pp. 57–90, May 2020, ISSN: 2573-5144. DOI: 10.1146/annurev-control-081219-082713. [Online]. Available: https://www.annualreviews.org/doi/10.1146/annurev-control-081219-082713.

[161] V. Hartwig, G. Giovannetti, N. Vanello, M. Lombardi, L. Landini, and S. Simi, "Biological Effects and Safety in Magnetic Resonance Imaging: A Review", *International Journal of Environmental Research and Public Health*, vol. 6, no. 6, pp. 1778–1798, Jun. 2009, ISSN: 1660-4601. DOI: 10.3390/ijerph6061778. [Online]. Available: http://www.mdpi.com/1660-4601/6/6/1778.

[162] G. Ziegelberger, P. Vecchia, M. Hietanen, A. Ahlbom, L. E. Anderson, E. Breitbart, F. R. De Gruijl, J. C. Lin, R. Matthes, A. P. Peralta, P. Söderberg, B. E. Stuck, A. J. Swerdlow, M. Taki, R. Saunders, and B. Veyret, "Guidelines on Limits of Exposure to Static Magnetic

Fields", *Health Physics*, vol. 96, no. 4, pp. 504–514, Apr. 2009, ISSN: 0017-9078. DOI: 10.1097/01.HP.0000343164.27920.4a. [Online]. Available: http://journals.lww.com/00004032-200904000-00010.

[163] D. J. Schaefer, J. D. Bourland, and J. A. Nyenhuis, "Review of Patient Safety in Time-Varying Gradient Fields", *Journal of Magnetic Resonance Imaging*, vol. 12, no. 1, pp. 20–29, Jul. 2000, ISSN: 10531807. DOI: 10.1002/1522-2586(200007)12:1<20::AID-JMRI3>3.0.CO;2-Y. [Online]. Available: https://onlinelibrary.wiley.com/doi/full/10.1002/1522-2586%28200007%2912%3A1%3C20%3A%3AAID-JMRI3%3E3.0.CO%3B2-Y%20https://onlinelibrary.wiley.com/doi/abs/10.1002/1522-2586%28200007%2912%3A1%3C20%3A%3AAID-JMRI3%3E3.0.CO%3B2-Y%20https://onlinelibrary.wiley.com/.

[164] S. Hügl, K. Rülander, T. Lenarz, O. Majdani, and T. S. Rau, "Investigation of ultra-low insertion speeds in an inelastic artificial cochlear model using custom-made cochlear implant electrodes", *European Archives of Oto-Rhino-Laryngology*, vol. 275, pp. 2947–2956, Dec. 2018, ISSN: 14344726. DOI: 10.1007/s00405-018-5159-1. [Online]. Available: https://doi.org/10.1007/s00405-018-5159-1.

[165] A. J. Petruska, J. Edelmann, and B. J. Nelson, "Model-Based Calibration for Magnetic Manipulation", *IEEE Transactions on Magnetics*, vol. 53, no. 7, Jul. 2017, ISSN: 00189464. DOI: 10.1109/TMAG.2017.2653080.

[166] F. J. Vanpoucke, P. P. B. Boermans, and J. H. Frijns, "Assessing the placement of a cochlear electrode array by multidimensional scaling", *IEEE Transactions on Biomedical Engineering*, vol. 59, no. 2, pp. 307–310, Feb. 2012, ISSN: 00189294. DOI: 10.1109/TBME.2011.2173198.

[167] R. F. Labadie and J. H. Noble, "Preliminary Results with Image-guided Cochlear Implant Insertion Techniques", *Otology and Neurotology*, vol. 39, no. 7, pp. 922–928, 2018, ISSN: 15374505. DOI: 10.1097/MAO.0000000000001850.

[168] A. D. Sweeney, M. L. Carlson, A. Rivas, M. L. Bennett, D. S. Haynes, and G. B. Wanna, "The limitations of computed tomography in adult cochlear implant evaluation", *American Journal of Otolaryngology - Head and Neck Medicine and Surgery*, vol. 35, no. 3, pp. 396–399, May 2014, ISSN: 1532818X. DOI: 10.1016/j.amjoto.2014.03.002.

[169] J. Wang and K. D. Wise, "A thin-film cochlear electrode array with integrated position sensing", *Journal of Microelectromechanical Systems*, vol. 18, no. 2, pp. 385–395, 2009, ISSN: 10577157. DOI: 10.1109/JMEMS.2008.2011722.

[170] H. Watanabe, J. Velmurugan, M. V. Mirkin, M. A. Svirsky, A. K. Lalwani, and R. R. Llinas, "Scanning electrochemical microscopy as a novel proximity sensor for atraumatic cochlear implant insertion", *IEEE Transactions on Biomedical Engineering*, vol. 61, no. 6, pp. 1822–1832, 2014, ISSN: 15582531. DOI: 10.1109/TBME.2014.2308058.

[171] M. Lathuillière, F. Merklen, J. P. Piron, M. Sicard, F. Villemus, N. Menjot de Champfleur, F. Venail, A. Uziel, and M. Mondain, "Cone-beam computed tomography in children with cochlear implants: The effect of electrode array position on ECAP", *International Journal of Pediatric Otorhinolaryngology*, vol. 92, pp. 27–31, Jan. 2017, ISSN: 18728464. DOI: 10.1016/j.ijporl.2016.10.033.

[172] D. Arweiler-Harbeck, V. D'heygere, M. Meyer, S. Hans, L. Waschkies, K. Anton, M. Heiler, and B. Höing, "Digital Live Imaging of intraoperative Electrocochleography – first description of feasibility and hearing preservation during Cochlear Implantation", *Laryngo-Rhino-Otologie*, vol. 100, no. S 02, May 2021, ISSN: 0935-8943. DOI: 10.1055/S-0041-1727690. [Online]. Available: http://www.thieme-connect.com/products/ejournals/html/10.1055/s-0041-1727690%20http://www.thieme-connect.de/DOI/DOI?10.1055/s-0041-1727690.

[173] F. J. Vanpoucke, A. J. Zarowski, and S. A. Peeters, "Identification of the impedance model of an implanted cochlear prosthesis from intracochlear potential measurements", *IEEE*

Transactions on Biomedical Engineering, vol. 51, no. 12, pp. 2174–2183, Dec. 2004, ISSN: 00189294. DOI: 10.1109/TBME.2004.836518.

[174] F. A. Di Lella, D. De Marco, F. Fernández, M. Parreño, and C. M. Boccio, "In Vivo Real-time Remote Cochlear Implant Capacitive Impedance Measurements", *Otology & Neurotology*, vol. 40, no. 5S Suppl 1, S18–S22, Jun. 2019, ISSN: 1531-7129. DOI: 10.1097/MAO.0000000000002214. [Online]. Available: http://journals.lww.com/00129492-201906001-00004.

[175] Q. Mesnildrey, O. Macherey, P. Herzog, and F. Venail, "Impedance measures for a better understanding of the electrical stimulation of the inner ear", *Journal of Neural Engineering*, vol. 16, no. 1, p. 016 023, Feb. 2019, ISSN: 17412552. DOI: 10.1088/1741-2552/aaecff. [Online]. Available: https://doi.org/10.1088/1741-2552/aaecff.

[176] N. Hafeez, X. Du, N. Boulgouris, P. Begg, R. Irving, C. Coulsan, and G. Tourrels, "Towards unblinding the surgeons: Complex electrical impedance for electrode array insertion guidance in cochlear implantiation", in *Proceedings of the International Symposium on Auditory and Audiological Research*, vol. 7, Danavox Jubilee Foundation, 2019, pp. 39–46. [Online]. Available: https://proceedings.isaar.eu/index.php/isaarproc/article/view/2017-06.

[177] P. A. Busby, K. L. Plant, and L. A. Whitford, "Electrode impedance in adults and children using the Nucleus 24 cochlear implant system", *Cochlear Implants International*, vol. 3, no. 2, pp. 87–103, 2002, ISSN: 14670100. DOI: 10.1179/cim.2002.3.2.87.

[178] E. Salkim, "Electrode Array Position Guiding in Cochlea Based on Impedance Variation : Computational Study", *Muş Alparslan Üniversitesi Mühendislik Mimarlık Fakültesi Dergisi*, vol. 1, no. 1, pp. 64–71, 2020.

[179] Y. Dong, J. Briaire, M. Siebrecht, H. Stronks, and J. Frijns, "Detection of Translocation of Cochlear Implant Electrode Arrays by Intracochlear Impedance Measurements", *Ear & Hearing*, vol. In Press, 2021.

[180] Ã. T. M. Klabbers, Ã. W. J. Huinck, and Ã. E. A. M. Mylanus, "Comparison Between Transimpedance Matrix (TIM) Measurement and X-ray Fluoroscopy for Intraoperative Electrode Array Tip Fold-Over Detection", *Otology & Neurotology*, no. 8, pp. 1–7, 2021. DOI: 10.1097/MAO.0000000000003290.

[181] S.-Y. Lee, Y. S. Kim, H. D. Jo, Y. Kim, M. Carandang, G. Huh, and B. Y. Choi, "Effects of in vivo repositioning of slim modiolar electrodes on electrical thresholds and speech perception.", *Scientific reports*, vol. 11, no. 1, p. 15 135, 2021, ISSN: 2045-2322. DOI: 10.1038/s41598-021-94668-6. [Online]. Available: http://www.ncbi.nlm.nih.gov/pubmed/34302030.

[182] J. Pile, G. B. Wanna, and N. Simaan, "Force-based flexible path plans for robotic electrode insertion", in *2014 IEEE International Conference on Robotics and Automation*, IEEE, 2014, pp. 297–303, ISBN: 9781479936854. DOI: 10.1109/ICRA.2014.6906625.

[183] D. F. Rogers and J. A. Adams, *Mathematical Elements for Computer Graphics*. 1989.

[184] J. M. Fitzpatrick, *Apparatus and methods of determining marker orientation in fiducial registration*, Feb. 2010.

Appendix A

Localization Error Investigation

1.1 Abstract

In image-guided surgery involving fiducials such as the surgery described in Chapter 2, surgical success hinges on accurate fiducial localization. A commonly used localization algorithm to compute the top of a Waypoint™ Anchor (FHC Inc., Bowdoin, Maine) has an incorrect offset from the localized centroid in the image to the extrapolated top of the anchor. In this work, this error was quantified to give users the ability to correct it if desired. For 0.3 mm isotropic voxel reconstructions, the error is between 0.15 mm and 0.17 mm. For 0.4 mm isotropic reconstructions, the error is between 0.14 mm and 0.17 mm, both with 95% confidence and assuming a Student's t-distribution. When it is important to know the location of the top of the anchor with high accuracy, the offset should be increased by 0.16 mm.

1.2 Methods

When bone anchors are present in image-guided surgeries, it is crucial to know the location of these bone anchors accurately in CT image space. Fitzpatrick developed an algorithm that automatically localizes a Waypoint Anchor in CT space ([184]). The algorithm works by first finding the anchor centroid $\boldsymbol{a}_m$ and anchor axis $\hat{\boldsymbol{u}}$ and then applying an offset term σ along the anchor axis to compute the anchor top $\boldsymbol{a}_t$:

$$\boldsymbol{a}_t = \boldsymbol{a}_m + \sigma\hat{\boldsymbol{u}}, \tag{A.1}$$

Qualitative observation of past clinical algorithm implementations have indicated that the offset term σ used to compute the anchor top is incorrect. The goal of this study was to quantify the offset error ϵ and apply this correction to compute the corrected position of the top of the anchor $\boldsymbol{a}_c$ as

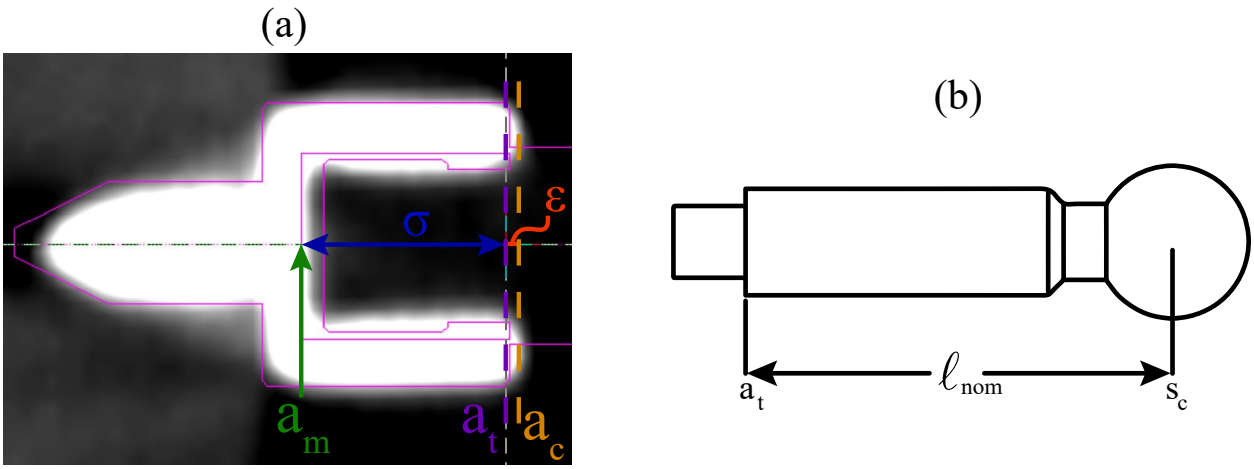

Figure 1.1: (a) Illustration of offset error variables and (b) Nominal extender length $\ell_{nom} = 0.7 \pm 0.001$ in

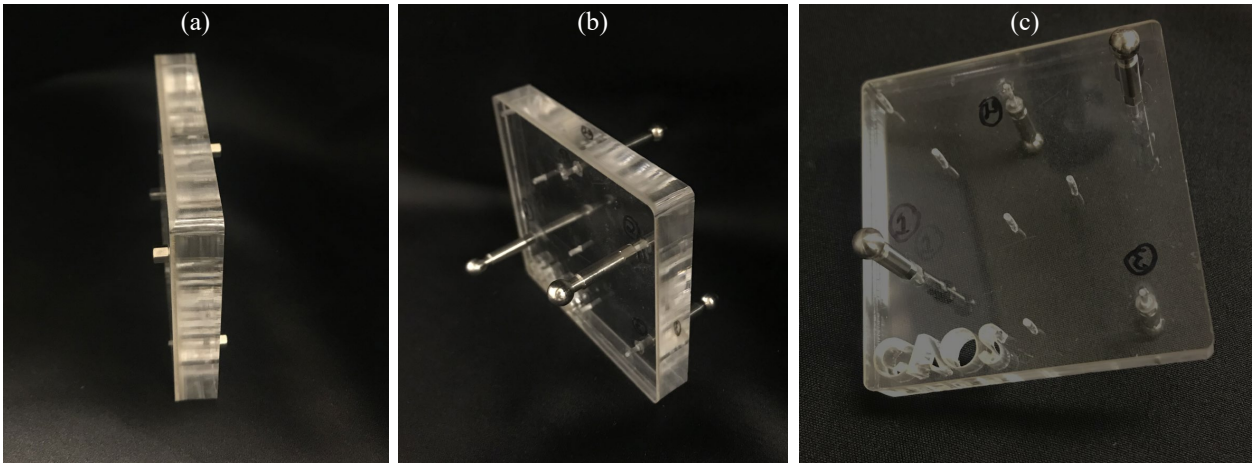

Figure 1.2: Acrylic block testing model

$$\boldsymbol{a}_c = \boldsymbol{a}_m + (\sigma + \epsilon)\hat{\boldsymbol{u}}, \tag{A.2}$$

(see Fig. 1.1(a) for visualization of parameter definitions).

In this work, an established point registration algorithm was leveraged ([154]) to compute the offset error in the current localization algorithm. Workflow began by localizing the anchors in image space with no extenders attached (Fig. 1.2(a)). Then, using the same anchors with extenders attached (see Fig. 1.2(b-c)), physical measurements of the extender sphere centers were taken using a coordinate measuring machine, named the "FARO® Gage Plus Arm" (FARO Technologies, Lake

Mary, FL), which will be referred to simply as the FARO for the remainder of this discussion (Fig. 1.3(a)). These two sets of measurements enabled rigid registration of the physically measured sphere centers to the image predicted sphere centers and offset correction determination.

To perform this study, an acrylic block (3 in x 3 in x 0.5 in) was fabricated with four fiducial anchors of interest (4 mm Waypoint FHC anchors) screwed into its body with the bottom of each anchor seat flush with the block face. Two anchors were screwed onto each 9 in^2 face at asymmetric locations (see Fig. 1.2(a)). The screws were then epoxied in place.

As mentioned, the goal of this study was to measure the anchor top locations in image space and the sphere locations with the extenders attached in physical space and compare the two to find the offset correction ϵ. First, the phantom model in Fig. 1.2(a) was used to localize the anchor positions in CT space using the clinical CT scanner in Fig. 1.3(b) - the Xoran® XCAT™ (Xoran® Technologies LLC., Ann Arbor MI). Fifteen images were acquired with the phantom model in various orientations and locations within the scanner's workspace. All fifteen images were reconstructed at isotropic voxel sizes of 0.3 mm and 0.4 mm. Next, the spherical extender shown in Fig. 1.1(b) (nominal length $\ell_{nom} = 0.7 \pm 0.001$ in) was attached to each anchor (Fig. 1.2(b-c)). The phantom model was rigidly fixed to the measuring table and the FARO was used to measure the position of the four sphere centers. Each sphere center was measured with the FARO three times.

1.2.1 Training Set

The acquired fifteen CT scans were partitioned into a training set (N = 10) and a test set (N = 5). In the training set, for each CT scan, the position of the top and the central axis vector of each anchor in image space were computed using the automatic algorithm. The predicted sphere positions in image space were then computed as

$$\boldsymbol{s}_{ci} = \boldsymbol{a}_t + \ell_{nom}\hat{\boldsymbol{u}}. \tag{A.3}$$

Next, these image space sphere positions were rigidly registered to the physically measured sphere positions. For each scan, this registration was done three times (once for each set of FARO

data). The function 'fminsearch' in MATLAB® (The MathWorks, Inc., Natick, MA) was used to find the extender length that minimized the FRE of the rigid point registration. In other words:

$$\arg\min_{\ell}(FRE). \tag{A.4}$$

The offset correction ϵ was then computed as the difference in ℓ_{nom} and the average fit length ℓ for each reconstruction set. Manufacturer variability in extender length was neglected here (approximately 0.03 mm).

1.2.2 Test Set

After computing the offset correction ϵ, this offset correction was then added in the source code for the automatic algorithm. The same steps were repeated for this test set of scans (N = 5) to test resulting accuracy with the new correction factor.

1.3 Results

Results of one of the point registrations between image space and physical space can be viewed in Fig. 1.4. Note that this registration was done three times for each scan (once for each set of FARO data). For a given CT scan, the FRE after registering to a set of FARO measurements had a standard deviation of approximately 0.005 mm among the three registrations. This variability was assumed to be negligible to the overall result for the remainder of the study. Fig. 1.6(a) and (b) show the clustered results for each of the three fits for a given scan number. For each scan, the average offset value was determined. For each reconstruction size in the training and test set, a *t*-test analysis was performed to determine whether the hypothesis that the offset values determined for that reconstruction came from a distribution with a mean of 0 and unknown variance could be rejected. The average offset error and *p*-value are reported below. H = 1 indicates that the null hypothesis can be rejected.

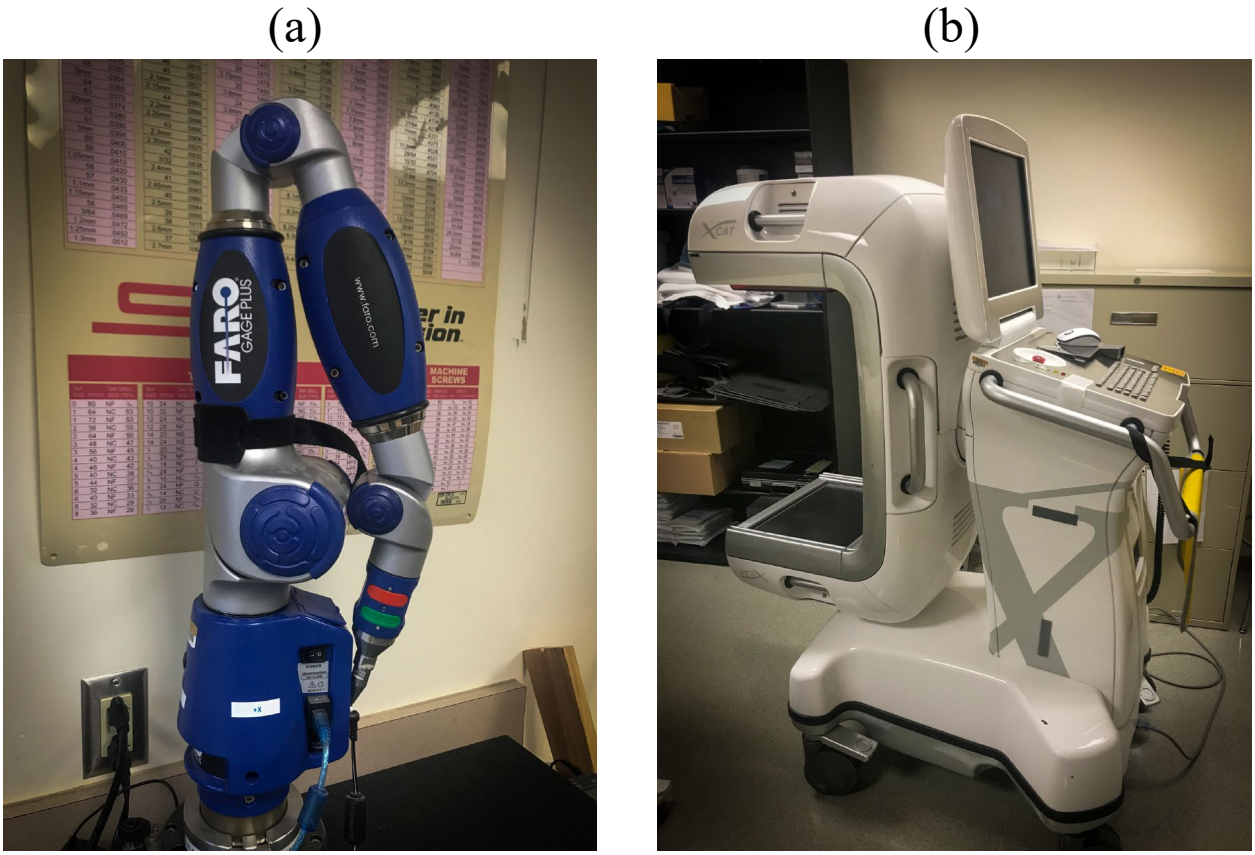

Figure 1.3: (a) FARO® Gage Plus Arm and (b) Xoran® XCAT CT Scanner

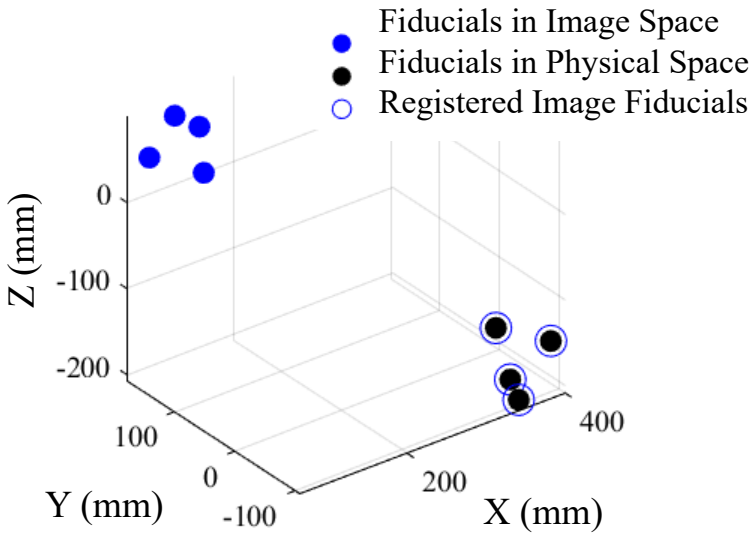

Figure 1.4: Example plot showing the result of one point registration

1.3.1 Training Set

The average offset error in the training set (N = 10) of the 0.3 mm reconstruction scans was 0.165 mm (H = 1, p-value = 3.6e-11) and of the 0.4 mm reconstruction was 0.155 mm (H = 1, p-value = 5.5e-10). Histograms of the residuals relative to the mean are shown in Fig. 1.5(a)). Although the sample size is limited, the residuals seem to be t-distributed. An overview of the training set data is shown in Fig. 1.6(a). Note that the residuals are randomly distributed about the average fit, supporting the hypothesis that this mean error is not just noise. These analyses resulted in an offset correction ϵ of 0.16 mm to be added into the source code to evaluate the scans in the test set of data.

Results for the test set of this reconstruction were created by modifying the source code of the localization algorithm to correct for the error found in the training set. In other words, ϵ was added to the offset term as in (A.2).

1.3.2 Test Set

Results of the the test set can be viewed in Fig. 1.5(b) and Fig. 1.6(b). Most importantly, in Fig. 1.6(b), it can be seen that for both the 0.3 mm and 0.4 mm reconstructions, the new average fit lines are within 0.03 mm of the nominal extender length, indicating that the correction factor was effective. The average offset error of the 0.3 mm reconstruction scans was -0.01 mm (H = 1, p-value = 0.04) and of the 0.4 mm reconstruction scans was -0.03 mm (H = 1, p-value = 0.001). Although the hypothesis that the offset error came from a distribution with a mean of zero is still rejected in this case, the p-value increased dramatically from the training set. This result can be partially explained by the decrease in N for the test set, and of course emphasizes that further refinement of the offset error is possible.

1.4 Discussion & Conclusion

In this study, the offset error inherent to a Waypoint localization algorithm was quantified. Limitations of this study include that only the Xoran CT scanner and 0.3 mm and 0.4 mm isotropic reconstructions were used. Future work should investigate whether different reconstruction sizes,

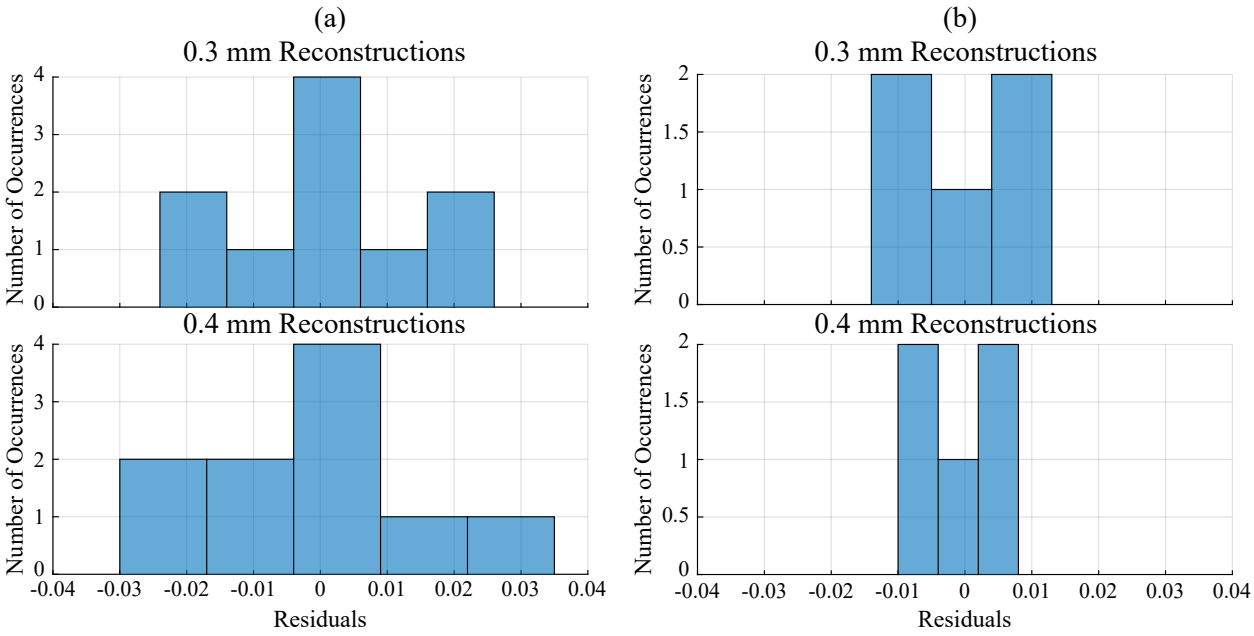

Figure 1.5: (a) Histogram of residuals in training set and (b) Histogram of residuals in testing set

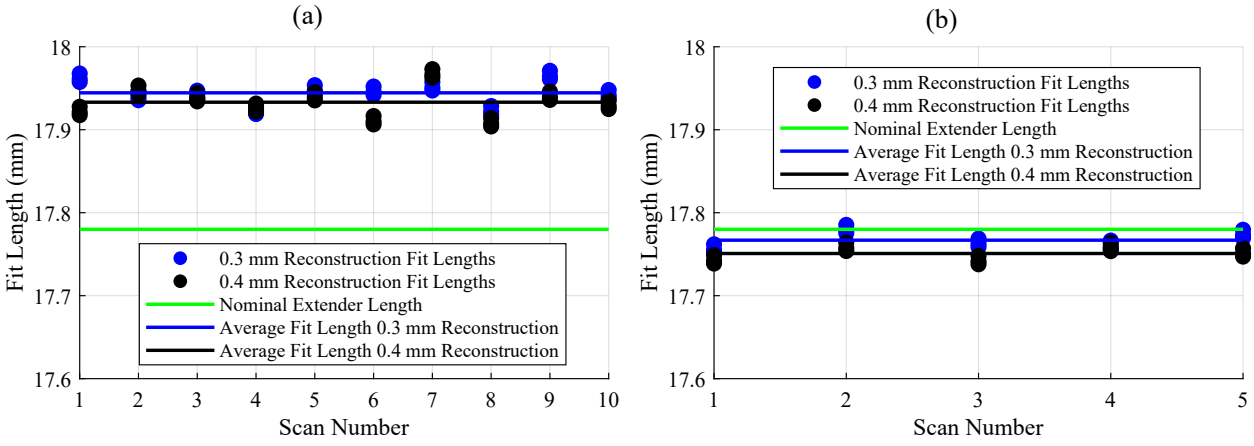

Figure 1.6: (a) Overview of training set results and (b) Overview of testing set results

anisotropic reconstructions, and different CT scanners would change the result. Furthermore, future studies could investigate whether anchor length influences the result. In this work the use of a model of the bone anchor whose screw portion is 4 mm long was exclusively investigated, but studies could also investigate error in localization of an alternative version 5 mm long screw.

Knowledge of this offset correction could prove crucial in the future if accuracy is extremely important. Furthermore, given the simplicity of the correction, the ease with which it can be corrected, and the lack of any know negative effects, it would be difficult to justify not correcting the error in any system that utilizes this localization algorithm. Although the magnitude of the error found in this study may have been inconsequential in the past, intervention has in recent years trended steadily toward smaller targets and encroached steadily closer to critical structures.